# Acoustic Reporter Genes for Noninvasive Imaging of Cellular Function

Thesis by
Arash Farhadi

In Partial Fulfillment of the Requirements for the
Degree of
Doctor of Philosophy in Biological Engineering


CALIFORNIA INSTITUTE OF TECHNOLOGY
Pasadena, California

2020
Defended April 9, 2020

Arash Farhadi
ORCID: 0000-0001-9137-8559

# ACKNOWLEDGEMENTS

> If you always do what you always did, you will always get what you always got.
>
> *Albert Einstein*

At Caltech, I have had the good fortune to pursue my doctoral research in an incredibly supportive environment. I want to first thank my PhD advisor, Mikhail Shapiro, for guiding me through this journey and for being an amazing mentor in every sense of the word. You have continuously challenged me to be more creative, to communicate better, to fearlessly pursue impactful research and for that I am grateful. You have been enthusiastic when I needed encouraging, insightful whenever I was at a roadblock, and always generous with your time.

I would like to thank my committee members, Dr. David Tirrell, Dr. Richard Murray, and Dr. Lihong Wang for their guidance, support and encouragement over the past few years.

I am also indebted to all of the past and present members of the Shapiro Lab for making research in the lab so enjoyable. It has been a privilege to collaborate and learn from such talented scientists. Thank you, Hunter for being a great officemate. I have enjoyed discussing science and politics with you and have greatly benefited from brainstorming our wild ideas. Thank you, Dan, Pradeep and Di for your friendship and for making me smile day in, day out. Blake, Mickey and Shannon, thank you for all your love and support. I have always been able to count on you; you have become my second family. Special gratitude belongs to Gabrielle, who exceeded all my expectations and has made major contributions to the work throughout this thesis. I look forward to seeing you accomplish great things during your PhD and future scientific career.

I would like to extend my deepest gratitude to my family for their patience, support and constant encouragement. To my parents (Mehrtaj Kaviani and Artadner Farhadi), your unconditional love and unwavering belief in me have been the single greatest source of motivation throughout the years and I am forever grateful. I appreciate all that you have done for me. Asha, Roozbeh and Shervin, thank you for being amazing siblings and a constant inspiration.

I have also benefited from the love and support of my family-in-law. Special thanks to Parvin Kavousi and Farsheid Koulena for taking me in as one of your own

and for sending me so much love and support. You have all helped me live a more balanced life by reminding me to take things a little less seriously.

I have saved my most important acknowledgement for last. Noushin, my brilliant best friend, loving partner, scientific consultant, my fiercest advocate – you believed in me when I doubt myself – thank you for coming on this journey with me. You patiently listened to countless hours of me obsessing about gas vesicles and helped me troubleshoot endless failed experiments. This thesis would not have been possible without your steadfast support and love. I am eternally grateful for your ability to restore balance and perspective in my life.

# ABSTRACT

The study of cellular function within the context of intact living organisms is a grand challenge in biological research. Addressing this challenge requires imaging tools that can visualize cells inside the body. If successful, this would greatly increase our ability to study a battery of processes from brain development to tumorigenesis, to monitoring cell-based therapeutics. To date, most common methods for imaging cellular processes such as gene expression have relied on optical reporters, such as fluorescent or luminescent proteins, which provide high molecular precision for studies in petri dishes and transparent organisms, but have limited performance in large animals due to the poor penetration of light in biological tissue. Conversely, magnetic resonance imaging (MRI) and ultrasound can image tissues at depth with high spatial and temporal resolution, but they lack molecular reporters analogous to the green fluorescent protein (GFP). As a result, they have made limited impact on biological research. To address this, we focus on developing biomolecular reporters for MRI and ultrasound – based on a unique class of air-filled protein nanostructures called gas vesicles – using them to image the location and function of cells deep inside the body.

This thesis begins with a brief review of genetically encoded materials for noninvasive imaging, highlighting key advances over the past two decades and providing context for the work below. We discuss the development of increasingly sophisticated tools starting from early efforts to engineer single molecule reporters to recent work on multi-component genetic machinery (including gas vesicles) with multi-modality capabilities. In Chapter 2, we present a platform for engineering the surface of gas vesicles to modulate their acoustic, surface charge, and molecular-targeting properties as injectable acoustic biomolecules. In Chapter 3, we present the recombinant expression of gas vesicles as injectable contrast agents in common lab strain bacteria to facilitate the genetic engineering of the entire gas vesicle gene cluster and to assist this technology's adoption by other (non-specialist) research groups. This work characterized the ultrasound and hyperpolarized $^{129}$Xenon-MRI contrast of gas vesicles as nanoscale contrast agents.

In a parallel effort, we developed a hybrid gene cluster that when introduced to microbes enables the imaging of their gene expression using ultrasound. These bacterial acoustic reporter genes were used to image the location of probiotic cells inside the gastrointestinal tract of mice. However, the ability for these genes to be expressed in mammalian cells had not been demonstrated and presented a major

challenge in synthetic biology. In Chapter 4, we addressed this by introducing the first mammalian acoustic reporter genes – a genetic program whose introduction to mammalian cells resulted in the expression of gas vesicles that can be visualized by ultrasound. These mammalian acoustic reporter genes will enable previously impossible approaches to monitoring the location, viability and function of mammalian cells *in vivo*.

In Chapter 5, we explore a new paradigm in MRI by taking advantage of the acousto-magnetic property of gas vesicles. Here, we present background-free MRI to address a longstanding challenge in untangling the signal of exogenous contrast agents from the endogenous MRI contrast produced by biological tissues. Chapter 6 explores the optical properties of gas vesicles as genetically encodable phase contrast agents in digital holographic imaging. Chapter 7 is a brief discussion of the potential future directions for this work.

The data presented in this thesis lays the ground for exciting new research on developing noninvasive biomolecular tools that will enable the discovery of novel biological processes.

# PUBLISHED CONTENT AND CONTRIBUTIONS

1. Farhadi, A., Ho, G. H., Sawyer, D. P., Bourdeau, R. W. & Shapiro, M. G. Ultrasound imaging of gene expression in mammalian cells. *Science* **365,** 1469–1475. doi:10.1126/science.aax4804 (2019).

   A.F. and M.G.S. conceived and planned the project. A.F. and G.H.H. performed the experiments. A.F. and R.W.B. designed the DNA sequences. A.F. and D.P.S. designed and optimized the ultrasound imaging sequences. A.F. analyzed the data. A.F. and M.G.S. wrote the manuscript with input from all authors.

2. Lu, G. J., Farhadi, A., Mukherjee, A. & Shapiro, M. G. Proteins, air and water: reporter genes for ultrasound and magnetic resonance imaging. *Current Opinion in Chemical Biology* **45,** 57–63. doi:10.1016/j.cbpa.2018.02.011 (2018).

   A.F. and G.J.L contributed equally to this manuscript. A.F. participated in the preparation of the manuscript.

3. Lu, G. J., Farhadi, A., Szablowski, J. O., Lee-Gosselin, A., Barnes, S. R., Lakshmanan, A., Bourdeau, R. W. & Shapiro, M. G. Acoustically modulated magnetic resonance imaging of gas-filled protein nanostructures. *Nature Materials* **17,** 456–463. doi:10.1038/s41563-018-0023-7 (2018).

   A.F., G.J.L., J.O.S., A.L-G. and M.G.S. designed, planned and carried out the experiments and analysed data. A.F. worked with G.J.L to perform the clustering-based molecular sensors experiments. A.F. assisted G.J.L. and M.G.S. with writing the manuscript.

4. Bourdeau, R. W., Lee-Gosselin, A., Lakshmanan, A., Farhadi, A., Kumar, S. R., Nety, S. P. & Shapiro, M. G. Acoustic reporter genes for noninvasive imaging of microorganisms in mammalian hosts. *Nature* **553,** 86–90. doi:10.1038/nature25021 (2018).

   A.F., R.W.B., A.L., A.L.-G. and S.P.N. prepared genetic constructs in *E. coli*. A.F., R.W.B., A.L., A.L.-G., and S.P.N. conducted *in vitro* ultrasound experiments. A.F., A.L., and A.L-G. conducted metabolic burden experiments in *E. coli* Nissle 1917 cells. A.F. assisted R.W.B. and M.G.S. with writing the manuscript.

5. Farhadi, A., Ho, G., Kunth, M., Ling, B., Lakshmanan, A., Lu, G., Bourdeau, R. W., Schroder, L. & Shapiro, M. G. Recombinantly Expressed Gas Vesicles as Nanoscale Contrast Agents for Ultrasound and Hyperpolarized MRI. *AIChE Journal* **64,** 2927–2933. doi:10.1002/aic.16138 (2018).

   A.F. and M.G.S. conceived and planned the project. A.F., G.H.H, M.K., B.L., A.L., G.J.L. and R.W.B. prepared the samples, collected and analyzed the data. A.F. prepared the samples used by M.K. and L.S. in the hyperpolarized

$^{129}$Xe MRI experiments. A.F. and M.G.S wrote the manuscript with input from all authors.

6. Maresca, D., Lakshmanan, A., Abedi, M., Bar-Zion, A., Farhadi, A., Lu, G. J., Szablowski, J. O., Wu, D., Yoo, S. & Shapiro, M. G. Biomolecular Ultrasound and Sonogenetics. *Annual Review of Chemical and Biomolecular Engineering* **9,** 229–252. doi:10.1146/annurev-chembioeng-060817-084034 (2018).

   A.F. participated in the preparation of the manuscript.

7. Lakshmanan, A., Lu, G. J., Farhadi, A., Nety, S. P., Kunth, M., Lee-Gosselin, A., Maresca, D., Bourdeau, R. W., Yin, M., Yan, J., Witte, C., Malounda, D., Foster, F. S., Schroder, L. & Shapiro, M. G. Preparation of biogenic gas vesicle nanostructures for use as contrast agents for ultrasound and MRI. *Nature Protocols* **12,** 2050–2080. doi:10.1038/nprot.2017.081 (2018).

   A.F., A.L., G.J.L., S.P.N. contributed equally to this manuscript. A.F., A.L., G.J.L., S.P.N. and M.G.S. conceived the manuscript layout and coordinated its writing. A.F., A.L., G.J.L., S.P.N., A.L-G., D. Maresca, D. Malounda, R.W.B. and M.G.S developed methods for GV production, functionalization, and characterization, as well as for ultrasound imaging. A.F., A.L., G.J.L., S.P.N. and M.G.S. wrote the manuscript with input from all authors.

8. Le Floc'h, J., Zlitni, A., Bilton, H. A., Yin, M., Farhadi, A., Janzen, N. R., Shapiro, M. G., Valliant, J. F. & Foster, F. S. In vivo Biodistribution of Radiolabeled Acoustic Protein Nanostructures. *Molecular Imaging and Biology* **20,** 230–239. doi:10.1007/s11307-017-1122-6 (2018).

   A.F. prepared the pristine purified gas vesicles and the fluorescent dye-conjugated gas vesicles used in this study and assisted in the preparation of the manuscript.

9. Piraner, D. I., Farhadi, A., Davis, H. C., Wu, D., Maresca, D., Szablowski, J. O. & Shapiro, M. G. Going Deeper: Biomolecular Tools for Acoustic and Magnetic Imaging and Control of Cellular Function. *Biochemistry* **56,** 5202–5209. doi:10.1021/acs.biochem.7b00443 (2017).

   A.F. participated in the preparation of the manuscript.

10. Lakshmanan, A., Farhadi, A., Nety, S. P., Lee-Gosselin, A., Bourdeau, R. W., Maresca, D. & Shapiro, M. G. Molecular Engineering of Acoustic Protein Nanostructures. *ACS Nano* **10,** 7314–22. doi:10.1021/acsnano.6b03364 (2016).

    A.F., A.L., and S.P.N. designed and planned experiments. A.F., A.L., S.P.N., A.L-G., and D.M. conducted the experiments and analyzed data. A.F. assisted A.L. and M.G.S. with writing the manuscript.

# TABLE OF CONTENTS

# LIST OF ILLUSTRATIONS

# LIST OF TABLES

*Chapter 1*

# GENETICALLY ENCODABLE MATERIALS FOR NONINVASIVE BIOLOGICAL IMAGING

This chapter is in large part a reformatted version of the manuscript entitled "Genetically Encodable Materials for Noninvasive Biological Imaging" currently under peer-review. Under the supervision of Mikhail Shapiro, I contributed to the writing of the manuscript with valuable input from Felix Sigmund and Gil Wesmeyer. The section on ultrasound imaging is in part from the manuscript entitled "Biomolecular Ultrasound and Sonogenetics" published in *Annual Review of Chemical and Biomolecular Engineering*[1]. Under the supervision of Mikhail Shapiro, I contributed to the preparation of the manuscript and wrote the 'Development of acoustic reporter genes' section.

## 1.1 The Need for Noninvasive Imaging of Gene Expression

Biology is complex. One of the best ways to unravel its mysteries is to look at biological processes and then turn these observations into models that summarize our understanding. Therefore, it should come as no surprise that many advances in biology arise from new abilities to observe previously inaccessible biological processes. For example, the development of the lens enabled Robert Hooke to access the microscopic world, allowing him to see and described the first (plant) cell, and the Golgi staining technique allowed Ramón y Cajal to see the cellular organization of the brain and create illustrations that inspired modern neuroscience. Few technologies have had as significant an impact as the green fluorescent protein (GFP) – an imaging agent that can be genetically encoded inside a cell, providing an intimate connection to its internal life cycle and molecular signals. Due to its success, GFP has become just one-of-among-many available reporter genes used by scientists. There are two common uses of reporter genes are: always-on configuration used to locate and track cells over time, and dynamic reporters used for connecting the expression of the reporter gene to the transcriptional state of the cell. Reporter genes can be engineered further to report on the molecular state of cells with genetically encoded calcium indicators (*i.e.* GCaMP) being the most widely used example.

Currently, most reporter genes rely on light, which due to its strong scattering

in biological tissue has limited utility beyond approximately one mm in depth[2]. Vast demand exists to go deeper, driven by the need to study cellular function within the context of intact organisms, the development of cell-based diagnostic and therapeutic agents, and the engineering of complex living materials.

Unlike optical imaging, ultrasound and magnetic resonance imaging (MRI) penetrate deep inside intact tissue, resulting in their widespread use in clinical medicine. Over the past 20 years, substantial effort has been devoted to developing genetically encodable reporters for these noninvasive imaging modalities: a "GFP for ultrasound" and a "GFP for MRI", resulting in important conceptual and practical advances. In this chapter, I will summarize key advances in the recent developments of richer, more complex biological materials using the tools of protein engineering and synthetic biology. A brief introduction to concepts in ultrasound imaging and MRI important to this thesis will be summarized below.

## 1.2 Ultrasound Imaging

Ultrasound is defined by sound wave frequencies above those audible to humans (> 20,000 Hz). Generated by transducers coupled to a transmission medium such as biological tissue, ultrasound waves travel through the medium and interact with its components to form images. In biological tissues, as in liquids, compression waves are dominant and are used for most modes of imaging. In tissue, sound waves travel at ~1540 m/s, and are reflected and scattered wherever they experience a change in acoustic impedance, which is a function of the local density and compressibility[3] (Fig. 1-1a). The relative homogeneity of the speed of sound in soft tissues results in sound waves remaining coherent as they traverse the tissue, enabling simple image reconstruction without major aberrations[4]. By comparison, visible light is strongly scattered in tissues, making it challenging for it to retain a ballistic path at depths greater than a few hundred microns (Fig. 1-1b).

Ultrasound reflection at tissue interfaces is highly directional and reveals anatomical contours. Soft tissues have similar acoustic impedance values, resulting in relatively low contrast between them; air and bones have much lower and higher acoustic impedances, respectively, resulting in strong reflections[4]. When the ultrasound wave encounters a target smaller than approximately 1/10$^{th}$ the wavelength, it is scattered omnidirectionally[5]. Biological tissues include a wide range of such scatterers in the form of fibers, cells and organelles. The echo from a single scatterer is usually very weak. When a large number of very close scatterers are imaged, the result is a dominant spatially coherent interference pattern called speckle[4]. The

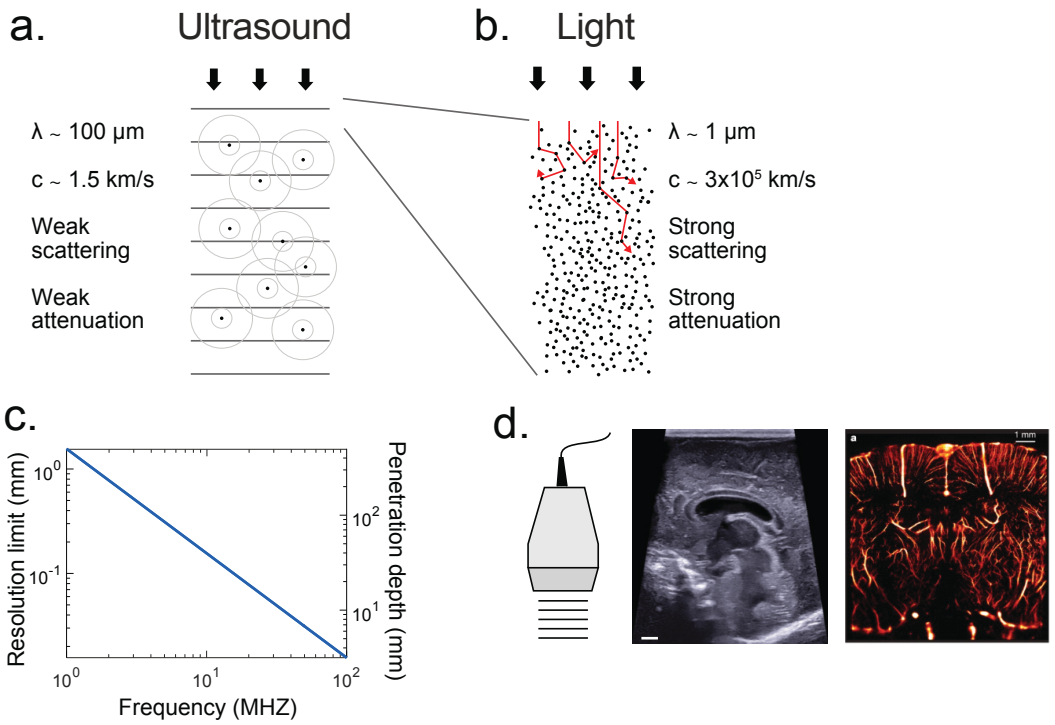


**Figure 1-1: Properties of ultrasound waves for imaging applications.** (A) Physical properties of ultrasound waves in biological tissues. (B) Physical properties of light traveling in biological tissue. (C) Fundamental tradeoff between ultrasound resolution and penetration depth as a function of frequency in brain tissue (penetration depth was assessed based on a 60-decibel round-trip attenuation). At an ultrasound frequency of 15 MHz, one can expect to image the brain 2 cm deep at a 100-µm resolution. (D) Illustration of ultrasound imaging capabilities; conventional B-mode image of an infant brain with a submillimeter resolution of cerebral structures; 15-MHz superresolution ultrasound image of the rat brain vasculature with an 8-µm resolution, breaking the classical tradeoff exposed in (C) (Adapted from Errico *et al.*[6])

amplitude of the ultrasound wave decreases exponentially as a function of depth. Part of the energy of the ultrasonic wave is absorbed in the tissue and dissipated as heat. Attenuation refers to both absorption and any reduction in wave amplitude due to reflection or scattering. Each tissue is characterized by a different attenuation coefficient value, which increases non-linearly with frequency[4].

Ultrasound imaging is the most prescribed diagnostic modality in clinical practice[7]. Typical equipment involves an ultrasound scanner and an ultrasound probe made of a linear array of transducer elements (*i.e.* 128 to 256 ultrasound transmitting/receiving elements)[8]. Numerous ultrasound imaging modes have been translated to clinical practice; several of these modes are relevant to biomolecular ultrasound and will be briefly outlined below.

**B-mode imaging**

Ultrasound scanners are primarily used to produce real-time 2-dimensional images of underlying tissue (Fig. 1-1d). These grayscale images are referred to as B-mode images (where B stands for brightness) and are acquired through transmission, into a tissue, of short ultrasound pulses and recording of backscattered echoes. The location of a scattering or reflecting source is reconstructed from the arrival time of its signal at each array element in a process known as beamforming. The position of a point in the reconstructed B-mode image depends on the time of flight of the echo and the position of the transmitting probe element. The in-depth or axial resolution of B-mode images depends on the wavelength ($\lambda = c_{tissue}/f_{US}$) and the number of cycles of vibration of the transmitted pulse. The axial resolution typically ranges from 500 µm (medical imaging) down to 50 µm (ultrasound biomicroscopy)[9]. Since both attenuation and resolution increase with frequency, there is an inherent tradeoff between resolution and imaging depth (Fig. 1-1c). The lateral resolution of B-mode images depends on the transmitted ultrasound beam width and is typically a few hundred microns. The transverse resolution or image thickness is usually on the order of a millimeter. B-mode imaging is used to image every organ of the body with the exception of bones or air-filled organs as the lungs.

**Contrast imaging**

Contrast-enhanced ultrasound relies on the administration of contrast agents to label specific aspects of anatomy or physiology. The conventional contrast agents used for this purpose are microbubbles: synthetic, micron-sized bubbles of gas stabilized by a lipid or protein shell[10–13]. When injected into the blood stream, microbubbles produce strong scattering as they resonate at ultrasound imaging frequencies (1–20 MHz). Dedicated ultrasound contrast modes have been developed to benefit from that resonant behavior, such as amplitude modulation[14] or phase inversion[15], allowing the detection of microbubbles *in vivo* with higher specificity. Amplitude modulation isolates nonlinear ultrasound signals by transmitting ultrasound waves at different amplitudes (for example one high amplitude wave and two half-amplitude waves) and by subtracting the high amplitude signal from the superposition of the fractional amplitudes, all the linear backscattered signal will cancel out to reveal the nonlinear ultrasound signals. Pulse inversion uses the transmission of ultrasound waves at 180° phase-shift, and the subtracted backscattered ultrasound suppresses linear signal to reveal nonlinear signals.

**Ultrafast imaging**

Conventional B-mode imaging utilizes a series of focused transmissions along an ultrasound array to form an image, such that the acquisition of a 10 cm-deep image with a 128-element probe takes at least $128 * 10\text{ cm} * 2/1540\text{ m/s} \sim 17$ ms, resulting in a framerate of 59 Hz. A major recent advance, known as ultrafast ultrasound, uses single plane wave transmissions, rather than focused line transmissions, to form images, resulting in a two-orders-of-magnitude acceleration in framerate[16]. The equivalent temporal resolution for a 10 cm image is $10\text{ cm} * 2/1540\text{ m/s} \sim 130$ µs, or 7,700 frames per second. This advance was made possible by improvements in computer hardware allowing flexible software beamforming. This technology was initially developed for shear wave elastography and later applied to Doppler imaging.

**Functional ultrasound imaging**

Ultrasound Doppler imaging detects the motion of red blood cells (RBCs) and, therefore, blood flow[17]. RBCs scatter weak ultrasound echoes, which can be captured with modern ultrasound probes. At a given depth in tissue, the temporal shifts observed in consecutive RBC echoes allow detection of the displacement of RBCs and derivation of a Doppler signal proportional to RBC velocity. By combining ultrafast ultrasound and Doppler imaging, ultrafast Doppler imaging has increased the sensitivity of conventional Doppler imaging by a factor 30. This leads to high resolution, high signal-to-noise ratio (SNR) maps of the brain vasculature in rodents[18]. The sequential acquisition of vascular maps of the brain with ultrafast Doppler has enabled the detection of neural activity through neurovascular coupling[19]. Research efforts are ongoing to turn functional ultrasound imaging of the brain into a full-fledged neuroscience modality which complements functional-MRI with improved spatiotemporal resolution, portability and cost.

## 1.3 Magnetic Resonance Imaging

Magnetic resonance imaging (MRI) is an imaging modality that interacts with the magnetic moment of nuclear spins, typically of protons ($^1$H) from water, due to their abundance in biological samples. Protons can be thought of as tiny molecular magnets with a magnetic moment (µ). When a sample is placed in a strong magnetic field ($B_1$), an ensemble of the protons align longitudinally, parallel to the applied magnetic field. In a typical MRI experiment, a pulsed radiofrequency wave is applied to tilt the aligned protons to the transverse plane, 90° from the $B_1$ plane,

and the resultant radiofrequency signal as the nuclear spins relax to equilibrium is detected and used to produce MR images.

Two common modes of acquiring MRI contrast are transverse $T_2$ (spin-spin) relaxation and longitudinal $T_1$ (spin-lattice) relaxation. For $T_2$ relaxation contrast, initially the transverse magnetic component of protons are in-phase but quickly begin to dephase (due local field inhomogeneities and the interaction between different spins) and the transverse magnetic components decay at an exponential time constant $T_2$. For $T_1$ relaxation constant, the longitudinal magnetic component recovers at an exponential time constant $T_1$ as the excited spins align back to the $B_1$ field and release their energy to their environment. $T_1$ and $T_2$ relaxation time constants can be affected a number of factors including type of nuclei, rate of motion of the molecule, chemical environment, presence of paramagnetic metal ions and temperature.

### 1.4 Genetically Encodable Materials: Small Proteins

The earliest genetically encoded reporter used for MRI was an enzyme working in conjunction with a synthetic organometallic contrast agent (Fig. 1-2a). In 2000, Louie *et al.* synthesized a $Gd^{3+}$ chelator named EgadMe that incorporated a sugar as part of its organic structure[20]. The coordination of $Gd^{3+}$ by water, which leads to $T_1$-weighted MRI contrast, was competitively inhibited by EgadMe's sugar moiety. The enzyme $\beta$-galactosidase, then commonly used as an optical reporter of gene expression visualized with sugar-containing chromogens, cleaved off the sugar on EgadMe and thereby increased MRI contrast. While this reporter has not been used beyond its initial demonstration in frog embryos due to its modest contrast change and challenging biodistribution, it inspired the development of other genetically encodable MRI reporters.

The first protein to produce MRI contrast in the absence of external reagents was the iron storage protein ferritin, which accumulates bioavailable paramagnetic iron inside an 8-nm protein shell (inner diameter) and produces $T_2$-weighted MRI contrast. In 2005, two groups independently showed that overexpression of this protein could result in contrast detectable *in vivo*[21,22]. To date, ferritin has been used in more MRI reporter gene studies than any other protein. However, it leaves much to be desired in terms of its performance, and significant efforts have been made to engineer improved ferritins and alternative protein nanocompartments, as described in the next section.

Besides ferritin, other iron-containing proteins used to generate MRI contrast include methemoglobin[25], transferrin, and the cytochrome P450-BM3. A variant

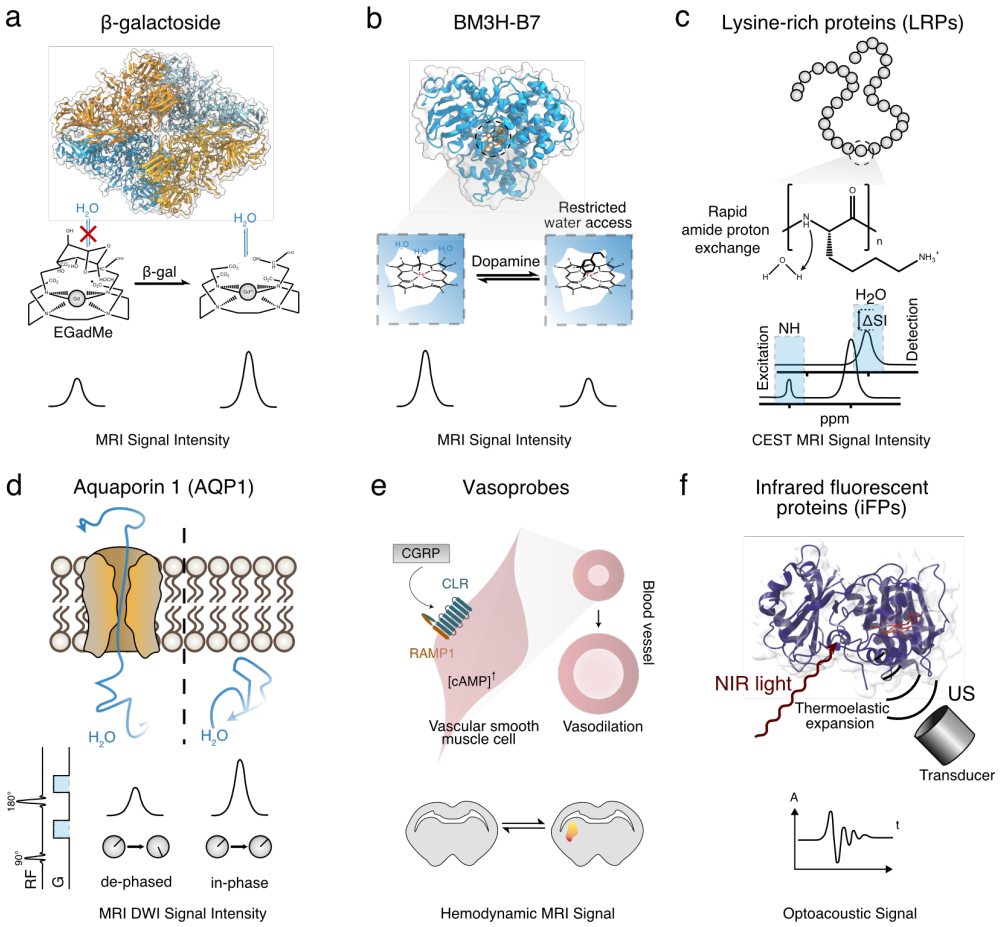


**Figure 1-2: Small proteins as genetically encoded contrast agents for noninvasive imaging.** (A) The tetrameric enzyme beta-galactosidase cleaves the galactopyranosyl ring on the synthetic $Gd^{3+}$ chelator EgadMe, leading to increased water binding and $T_1$-weighted MRI contrast. (B) The heme-binding domain of P450-BM3 was evolved to selectively bind the neurotransmitter dopamine to alter water access to the paramagnetic $Fe^{3+}$, yielding a molecular sensor of dopamine for $T_1$-weighted MRI. (C) Designed lysine repeat proteins (LRPs) rapidly exchange amide protons with water, thus yielding enhanced contrast in chemical exchange saturation transfer (CEST) MRI. (D) Reporter gene for diffusion-weighted MRI based on increased water diffusion across the cell membrane after overexpression of Aquaporin 1 (AQP1) (E) Hemodynamic contrast mechanism based on local expression and release of vasoactive peptides lead to increased blood flow detectable with fMRI or other imaging techniques sensitive to hemodynamics. (Adapted from Desai *et al.*[23]) (F) Bacterial phytochrome-derived infrared fluorescent proteins (iFPs) can serve as contrast agents for optoacoustic imaging. When absorbing near-infrared laser pulses, the chromophores transform photons into pressure waves detectable with ultrasound. PDB structures 3J7H ($\beta$-galactosidase), 4DU2 (BM3h-B7) and 4CQH (iFP 2.0) were visualized using ChimeraX[24].

of the latter protein was the first MRI reagent engineered with the help of directed evolution and served as a dynamic molecular sensor of dopamine[26] (Fig. 1-2b). While versions of this sensor have been used to map neurotransmitter release in the brain, it has so far been employed as an injectable contrast agent rather than one expressed locally in the tissue. Besides iron, proteins have been engineered to produce MRI contrast by binding other paramagnetic metal ions such as $Gd^{3+}$ ref.[27]. In addition, transporters such as the transferrin receptor and OATP1 have been used to selectively accumulate externally administered iron and $Gd^{3+}$ chelates, respectively[28,29].

Metals are not the only way to achieve MRI contrast. Other early work on protein-based MRI contrast agents focused on proteins with large numbers of exchangeable protons that can be imaged with chemical exchange saturation transfer (CEST) MRI[30] (Fig. 1-2c). One of the main advantages of CEST-based reporter genes is that they do not require metal cofactors, which may have limited *in situ* availability. On the other hand, they must typically be expressed at relatively high concentrations and imaged at high field strengths to be detected above the background of endogenous cellular proteins. More recently, reporter genes for CEST MRI have also been developed based on enzymes that catalyze the intracellular accumulation of synthetic CEST-active substrates[31].

While these pioneering approaches demonstrated the feasibility of protein-based MRI contrast, they have not been widely adopted by the broader biological community. The primary reasons include the requirement for relatively high concentrations, the need for metal cofactors, and competition from background tissue contrast[32].

Recently another class of non-metallic MRI reporter genes was introduced that overcomes some of these limitations. These reporters produce contrast in diffusion-weighted imaging (DWI) by altering the apparent diffusivity of water in tissue (Fig. 1-2d). Recognizing that the cell membrane is a dominant barrier to water diffusion, Mukherjee *et al.* showed that the overexpression of aquaporin, a simple transmembrane channel that exclusively conducts water, could increase the apparent diffusivity of model tissues by up to 200%, resulting in a dramatic change in DWI contrast[33]. An experiment in mice showed that intracranial tumors triggered to express aquaporin could be distinguished by DWI. In a similar study published at nearly the same time, Schilling *et al.* overexpressed the urea transporter UT-B, which co-transports water with urea and also acts as a passive water channel[34].

Another innovative mechanism for genetically encodable MRI contrast is based

on vasoactive peptides whose expression leads to local vasodilation, resulting in fMRI-like contrast[23] (Fig. 1-2e). This allows a modest concentration of peptide to produce a relatively large signal. Reliance on hemodynamic signals complicates imaging procedures, but maybe extendable beyond MRI to other hemodynamic modalities. In addition, vasoactive probes can be engineered as sensors with activity conditioned on other molecules[35].

Unlike in the case of MRI, in which reporter genes had to be developed from scratch, the task of generating optoacoustic contrast with proteins was, in some ways, more straightforward. Optoacoustic imaging is a fast, volumetric technique that can map the distribution of photoabsorbers at deeper tissue layers than accessible by conventional optical microscopy by converting light absorption into sound waves via thermoelastic expansion[36,37]. Any photoabsorbing molecule that dissipates at least some of the absorbed energy non-radiatively can in principle produce optoacoustic contrast.

Genetically expressed chromoproteins can provide sufficient optoacoustic contrast, especially if they possess a high extinction coefficient in the near-infrared range in which absorbance from endogenous molecules such as hemoglobin is relatively low (Fig. 1-2f). In addition, low quantum yield is desired to maximize the conversion of photoexcitation into heat. These conditions can be fulfilled in bacteriophytochromes in which biliverdin serves as a chromophore[38–40].

Particularly attractive for increasing signal-to-noise are reversibly photoswitchable chromoproteins whose signal time course can be differentiated from static background signals even if the latter have higher amplitude[41]. Multiplexing of several reversibly switchable chromoproteins can be achieved by temporal unmixing of the respective signal time courses. In addition, the concentration-independent switching kinetics can be used to correct signal degradation due to spatially varying intensities of the illumination[42,43]. This strategy to suppress static background was particularly effective using chromoproteins with absorbance spectra in the near-infrared window[44]. Furthermore, molecules that change their absorbance spectrum as a function of surrounding analytes can be used as dynamic optoacoustic sensors. This mechanism was showcased by adapting GCaMP for optoacoustic imaging of calcium transients in zebrafish[45]. The tissue depth and sensitivity with which optoacoustic reporters and sensors can be visualized can be improved by using chromoproteins with absorption spectra further toward near-infrared wavelengths[46].

## 1.5 Genetically Encodable Materials: Protein Nanocompartments

As briefly discussed above, the primary mammalian iron-storage compartment ferritin has been over-expressed to generate $T_2$-weighted MRI contrast. However, its performance is limited by the relatively small size of its iron core (7-8 nm[47]) and its weak magnetism (mostly anti-ferromagnetic[48] with paramagnetic surface spins). Several groups have attempted to improve the properties of mammalian ferritin. A fusion of the heavy and light chain was, for instance, proposed to improve performance as a one-component system[49]. Two prokaryotic one-component ferritins were also subjected to a mutational screen, yielding variants with improved iron occupancy[50,51]. However, the highly conserved iron transport and ferroxidase functionalities in ferritins seem to limit the improvement possible via protein engineering.

Could larger genetically controlled nanocompartments be generated that are more modular than ferritins and provide larger storage capacity? Nanostructures that self-assemble from proteinaceous building blocks are widespread in nature and have long been explored as miniature reaction vessels in semi-synthetic approaches. Douglas *et al.* showed in 2002 that the interior of the capsid encoded by the Cowpea chlorotic mottle virus (CCMV) could be subjected to electrostatic engineering to facilitate iron-mineralization *in vitro*[52].

Recently it was shown that members of a large family of prokaryotic nanocompartments called encapsulins[53–55] could be heterologously expressed in mammalian cells (Fig. 1-3). There they self-assemble, auto-encapsulate ferritin-like cargo proteins and lead to non-toxic iron biomineralization of up to an order of magnitude more iron compared to ferritin[56]. Heterologous expression of encapsulin variants enabled $T_2^*$ contrast enhancement in mammalian cells in culture and upon xenografting into rat brains[56] (Fig. 1-3a, b). Thanks to the electron-dense iron-oxide core, encapsulins are also readily detectable as fiducial markers in cryo-electron tomograms[56]. Different variants of encapsulants can also serve as multiplexable reporter genes for conventional transmission electron microscopy (TEM) to, for instance, label neuronal types or states in model organisms based on distinct geometrical features[57] (Fig. 1-3b, d). The genetically controlled iron biomineralization thus enables multimodal molecular imaging that can be cross-registered across vast scales ranging from MRI to electron microscopy. The two-component encapsulin-shell:ferroxidase system furthermore enables functionalization of the inner surface with proteins that can modify the crystallization process and redox state of iron, such as peptides derived from magnetotactic bacteria[56]. Notably, overexpression of

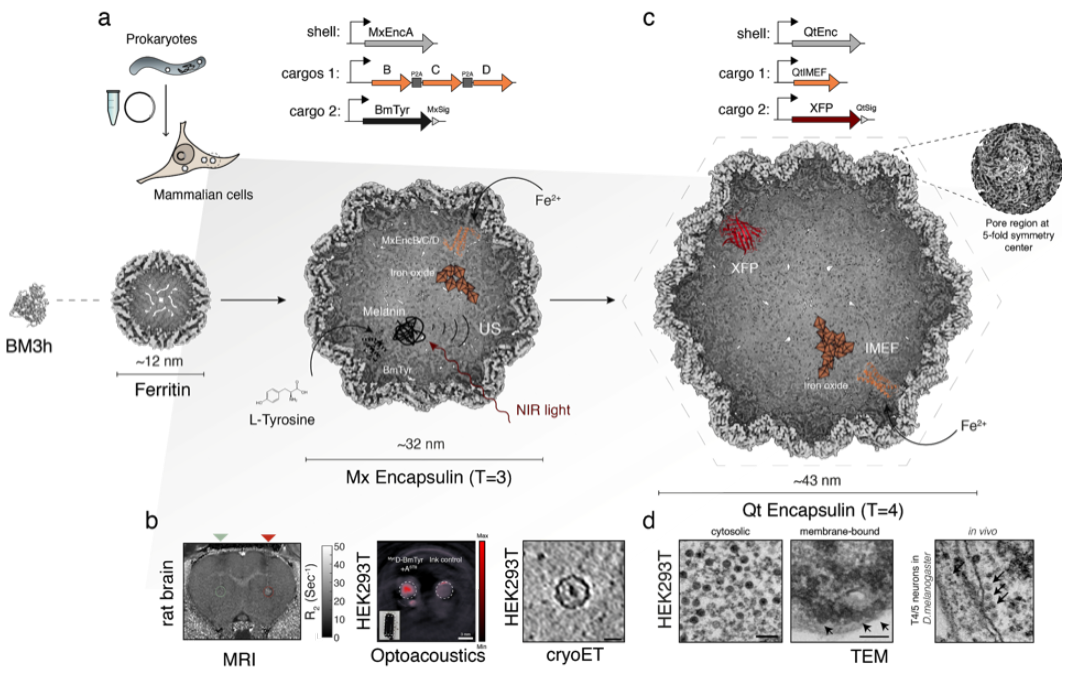


**Figure 1-3: Proteinaceous nanocompartments as multiscale contrast agents.** Schematic summarizing work on metalloproteins for molecular imaging applications. (A) Genetic constructs for expression of the *M. xanthus* encapsulin system in mammalian systems consisting of its shell forming monomer MxEncA and a multigene expression cassette for co-expression of its endogenous cargo proteins (MxEncBCD) or engineered cargos such as a soluble bacterial tyrosinase (BmTyr) with a C-terminal encapsulation signal. Cutaway view of the MxEnc nanocompartment (T=3) schematically showing internal cargo proteins either yielding iron oxides for detection in MRI or cryoET or melanin pigments that afford (B) detection by MRI, optoacoustics, and cryo-electron tomography. (Adapted from Sigmund *et al.*[56].) (C) Genetic constructs for expression of the *Q. thermotolerans* encapsulin system in mammalian systems consisting of its shell forming monomer QtEnc and its iron-mineralizing cargo protein QtIMEF, or other engineered cargos such as fluorescent proteins. Cutaway view of the larger QtEnc nanocompartment (T=4 icosahedral symmetry) showing a zoom-in onto the pore region at the five fold symmetry center and docked QtIMEF cargo yielding effective iron biomineralization affording contrast in TEM images of (D) HEK293T cells and T4/5 Drosophila neurons. (Adapted from Sigmund *et al.*[57].) Structures of BM3h (PDB: 4DU2), ferritin (EMD-2788), Mx Encapsulin (EMD-5917), BmTyr (PDB: 3NM8), Qt Encapsulin (EMD-4879) and QtIMEF (PDB: 6N63) were visualized using ChimeraX[24].

iron-filled encapsulins from *Myxococcus xanthus* allowed for magnetically actuated cell sorting (MACS) using standard commercial columns, whereas expressing iron-loaded ferritin did not enable this feature[56]. Similarly, substantial MRI contrast and MACS separation were also enabled in *E. coli* expressing a fusion protein mediating iron oxidation and accumulation into a disordered ferrogel[58].

While the preceding results demonstrate that high levels of paramagnetic iron can be effective, even stronger MRI contrast and magnetic manipulation could be

achieved with the formation of superparamagnetic or ferromagnetic magnetite or maghemite crystals, such as those found in the magnetosomes of magnetotactic bacteria[59]. To date, magnetosomes have only been heterologously expressed in a close genetic relative of magnetotactic bacteria[60]. This remarkable feat has, however, not yet been achieved in common prokaryotes applied in biotechnology or eukaryotic cells.

Encapsulins can also be engineered to form nanomaterials with other material properties, such as strong photoabsorbance. This feature can, for instance, be achieved by selective targeting of enzymatic activity to the encapsulin lumen by either complementing split enzymes inside the compartment or by attaching a degradation signal that ablates all copies of the enzyme that are not encapsulated. In this way, robust contrast can be obtained in optoacoustic images by encapsulating a soluble bacterial tyrosinase, which converts tyrosine molecules entering through the shell's pores into polymeric melanin that becomes trapped in the lumen (Fig. 1-3a). Melanin has a broad absorbance spectrum reaching into the near-infrared range and generates strong signals in optoacoustic imaging[61] (Fig. 1-3b). However, melanin, in its natural form, for example in human skin, is sequestered in membrane-enclosed melanosomes expressed by specialized melanophore cells because it tends to be toxic when freely available in cells. Compartmentalizing melanin formation into encapsulin-based "designer melanosomes" thus successfully emulates detoxification by sequestration. Given that multiple enzymes can be arrayed inside encapsulins, biosynthetic pathways for pigments such as violacein[62], with sharper absorption spectra than melanin, could be produced inside encapsulins to optimize multiplexing via multispectral optoacoustic tomography (MSOT). Such use of biosynthetic pigments can be superior to chromoproteins, which have a comparably lower photostability, presenting challenges, especially for optoacoustic microscopy techniques that apply relatively high energy densities to the sample.

Inspired by the capability of animals such as the cuttlefish to change their skin color by relocalizing pigment-filled organelles inside dedicated chromatophore cells, it was recently furthermore demonstrated that melanin-filled melanophore can be turned into optoacoustic sensors for imaging the activation of the important class of G-protein-coupled receptors (GPCRs)[63]. GPCR-ligand-induced agglomeration of the melanin-filled cellular organelles inside the reporter cells could not only be detected via an increase in the optoacoustic signal amplitude but also by a shift in the optoacoustic signal frequency, providing an orthogonal means of observing dynamically changing molecular contrast[63].

## 1.6 Genetically Encodable Materials: Proteins with gas

The ability of gas to produce contrast is well-established for both ultrasound and MRI. Synthetic ultrasound contrast agents include microbubbles, which obtain their ability to scatter sound waves from their differential density and compressibility relative to aqueous tissue[64]. Meanwhile, the differential magnetic susceptibility of air-filled body cavities (such as lungs and nasal passages) relative to tissue distorts MR images. Can the unique properties of gas be harnessed in the context of genetically encodable materials?

In 2014, Shapiro *et al.* described the use of a unique class of air-filled protein nanostructures, called gas vesicles (GVs), as acoustic biomolecules for ultrasound imaging[65]. GVs are made of a 2-nm thick protein shell that assembles into a hollow nanostructure with dimensions on the order of 100 nm (Fig. 1-4a). GVs are natively expressed as flotation devices in a number of waterborne microbes, where they are encoded by operons of 8-14 genes, including structural proteins and assembly factors essential for GV formation. The large acoustic impedance mismatch between the GVs' gaseous interior and surrounding aqueous media allows these nanoparticles to produce ultrasound contrast *in vitro* and *in vivo*. In addition, the ability of certain natural and engineered GV genotypes to undergo buckling mechanical deformations under ultrasound results in nonlinear contrast, facilitating their detection against background tissue[66–69]. Since GVs are genetically encodable, their mechanics can be tuned using protein engineering techniques, and they can be functionalized with new surface properties and targeting moieties[68,70].

To turn GVs into acoustic reporter genes (ARGs) for ultrasound, the polycistronic gene clusters encoding GV assembly must be adapted from their native organisms into new species. This was first accomplished in bacteria. By combining GV genes from two organisms, *Anabaena flos-aquae* and *Bacillus megaterium*, a hybrid cluster was developed (Fig. 1-4b) that encodes the expression of GVs in *E. coli* and *Salmonella typhimurium*, two commensal microbes and common chassis for synthetic biology[74]. This approach enabled the imaging of bacterial gene expression inside the GI tract of mice. Bacterial ARGs open the possibility of studying and tracking microbial interactions inside mammalian hosts with ultrasound, and can be a powerful tool in the development of microbial diagnostics and therapeutics[75]. Significant scope exists to optimize the expression and acoustic properties of bacterial ARGs, and to deploy them in a greater number of species and *in vivo* scenarios. In each application, it will be critical to verify that ARG expression does not present an unacceptable metabolic burden or change in cell phenotype.

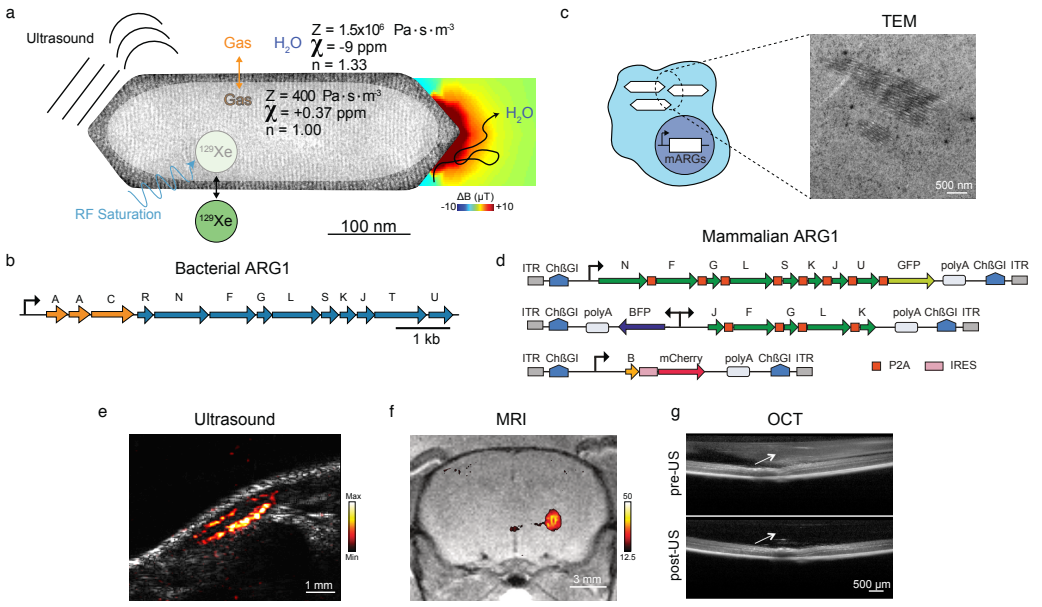


**Figure 1-4: Genetically encodable air-filled protein nanostructures as multimodality contrast agents.** (A) Transmission electron micrograph of a gas vesicle, and a diagram of the various material properties used to produce contrast in imaging modalities. Z, acoustic impedance; $\chi$ magnetic susceptibility; n, index of refraction. (B) Engineered bacterial gene cluster, ARG1, comprising genes from *Anabaena flos-aquea* (orange) and *Bacillus megaterium* (blue) that encode the heterologous expression of GVs in bacteria. (C) Representative electron micrograph of heterologously expressed GVs in the cytosol of mammalian cells. (D) Synthetic mammalian operon, mARG1, comprising 9 genes originating from *B. megaterium* that result in GV expression in mammalian cells. (E-G) GVs as genetically encodable contrast agents and reporter genes for *in vivo* (E) ultrasound imaging[71], (F) magnetic resonance imaging[72] and (G) optical coherence tomography[73].

After bacterial expression, the next major milestone was to develop ARGs for mammalian cells. Transferring a large polycistronic program for self-assembly from prokaryotes to eukaryotes is a major challenge in synthetic biology due to the differential handling of transcription and translation between these kingdoms and the need to ensure proper folding, stoichiometry and assembly of the constituent proteins. Farhadi *et al.* overcame this challenge by constructing mammalian ARG operons based on 9 genes from *B. megaterium*, stringing groups of these genes together using viral 2A self-cleavage peptides and controlling stoichiometry though copy number[71] (Fig. 1-4c, d). ARG expression could then be imaged in human cells *in vitro* at volumetric densities below 0.5% and in cells expressing just a few GVs per cell. *In vivo* ARG expression was imaged in a mouse tumor xenograft, revealing localized gene expression with a spatial resolution of 100 μm (Fig. 1-4e). ARG imaging in mammalian cells was enabled by a highly sensitive ultrasound imaging

paradigm taking advantage of strong acoustic emissions from GVs as they collapse in response to acoustic pressure. Further optimization is needed to turn mammalian ARGs into a commonly used reporter gene. For example, expression in primary cells such as neurons and immune cells will benefit from the packaging of ARGs into viral vectors, which typically requires a smaller genetic footprint. Additional study of the immune response to GVs and GV-expression is also needed to enable clinical translation of this technology in the context of cell-based diagnostics and therapeutics.

Can GVs also serve as reporter genes for MRI? This possibility was realized by Lu *et al.* by demonstrating that the presence of GVs leads to dephasing of proton nuclear spins, yielding $T_2/T_2^*$-weighted MRI contrast. This phenomenon is based on the magnetic susceptibility difference between the air-filled interior of GVs (slightly paramagnetic) and surrounding aqueous media (diamagnetic) (Fig. 1-4a)[72]. Furthermore, the collapse of GVs with ultrasound during MRI acquisition allowed acoustic modulation of the GVs' MRI contrast and the acquisition of background-subtracted images. This allowed their molecular contrast to be easily distinguished from potentially confounding endogenous contrast sources, as demonstrated *in vitro* and in several mouse organs (Fig. 1-4f). In addition to conventional proton MRI, GVs are also able to serve as contrast agents for hyperpolarized $^{129}$Xe ref.[76]. In this application, the protein shell of GVs allows xenon dissolved in the surrounding solution to partition in and out of the GV, enabling the production of CEST contrast. Because hyperpolarization greatly boosts the signal obtained from each nucleus, this scheme increases the sensitivity of GV detection, reaching sub-nM levels. Since the introduction of GVs as the first reporter gene for $^{129}$Xe-MRI, other proteins have also been shown to bind xenon and produce CEST contrast[77].

Besides ultrasound and MRI, the gaseous core of GVs provides an opportunity for their use as genetically encodable contrast agents for optical imaging techniques sensitive to refractive index, which differs substantially between air and water (Fig. 1-4a). For example, it was recently shown that GVs can serve as contrast agents for optical coherence tomography (OCT), a modality widely used in biomedical imaging due to its ability to provide single-μm spatial resolution at tissue depths of several mm. In this application, GVs play a role directly analogous to ultrasound by backscattering photons, as shown *in vitro* and the mouse eye[73] (Fig. 1-4g). In a separate study, it was shown that the propagation of light waves through GVs distorts their phase, allowing GVs and GV-expressing cells to be visualized using digital holographic microscopy (DHM), a volumetric imaging technique with unique

advantages for *in vitro* microscopy[78].

Alongside their uses in imaging, GVs can transduce ultrasound into mechanical force[79] and inertial bubble cavitation[80], allowing GVs and GV-expressing cells to be manipulated with acoustic fields and serve as therapeutic agents for targeted cell killing and drug release. These additional capabilities enable new possibilities in cellular actuation, engineered living materials[81] and theranostics that are beyond the scope of this Introduction.

### 1.7 Genetically Encodable Materials: Outlook

The new materials and approaches described above are already providing unprecedented ways to visualize cellular function *in vivo*. However, many challenges and opportunities remain for improved performance and broader applications. While most of the materials used as genetically encoded contrast agents have been derived from naturally evolved genes, it should be possible to access a wider range of physical properties through *de novo* protein design, taking advantage of rapid progress in the engineering of proteins with new structure, self-assembly, and function[82]. As with natural proteins, *de novo* constructs for imaging could be improved with directed evolution[26] and machine learning[83], and new properties could be added by employing non-canonical amino acids and bio-orthogonal chemistry[84]. Going beyond proteins, new ways to generate complex structures with nucleic acids, sugars, and other cellular polymers may enable new functionality. In parallel, natural genomes containing the Earth's collective evolutionary diversity will doubtless continue to offer unexpected new materials and inspiration for biomimetic designs.

Here, we have emphasized the advantages of leveraging more complex, self-assembling biomaterials. Continuing to engineer such materials and harness even more complex structures such as magnetosomes will require operating at the limits of synthetic biology, including not just improved ways of combining and delivering genes, but gaining control over cellular phases, compartments, and specialized organelles. Besides, modifications of the host cell's genome may also be needed to enable the expression of new materials or minimize the impact on host cell viability and function. In addition, it may be possible to leverage the dynamic behavior of synthetic biological circuits to produce time-varying signals to enhance the sensitivity and specificity of imaging. Achieving these goals is likely to advance not just biological imaging, but synthetic biology itself[85].

Another relatively unexplored frontier in biological imaging *in vivo* is the development of dynamic sensors for cellular signals ranging from extracellular

neurotransmitters and proteases to intracellular ions such as calcium. A wide array of dynamic biosensors is available for fluorescence microscopy[86], while relatively few examples have been put forward for ultrasound, MRI or optoacoustic imaging.

With these improvements in performance and capabilities, genetically encodable reporters for noninvasive imaging will play a more significant role in basic biology, cell-based diagnostics, therapeutics, and engineered living materials. It may one day be possible for biologists to order a GV-expressing or encapsulin-expressing transgenic mouse to study the function of a certain cell type *in vivo* as easily as is standard today with mouse lines expressing GFP, or to select from a catalog of viral vectors expressing these reporters for convenient labeling of cells or tissues. In engineered living materials[81], these same reporters are likely to play an increasing role as cell-based, and cell-made structures continue to scale in dimensions beyond the reach of optical microscopy. Finally, genetically encoded reporters have the opportunity to help address the need to track and monitor the performance of genetic and cellular therapeutics during both preclinical development and deployment in patients. The possibility that some of the materials discussed in this chapter can also serve as agents for cellular manipulation and therapy will help propel them deeper into each of these application areas.

## References


1. Maresca, D. *et al.* Biomolecular Ultrasound and Sonogenetics. *Annu. Rev. Chem. Biomol. Eng.* **9,** 229–252 (2018).
2. Piraner, D. I. *et al.* Going Deeper: Biomolecular Tools for Acoustic and Magnetic Imaging and Control of Cellular Function. *Biochemistry* **56,** 5202–5209 (2017).
3. Szabo, T. L. *Diagnostic ultrasound imaging: inside out* ISBN: 0126801452 (Academic Press, 2004).
4. Azhari, H. *Basics of biomedical ultrasound for engineers* ISBN: 0470561467 (John Wiley & Sons, 2010).
5. Cobbold, R. S. *Foundations of biomedical ultrasound* ISBN: 0199775125 (Oxford University Press, 2006).
6. Errico, C. *et al.* Ultrafast ultrasound localization microscopy for deep super-resolution vascular imaging. *Nature* **527,** 499–502 (2015).
7. Liang, H.-D., Noble, J. A. & Wells, P. N. T. Recent advances in biomedical ultrasonic imaging techniques. *Interface Focus* **1,** 475–476 (2011).
8. Powers, J. & Kremkau, F. Medical ultrasound systems. *Interface focus* **1,** 477–489 (2011).
9. Foster, F. S., Pavlin, C. J., Harasiewicz, K. A., Christopher, D. A. & Turnbull, D. H. Advances in ultrasound biomicroscopy. *Ultrasound in Medicine and Biology* **26,** 1–27 (2000).
10. Ferrara, K., Pollard, R. & Borden, M. Ultrasound microbubble contrast agents: fundamentals and application to gene and drug delivery. *Annual review of biomedical engineering* **9** (2007).
11. Paefgen, V., Doleschel, D. & Kiessling, F. Evolution of contrast agents for ultrasound imaging and ultrasound-mediated drug delivery. *Frontiers in pharmacology* **6** (2015).
12. Unnikrishnan, S. & Klibanov, A. L. Microbubbles as ultrasound contrast agents for molecular imaging: preparation and application. *American journal of roentgenology* **199,** 292–299 (2012).
13. Frinking, P. J. A., Bouakaz, A., Kirkhorn, J., Ten Cate, F. J. & de Jong, N. Ultrasound contrast imaging: current and new potential methods. *Ultrasound in Medicine and Biology* **26,** 965–975 (2000).
14. Mor-Avi, V. *et al.* Combined assessment of myocardial perfusion and regional left ventricular function by analysis of contrast-enhanced power modulation images. *Circulation* **104,** 352–7 (2001).

15. Simpson, D. H., Chin, C. T. & Burns, P. N. Pulse inversion Doppler: a new method for detecting nonlinear echoes from microbubble contrast agents. *IEEE Transactions on Ultrasonics, Ferroelectrics, and Frequency Control* **46,** 372–82 (1999).

16. Tanter, M. & Fink, M. Ultrafast imaging in biomedical ultrasound. *IEEE Transactions on Ultrasonics, Ferroelectrics, and Frequency Control* **61,** 102–119 (2014).

17. Evans, D. H., Jensen, J. A. & Nielsen, M. B. Ultrasonic colour Doppler imaging. *Interface Focus* **1,** 490–502 (2011).

18. Mace, E. *et al.* Functional ultrasound imaging of the brain: theory and basic principles. *IEEE Transactions on Ultrasonics, Ferroelectrics, and Frequency Control* **60,** 492–506 (2013).

19. Mace, E. *et al.* Functional ultrasound imaging of the brain. *Nature Methods* **8,** 662–4 (2011).

20. Louie, A. Y. *et al.* In vivo visualization of gene expression using magnetic resonance imaging. *Nature Biotechnology* **18,** 321–325 (2000).

21. Genove, G., DeMarco, U., Xu, H., Goins, W. F. & Ahrens, E. T. A new transgene reporter for in vivo magnetic resonance imaging. *Nature Medicine* **11,** 450–454 (2005).

22. Cohen, B., Dafni, H., Meir, G., Harmelin, A. & Neeman, M. Ferritin as an endogenous MRI reporter for noninvasive imaging of gene expression in C6 glioma tumors. *Neoplasia* **7,** 109–117 (2005).

23. Desai, M., Slusarczyk, A. L., Chapin, A., Barch, M. & Jasanoff, A. Molecular imaging with engineered physiology. *Nature Communications* **7,** 13607 (2016).

24. Goddard, T. D. *et al.* UCSF ChimeraX: Meeting modern challenges in visualization and analysis. *Protein Sci.* **27,** 14–25 (2018).

25. Duewell, S., Kasserra, C. E., Jezzard, P. & Balaban, R. S. Evaluation of methemoglobin as an autologous intravascular MRI contrast agent. *Magn. Reson. Med.* **35,** 787–789 (1996).

26. Shapiro, M. G. *et al.* Directed evolution of a magnetic resonance imaging contrast agent for noninvasive imaging of dopamine. *Nature Biotechnology* **28,** 264–270 (2010).

27. Yang, J. J. *et al.* Rational design of protein-based MRI contrast agents. *J. Am. Chem. Soc.* **130,** 9260–9267 (2008).

28. Deans, A. E. *et al.* Cellular MRI contrast via coexpression of transferrin receptor and ferritin. *Magn. Reson. Med.* **56,** 51–59 (2006).

29. Patrick, P. S. *et al.* Dual-modality gene reporter for in vivo imaging. *Proceedings of the National Academy of Sciences* **111,** 415–420 (2014).

30. Gilad, A. A. *et al.* Artificial reporter gene providing MRI contrast based on proton exchange. *Nature Biotechnology* **25,** 217–219 (2007).

31. Yuan, Y. *et al.* Furin-mediated intracellular self-assembly of olsalazine nanoparticles for enhanced magnetic resonance imaging and tumour therapy. *Nature Materials* **18,** 1376–1383 (2019).

32. Mukherjee, A., Davis, H. C., Ramesh, P., Lu, G. J. & Shapiro, M. G. Biomolecular MRI reporters: Evolution of new mechanisms. *Prog. Nucl. Magn. Reson. Spectrosc.* **102-103,** 32–42 (2017).

33. Mukherjee, A., Wu, D., Davis, H. C. & Shapiro, M. G. Non-invasive imaging using reporter genes altering cellular water permeability. *Nature Communications* **7,** 13891 (2016).

34. Schilling, F. *et al.* MRI measurements of reporter-mediated increases in transmembrane water exchange enable detection of a gene reporter. *Nature Biotechnology* **35,** 75–80 (2017).

35. Ohlendorf, R. *et al. Target-responsive vasoactive probes for ultrasensitive molecular imaging* 2019.

36. Ntziachristos, V. Going deeper than microscopy: the optical imaging frontier in biology. *Nature Methods* **7,** 603–614 (2010).

37. Wang, L. V. & Hu, S. Photoacoustic tomography: in vivo imaging from organelles to organs. *Science* **335,** 1458–1462 (2012).

38. Shu, X. *et al.* Mammalian expression of infrared fluorescent proteins engineered from a bacterial phytochrome. *Science* **324,** 804–807 (2009).

39. Filonov, G. S. *et al.* Bright and stable near-infrared fluorescent protein for in vivo imaging. *Nature Biotechnology* **29,** 757–761 (2011).

40. Fuenzalida Werner, J. P. *et al.* Structure-Based Mutagenesis of Phycobiliprotein smURFP for Optoacoustic Imaging. *ACS Chem. Biol.* **14,** 1896–1903 (2019).

41. Stiel, A. C. *et al.* High-contrast imaging of reversibly switchable fluorescent proteins via temporally unmixed multispectral optoacoustic tomography. *Opt. Lett.* **40,** 367–370 (2015).

42. Deán-Ben, X. L. *et al.* Light fluence normalization in turbid tissues via temporally unmixed multispectral optoacoustic tomography. *Opt. Lett.* **40,** 4691–4694 (2015).

43. Luıs Deán-Ben, X. *et al. Light fluence estimation by imaging photoswitchable probes with temporally unmixed multispectral optoacoustic tomography* in *Biomedical Optics 2016* (Optical Society of America, Fort Lauderdale, Florida United States, 2016), OTu2A.6.

44. Yao, J. *et al.* Multiscale photoacoustic tomography using reversibly switchable bacterial phytochrome as a near-infrared photochromic probe. *Nature Methods* **13,** 67–73 (2016).

45. Deán-Ben, X. L. *et al.* Functional optoacoustic neuro-tomography for scalable whole-brain monitoring of calcium indicators. *Light Sci Appl* **5,** e16201 (2016).

46. Qian, Y. *et al.* A genetically encoded near-infrared fluorescent calcium ion indicator. *Nature Methods* **16,** 171–174 (2019).

47. Jutz, G., van Rijn, P., Santos Miranda, B. & Böker, A. Ferritin: a versatile building block for bionanotechnology. *Chem. Rev.* **115,** 1653–1701 (2015).

48. Gossuin, Y., Gillis, P., Hocq, A., Vuong, Q. L. & Roch, A. Magnetic resonance relaxation properties of superparamagnetic particles. *Wiley Interdiscip. Rev. Nanomed. Nanobiotechnol.* **1,** 299–310 (2009).

49. Iordanova, B., Robison, C. S. & Ahrens, E. T. Design and characterization of a chimeric ferritin with enhanced iron loading and transverse NMR relaxation rate. *J. Biol. Inorg. Chem.* **15,** 957–965 (2010).

50. Matsumoto, Y., Chen, R., Anikeeva, P. & Jasanoff, A. Engineering intracellular biomineralization and biosensing by a magnetic protein. *Nature Communications* **6,** 8721 (2015).

51. Liu, X. *et al.* Engineering Genetically-Encoded Mineralization and Magnetism via Directed Evolution. *Sci. Rep.* **6,** 38019 (2016).

52. Douglas, T. *et al.* Protein engineering of a viral cage for constrained nanomaterials synthesis. *Adv. Mater.* **14,** 415 (2002).

53. McHugh, C. A. *et al.* A virus capsid-like nanocompartment that stores iron and protects bacteria from oxidative stress. *EMBO J.* **33,** 1896–1911 (2014).

54. He, D. *et al.* Structural characterization of encapsulated ferritin provides insight into iron storage in bacterial nanocompartments. *Elife* **5** (2016).

55. Giessen, T. W. & Silver, P. A. Widespread distribution of encapsulin nanocompartments reveals functional diversity. *Nature Microbiology* **2,** 17029 (2017).

56. Sigmund, F. *et al.* Bacterial encapsulins as orthogonal compartments for mammalian cell engineering. *Nature Communications* **9,** 1990 (2018).

57. Sigmund, F. *et al.* Iron-sequestering nanocompartments as multiplexed Electron Microscopy gene reporters. *ACS nano* **13,** 8114–8123 (2019).

58. Ramesh, P. *et al.* Ultraparamagnetic Cells Formed through Intracellular Oxidation and Chelation of Paramagnetic Iron. *Angew. Chem. Int. Ed Engl.* **57,** 12385–12389 (2018).

59. Komeili, A. Molecular mechanisms of compartmentalization and biomineralization in magnetotactic bacteria. *FEMS Microbiol. Rev.* **36,** 232–255 (2012).

60. Kolinko, I. *et al.* Biosynthesis of magnetic nanostructures in a foreign organism by transfer of bacterial magnetosome gene clusters. *Nature Nanotechnology* **9,** 193–197 (2014).

61. Stritzker, J. *et al.* Vaccinia virus-mediated melanin production allows MR and optoacoustic deep tissue imaging and laser-induced thermotherapy of cancer. *Proceedings of the National Academy of Sciences* **110,** 3316–3320 (2013).

62. Jiang, Y. *et al.* Violacein as a genetically-controlled, enzymatically amplified and photobleaching-resistant chromophore for optoacoustic bacterial imaging. *Sci. Rep.* **5,** 11048 (2015).

63. Lauri, A. *et al.* Whole-Cell Photoacoustic Sensor Based on Pigment Relocalization. *ACS Sens* **4,** 603–612 (2019).

64. Paefgen, V., Doleschel, D. & Kiessling, F. Evolution of contrast agents for ultrasound imaging and ultrasound-mediated drug delivery. *Front. Pharmacol.* **6,** 197 (2015).

65. Shapiro, M. G. *et al.* Biogenic gas nanostructures as ultrasonic molecular reporters. *Nature Nanotechnology* **9,** 311–316 (2014).

66. Maresca, D. *et al.* Nonlinear ultrasound imaging of nanoscale acoustic biomolecules. *Appl. Phys. Lett.* **110** (2017).

67. Maresca, D., Sawyer, D. P., Renaud, G., Lee-Gosselin, A. & Shapiro, M. G. Nonlinear X-Wave Ultrasound Imaging of Acoustic Biomolecules. *Phys. Rev. X* **8,** 041002 (2018).

68. Lakshmanan, A. *et al.* Molecular Engineering of Acoustic Protein Nanostructures. *ACS Nano* **10,** 7314–7322 (2016).

69. Cherin, E. *et al.* Acoustic Behavior of Halobacterium salinarum Gas Vesicles in the High-Frequency Range: Experiments and Modeling. *Ultrasound Med. Biol.* **43,** 1016–1030 (2017).

70. Lakshmanan, A. *et al.* Preparation of biogenic gas vesicle nanostructures for use as contrast agents for ultrasound and MRI. *Nature Protocols* **12,** 2050–2080 (2017).

71. Farhadi, A., Ho, G. H., Sawyer, D. P., Bourdeau, R. W. & Shapiro, M. G. Ultrasound imaging of gene expression in mammalian cells. *Science* **365,** 1469–1475 (2019).

72. Lu, G. J. *et al.* Acoustically modulated magnetic resonance imaging of gas-filled protein nanostructures. *Nature Materials* **17,** 456–463 (2018).

73. Lu, G. J. *et al.* Genetically Encodable Contrast Agents for Optical Coherence Tomography. *ACS Nano* (2020).

74. Bourdeau, R. W. *et al.* Acoustic reporter genes for noninvasive imaging of microorganisms in mammalian hosts. *Nature* **553,** 86–90 (2018).

75. Riglar, D. T. & Silver, P. A. Engineering bacteria for diagnostic and therapeutic applications. *Nature Reviews Microbiology* **16,** 214–225 (2018).

76. Shapiro, M. G. *et al.* Genetically encoded reporters for hyperpolarized xenon magnetic resonance imaging. *Nature Chemistry* **6,** 629–634 (2014).

77. Wang, Y., Roose, B. W., Palovcak, E. J., Carnevale, V. & Dmochowski, I. J. A genetically encoded $\beta$-lactamase reporter for ultrasensitive $^{129}$Xe NMR in Mammalian Cells. *Angew. Chem. Int. Ed.* **55,** 8984–8987 (2016).

78. Farhadi, A. *et al. Genetically encoded phase contrast agents for digital holographic microscopy* 2019.

79. Wu, D. *et al. Genetically encoded nanostructures enable acoustic manipulation of engineered cells* 2019.

80. Bar-Zion, A. *et al. Acoustically Detonated Biomolecules for Genetically Encodable Inertial Cavitation* 2019.

81. Gilbert, C. & Ellis, T. Biological Engineered Living Materials: Growing Functional Materials with Genetically Programmable Properties. *ACS Synth. Biol.* **8,** 1–15 (2019).

82. Huang, P.-S., Boyken, S. E. & Baker, D. The coming of age of de novo protein design. *Nature* **537,** 320–327 (2016).

83. Yang, K. K., Wu, Z. & Arnold, F. H. Machine-learning-guided directed evolution for protein engineering. *Nature Methods* **16,** 687–694 (2019).

84. Lang, K. & Chin, J. W. Cellular incorporation of unnatural amino acids and bioorthogonal labeling of proteins. *Chem. Rev.* **114,** 4764–4806 (2014).

85. Gilad, A. A. & Shapiro, M. G. Molecular Imaging in Synthetic Biology, and Synthetic Biology in Molecular Imaging. *Molecular Imaging and Biology* **19,** 373–378 (2017).

86. Palmer, A. E., Qin, Y., Park, J. G. & McCombs, J. E. Design and application of genetically encoded biosensors. *Trends Biotechnol.* **29,** 144–152 (2011).

*Chapter 2*

# MOLECULAR ENGINEERING OF ACOUSTIC PROTEIN NANOSTRUCTURES

This chapter is in large part a reformatted version of the manuscript entitled " Molecular Engineering of Acoustic Protein Nanostructures" published by Lakshmanan, A., Farhadi, A., Nety, S.P., Lee-Gosselin, A., Bourdeau, R.W., Maresca, D., and Shapiro M.G., in *ACS Nano*[1]. Under the supervision of Mikhail Shapiro, my contributions to the work was to help design and conduct the experiments in addition to analyzing and interpreting the data, in particular experiments related to engineering the surface properties of gas vesicles to modulate their surface charge and human cell targeting capabilities.

## 2.1 Abstract

Ultrasound is among the most widely used biomedical imaging modalities, but has limited ability to image specific molecular targets due to the lack of suitable nanoscale contrast agents. Gas vesicles – genetically encoded protein nanostructures isolated from buoyant photosynthetic microbes – have recently been identified as novel nanoscale reporters for ultrasound. Their unique physical properties give gas vesicles major advantages over conventional microbubble contrast agents, including nanoscale dimensions and inherent physical stability. Furthermore, as a genetically encoded material, gas vesicles present the possibility that the nanoscale mechanical, acoustic and targeting properties of an imaging agent can be engineered at the level of its constituent proteins. Here, we demonstrate for the first time that genetic engineering of gas vesicles results in nanostructures with novel mechanical, acoustic, surface and functional properties to enable new types of harmonic, multiplexed and multimodal imaging, as well as cell-specific molecular targeting. These results establish an unprecedented biomolecular platform for the engineering of acoustic nanomaterials to address a critical unmet need in biology and medicine.

## 2.2 Introduction

Ultrasound is among the most widely used biomedical imaging modalities due to its superior spatiotemporal resolution, safety, cost and ease of use compared to other techniques such as magnetic resonance and nuclear imaging. In addition to visualizing anatomy and physiology, ultrasound can take advantage of contrast agents to more specifically image blood flow, discern the location of certain molecular targets, and resolve structures beyond its normal wavelength limit via super-localization.[2,3] However, existing "microbubble" contrast agents–micron-sized bubbles of gas stabilized by a biocompatible shell–face limitations as molecular reporters due to their size and inherent physical instability, restricting their use to primarily within the vasculature.[4,5] Recently, we introduced gas vesicles (GVs) as a new class of nanoscale imaging agents for ultrasound.[6] GVs are gas-filled protein-shelled nanostructures (Fig. 2-1a) expressed intracellularly in certain bacteria and archaea as a mechanism to regulate cellular buoyancy in aqueous environments.[7,8] GVs have widths of 45-250 nm and lengths of 100-800 nm depending on their genetic origins.[7,8] Unlike microbubbles, which trap pre-loaded gas in an unstable configuration, GVs' 2-nm thick protein shells exclude water but permit gas to freely diffuse in and out from the surrounding media[7] (Fig. 2-1b), making them physically stable despite their nanometer size. GVs produce robust ultrasound contrast across a range of frequencies at picomolar concentrations, exhibit harmonic scattering to enable enhanced detection versus background *in vivo*, and have species- dependent thresholds for pressure-induced collapse to enable multiplexed imaging.[6] Furthermore, the genetic encodability of GVs raises the possibility of engineering the properties of these nanoscale imaging agents at the level of their protein composition and DNA sequence. Here, we establish this capability for the first time by biochemically and genetically engineering the mechanical, acoustic, surface and targeting properties of GVs from the cyanobacterium *Anabaena flos-aquae* (Ana GVs).

Ana GVs are cone-tipped cylindrical structures with a diameter of approximately 140 nm and length of 200-800 nm (Fig. 2-1a, b). These structures are encoded by a cluster of 9 different genes, including the two primary structural proteins, GvpA and GvpC, and several putative minor components and chaperones[8–10] (Fig. 2-1b). GvpA is a 7.4 kDa amphiphilic protein that assembles into the main structural backbone of the GV shell by forming 4.6 nm-wide ribs that run perpendicular to the long axis of the nanostructure[11,12](Fig. 2-1c). GvpC is the second most abundant protein, and strengthens the GV shell by binding to its exterior surface.[12,13] This protein comprises five highly conserved 33-amino acid repeats with

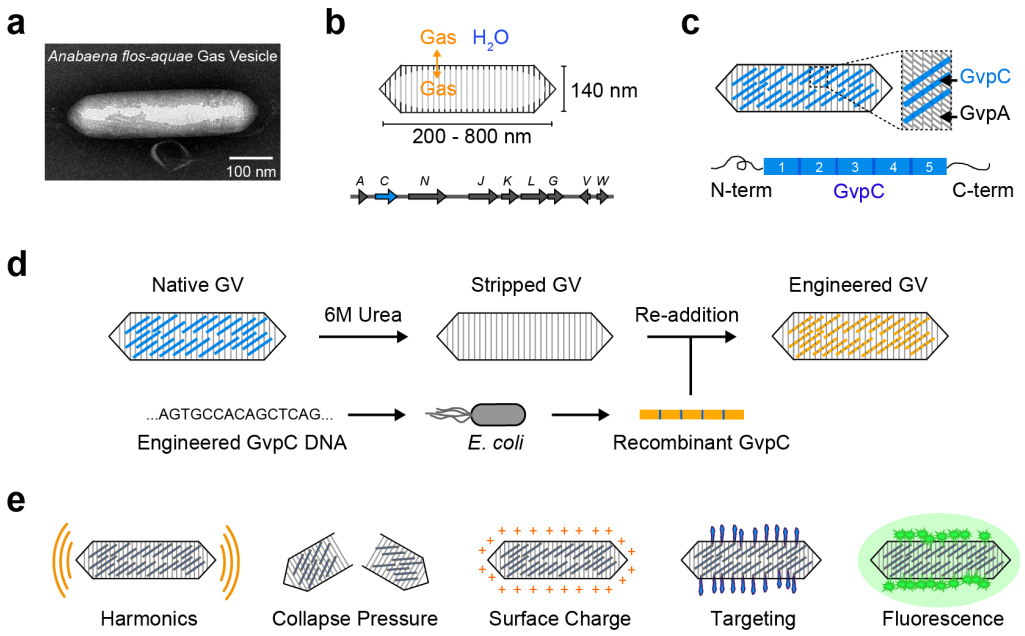


**Figure 2-1: Molecular engineering platform for acoustic protein nanostructures.** (a) Transmission Electron Microscopy (TEM) image of a single Ana GV. (b) Schematic illustration of Ana GV, and the gene cluster encoding GvpA, GvpC and several other essential proteins. (c) GvpA and GvpC are the two major structural constituents of GVs, with GvpA ribs (gray) forming the primary GV shell and the outer scaffold protein GvpC (blue) conferring structural integrity. Each GvpC molecule has five 33-amino acid repeats flanked by N- and C- terminal regions (d) Paradigm for modular genetic engineering of Ana GVs. Native gas vesicles are treated with 6M urea to produce stripped Ana GVs without native GvpC (blue). Genetically engineered GvpC is recombinantly expressed in *Escherichia coli* (orange) and added to the stripped Ana GVs during dialysis to create engineered GVs with a modified GvpC layer. (e) GvpC engineering can be used to modulate the properties of acoustic GV nanostructures including their harmonic response, collapse pressure, surface charge, targeting specificity and fluorescence.

predicted alpha-helical structure, and is believed to bind across GvpA ribs to provide structural reinforcement[12] (Fig. 2-1c). In biochemical studies, removal of GvpC and truncations to its sequence were shown to result in a reduced threshold for Ana GV collapse under hydrostatic pressure.[13,14] In addition, previous studies in other species have demonstrated that GvpC can tolerate fusions of bacterial and viral polypeptides.[15,16] Given these properties, we hypothesized that GvpC could serve as a versatile platform for molecular engineering of GV-based ultrasound contrast agents. Specifically, we predicted that changes in GV mechanical properties resulting from the removal, addition, or modification of GvpC would alter the acoustic properties of Ana GVs, thereby allowing us to tune their ultrasound response and enable harmonic and multiplexed imaging (Figure 2-1d, e). Furthermore, we hy-

pothesized that GvpC could serve as a modular genetic hook enabling the tuning of GV surface properties such as zeta potential, the display of ligands for reduced or enhanced cellular targeting and uptake, and the attachment of fluorescent proteins to enable multimodal imaging (Figure 2-1e).

## 2.3 Results and Discussions

**Modular Genetic Engineering Platform for Acoustic Protein Nanostructures.** To enable modular molecular engineering of Ana GVs, we established a platform in which genetically engineered GvpC variants are recombinantly expressed in *Escherichia coli* and subsequently added to Ana GVs that have been purified from *A. flos-aquae* and stripped of their native GvpC proteins (Figure 2-1d). The GVs were isolated by hypertonic and detergent-mediated lysis, followed by purification with centrifugally assisted floatation. Native GvpC was removed by treating the GVs with 6 M urea, which leaves the GvpA-based shell intact.[13,14] We produced genetically engineered variants of Ana GvpC containing N- or C-terminal hexahistidine sequences in *E. coli* and purified the resulting inclusion bodies by nickel chromatography in 6 M urea. Dialysis of recombinant GvpC in the presence of stripped Ana GVs into physiological buffer resulted in Ana GVs with a new, engineered GvpC layer (Figure 2-1d). Sodium dodecyl sulphate polyacrylamide gel electrophoresis (SDS-PAGE) analysis confirmed the complete removal of GvpC from native Ana GVs and the re-addition of engineered proteins (Figure 2-S1).

**Genetic Engineering Enables Tuning of Collapse Pressure for Acoustic Multiplexing.** The gaseous interior of GVs can be collapsed with hydrostatic and acoustic pressure, erasing their ultrasound scattering signal and enabling multiplexed imaging of GVs with distinct collapse pressure thresholds.[6] To determine whether genetic tuning could enable enhanced multiplexing, we engineered three Ana GV variants with distinct mechanical properties. ΔGvpC comprises GVs completely lacking the outer GvpC layer; ΔN&C contains a truncated form of GvpC without its N- and C-terminal regions; $GvpC_{WT}$ has an engineered GvpC protein that closely resembles the wild-type sequence (Figure 2-2a). We assessed the hydrostatic collapse behavior of these nanostructures using pressurized absorbance spectroscopy, in which the optical density of GVs (which scatter 500 nm light when intact) is measured under increasing hydrostatic pressure. This provides a rapid assessment of GV mechanics and allows comparisons to literature.[7] Our three variants spanned a dynamic range of 380 kPa (Figure 2-2b, Table 2-S1). ΔGvpC had the lowest collapse pressure midpoint at 195.3 ± 0.3 kPa, the ΔN&C variant showed an inter-

mediate value of 374.3 ± 1 kPa, and $GvpC_{WT}$ had the highest value of 569.9 ± 4 kPa (Table 2-S1, N =7, ± SEM). To ensure that the decrease in collapse pressure for the ΔN&C variant was not due to unsaturated binding caused by reduced affinity of this GvpC variant for GvpA, we measured collapse midpoints as a function of re-added GvpC concentration and confirmed that binding was near saturation (Figures 2-S2, 2-S3).

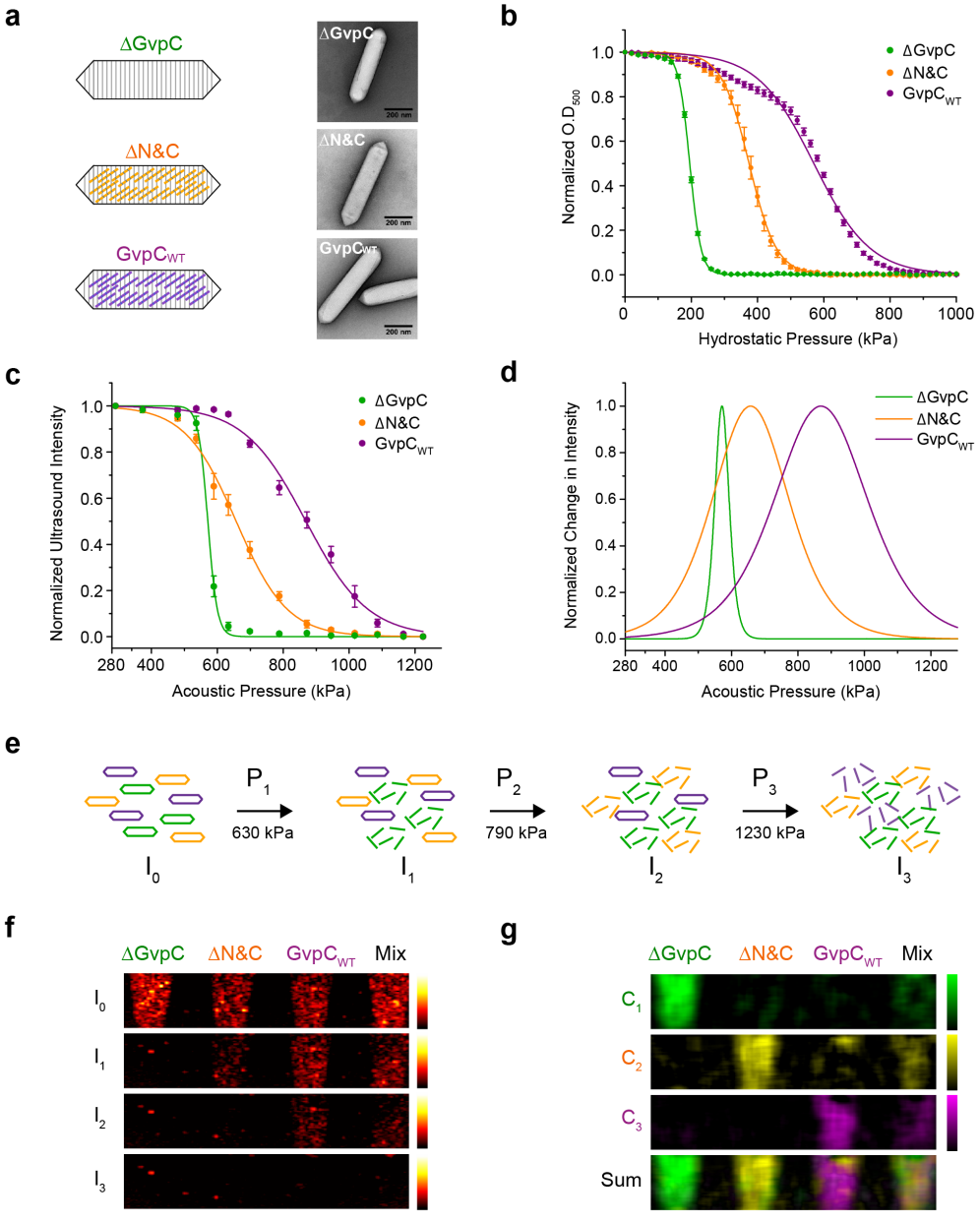


**Figure 2-2:** (Caption on next page.)

**Figure 2-2: GvpC engineering enables tuning of GV collapse pressurenvpC engineering enables tuning of GV collapse pressure for acoustic multiplexing.** (a) Schematic illustration of the three engineered GV variants used for acoustic multiplexing. ΔGvpC, ΔN&C and $GvpC_{WT}$ variants are represented by green, orange and purple colors respectively. Accompanying TEM images show the conservation of GV shape among the three variants (scale bars are 200 nm). (b) Optical density measurements of engineered Ana GVs as a function of hydrostatic pressure (N=7 independent preparations, error bars are SEM). The data was fitted with a Boltzmann sigmoid function. Fit parameters and $R^2$ values are provided in Table 2-S1. (c) Acoustic collapse curves for the GV variants showing normalized ultrasound signal intensity as a function of increasing peak positive pressure from 290 kPa to 1.23 MPa (N= 3 independent trials, error bars are SEM). The data was fitted with a Boltzmann sigmoid function (parameters provided in Table 2-S2), the derivatives of which with respect to pressure are plotted in (d). (e) Schematic illustration of acoustic spectral unmixing, showing serial collapse of the GV variants based on their critical collapse pressure and indicating the pressures used in panels f and g. (f) Ultrasound images of an agarose phantom containing wells with ΔGvpC, ΔN&C and $GvpC_{WT}$ and a mixture of the three variants (all GVs at final OD 1.0 in PBS), acquired at 6.25 MHz. $I_0$; before collapse $I_1$: after collapse at 630 kPa $I_2$: after collapse at 790 kPa $I_3$: after collapse at 1230 kPa. (g) Spectrally unmixed images processed from the raw ultrasound data in (f). The bottom panel shows an overlay of the three unmixed channels $C_1$, $C_2$, and $C_3$.

Next, we evaluated collapse profiles under ultrasound. GVs were imaged in multiwell agarose phantoms at 6.25 MHz while being subjected to ultrasound pulses with increasing peak positive pressure amplitudes ranging from 290 kPa to 1.23 MPa. Similar to trends observed for hydrostatic collapse, the ΔGvpC variant collapses under the lowest acoustic pressure, followed by ΔN&C and $GvpC_{WT}$ (Figure 2-2c, Table 2-S2). Notably, the collapse midpoints in the acoustic regime were substantially higher than in the hydrostatic regime. This is explained by GVs having a gas efflux time of approximately 1.5 μs,[17] which is too slow for gas molecules contained in the GV to exit the nanostructure during the 80 ns positive half-cycle of 6.25 MHz ultrasound, allowing the gas to compressively reinforce the GV shell. On the other hand, under hydrostatic conditions, pressure changes occur on the time scale of seconds, allowing gas molecules to exit the GV during pressurization and resulting in the shell carrying the full compressive load by itself.[18] We also note that the acoustic collapse curves appear somewhat more closely spaced than hydrostatic collapse curves, which can be explained by the applied acoustic pressure field having a nonuniform profile over the imaged GV sample. Fitting a Boltzmann sigmoidal function to these collapse curves reveals a unique acoustic collapse spectrum for each engineered GV (Figure 2-2d).

To take advantage of the distinct acoustic collapse spectra of GV variants for

multiplexed imaging, we developed a pressure spectral unmixing paradigm. This paradigm posits that the total signal for a mixed population of GVs in any given pixel is the sum of signals contributed by each subpopulation present in that pixel. Images acquired after sequentially applying collapse pulses of increasing pressure ($P_i$) reveal changes in pixel-wise signal intensity ($I$) that provide information about the abundance of each GV type in the pixel (Figure 2-2e). This information is extracted by multiplying the measured differential signals:

$$\Delta_i = I(P_{i-1}) - I(P_i)$$

by the inverse of a matrix containing the collapse spectrum of each type of GV, denoted by $\alpha_{i,j}$. The contribution of each GV type to the observed signal represented as $C_j$ is given by the matrix operation:

$$C = \alpha^{-1}\Delta$$

We used pressure spectral unmixing to obtain multiplexed images of our three GV variants. Figure 2-2f shows ultrasound images taken at a nondestructive baseline pressure before and after exposing the GV samples to three sequentially increasing collapse pulses. The spectrally unmixed images (Figure 2-2g) uniquely identify acoustic signals from each GV variant. Figure 2-S4 shows the matrix of coefficients used to generate these images. We anticipate that this combination of engineered GVs and pressure spectral unmixing will be useful in many scenarios requiring ultrasound imaging of multiple molecular targets in the same sample.

**Molecular Engineering Enables Modulation of Harmonic Ultrasound Signals.** Nonlinear signals from ultrasound contrast agents can dramatically enhance their ability to be distinguished from background tissues, which mainly scatter linearly.[19,20] In our initial description of GVs as ultrasound reporters, we found that GVs from *Halobacterium salinarum* (Halo GVs) produce strong nonlinear signals in the form of harmonics filtering around the fundamental and second harmonic frequencies showed a substantial difference in the harmonic acoustic response of GV variants ($p < 0.01$, N= 7, paired t test), for the same level of fundamental signal (Figure 2-3b-e). The harmonic signals from ΔGvpC were 3.71 fold higher than $GvpC_{WT}$ (Figure 2-3e). These results demonstrate that protein engineering can be used to modulate the acoustic properties of a nanostructure.

To show that engineered Ana GV variants are capable of producing harmonic signals *in vivo*, we performed intravenous injections of the ΔGvpC and $GvpC_{WT}$ variants into live, anaesthetized mice. Ultrasound imaging of the inferior vena cava

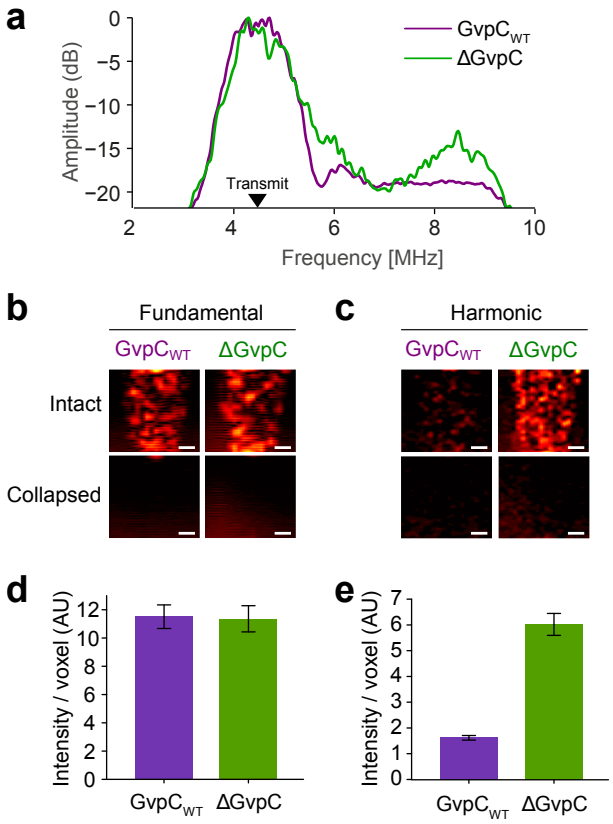


**Figure 2-3: GV engineering enables modulation of harmonic signals *in vitro*.** (a) Power spectrum of signal backscattered from ΔGvpC (green) and GvpC$_{WT}$ (purple) variants in an agarose phantom in response to 4.46 MHz pulses. (b) Fundamental and (c) second harmonic ultrasound images of ΔGvpC and GvpC$_{WT}$ acquired with 4.46 MHz transmission and band-pass filtered around 4.46 and 8.92 MHz respectively. Images are shown before and after collapse using a high power burst from the transducer to collapse the GVs. Scale bars are 1 mm. (d) Mean fundamental and (e) harmonic signals from ΔGvpC and GvpC$_{WT}$ variants after filtering at the indicated frequencies (N = 7 independent measurements, error bars are SEM). Data in all panels comes from GVs prepared at OD 2.5 in PBS and loaded into 1% agarose phantoms.

(IVC) was performed in fundamental and second harmonic modes (transmission at 4.46 MHz and reception filtered around 4.46 and 8.9 MHz center frequencies, respectively). Figure 2-4a provides a schematic illustration of the *in vivo* experiment. Five seconds after the start of the injection, enhanced nonlinear signals were observed for the ΔGvpC variant compared to GvpC$_{WT}$, while their fundamental signals were comparable (Figure 2-4b-d). Repeated trials showed a statistically significant difference ($p < 0.01$, N = 6, paired t test) in the harmonic response of the two variants for the same level of fundamental signal (Figure 2-4e), consistent

with *in vitro* results. The ability to genetically tune the harmonic properties of GV contrast agents will enhance their utility for *in vitro* and *in vivo* imaging.

**Genetic Engineering Enables Tuning of Surface Charge, Targeting Specificity, and Multimodal Imaging.** After demonstrating the ability of GvpC to serve as a genetic platform for tuning the mechanical and acoustic properties of GVs, we examined its capacity to enable the engineering of GV surface and targeting properties. To do so, we used the C- terminus of GvpC as a modular site for protein fusion (Figures 2-5a and 2-S5). As a first proof of concept, we tested the ability of GvpC fusions to modulate GV surface charge, an important property that influences the behavior of nanostructures in solution and *in vivo*.[21] We fused GvpC with the lysine-rich protein (LRP), which contains 100 positive charges at physiological pH. Re-addition of this protein to GVs resulted in nanostructures with 28 ± 4 mV higher

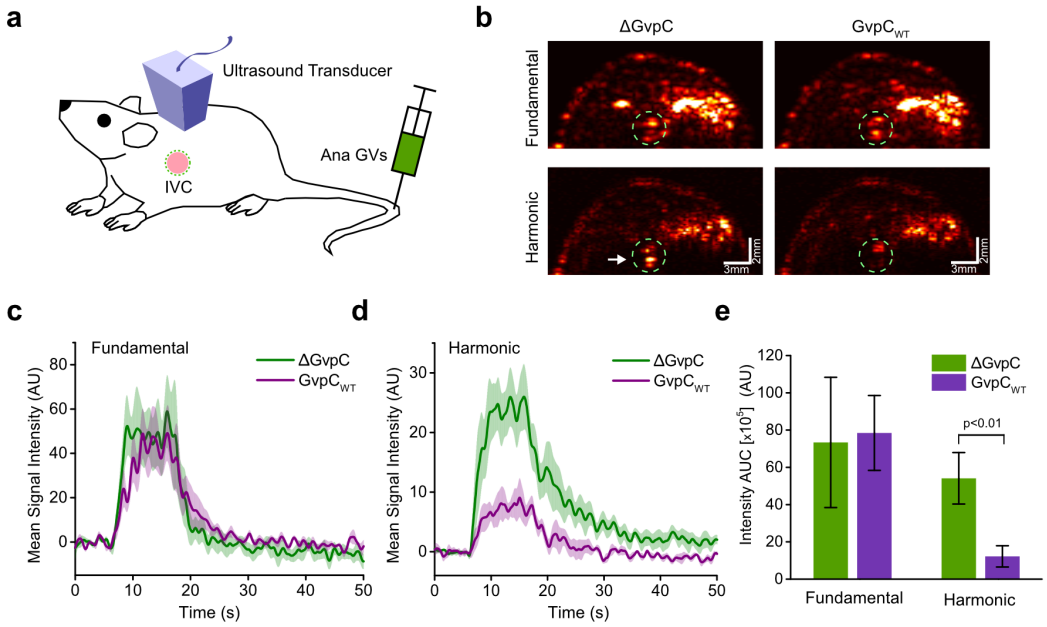


**Figure 2-4: GV engineering enables modulation of harmonic signals *in vivo*.** (a) Schematic depiction of intravenous GV injection and *in vivo* ultrasound imaging during passage through the inferior vena cava (IVC). (b) Fundamental and second harmonic ultrasound images taken at 4.46 MHz transmission frequency and band-pass filtered receive around 4.46 and 8.92 MHz respectively. Engineered Ana GVs at OD 23.5 in PBS were used for injections. The IVC ROI used for subsequent analysis is circled in green. The white arrow points to the increased harmonic signal observed in the IVC for the ΔGvpC variant. Time course of the mean (c) fundamental and (d) harmonic acoustic signal in the IVC before, during and after steady infusion, with shaded regions representing SEM (N = 6 mice). (e) Histogram showing the area under the curve (AUC) of average fundamental and harmonic contrast in the IVC after ΔGvpC and GvpC$_{WT}$ GV injections (N=6, error bars are SEM).

zeta potential compared to $GvpC_{WT}$ (Figure 2-5b).

Next, we tested the ability of GvpC fusions to endow GVs with functionality for specific cellular targeting. A well-studied receptor-targeting peptide is arginyl-glycylaspartic acid (RGD), which binds effectively to a wide range of integrins.[22] GVs engineered to express $GvpC_{RGD}$ on their surface were compared with wild-type GvpC and scrambled $GvpC_{RDG}$ controls in terms of their ability to target the integrin-overexpressing U87 human glioblastoma cell line *in vitro*. The GVs were chemically conjugated with the Alexa Fluor-488 fluorophore for visualization using confocal microscopy. GVs functionalized with RGD exhibited a marked increase in cell binding compared to controls (Figure 2-5c, d). This technique presents a generalizable approach for future studies targeting GVs to molecular markers *in vivo*.

Using a similar engineering strategy, we created GvpC fusions to modulate the interaction of GVs with macrophages, which are both imaging targets and important actors in nanoparticle clearance from circulation. CD47, present on endogenous cell membranes in humans, mice, and other mammals, is a well-studied putative marker of self. Discher and colleagues recently described a minimized peptide from the human CD47 protein, dubbed the "self" peptide, which led to reduced uptake of cells and nanoparticles by the mononuclear phagocytic system.[23] On the other hand, polycationic peptides such as polyarginine (R8) promote particle uptake by phagocytic cells.[24] By fusing each of these molecules to GvpC, we tested whether genetic engineering could modulate GV uptake in mouse leukaemic monocyte macrophage cell line (RAW 264.7) murine macrophages. As visualized by confocal microscopy, GVs genetically functionalized with $GvpC_{mCD47}$ showed reduced macrophage uptake compared to GVs with $GvpC_{WT}$. On the other hand, GVs functionalized with $GvpC_{R8}$ were taken up much more efficiently (Figure 2-5e, f). These molecular strategies can be used in future studies to enable cellular labeling for *in vivo* tracking applications or to enhance the circulation lifetime of targeted GVs.

Finally, to further simplify GV functionalization, we developed a highly modular approach through which the GV surface can be covalently conjugated to other recombinant proteins through a facile process that does not involve urea treatment and dialysis. To achieve this goal, we fused GvpC with SpyTag (ST), a 13-residue peptide that forms a covalent amide bond with a partner SpyCatcher protein under physiological conditions.[25] This system allows SpyTagged GVs to be functionalized with SpyCatcher fusions in a rapid biocompatible reaction. We found that

$GvpC_{ST}$ binds to GVs with similar stoichiometry to $GvpC_{WT}$ and provides reinforcement against pressure-induced collapse (Figure 2-S6). Each modified GV had an average of 1000 SpyTag functionalities (Figure 2-S7). To demonstrate the utility of this modular functionalization approach, we reacted these GVs with the recombinantly expressed fluorescent protein SpyCatcher-mNeonGreen (SC-mNG) to enable multimodal acoustic and fluorescent imaging. The resulting fluorescent GVs were purified by buoyancy enrichment. SDS-PAGE analysis confirmed SpyTag-SpyCatcher covalent bond formation (Figure 2-S8), and Figure 2-5g shows multimodal imaging of mNG-labeled GVs with ultrasound and fluorescence. The ultrasound images show similar echogenicity between fluorescently labeled GVs, wild-type, and unreacted controls (Figure 2-5h). $GvpC_{WT}$ Ana GVs do not show any fluorescence after reaction with SC-mNG (Figure 2-5g, h), highlighting the specificity of the SpyTag-SpyCatcher reaction and confirming that buoyancy enrichment eliminates unreacted fluorescent proteins (Figure 2-S8). Notably, labeled ST-GVs remain fluorescent after acoustic pressure-induced collapse, which may be useful for follow-up histological examinations after ultrasound imaging. These results establish the GvpCST-SpyCatcher system as a highly modular and convenient approach to generate functionalized GVs, thereby enabling dual-mode imaging of these nanostructures.

## 2.4 Conclusions

In summary, our results demonstrate the genetic engineering of a biologically derived acoustic nanomaterial, which we use as an imaging agent for ultrasound. Remarkably, a single constituent protein on the surface of GVs can serve as a genetic platform to modulate the mechanical, acoustic, surface, and targeting properties of these nanostructures. This molecular engineering capability will enable the design of GV-based contrast agents with enhanced harmonic responses, biodistribution, multiplexing, multimodal detection, and molecular targeting to help ultrasound fulfill its potential as a high-performance modality for molecular imaging. In addition, as a nanomaterial with genetically tunable mechanical properties, GVs may create opportunities for applications outside biology and medicine.

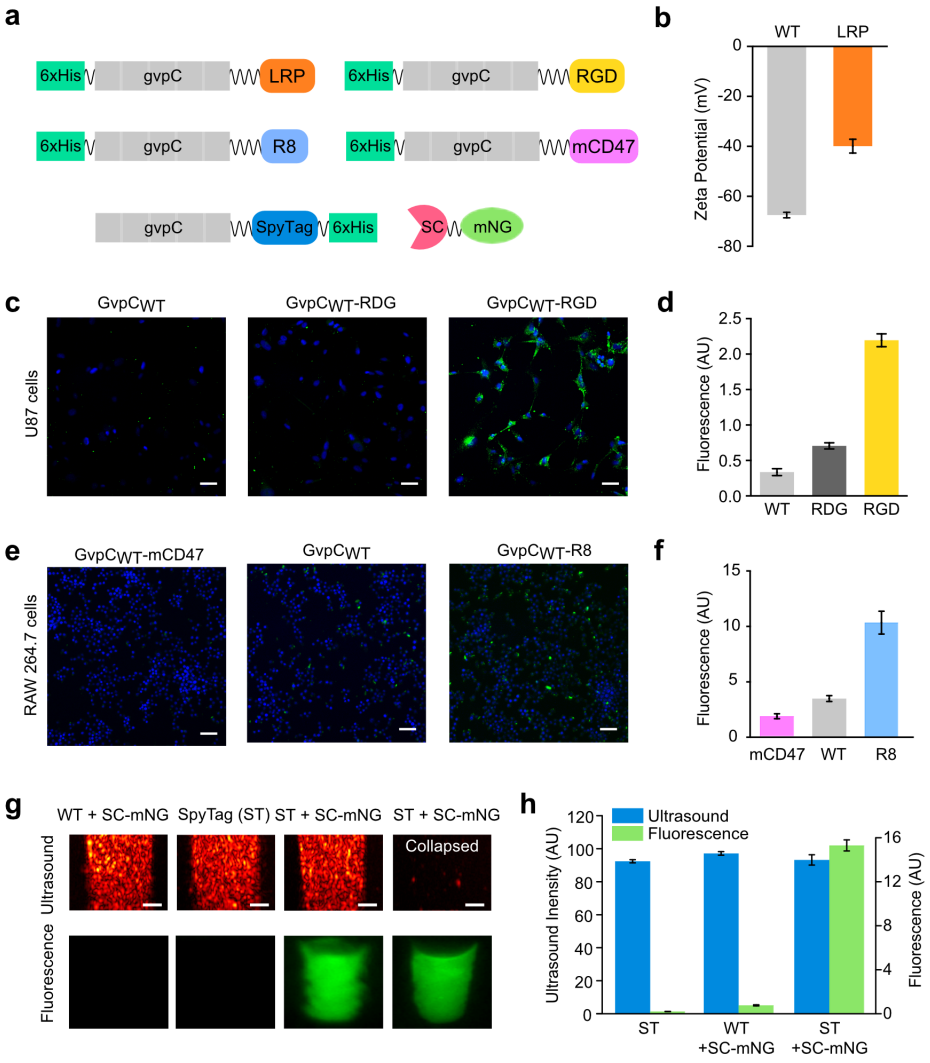


**Figure 2-5: Genetic engineering of GV surface properties, cellular targeting and multimodal imaging.** (a) Diagram of GvpC genetic fusions used to engineer novel GV properties and functions. (b) Zeta potential measurements of engineered GVs having GvpC fused to LRP and wild-type GvpC (N = 4, error bars are SEM) (c) Confocal fluorescence images showing RGD-functionalized, RDG-functionalized and wild-type Alexa Fluor-488 fluorescently labeled (green) GVs after 24 hr incubation with U87 glioblastoma cells (DAPI-stained nuclei, blue). Scale bars are 50 µm (d) Mean GV fluorescence measured for each condition in (c) (N = 3, error bars are SEM). (e) Confocal fluorescence images of RAW 264.7 macrophages (DAPI-stained nuclei, blue) incubated for 30 min with fluorescently labeled GVs (green) displaying GvpC fused to mCD47, R8 or wild-type GvpC. Scale bars are 50 µm. (f) Mean GV fluorescence measured for each condition in (e) (N = 3, error bars are SEM). (g) Top panel: Ultrasound images of engineered and SpyCatcher-mNeonGreen (SC-mNG) reacted GVs at OD 2.5 in PBS, acquired using a 19 MHz transmission pulse in fundamental mode. Scale bars are 1 mm. Bottom panel: Fluorescence images of the agarose phantoms before and after acoustic collapse. (h) Mean ultrasound and fluorescence signals from the GV samples tested in (g). (N ≥ 4, error bars are SEM).

## 2.5 Methods

**Gas Vesicle Preparation.** Ana was cultured in Gorham's media supplemented with BG-11 solution (Sigma, St. Louis, MO) and 10 mM sodium bicarbonate ($NaHCO_3$)at 25°C, 100 rpm shaking, and 1% $CO_2$ under a 14h light cycle and 10 h dark cycle. Once confluency was reached, the cultures were transferred to sterile separating funnels, and the buoyant cells were allowed to float to the top and separate from the spent media over a 48h period. Ana GVs were harvested by hypertonic lysis of the buoyant cells with 500 mM sorbitol and 10% Solulyse (Genlantis, San Diego, CA). Purification was done by repeated centrifugally assisted floatation followed by resuspension in 1x phosphate buffered saline (PBS) (Corning, Union City, CA). GV concentration was determined by pressure-sensitive OD measurements at 500 nm ($OD_{PS,500}$). Precollapsed GVs prepared by application of hydrostatic pressure in a capped syringe were used as the blank.

**Expression and Purification of Ana GvpC Variants.** The Ana GvpC gene sequence codon-optimized for *E. coli* expression was synthesized by Life Technologies, Santa Clara, CA. Ana GvpC was cloned into a pET28a(+) plasmid (Novagen, Temecula, CA) downstream of a T7 promoter with an N- or C-terminal His-tag. All constructs were made via restriction cloning, KLD mutagenesis, or Gibson assembly using enzymes from New England Biolabs, Ipswich, MA. Purified plasmids with the genetically engineered GvpC constructs were transformed into BL21(DE3) cells (Invitrogen, Carlsbad, CA). Starter cultures were diluted 1:250 in Terrific Broth (Sigma, St. Louis, MO) and allowed to reach $OD_{600}$ ~0.4-0.7 (250 rpm shaking at 37°C). Protein expression was induced by addition of isopropyl $\beta$-D-1-thiogalactopyranoside (to a final concentration of 1 mM), and cells were harvested by centrifugation after expression at 30°C for 6 h.

GvpC in the form of inclusion bodies was purified by lysing the cells using Solulyse supplemented with DNaseI (10 µg/mL) and lysozyme (400 µg/mL) at room temperature. Inclusion bodies were recovered by centrifugation at 27,000g for 15 min in an ultracentrifuge. The inclusion body pellets were resuspended in 20 mM Tris-HCl buffer with 500 mM sodium chloride (NaCl) and 6 M urea (pH 8.0) and incubated with Ni-NTA resin (Qiagen, Valencia, CA) for 2 h at 4°C. After washing, proteins were eluted using 250 mM imidazole. Bradford assay was used to measure the concentration of the purified protein. Recombinant GvpC variants were verified to be >95% pure by SDS- PAGE analysis.

**Ana GV Stripping and Re-Addition of Engineered GvpC Variants.** Native Ana GVs were stripped of their outer GvpC layer by treatment with 6 M urea

solution buffered with 100 mM Tris-HCl (pH 8.5). Two rounds of centrifugally assisted floatation followed by removal of the subnatant layer were done to ensure complete removal of native GvpC, as confirmed by SDS-PAGE. Stripped Ana GVs were then combined with 2x molar excess of the engineered GvpC variant in 6 M urea buffer after accounting for a 1:25 binding ratio of GvpC:GvpA. Estimating 12,768 GvpA molecules per Ana GV and 564.2 pM of GVs per $OD_{PS,500}$ (1 cm path length), the molar concentration of GvpA per $OD_{PS,500}$ of Ana GVs was determined to be 7.2 μM and used for calculating the amount of engineered GvpC to be added. The engineered GvpC was then allowed to slowly refold onto the surface of the stripped Ana GVs by dialysis against 1x PBS for >12 h at 4°C using a regenerated cellulose membrane with a 6-8 kDa MW cutoff (Spectrum Laboratories, Rancho Dominguez, CA). Dialyzed samples were subjected to at least two rounds of centrifugally assisted floatation to remove any excess unbound GvpC.

**Transmission Electron Microscopy.** GV samples were diluted to $OD_{PS,500}$ ~0.2 in 10 mM HEPES buffer containing 150 mM NaCl (pH 8) and spotted on Formvar/Carbon 200 mesh grids (Ted Pella, Redding, CA) that were rendered hydrophilic by glow discharging (Emitek K100X). GV samples were negatively stained using 2% uranyl acetate. Images were acquired using the Tecnai T12 LaB6 120 kV transmission electron microscope (TEM) equipped with a Gatan Ultrascan 2k x 2k CCD and "Leginon" automated data collection software suite.

**Pressurized Absorbance Spectroscopy.** GV samples were diluted to $OD_{PS,500}$ ~0.2 and loaded onto a flow-through, 1 cm path-length quartz cuvette (Hellma Analytics, Plainview, NY) that was connected to a $N_2$ cylinder through a pressure controller (Alicat Scientific, Tucson, AZ). The pressure was increased stepwise in 20 kPa increments up to 1 MPa, and the $OD_{PS,500}$ at each step was measured using a spectrophotometer (EcoVis, OceanOptics, Winter Park, FL). Fully collapsed GV sample was used as the blank.

***In Vitro* Ultrasound Imaging.** Imaging phantoms were prepared from 1% agarose in PBS. Two times concentrated GV samples were mixed 1:1 with melted 1% agarose at 50°C, and 100 μL of the mixture was quickly loaded into the phantom wells. Imaging was performed using a Verasonics Vantage programmable ultrasound scanning system. The L11-4v or L22-14v 128-element linear array transducers (Verasonics, Kirkland, WA) were used for image acquisition, with a pitch of 0.3 mm or 0.1 mm and elevation focus of 15-20 mm or 6 mm, respectively. The phantom was placed on a custom 3-D printed holder, and the transducer was mounted on a computer-controlled 3-D translating stage (Velmex, Inc., Bloomfield,

NY). During imaging, the transducer was immersed in PBS at an elevation that positioned the focal zone of the ultrasound beam at the center of the sample well. All images were acquired using a conventional B-mode sequence with 128 ray lines.

The acoustic multiplexing and collapse spectrum measurements were obtained by using GV samples at a final OD of 1 and a transmit frequency of 6.25 MHz on the L11-4v, with a four-cycle pulse and transmit focus of 20 mm, focal ratio (F-number) of 2, and persistence of 90. The images were acquired at a transmit voltage of 1.6 V. To collapse GVs, acoustic pressure was delivered to the specimen by lowering the F-number to 0.1 and ramping up the voltage gradually. At each collapse step, the transducer was translated in the y and z planes to ensure homogeneous GV collapse over the entire well.

Nonlinear imaging experiments were performed using the L11-4v transducer with a transmit frequency of 4.46 MHz and receive filtering using a 2 MHz band-pass around 4.46 and 8.92 MHz for the fundamental and second harmonic signals, respectively. GV samples at OD 2.5 were imaged at 2.5 V and F-number 3 using a three-cycle pulse and a persistence of 90.

***In Vivo* Ultrasound Imaging.** Intravenously injected GVs were imaged in 5-7 week old female severe combined immunodeficiency mice using the L11-4v transducer. To be consistent with *in vitro* experiments, a transmit frequency of 4.46 MHz and reception frequencies of 4.46 and 8.92 MHz were used for the fundamental and nonlinear imaging, respectively. Imaging was done at 2.5 V using a three-cycle pulse at an F-number 3 and persistence of 20. The mice were maintained under isofluorane anesthesia on a heated imaging platform. Images were acquired at a rate of 16 frames/s for ~50 s. A 50 μL volume of GVs at OD 23.5 in PBS was infused ~5 s after the start of the experiment at a flow rate of 0.3 $mL \cdot min^{-1}$. Between sample injections, a 10 s high-power burst from the transducer was used to completely collapse any residual GVs in circulation.

**Image Analysis.** Matrix Laboratory (MATLAB) and ImageJ (NIH, Bethesda, MD) were used to process *in vitro* and *in vivo* ultrasound data. Regions of interest (ROIs) were manually defined so as to capture signals from the entire sample well or the IVC. ROI dimensions were preserved between different GV samples and the mean intensity per pixel calculated using all pixels within the ROI. Quantification of *in vitro* harmonic and fundamental GV signals was performed by subtraction of the postcollapse images from the precollapse images. *In vivo* IVC signals were analyzed for all acquired frames over the 50 s imaging window, and smoothed infusion time-course curves were generated using locally weighted scatterplot smoothing. Area

under the curve (AUC) values were obtained from the raw data normalized to the preinfusion baseline. Acoustic spectral unmixing was performed using MATLAB after applying a spectral averaging filter with a kernel size of [20 20] pixels to reduce out-of-well noise. Pseudocolor assignments and merging of spectrally unmixed images were performed using ImageJ (color maps are shown next to the images in Figure 2-2g).

**Zeta Potential Measurements.** Zeta potentials of GVs with GvpC-WT and GvpC-LRP were measured using Brookhaven Instruments Corporation Zeta-PALS instrument (Hotsville, NY). 40 μL of GVs (in PBS) was added to 1.5 mL of double-distilled water at a final concentration of 35 pM and conductance of 1 mS. Electrodes were placed in the cuvette with the samples, and average zeta potential for each run was determined from 10 measurements.

***In Vitro* Characterization of Functionalized GVs.** Alexa-488 succinimidyl ester fluorescent dye (Invitrogen, Carlsbad, CA) was reacted with GVs in PBS for 2 h at 10,000:1 molar excess of dye to GVs. Excess succimidyl ester was quenched with 10 mM Tris. Fluorescently labeled GVs were purified using dialysis against PBS. Cells were seeded on 22 x 22 mm coverglass and cultured for 24 h prior to the start of the experiments. Due to the buoyant nature of GVs, *in vitro* characterization was carried out using modified 6-well plates that contain 3 pegs to enable inverted cell growth (facing down). For receptor ($\alpha_v\beta_3$) targeting experiments, 16 μL of fluorescently labeled GVs ($GvpC_{WT}$, $GvpC_{WT}$-RGD, and $GvpC_{WT}$- RDG) at 1.2 nM were added to U87 cells (ATCC, Manassas, VA) and incubated for 24 h. To test phagocytic uptake using $GvpC_{WT}$, $GvpC_{WT}$-mCD47, and $GvpC_{WT}$-R8, 8 μL of fluorescently labeled GVs at 1.2 nM was added to RAW 264.7 cells (ATCC). After the allotted GV incubation, cells were washed 3x with PBS, fixed with 4% paraformaldehyde, and mounted with 4′,6-diamidino-2-phenylindole (DAPI)-containing mounting media. Confocal fluorescence images were acquired using inverted Zeiss LSM 710 NLO (Thornwood, NY) using a 20x objective.

**SpyTag-SpyCatcher Functionalization of Ana GVs.** SpyTag-Ana GVs were prepared using the re-addition protocol described above. SC-mNG was expressed and purified from BL21 *E. coli* using nondenaturing Ni-NTA purification. ST-GVs (OD 5-10) were incubated with SC-mNG at a 2x molar excess of SpyCatcher:SpyTag in PBS for 1 h at room temperature. GVs were spun at 300g for 4 h twice in order to remove excess unbound protein; the supernatant containing GVs was resuspended in fresh PBS.

ST-GV (±SC-mNG) and WT-GV (+SC-mNG) samples were prepared in a 1%

agarose phantom at a final OD of 2.5 and imaged with the Verasonics L22-14 V transducer at 19 MHz, 5.0 V, and F- number 3 with a persistence of 90. The agarose phantom was also imaged through the green channel of a BioRad Chemidoc MP system (Hercules, CA). The fluorescence intensity of the ST-GV (±SC- mNG) and WT-GV (+SC-mNG) samples was determined by first collapsing the samples and then measuring fluorescence intensity (ex 506 nm, em 550 nm) in a Molecular Devices SpectraMax M5 plate reader (Sunnyvale, CA).

## References


1. Lakshmanan, A. *et al.* Molecular Engineering of Acoustic Protein Nanostructures. *ACS Nano* **10,** 7314–7322 (2016).
2. Cosgrove, D. & Harvey, C. Clinical uses of microbubbles in diagnosis and treatment. *Med. Biol. Eng. Comput.* **47,** 813–26 (2009).
3. Errico, C. *et al.* Ultrafast ultrasound localization microscopy for deep super-resolution vascular imaging. *Nature* **527,** 499–502 (2015).
4. Kaufmann, B. A. & Lindner, J. R. Molecular imaging with targeted contrast ultrasound. *Curr. Opin. Biotechnol.* **18,** 11–6 (2007).
5. Ferrara, K., Pollard, R. & Borden, M. Ultrasound microbubble contrast agents: fundamentals and application to gene and drug delivery. *Annu. Rev. Biomed. Eng.* **9,** 415–47 (2007).
6. Shapiro, M. G. *et al.* Biogenic gas nanostructures as ultrasonic molecular reporters. *Nature nanotechnology* **9,** 311–316 (2014).
7. Walsby, A. E. Gas vesicles. *Microbiol. Rev.* **58,** 94–144 (1994).
8. Pfeifer, F. Distribution, formation and regulation of gas vesicles. *Nat. Rev. Microbiol.* **10,** 705–15 (2012).
9. Kinsman, R. & Hayes, P. Genes encoding proteins homologous to halobacterial Gvps N, J, K, F & L are located downstream of gvpC in the cyanobacterium Anabaena flos-aquae. *DNA Sequence* **7,** 97–106 (1997).
10. Hayes, P. & Powell, R. ThegvpA/C cluster ofAnabaena flos-aquae has multiple copies of a gene encoding GvpA. *Archives of microbiology* **164,** 50–57 (1995).
11. Walsby, A. E. & Hayes, P. K. Gas vesicle proteins. *Biochemical Journal* **264,** 313 (1989).
12. Buchholz, B., Hayes, P. & Walsby, A. The distribution of the outer gas vesicle protein, GvpC, on the Anabaena gas vesicle, and its ratio to GvpA. *Microbiology* **139,** 2353–2363 (1993).
13. Hayes, P., Buchholz, B. & Walsby, A. Gas vesicles are strengthened by the outer-surface protein, GvpC. *Archives of microbiology* **157,** 229–234 (1992).
14. Kinsman, R., Walsby, A. & Hayes, P. GvpCs with reduced numbers of repeating sequence elements bind to and strengthen cyanobacterial gas vesicles. *Molecular microbiology* **17,** 147–154 (1995).
15. DasSarma, S. *et al.* An improved genetic system for bioengineering buoyant gas vesicle nanoparticles from Haloarchaea. *BMC biotechnology* **13,** 1 (2013).
16. Sremac, M. & Stuart, E. S. Recombinant gas vesicles from Halobacterium sp. displaying SIV peptides demonstrate biotechnology potential as a pathogen peptide delivery vehicle. *BMC biotechnology* **8,** 9 (2008).

17. Walsby, A. E., Revsbech, N. P. & Griffel, D. H. The gas-permeability coefficient of the cyanobacterial gas vesicle wall. *Journal of General Microbiology* **138,** 837–845 (1992).

18. Cherin, E. *et al.* Acoustic Behavior of Halobacterium salinarum Gas Vesicles in the High-Frequency Range: Experiments and Modeling. *Ultrasound in Medicine & Biology* **43,** 1016–1030 (2017).

19. Burns, P. N. Harmonic imaging with ultrasound contrast agents. *Clin. Radiol.* **51,** 50–55 (1996).

20. Maresca, D. *et al.* Imaging microvasculature with contrast-enhanced ultraharmonic ultrasound. *Ultrasound in medicine & biology* **40,** 1318–1328 (2014).

21. Blanco, E., Shen, H. & Ferrari, M. Principles of nanoparticle design for overcoming biological barriers to drug delivery. *Nature biotechnology* **33,** 941–951 (2015).

22. Ruoslahti, E. RGD and other recognition sequences for integrins. *Annual review of cell and developmental biology* **12,** 697–715 (1996).

23. Rodriguez, P. L. *et al.* Minimal" Self" peptides that inhibit phagocytic clearance and enhance delivery of nanoparticles. *Science* **339,** 971–975 (2013).

24. Brock, R. The uptake of arginine-rich cell-penetrating peptides: putting the puzzle together. *Bioconjugate chemistry* **25,** 863–868 (2014).

25. Zakeri, B. *et al.* Peptide tag forming a rapid covalent bond to a protein, through engineering a bacterial adhesin. *Proc Natl Acad Sci U S A* **109,** E690–7 (2012).

## 2.6 Supplementary Information

| GV Variants | Midpoint of Collapse ($P_c$) (kPa) | $P_c$ (SEM) (kPa) | ΔP (kPa) | ΔP (SEM) (kPa) | Adj. R-Square |
|---|---|---|---|---|---|
| ΔGvpC | 195.30 | 0.27 | 17.01 | 0.24 | 0.999 |
| ΔN&C | 374.30 | 1.01 | 41.46 | 0.89 | 0.999 |
| $GvpC_{WT}$ | 569.85 | 3.64 | 84.87 | 3.21 | 0.992 |

**Table 2-S1:** Hydrostatic midpoint of collapse for engineered Ana GVs used in acoustic multiplexing experiments (Figure 2-2b). The data was fitted with a Boltzmann sigmoid function of the form $f(p) = (1 + e^{(p-p_c)/\Delta p})^{-1}$ with $p_c$ representing the average midpoint of collapse. Fit parameters and $R^2$ values for each of the GV variants are provided in the table.

| GV Variants | Midpoint of Collapse (Pc) (kPa) | $P_c$ (SEM) (kPa) | ΔP (kPa) | ΔP (SEM) (kPa) | Adj. R-Square |
|---|---|---|---|---|---|
| ΔGvpC | 571.00 | 1.51 | 14.48 | 1.03 | 0.998 |
| ΔN&C | 657.04 | 3.94 | 77.47 | 3.70 | 0.997 |
| $GvpC_{WT}$ | 868.81 | 6.56 | 94.00 | 5.57 | 0.994 |

**Table 2-S2:** Hydrostatic midpoint of collapse for engineered Ana GVs used in acoustic multiplexing experiments (Figure 2-2c). The data was fitted with a Boltzmann sigmoid function of the form $f(p) = (1 + e^{(p-p_c)/\Delta p})^{-1}$ with $p_c$ representing the average midpoint of collapse. Fit parameters and $R^2$ values for each of the GV variants are provided in the table.

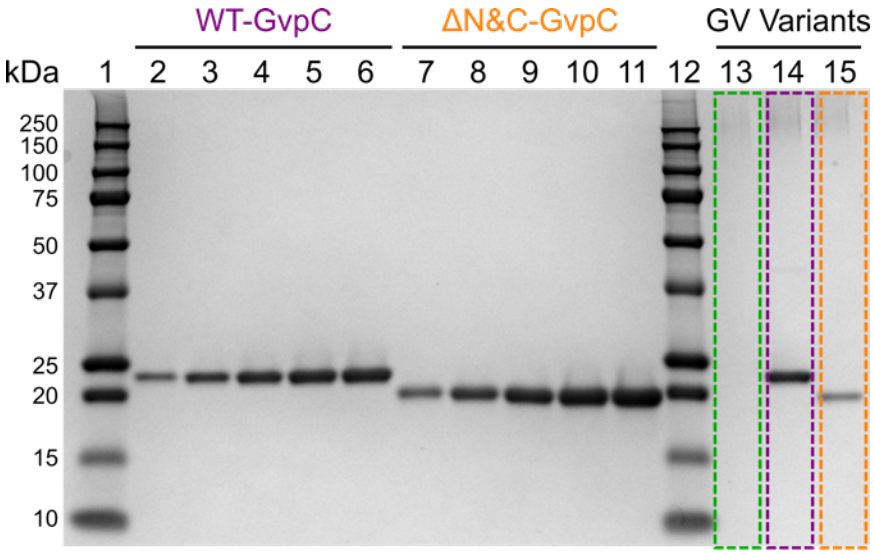


| Lane | Sample |
|---|---|
| 1 | Ladder |
| 2 | WT-GvpC (200ng) |
| 3 | WT-GvpC (400ng) |
| 4 | WT-GvpC (600ng) |
| 5 | WT-GvpC (800ng) |
| 6 | WT-GvpC (1000ng) |
| 7 | ΔN&C-GvpC (200ng) |
| 8 | ΔN&C-GvpC (400ng) |
| 9 | ΔN&C-GvpC (600ng) |
| 10 | ΔN&C-GvpC (800ng) |
| 11 | ΔN&C-GvpC (1000ng) |
| 12 | Ladder |
| 13 | ΔGvpC Ana GVs (OD: 5) |
| 14 | $GvpC_{WT}$ Ana GVs (OD: 5) |
| 15 | ΔN&C Ana GVs (OD: 5) |

**Figure 2-S1:** SDS-PAGE analysis confirming the complete removal of GvpC from native Ana GVs (lane 13) and the re-addition of engineered proteins (lane 14-15). Quantification of re-added GvpC on urea-stripped Ana GVs was done by comparison against a standard curve (200 - 1000 ng) of the pure proteins (lanes 2-6 for WT-GvpC and lanes 7-11 for ΔN&C-GvpC). The number of re-added GvpC molecules was determined to be 1980 per GV for $GvpC_{WT}$ and 877 per GV for ΔN&C-GvpC respectively.

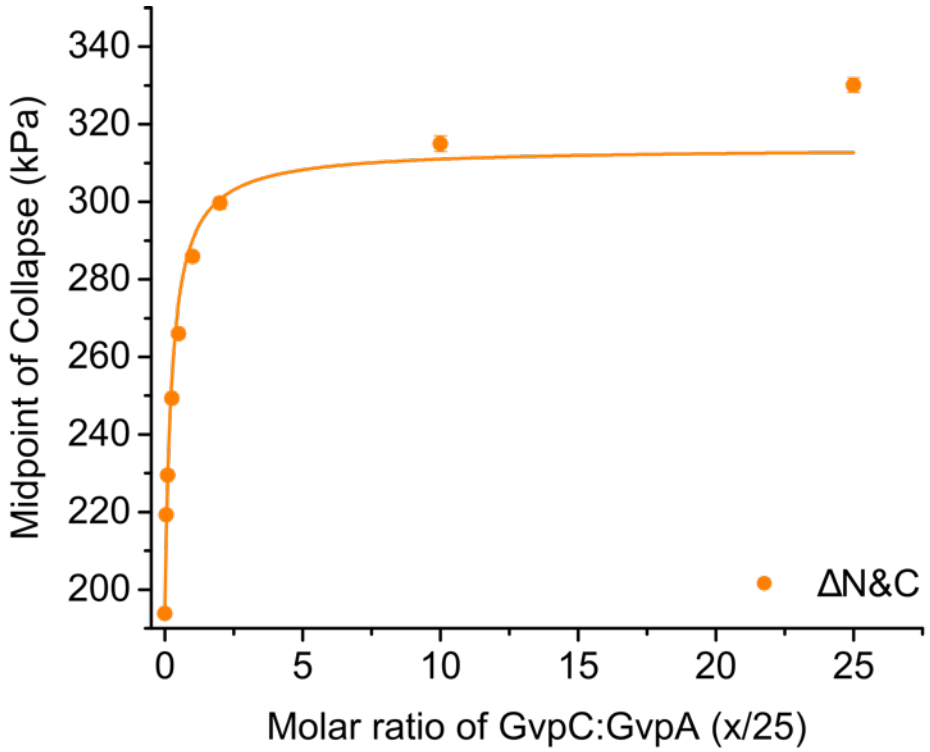


| Molar ratio of GvpC : GvpA (x/25) | Midpoint of Collapse (Pc) (kPa) | $P_c$ (SEM) (kPa) | ΔP (kPa) | ΔP (SEM) (kPa) | Adj. R-Square |
|---|---|---|---|---|---|
| 0 | 193.77 | 0.31 | 16.72 | 0.27 | 0.999 |
| 0.05 | 219.29 | 0.46 | 20.44 | 0.40 | 0.999 |
| 0.1 | 229.47 | 0.62 | 21.9 | 0.55 | 0.999 |
| 0.25 | 249.28 | 0.99 | 28.07 | 0.88 | 0.998 |
| 0.5 | 266.01 | 1.13 | 30.94 | 0.99 | 0.998 |
| 1 | 285.85 | 1.19 | 33.95 | 1.05 | 0.998 |
| 2 | 299.66 | 1.53 | 40.31 | 1.35 | 0.997 |
| 10 | 314.99 | 2.01 | 50.84 | 1.77 | 0.996 |
| 25 | 330.11 | 1.88 | 50.75 | 1.65 | 0.997 |

**Figure 2-S2:** Midpoint of collapse (hydrostatic) plotted as a function of re-added GvpC concentration for the ΔN&C variant. The midpoint of collapse was determined by fitting the raw data with a Boltzmann sigmoid function of the form $f(p) = (1 + e^{(p-p_c)/\Delta p})^{-1}$ with $p_c$ representing the average midpoint of collapse. Fit parameters and $R^2$ values for each of the GV variants are provided. The saturation curve was plotted by fitting the data to a bimolecular binding function of the form $f(x) = C_1 * x/(K_d + x) + C_2$.

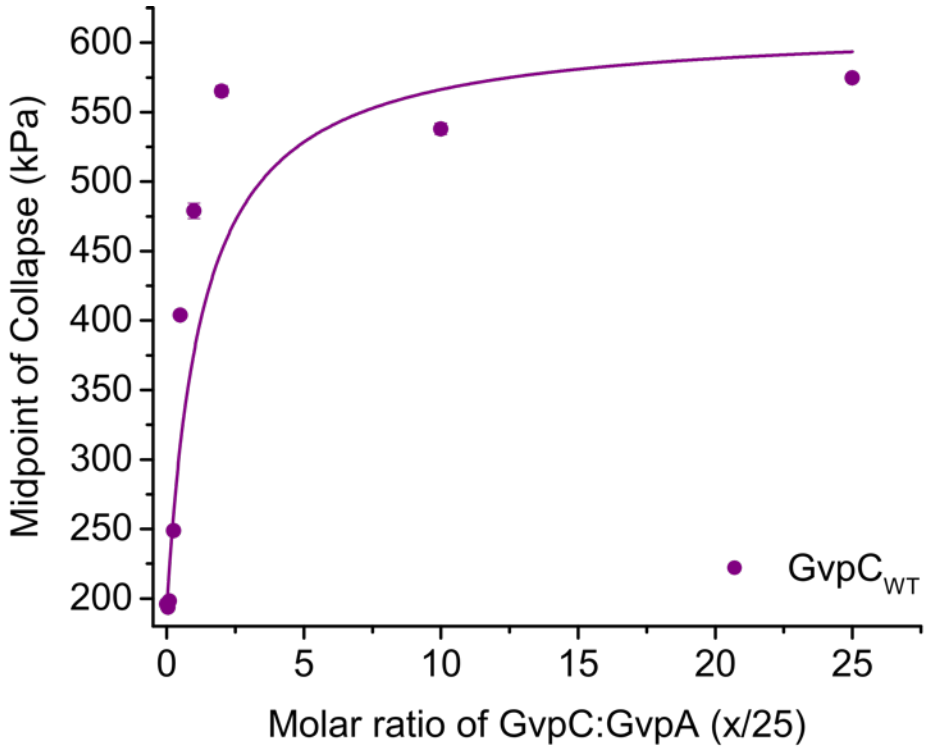


| Molar ratio of GvpC : GvpA (x/25) | Midpoint of Collapse (Pc) (kPa) | $P_c$ (SEM) (kPa) | ΔP (kPa) | ΔP (SEM) (kPa) | Adj. R-Square |
|---|---|---|---|---|---|
| 0 | 195.95 | 0.21 | 16.23 | 0.18 | 0.999 |
| 0.05 | 193.48 | 0.43 | 17.54 | 0.38 | 0.999 |
| 0.1 | 198.12 | 0.91 | 19.90 | 0.80 | 0.998 |
| 0.25 | 248.68 | 1.24 | 33.60 | 1.09 | 0.998 |
| 0.5 | 403.93 | 2.24 | 61.03 | 1.98 | 0.996 |
| 1 | 479.01 | 5.50 | 108.11 | 4.88 | 0.985 |
| 2 | 565.15 | 3.92 | 79.10 | 3.46 | 0.990 |
| 10 | 537.95 | 4.24 | 86.97 | 3.74 | 0.989 |
| 25 | 574.72 | 2.29 | 62.93 | 2.03 | 0.996 |

**Figure 2-S3:** Midpoint of collapse (hydrostatic) plotted as a function of re-added GvpC concentration for the $GvpC_{WT}$ variant. The midpoint of collapse was determined by fitting the raw data with a Boltzmann sigmoid function of the form $f(p) = (1 + e^{(p-p_c)/\Delta p})^{-1}$ with $p_c$ representing the average midpoint of collapse. Fit parameters and $R^2$ values for each of the GV variants are provided. The saturation curve was plotted by fitting the data to a bimolecular binding function of the form $f(x) = C_1 * x/(K_d + x) + C_2$.

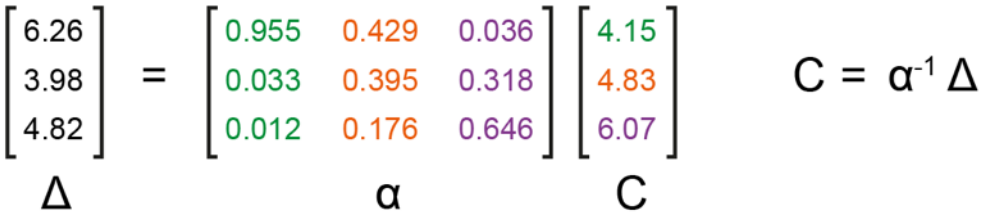


**Figure 2-S4:** Matrix of coefficients used for generating spectrally unmixed images shown in Figure 2-2g from the pixel-wise ultrasound signal intensities in Figure 2-2f (I), before and after exposing the GV samples to three sequentially increasing acoustic pressures ($P_i$). $\Delta$ represents the measured differential signals with $\Delta_i = I(P_{i-1}) - I(P_i)$, while $\alpha$ is the matrix containing the acoustic collapse spectrum for each GV variant ($\alpha_{i,j}$). C represents the contribution of each GV variant to the observed signal, with $C_j$ calculated by the matrix operation: $C = \alpha^{-1}\Delta$.

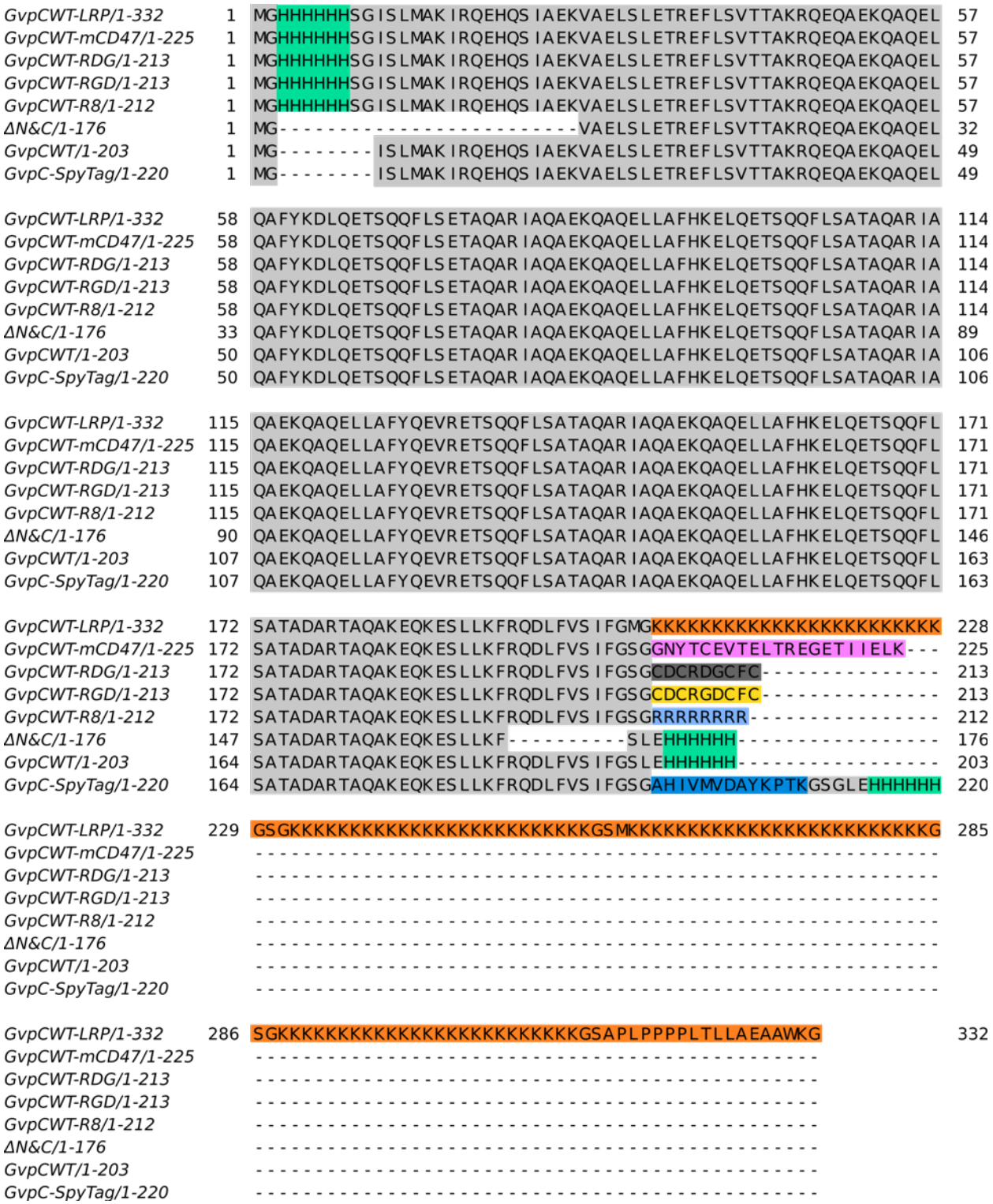


**Figure 2-S5:** Clustal Omega sequence alignment of all the genetically engineered GvpC proteins used in our study. Colors highlight important features and are set to match the schematic illustration in Figure 2-5a.

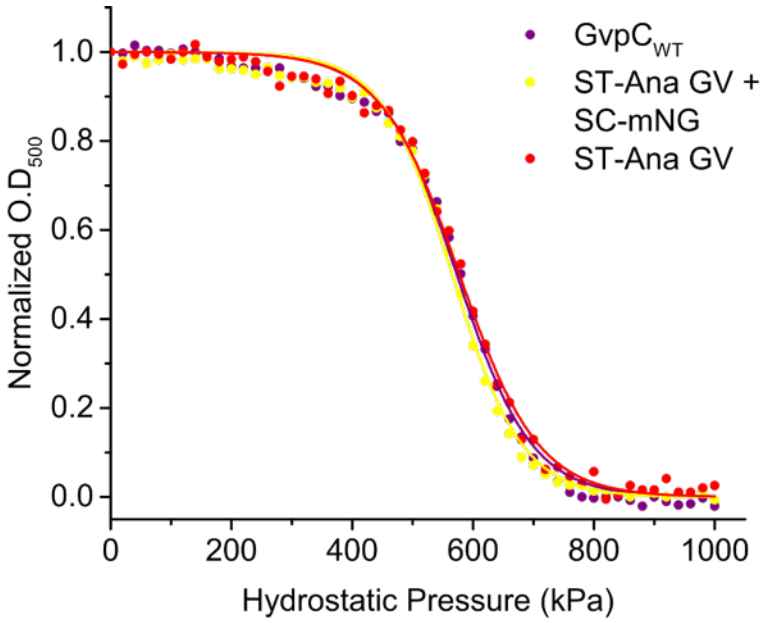


| GV Variants | Midpoint of Collapse ($P_c$) (kPa) | $P_c$ (SEM) (kPa) | ΔP (kPa) | ΔP (SEM) (kPa) | Adj. R-Square |
|---|---|---|---|---|---|
| GvpC$_{WT}$ | 572.84 | 2.33 | 62.00 | 2.05 | 0.996 |
| ST-Ana GV + SC-mNG | 565.13 | 2.18 | 57.70 | 1.92 | 0.996 |
| ST-Ana GV | 577.31 | 2.29 | 65.09 | 2.01 | 0.996 |

**Figure 2-S6:** Optical density measurements of engineered Ana GVs as a function of hydrostatic pressure. The data was fitted with the Boltzmann sigmoid function $f(p) = (1 + e^{(p-p_c)/\Delta p})^{-1}$ and the table provides the midpoint of collapse as well as other fit parameters and $R^2$ values. The data show that the collapse profile is unaltered even after reacting the ST-GVs with SC-mNG fluorescent protein.

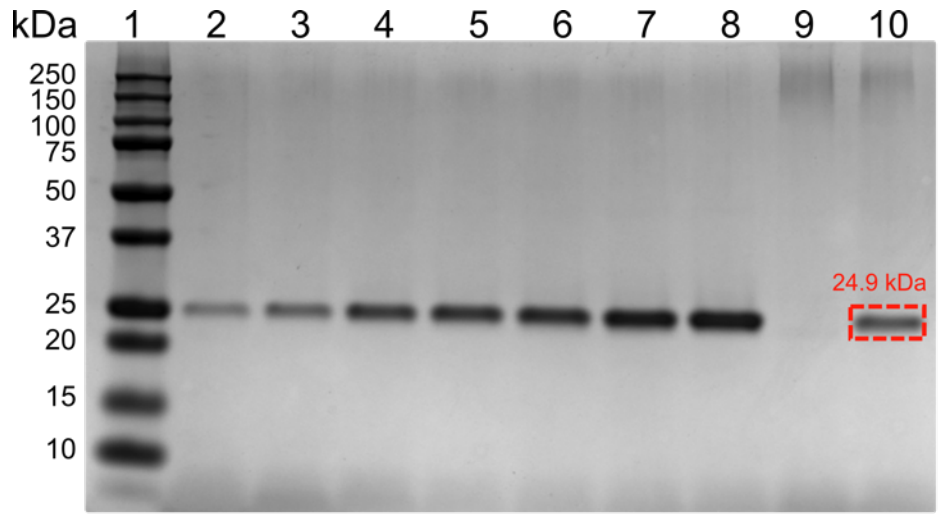


| Lane | Sample |
|---|---|
| 1 | Ladder |
| 2 | GvpC-ST (100ng) |
| 3 | GvpC-ST (200ng) |
| 4 | GvpC-ST (400ng) |
| 5 | GvpC-ST (500ng) |
| 6 | GvpC-ST (600ng) |
| 7 | GvpC-ST (800ng) |
| 8 | GvpC-ST (1000ng) |
| 9 | ΔGvpC Ana GVs (OD: 7.8) |
| 10 | ST-Ana GVs (OD: 3.0) |

**Figure 2-S7:** SDS-PAGE quantification of SpyTag functionalities on the surface of engineered Ana GVs. Comparison of ST-Ana GVs (lane 10) against a standard curve comprising GvpC-ST concentrations ranging from 100-1000 ng (lanes 2-8) shows that each modified GV has ~1000 SpyTag functionalities. Stripped Ana GVs used for GvpC-ST re-addition (lane 9) have negligible amount of native GvpC.

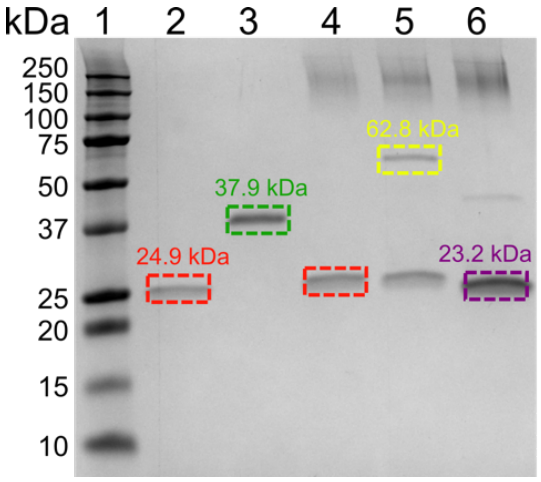


| Lane | Sample |
|---|---|
| 1 | Ladder |
| 2 | GvpC-ST (24.9 kDa) |
| 3 | SC-mNG (37.9 kDa) |
| 4 | ST-Ana GVs (OD:3) |
| 5 | ST-Ana GVs (OD: 3) + SC-mNG (62.8 kDa) |
| 6 | $GvpC_{WT}$ Ana GVs (OD: 6) + SC-mNG |

**Figure 2-S8:** SDS-PAGE analysis confirms SpyTag-SpyCatcher bond formation (yellow) upon a one-hour incubation of ST-GVs having an outer layer of GvpC-SpyTag (red) with SpyCatcher-mNeonGreen (green). Incubation of Ana GVs containing an outer layer of WT-GvpC (purple) with SC-mNG, followed by buoyancy purification to remove unreacted fluorescent molecules results in GVs that are not fluorescent as shown in Figure 2-5g (left bottom panel). This also highlights the specificity of the SpyTag-SpyCatcher reaction and confirms that all the unreacted fluorescent molecules are completely removed during buoyancy purification.

*Chapter 3*

# RECOMBINANTLY EXPRESSED GAS VESICLES AS NANOSCALE CONTRAST AGENTS FOR ULTRASOUND AND HYPERPOLARIZED MRI

This chapter is in large part a reformatted version of the manuscript entitled "Recombinantly Expressed Gas Vesicles as Nanoscale Contrast Agents for Ultrasound and Hyperpolarized MRI" published by Farhadi, A., Ho, G.H., Kunth, M., Ling, B., Lakshmanan, A., Lu, G., Bourdeau, R.W., Schröder, L., and Shapiro M.G., in *AIChE Journal*[1]. Under the supervision of Mikhail Shapiro, my contributions to this work was to conceive, design and conduct the experiments, and analyze and interpret the data, and write the manuscript. Thanks to Gabrielle Ho, Bill Ling, Anupama Lakshmanan, George Lu, and Raymond Bourdeau for the assistance with sample preparation and data collection, and Martin Kunth and Lief Schröder for collecting and analyzing the hyperpolarized $^{129}$Xe-MRI.

## 3.1 Abstract

Ultrasound and hyperpolarized magnetic resonance imaging enable the visualization of biological processes in deep tissues. However, few molecular contrast agents are available to connect these modalities to specific aspects of biological function. We recently discovered that a unique class of gas-filled protein nanostructures known as gas vesicles could serve as nanoscale molecular reporters for these modalities. However, the need to produce these nanostructures via expression in specialized cultures of cyanobacteria or haloarchaea limits their broader adoption by other laboratories and hinders genetic engineering of their properties. Here, we describe recombinant expression and purification of *Bacillus megaterium* gas vesicles using a common laboratory strain of *Escherichia coli*, and characterize the physical, acoustic and magnetic resonance properties of these nanostructures. Recombinantly expressed gas vesicles produce ultrasound and hyperpolarized $^{129}$Xe MRI contrast at sub-nanomolar concentrations, thus validating a simple platform for their production and engineering.

## 3.2 Introduction

Optical reporters such as organic dyes and fluorescent and luminescent proteins have enabled many biological discoveries. However, the poor penetration of light into tissue limits the use of these reporters in intact animal models and human patients[2]. In contrast, noninvasive imaging techniques such as ultrasound and magnetic resonance imaging (MRI) are capable of visualizing deep tissues, but have fewer molecular reporters to connect them to specific biological phenomena[3]. Ultrasound is among the most widely used biomedical imaging modalities, offering high spatial and temporal resolution (~100 μm and sub-millisecond) while penetrating deep into the organism[4]. Ultrasound contrast is produced by sound wave scattering at interfaces between materials with different density or stiffness. Likewise, MRI is capable of whole-body imaging with spatial resolution on the order of 100 μm, and uses a variety of contrast mechanisms arising from nuclear spin behavior[5]. Among these mechanisms, hyperpolarized MRI provides particularly high molecular sensitivity by using nuclei, such as $^{129}$Xe, prepared with non-equilibrium polarization several orders of magnitude higher than that available under equilibrium conditions[6]. Hyperpolarized $^{129}$Xe can be administered through inhalation or injection for *in vivo* imaging.

Hyperpolarized MRI and ultrasound have few molecular reporters for biological imaging. Conventional ultrasound contrast agents comprise microbubbles, which are limited by their micron scale and physical instability to imaging primarily intravascular targets[7,8]. Nanoscale synthetic reporters for this modality are in development,[9–11] but have not reached wide- spread use. Meanwhile, common contrast agents for hyperpolarized $^{129}$Xe-MRI comprise organic cage compounds which reversibly bind xenon and produce contrast through hyperpolarized chemical exchange saturation transfer (HyperCEST)[12–15]. Most such molecules, while detectible, have relatively low solubility in water and can be difficult to deliver to tissues.

To address these limitations, we recently introduced a unique class of air-filled protein nanostructures called gas vesicles (GVs) as genetically encodable reporters for ultrasound and hyperpolarized MRI[16–21]. GVs are naturally expressed in aqueous photosynthetic bacteria and archaea as a means to achieve buoyancy[22,23]. GVs have dimensions on the order of 100 nm, comprising a 2-nm-thick protein shell that allows gas to freely diffuse in and out of their hollow interior while preventing water from condensing into a liquid in their core (Figure 3-1a). The contents of GVs reflect the gases dissolved in surrounding liquid media. The GV shell is primarily formed from gas vesicle protein A or B (gvpA/B), and in some species is supported by an

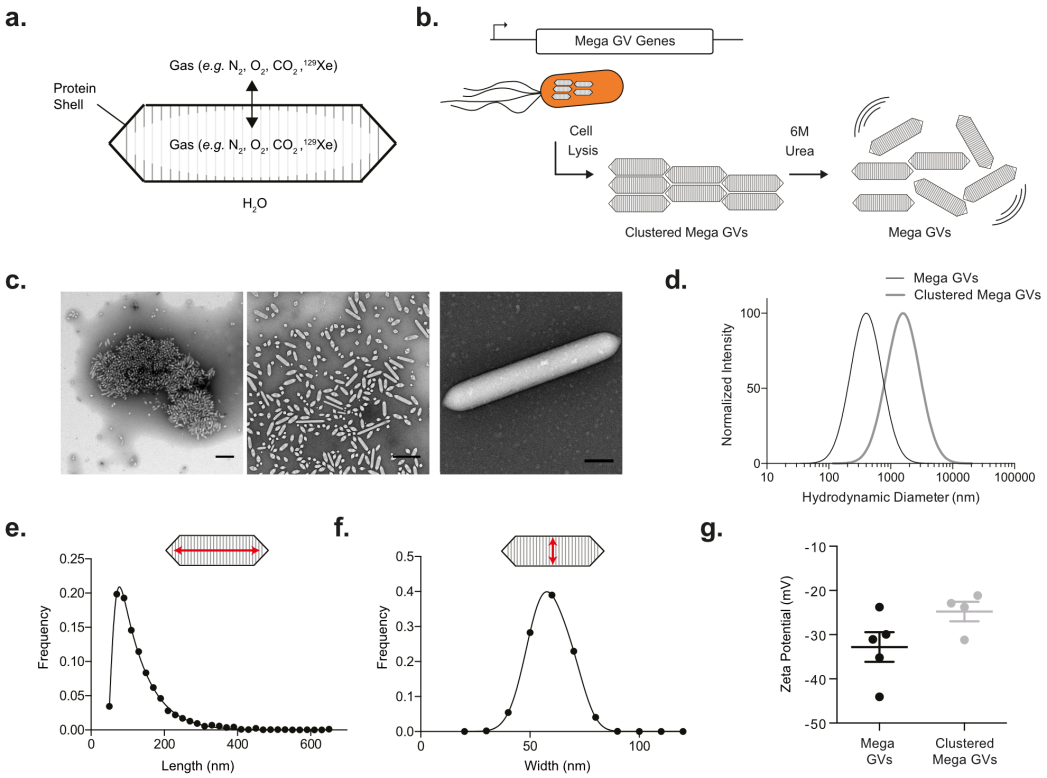


**Figure 3-1: Recombinantly expressed Mega GVs.** (a) Schematic of Mega gas vesicles, hollow protein nanostructures that allow gas to diffuse through the protein shell but keep water from condensing in the core. (b) Mega GVs are heterologously expressed in *E. coli*, purified and declustered for characterization as ultrasound and hyperpolarized MRI contrast agents. (c) Transmission electron micrograph of purified recombinant GVs, (left) Mega GVs form micron sized clusters upon cell lysis, which can be declustered using 6M urea (center). (Representative image of mature Mega GV recombinantly expressed in *E. coli* (right). Scale bars are 500 nm for left and center images, and 100 nm for right image.) (d) Hydrodynamic diameter of clustered Mega GVs are 1.7 µm and upon declustering, Mega GVs are 164 nm. (N=4 independent preparations for clustered Mega GVs and N=5 independent preparations for Mega GVs.) (e-f) Histogram of length and width of Mega GVs using TEM analysis. (Measurements represent 3487 particles from N=4 independent biological preparations.) (g) Zeta potential measurements of Mega GVs and clustered Mega GVs. (N = 4, error bars are ± SEM).

external scaffolding protein known as gas vesicle protein C (gvpC). In addition, 7-11 assembly factor genes are required for GV formation.

We recently demonstrated that GVs purified from native host cells such as *Anabaena flos-aquae* (Ana) and *Halobacterium NRC-1* (Halo) can be used as biomolecular reporters for both ultrasound and hyperpolarized $^{129}$Xe-MRI[16,17,20]. The former capability arises from the ability of GVs to scatter sound waves via non-linear interactions with the acoustic field[19,21]. The latter contrast arises from the ability of GVs

to act as hosts for hyperpolarized $^{129}$Xe, allowing their detection using HyperCEST pulse sequences. Building on these initial discoveries, we have developed methods to engineer the scaffolding protein of Ana GVs to modify their acoustic and targeting properties[18], and devised optimized pulse sequences for improved ultrasound contrast[21]. GVs produce ultrasound contrast when injected in circulation or in the gastrointestinal tract of the mammalian host.[16,18,21,24] However, this work has utilized GVs expressed in their native hosts, which require special culture conditions not available in all laboratories, and are more cumbersome to engineer genetically than conventional laboratory bacterial species. To overcome these limitations, we set out to establish a system for producing GVs in a common laboratory strain of *E. coli* and characterize their essential properties as nanoscale reporters for ultrasound and hyperpolarized $^{129}$Xe-MRI.

### 3.3 Results and Discussions

**Recombinant Expression and Physical Characterization.** As a starting point for recombinant GV production, we chose a GV gene cluster from *Bacillus megaterium* (Mega) that was previously shown to be compatible with *E. coli* expression in a study where the GVs were not purified to examine their properties[25]. We cloned this gene cluster into a high copy *E. coli* expression plasmid, downstream of a T7-LacO inducible promoter. A bacterial strain used for protein overexpression, Rosetta 2(DE3)pLysS, was transformed with the plasmid and induced to express Mega GVs for 22 hours. After gentle lysis, GVs could be separated from cellular debris through buoyancy purification (Figure 3-1b).

Immediately after purification, Mega GVs were clustered, as observed by transmission electron microscopy (TEM) (Figure 3-1c). Dynamic light scattering (DLS) revealed a mean hydrodynamic diameter of 1733 ± 113 nm (Figure 3-1d). Hypothesizing that the clustering is mediated by a denaturable non-covalent interaction involving proteins, we attempted to de-cluster the Mega GVs by treating them with 6M urea, based on previous findings that urea treatment can remove surface proteins from Ana GVs without compromising their shells[18,26]. Urea treatment resulted in declustered GVs with an average hydrodynamic diameter of 164 ± 19 nm (Figure 3-1d). Quantitative analysis of TEM data revealed that Mega GVs have diameters of 59 ± 9 nm and lengths of 129 ± 70 nm (Figure 3-1e-f). Assuming a tapered cylindrical shape, this corresponds to a single-GV volume of 0.2 attoliter (0.054-0.48 attoliter), which is approximately 32 times smaller than for Ana and Halo GVs[20]. Individual Mega GVs had an average zeta potential of -32.8 ± 10 mV (Figure 3-1g).

A zeta potential of -24.8 ± 4 mV in clustered Mega GVs indicated that positively charged molecules were associated with negatively charged GVs in the cluster.

Based on the average dimensions and geometry of GVs observed by TEM (cylindrical with conical tips), an assumed shell thickness of 18 Å based on GvpA homology to Ana[23], and a protein density of 1.4 g/ml, we calculated the average molecular weight of Mega GVs to be 71.7 MDa. Because GVs scatter light, it is practically convenient to measure their molar concentration using their optical density at 500 nm ($OD_{500}$). To establish the relationship between $OD_{500}$ and concentration, the protein concentration of Mega GVs was measured using a Pierce 660-nm assay to be 145 μg/mL per $OD_{500}$. Using the average molecular weight, this corresponds to a molar concentration of 2.03 nM/$OD_{500}$. When Mega GVs are clustered, they scatter light more strongly, with declustering leading to an average 6-fold reduction in light scattering. Thus, the concentration of clustered Mega GVs can be estimated as 338 pM/$OD_{500}$.

A key property of GVs useful in both ultrasound and MR imaging applications is their ability to irreversibly collapse under specific amounts of pressure (Figure 3-2a). This enables background-subtracted and multiplexed imaging, and provides convenient experimental controls, since collapsed GVs cease to produce contrast. Upon collapse, GVs also lose their ability to scatter light, causing opaque GV solutions to become clear (Figure 3-2b). To characterize the critical collapse pressure of Mega GVs, we measured the optical scattering of GV suspensions as a function of applied hydrostatic pressure. Clustered and unclustered Mega GVs had hydrostatic collapse midpoints of 660 kPa and 767 kPa, respectively (Figure 3-2c).

**Ultrasound Contrast.** The gaseous core of GVs allows these structures to function as ultrasound contrast agents[16,18,19,21]. To evaluate the ability of Mega GVs to serve this function, these nanostructures were embedded in acoustically transparent agarose phantoms and imaged with ultrasound at 18 MHz, a frequency within the range commonly used for preclinical imaging. Mega GVs produced B-mode ultrasound contrast at concentrations as low as 40 pM, with stronger contrast at increasing concentrations (Figure 3-3a-b). Given their larger size, we expected micron-sized clusters of GVs to produce stronger ultrasound contrast than the nano-sized Mega GVs, since both of them are small enough relative to the wavelength to be in the Rayleigh scattering regime[19]. At equal concentrations, clustered Mega GV contrast was 54% stronger.

Acoustic pressures above critical collapse points allow GVs to be collapsed *in situ*, enabling background subtraction and multiplexing in imaging experiments[16,18].

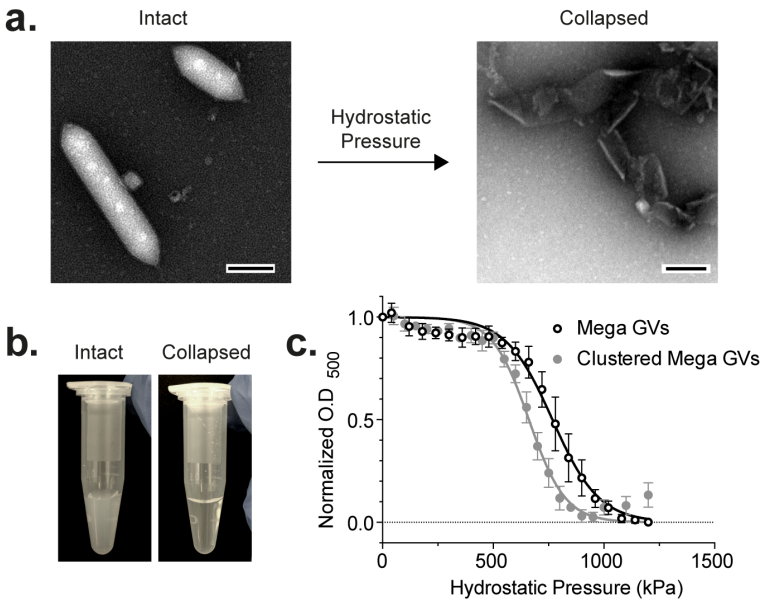


**Figure 3-2: Hydrostatic collapse of recombinant Mega GVs.** (a) Representative TEM image of Mega GVs (left) under hydrostatic pressure beyond critical collapse causes the gas vesicle wall to unravel (right). (Scale bars are 100 nm.) (b) Intact Mega GVs scatter light when in suspension (left) and become clear upon collapse as their gaseous core dissolves in solution (right). (c) Optical density measurement of clustered Mega and Mega GVs as a function of hydrostatic pressure. Data is fit to a Boltzmann sigmoid function of the form $f(p) = (1 + e^{(p-p_c)/\Delta p})^{-1}$ with $p_c$ representing average midpoint of collapse and Δp representing the slope (N=4, error bars are ± SEM).

These acoustic collapse mid-points can be significantly higher than their hydrostatic counterparts due to the microsecond kinetics of gas exchange through the GVs shell[27]: while under hydrostatic conditions, gas molecules have time to escape through the GV wall during compression, the microsecond cycles of ultrasound are too rapid, resulting in gas staying in the shell and contributing to deformation resistance under pressure[19,21]. To establish the critical mid-points for Mega GVs, we imaged them with ultrasound while applying increasing acoustic pressures at 18 MHz. The resulting collapse mid-points were 2.2 and 1.9 MPa for Clustered Mega and Mega GVs, respectively (Figure 3-3c). These pressures provide ample range for the GVs to be imaged with relatively strong acoustic excitation, while being low enough for most ultrasound transducers to be able to collapse them.

**Hyperpolarized $^{129}$Xe-MRI Contrast.** Dissolved xenon can partition in and out of the gaseous GV interior (Figure 3-1a). The distinct chemical environment of this compartment results in a specific chemical shift of the $^{129}$Xe magnetic resonance frequency, enabling sensitive imaging of GVs using $^{129}$Xe HyperCEST

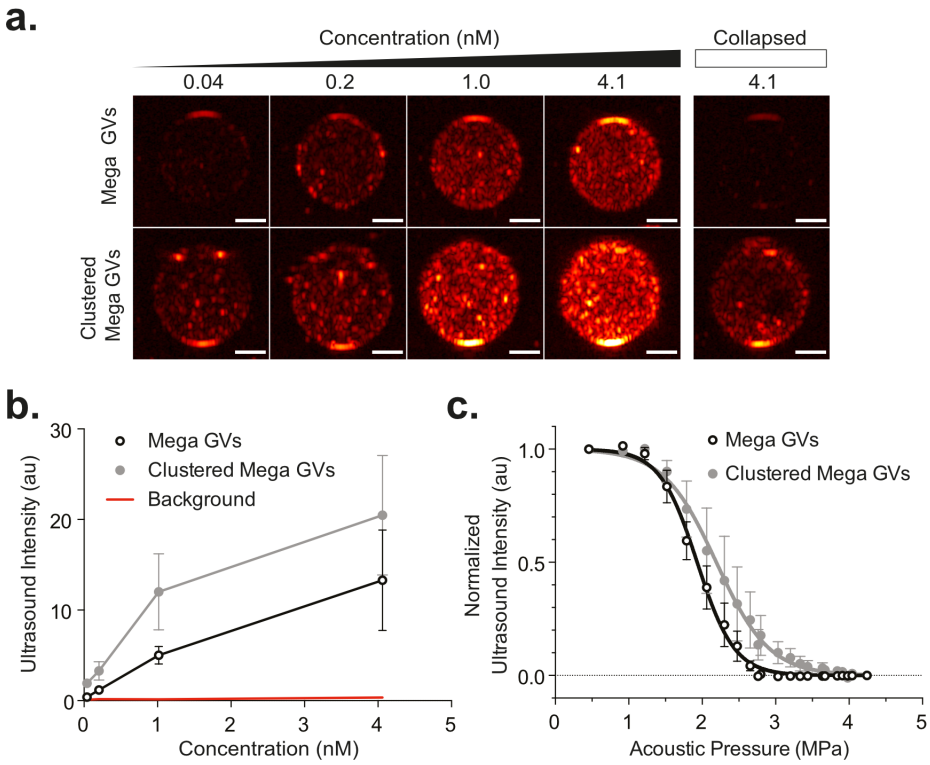


**Figure 3-3: Recombinant Mega GVs as ultrasound contrast agents.** (a) B-mode ultrasound images of Mega GVs (top row) and clustered Mega GVs (bottom row) showing increased intensity as a function of concentration (40, 203, 1015, and 4060 pM GV particles) in 1% agarose phantom using a 18 MHz imaging transducer under 0.91 MPa acoustic pressure. Ultrasound images of 4060 pM Mega GVs (top right) and clustered Mega GVs (bottom right) after 4.2 MPa ultrasound insonation. (Representative images from N=4 independent preparations. Scale bars are 1 mm.) (b) Graph of average ultrasound intensities for Mega GVs and clustered Mega GVs as a function of concentration (N=4 independent preparations, error bars are ± SEM.) (c) Acoustic collapse measurements of Mega GVs and clustered Mega GVS as a function of acoustic pressure. Data is fit to a Boltzmann sigmoid function of the form $f(p) = (1 + e^{(p-p_c)/\Delta p})^{-1}$ with $p_c$ representing average midpoint of collapse and $\Delta$p representing the slope (N=4, error bars are SEM).

MRI[6,17]. To evaluate the MRI performance of Mega GVs, we imaged them at 9.4 Tesla in a phantom bubbled with $^{129}$Xe gas that was hyperpolarized using spin-exchange optical pumping[20,28] (Figure 3-4a). Using the distinct chemical shift of $^{129}$Xe in the GV interior, the gas atoms can be selectively saturated with on-resonance radio frequency (RF) pulses, while exchanging with $^{129}$Xe in solution, resulting in a decrease in the overall $^{129}$Xe signal (Figure 3-4b). A stepwise sweep of the saturation frequency while monitoring the remaining total polarization allowed us to identify a saturation peak for the xenon in Mega GVs at -174 ppm relative to free dissolved xenon. Ten second saturation pulses at this frequency produced significant HyperCEST effects for Mega GVs at concentrations as low as 40.6 pM (Figure 3-4c). The intensity of the HyperCEST effect with respect to the GV concentration followed an exponential relationship (Figure 3-4d). This can be understood as the increasing GV concentration causing a linear increase in the Lorentzian-shaped depolarization rate of xenon, with the set saturation time causing an added exponential weighting[29–31].

## 3.4 Conclusions

Recombinant expression of Mega GVs in *E. coli* provides a convenient platform for the simple and rapid production of gas-filled protein nanostructures for applications in molecular imaging, within which GVs offer unique advantages alongside other emerging nanoscale and protein-based reporters[3,5,9,32]. In future studies, this expression system could also facilitate the genetic engineering of GV properties. Compared to the more established Ana and Halo GVs, Mega GVs are 32-times smaller by volume, but nevertheless able to produce significant ultrasound and $^{129}$Xe-MRI contrast. Their nanoscale size may facilitate the use of Mega GVs as targeted contrast agents following systemic administration. At the same time, the natively clustered form of Mega GVs has greater ultrasound contrast per GV, which may be also useful in certain applications. Overall, we anticipate that the unique properties of Mega GVs, together with their convenient heterologous expression and purification, will help these proteins rise to the top as a starting point for developing GV-based nanotechnologies.

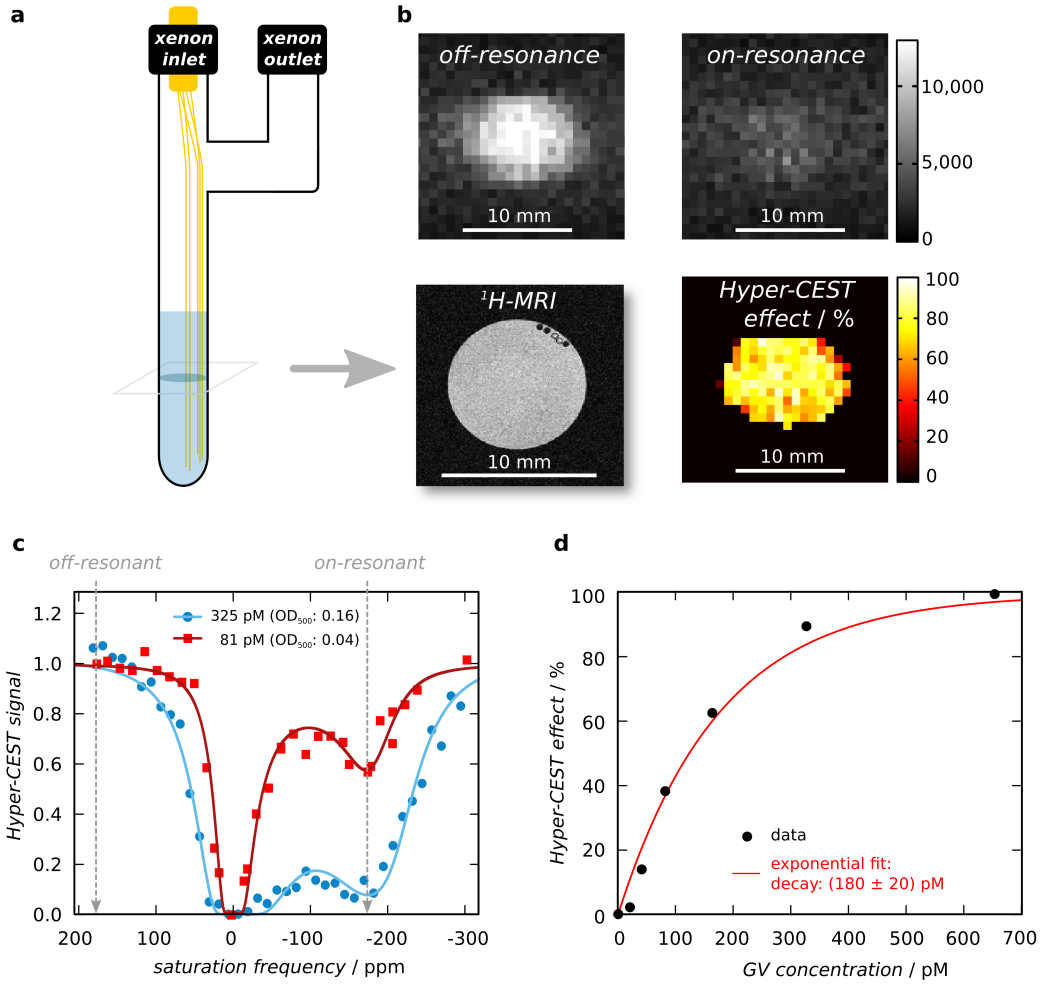


**Figure 3-4: Hyperpolarized $^{129}$Xe-MRI of recombinant Mega GVs.** (a) Illustration of HyperCEST MRI phantom used to bubble hyperpolarized $^{129}$Xe gas in solution containing Mega GVs during MRI acquisition. (b) Representative axial images of 325 pM Mega GVs acquired with off-resonant saturation at +174 ppm (top left) or on-resonant saturation at -174 ppm (top right), and their normalized difference (bottom right). Proton-MRI depicts axial plane containing GVs in PBS (bottom left). (Scale bars are 5 mm.) (c) Representative HyperCEST z-spectra (RF cw-saturation of 35 μT for 10 s) for Mega GVs at a concentration of 325 pM (blue circles) or 81 pM (red squares) in PBS at room temperature. Each data set was fitted to an exponential-Lorentzian. (d) The percent HyperCEST effect as a function of Mega GV concentration. Data was fitted to an exponential function of the form $f(c) = 100(1 - e^{-c/\tau})$ with $\tau$ representing recovery rate and $c$ representing concentration to facilitate visualization.

### 3.5 Methods

**Mega Gas Vesicle Expression and Purification.** The pST39 plasmid containing the GV gene cluster from *Bacillus megaterium* (Addgene ID 91696) was transformed into Rosetta 2(DE3)pLysS chemically competent *E. coli* (EMD Millipore, Temecula, CA) and cultured in Luria Broth (LB) supplemented with 1% glucose, 100 µg/mL ampicillin, and 25 µg/mL chloramphenicol at 37°C and 250 rpm shaking overnight. At confluency, 2.5 mL of starter culture was inoculated into 250 mL LB supplemented with 0.2% glucose, 100 µg/mL ampicillin, and 25 µg/mL chloramphenicol at 37°C and 250 rpm shaking until $OD_{600}$ reached 0.4 to 0.6. Gas vesicle expression was induced with 20 µM Isopropyl $\beta$-D-1-thiogalactopyranoside (IPTG) and continued to grow at 30°C and 250 rpm shaking for 22 hours. The cultures were then centrifugated at 600g for 1 hour and the mid-natant between the buoyant cell fraction and pellet was removed. The whole cell population was then lysed by the addition of 10% SoluLyse-Tris reagent (Genlantis, San Diego, CA), 250 µg/ml lysozyme (Sigma-Aldrich, St. Louis, MO) and 10 µg/ml DNAseI (New England Biolabs, Ipswich, MA) and rotated gently for 20 minutes at room temperature. GVs then underwent four rounds of buoyancy purification, which consisted of isolating the buoyant layer via centrifugation, followed by resuspension in phosphate buffered saline (PBS). Some of the purified GV were then declustered with the addition of urea to a final concentration of 6M and purified again in PBS via 3 rounds of buoyancy isolation. Protein concentration was measured using the Pierce 660 nm protein assay (Thermo Fischer Scientific, Waltham, MA).

**Electron Microscopy.** GV samples were diluted to $OD_{500}$ ~0.2 in 10 mM HEPES buffer and spotted on Formvar/Carbon 200 mesh grids (Ted Pella, Redding, CA), which were rendered hydrophilic by glow discharging (Emitek K100X). Unclustered Mega GVs were negatively stained using 2% uranyl acetate. Images were acquired using the Tecnai T12 LaB6 120 kV transmission electron microscope (TEM) equipped with a Gatan Ultrascan 2k x 2k CCD camera.

**Dynamic Light Scattering and Zeta Potential Measurement.** Hydrodynamic diameter and Zeta potential of GVs were measured with a Zeta-PALS analyzer (Brookhaven Instruments Corporation, Hotsville, NY). GVs were diluted to $OD_{500}$ of 0.2 in 50 µL for DLS measurements. The reported hydrodynamic diameter for each sample was taken using 5 measurements of well-mixed samples. Zeta potential measurements were taken of GVs mixed in 1.5 mL of double-distilled water at a conductance of 100 µS.

**Pressurized Absorbance Spectroscopy.** GV samples were diluted to $OD_{500}$

of 0.5 and loaded into a flow-through, 1 cm path-length quartz cuvette (Hellma Analytics, Plainview, NY) that was connected to a $N_2$ cylinder through a pressure controller (Alicat Scientific, Tucson, AZ). The pressure was increased stepwise in 50 kPa increments up to 1 MPa, followed by 100 kPa increments up to 1.2 MPa, and the $OD_{500}$ at each step was measured using a spectrophotometer (EcoVis, OceanOptics, Winter Park, FL). The absorbance reading at 0 MPa and the lowest $OD_{500}$ were used as the maximum and minimum, respectively, for normalization.

**Ultrasound Imaging.** Imaging phantoms were made from 1% agarose in PBS casted using a custom 3D printed inverted 96 well mold. GVs were prepared at twice the imaging concentration in PBS and mixed at 1:1 volume with 1% agarose at 65°C, then loaded in the wells of the agarose phantom. The phantom was positioned to allow imaging of the axial plane. Ultrasound images were acquired using a L22-14V 128-element linear array transducer and programmable scanner (Vantage, Verasonics, Kirkland, WA). The transducer was mounted on a computer-controlled 3D translation stage (Velmex, Bloomfield, NY). For imaging, the transducer and phantoms were submerged in PBS for acoustic coupling, and the center of the wells was placed at a 7.5 mm depth relative to the transducer face. B-mode ultrasound images for the concentration series were acquired using 0.91 MPa peak positive acoustic pressure, at 18 MHz frequency, with a f-number of 2.0. Maximal collapse was achieved with exposure to 4.2 MPa peak positive acoustic pressure. Acoustic collapse measurements were acquired at 0.46 MPa after the GVs were insonated with the indicated ultrasound pressures. Ultrasound images are displayed with square-root compression and decompressed for data analysis. Ultrasound data was analyzed using a custom MATLAB script to select the region of interest (ROI) of each image and calculate the average pixel intensity. Data represent four biological replicates for each sample (N=4), with representative images shown in the figures.

**Hyperpolarized Xe Spectroscopy and Imaging.** A gas mixture of 5% $^{129}$Xe (26.4% of natural abundance), 10% $N_2$ and 85% He was hyperpolarized by spin-exchange optical pumping under continuous flow using a custom-designed polarizer (150 W line-narrowed infrared laser; full-width-at-half-maximum of 0.5 nm)[28]. GVs were diluted in PBS to concentrations ranging from 650 pM to 20.32 pM. Hyperpolarized Xe was bubbled through the solution at an overpressure of 50 kPa (total pressure of 150 kPa) with a flow rate of 20 mL/min. All experiments were conducted at 20°C at 9.4 Tesla. Hyperpolarized $^{129}$Xe-MR images were acquired using a rapid acquisition with relaxation enhancement (RARE) pulse sequence modified for saturation transfer using the magnetization transfer module in ParaVision

6 (Bruker, Billerica, MA). Each GV sample was measured with hyperpolarized Xe-MRI separately, starting with the sample containing the highest GV concentration (to adjust RF cw-saturation pulse parameters to transfer saturation to 100% accordingly). All HyperCEST experiments used RF cw-saturation of 35 μT for 10 seconds. The HyperCEST effect was quantified as the fractional change in signal following on-resonance saturation compared to off-resonance saturation.

## References


1. Farhadi, A. *et al.* Recombinantly expressed gas vesicles as nanoscale contrast agents for ultrasound and hyperpolarized MRI. *AIChE Journal* **64,** 2927–2933 (2018).
2. Ntziachristos, V. Going deeper than microscopy: the optical imaging frontier in biology. *Nature methods* **7,** 603–614 (2010).
3. Piraner, D. *et al.* Going Deeper: Biomolecular Tools for Acoustic and Magnetic Imaging and Control of Cellular Function. *Biochemistry* (2017).
4. Foster, F. S., Pavlin, C. J., Harasiewicz, K. A., Christopher, D. A. & Turnbull, D. H. Advances in ultrasound biomicroscopy. *Ultrasound in medicine & biology* **26,** 1–27 (2000).
5. Mukherjee, A., Davis, H. C., Ramesh, P., Lu, G. J. & Shapiro, M. G. Biomolecular MRI Reporters: evolution of new mechanisms. *Progress in Nuclear Magnetic Resonance Spectroscopy* (2017).
6. Barskiy, D. A. *et al.* NMR Hyperpolarization Techniques of Gases. *Chemistry* **23,** 725–751 (2017).
7. Ferrara, K., Pollard, R. & Borden, M. Ultrasound microbubble contrast agents: fundamentals and application to gene and drug delivery. *Annual review of biomedical engineering* **9** (2007).
8. Abou-Elkacem, L., Bachawal, S. V. & Willmann, J. K. Ultrasound molecular imaging: Moving toward clinical translation. *Eur J Radiol* **84,** 1685–93 (2015).
9. Chen, F. *et al.* Exosome-like silica nanoparticles: a novel ultrasound contrast agent for stem cell imaging. *Nanoscale* **9,** 402–411 (2017).
10. Sheeran, P. S., Luois, S. H., Mullin, L. B., Matsunaga, T. O. & Dayton, P. A. Design of ultrasonically-activatable nanoparticles using low boiling point perfluorocarbons. *Biomaterials* **33,** 3262–9 (2012).
11. Foroutan, F. *et al.* Sol-gel synthesis and electrospraying of biodegradable (P2O5)55-(CaO)30-(Na2O)15 glass nanospheres as a transient contrast agent for ultrasound stem cell imaging. *ACS Nano* **9,** 1868–1877 (2015).
12. Schröder, L., Lowery, T. J., Hilty, C., Wemmer, D. E. & Pines, A. Molecular imaging using a targeted magnetic resonance hyperpolarized biosensor. *Science* **314,** 446–9 (2006).
13. Schröder, L. Xenon for NMR biosensing – Inert but alert. *Physica Medica* **29,** 3–16 (2013).
14. Roose, B. W., Zemerov, S. D. & Dmochowski, I. J. Nanomolar small-molecule detection using a genetically encoded (129)Xe NMR contrast agent. *Chem Sci* **8,** 7631–7636 (2017).

15. Wang, Y. & Dmochowski, I. J. An Expanded Palette of Xenon-129 NMR Biosensors. *Acc Chem Res* **49,** 2179–2187 (2016).

16. Shapiro, M. G. *et al.* Biogenic gas nanostructures as ultrasonic molecular reporters. *Nature Nanotechnology* **9,** 311–316 (2014).

17. Shapiro, M. G. *et al.* Genetically encoded reporters for hyperpolarized xenon magnetic resonance imaging. *Nature Chemistry* **6,** 629–634 (2014).

18. Lakshmanan, A. *et al.* Molecular Engineering of Acoustic Protein Nanostructures. *ACS Nano* **10,** 7314–7322 (2016).

19. Cherin, E. *et al.* Acoustic Behavior of Halobacterium salinarum Gas Vesicles in the High-Frequency Range: Experiments and Modeling. *Ultrasound in Medicine & Biology* **43,** 1016–1030 (2017).

20. Lakshmanan, A. *et al.* Preparation of biogenic gas vesicle nanostructures for use as contrast agents for ultrasound and MRI. *Nature protocols* **12,** 2050 (2017).

21. Maresca, D. *et al.* Nonlinear ultrasound imaging of nanoscale acoustic biomolecules. *Appl Phys Lett* **110,** 073704 (2017).

22. Pfeifer, F. Distribution, formation and regulation of gas vesicles. *Nature Reviews Microbiology* **10,** 705–15 (2012).

23. Walsby, A. E. Gas vesicles. *Microbiol Rev* **58,** 94–144 (1994).

24. Bourdeau, R. W. *et al.* Acoustic reporter genes for noninvasive imaging of microorganisms in mammalian hosts. *Nature* **553,** 86–90 (2018).

25. Li, N. & Cannon, M. C. Gas vesicle genes identified in Bacillus megaterium and functional expression in Escherichia coli. *J Bacteriol* **180,** 2450–8 (1998).

26. Hayes, P., Buchholz, B. & Walsby, A. Gas vesicles are strengthened by the outer-surface protein, GvpC. *Archives of microbiology* **157,** 229–234 (1992).

27. Walsby, A. E., Revsbech, N. P. & Griffel, D. H. The Gas-Permeability Coefficient of the Cyanobacterial Gas Vesicle Wall. *Journal of General Microbiology* **138,** 837–845 (1992).

28. Witte, C., Kunth, M., Rossella, F. & Schroder, L. Observing and preventing rubidium runaway in a direct-infusion xenon-spin hyperpolarizer optimized for high-resolution hyper-CEST (chemical exchange saturation transfer using hyperpolarized nuclei) NMR. *J Chem Phys* **140,** 084203 (2014).

29. Zaiss, M. & Bachert, P. Chemical exchange saturation transfer (CEST) and MR Z-spectroscopy in vivo: a review of theoretical approaches and methods. *Physics in Medicine and Biology* **58,** R221–R269 (2013).

30. Zaiss, M., Schnurr, M. & Bachert, P. Analytical solution for the depolarization of hyperpolarized nuclei by chemical exchange saturation transfer between free and encapsulated xenon (HyperCEST). *Journal of Chemical Physics* **136** (2012).

31. Kunth, M., Witte, C. & Schröder, L. Quantitative chemical exchange saturation transfer with hyperpolarized nuclei (qHyper-CEST): Sensing xenon-host exchange dynamics and binding affinities by NMR. *J. Chem. Phys.* **141,** 194202 (2014).

32. Wang, Y., Roose, B. W., Palovcak, E. J., Carnevale, V. & Dmochowski, I. J. A Genetically Encoded $\beta$-Lactamase Reporter for Ultrasensitive 129Xe NMR in Mammalian Cells. *Angewandte Chemie International Edition* **55,** 8984–8987 (2016).

*Chapter 4*

# ULTRASOUND IMAGING OF GENE EXPRESSION IN MAMMALIAN CELLS

This chapter is in large part a reformatted version of the manuscript entitled "Ultrasound Imaging of Gene Expression in Mammalain Cells" published by Farhadi, A., Ho, G.H., Sawyer, D.P., Bourdeau, R.W., and Shapiro, M.G., in *Science*[1]. Under the supervision of Mikhail Shapiro, my contributions to this work were to conceive, design and conduct the experiments, analyze and interpret the data, and write the manuscript. Thanks to Gabrielle Ho and Daniel Sawyer for assistance with the experiments, and Raymond Bourdeau assistance in the DNA sequence designs.

## 4.1 Abstract

The study of cellular processes occurring inside intact organisms requires methods to visualize cellular functions such as gene expression in deep tissues. Ultrasound is a widely used biomedical technology enabling noninvasive imaging with high spatial and temporal resolution. However, no genetically encoded molecular reporters are available to connect ultrasound contrast to gene expression in mammalian cells. To address this limitation, we introduce mammalian acoustic reporter genes. Starting with a gene cluster derived from bacteria, we engineered a eukaryotic genetic program whose introduction into mammalian cells results in the expression of intracellular air-filled protein nanostructures called gas vesicles, which produce ultrasound contrast. Mammalian acoustic reporter genes allow cells to be visualized at volumetric densities below 0.5% and permit high-resolution imaging of gene expression in living animals.

## 4.2 Introduction

The study of cellular function within the context of intact living organisms is a grand challenge in biological research and synthetic biology[2]. Addressing this challenge requires imaging tools to visualize specific cells in tissues ranging from the developing brain to tumors, and to monitor gene- and cell-based therapeutic agents *in vivo*[3]. However, most common methods for imaging cellular processes such as gene expression rely on fluorescent or luminescent proteins, which have limited performance in intact animals due to the poor penetration of light in biological

tissue[4,5]. On the other hand, ultrasound easily penetrates most tissues, enabling deep noninvasive imaging with excellent spatial and temporal resolution (~100 μm and ~1 ms, respectively)[3,6]. These capabilities, along with its safety, portability and low cost, have made ultrasound a widely used technology in biomedicine. Despite these advantages, to date ultrasound has played a relatively small role in cellular imaging due to the lack of appropriate genetically encoded reporters.

Recently, biomolecular contrast agents for ultrasound were introduced based on gas vesicles, air-filled protein nanostructures which evolved in certain waterborne bacteria and archaea to provide cellular buoyancy[7,8]. Gas vesicles comprise a 2 nm-thick protein shell enclosing a gas compartment with dimensions on the order of 100 nm. The acoustic impedance mismatch between their gas interior and surrounding aqueous media allows gas vesicles to strongly scatter sound waves and thereby serve as ultrasound contrast agents[9–13]. In their native organisms, gas vesicles are encoded by clusters of 8-14 genes, including one or two primary structural proteins, and several other essential genes encoding putative assembly factors or minor shell constituents.

The use of gas vesicles as reporter genes requires the heterologous expression of their cognate multi-gene operon in a new cellular host, ensuring proper transcription and translation of each gene, functional folding of each corresponding protein and appropriate stoichiometry and co-localization of the constituents for gas vesicle assembly. Recently, a genetic engineering effort succeeded in expressing gas vesicles as acoustic reporter genes (ARGs) in commensal bacteria, allowing their imaging in the mouse gastrointestinal tract[14]. If ARGs could be developed for mammalian cells, this would enable the study of how such cells develop, function and malfunction within the context of model organisms and enable the *in vivo* imaging of mammalian cells engineered to perform diagnostic or therapeutic functions[15–17]. However, developing ARGs for mammalian cells represents an even greater synthetic biology challenge due to the differences in transcription, translation, co-localization and protein folding between prokaryotes and eukaryotes[18–20]. To our knowledge, no genetic operon larger than 6 genes has been moved between these domains of life[21].

### 4.3 Results and Discussions

Here, we describe the expression of ARGs in mammalian cells to enable ultrasound imaging of mammalian gene expression. To identify a set of genes capable of encoding gas vesicle assembly in mammalian cells, we synthesized individual gas vesicle genes from three different microbial species using codons

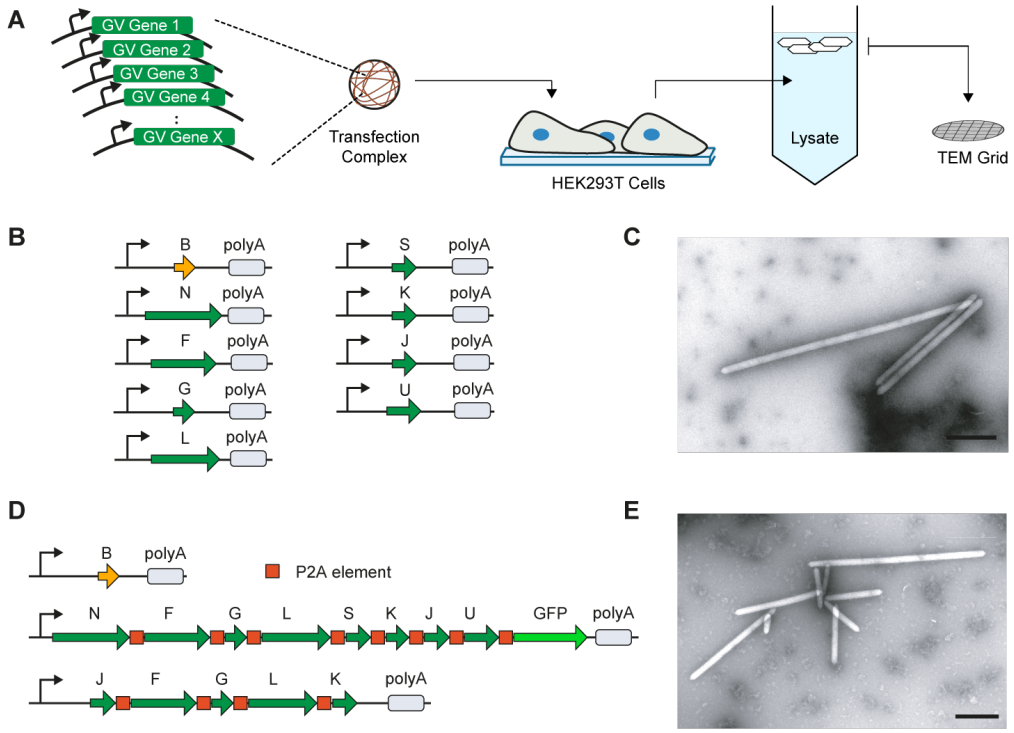


**Figure 4-1: Engineering of mammalian acoustic reporter genes.** (a) Schematic of the transient co-transfection assay used to identify combinations of genes capable of producing gas vesicles in mammalian cells. (b) Schematic of nine genes from *B. megaterium* capable of encoding gas vesicle expression in mammalian cells. Thin arrow denotes CMV promoter. polyA denotes SV40 polyadenylation element. (c) Representative TEM image of purified gas vesicles expressed in HEK293T cells. (d) Gene cassettes comprising the mammalian acoustic reporter gene construct, mARG. (e) Representative TEM image of gas vesicles purified from HEK293T cells transiently transfected with mARGs for 72 hours. All scale bars represent 500 nm.

optimized for human expression, cloned each gene into a separate monocistronic plasmid and transiently co-transfected mixtures of the genes from each species into HEK293T cells (Fig. 4-1a). After allowing 72 hours for protein expression, we gently lysed the cells ( $2x10^6$ cells per sample), and centrifugated the lysate to enrich for buoyant particles, which would include any gas vesicles. The top fraction of the centrifugated lysate was then screened for gas vesicles using transmission electron microscopy (TEM). These experiments took advantage of the intrinsic stochasticity of transient transfection – in terms of the ratios of genes and the overall DNA quantity delivered to each cell – to simultaneously sample a broad range of gene stoichiometries and expression levels without prior knowledge of solutions leading to gas vesicle formation.

The co-transfection of the gas vesicle genes from *Halobacterium salinarum* and *Anabaena flos-aquae* did not lead to the formation of detectable gas vesicles. However, the co-transfection of 9 gas vesicle-forming genes from *Bacillus megaterium* (Fig. 4-1b) resulted in the production of unmistakable gas vesicles as evidenced by their appearance in TEM images (Fig. 4-1c). The 9 genes originate from an eleven-gene *B. megaterium* gene cluster previously used to express gas vesicles in *E. coli*[14,22], with the exception of *GvpR* and *GvpT*, which were found to be unnecessary for gas vesicle formation (Fig. 4-S1).

Using the 9 genes identified in our stochastic screen, we set out to construct a polycistronic mammalian operon for consistent gas vesicle expression by joining these genes using the viral co-translational self-cleavage peptide P2A[23]. Having determined that all genes except *GvpB* could tolerate P2A peptide additions (Fig. 4-S2 and Table 4-S1), we constructed a polycistronic plasmid containing the 8 P2A-tolerant gas vesicle genes connected by P2A sequences, and co-transfected it into HEK293T cells together with a plasmid encoding *GvpB*. Unfortunately, this did not result in the production of gas vesicles. We hypothesized that one or more of the genes in our polycistronic plasmid was expressed at an insufficient level, and used a complementation assay to identify *GvpJ, GvpF, GvpG, GvpL* and *GvpK* as bottleneck genes (Fig. 4-S3). This led us to construct a polycistronic "booster" plasmid containing these five genes, ordered to minimize P2A modifications to *GvpJ* and *GvpK*, which were found to be most limiting. The co-transfection of the booster plasmid together with the two plasmids above (Fig. 4-1d) enabled robust expression of gas vesicles in cells (Fig. 4-1e). We named this set of three genetic constructs mammalian acoustic reporter genes, or mARGs.

After establishing polycistronic constructs for mammalian gas vesicle assembly, we used an integrase[24,25] to incorporate them into the cellular genome for stable expression under a doxycycline-inducible TRE3G promoter, with fluorescent proteins added to each construct as transfection indicators (Fig. 4-2a). We transfected these plasmids into HEK293-tetON cells and used flow cytometry to sort cells according to their expression level of each fluorescent reporter. We found that the cell population combining the strongest expression of each construct produced the largest quantity of gas vesicles (Fig. 4-2b, Fig. 4-S4a-d). To ensure that mARG expression was not limited to HEK293 cells, we also transfected Chinese hamster ovary cells (CHO-K1), and obtained similar results (Fig. 4-S4e-g).

To generate a stable monoclonal cell line expressing mARGs for detailed analysis, we sorted individual high-expression HEK293-tetON cells for monoclonal

growth (Fig. 4-2c), producing 30 cell lines, which we screened for viability, fluorescence and gas vesicle formation (Fig. 4-2d, Table 4-S2). The number of gas vesicles per cell was then estimated from TEM images, and a cell line yielding the largest quantity of gas vesicles was selected and named mARG-HEK. When induced for 72 hours with 1 µg/mL of doxycycline and 5 mM sodium butyrate (to reduce epigenetic silencing), this cell line produced on average 45 gas vesicles per cell (Fig. 4-2e). Using thin-section TEM, gas vesicles could clearly be seen in the cytosol of indivi-

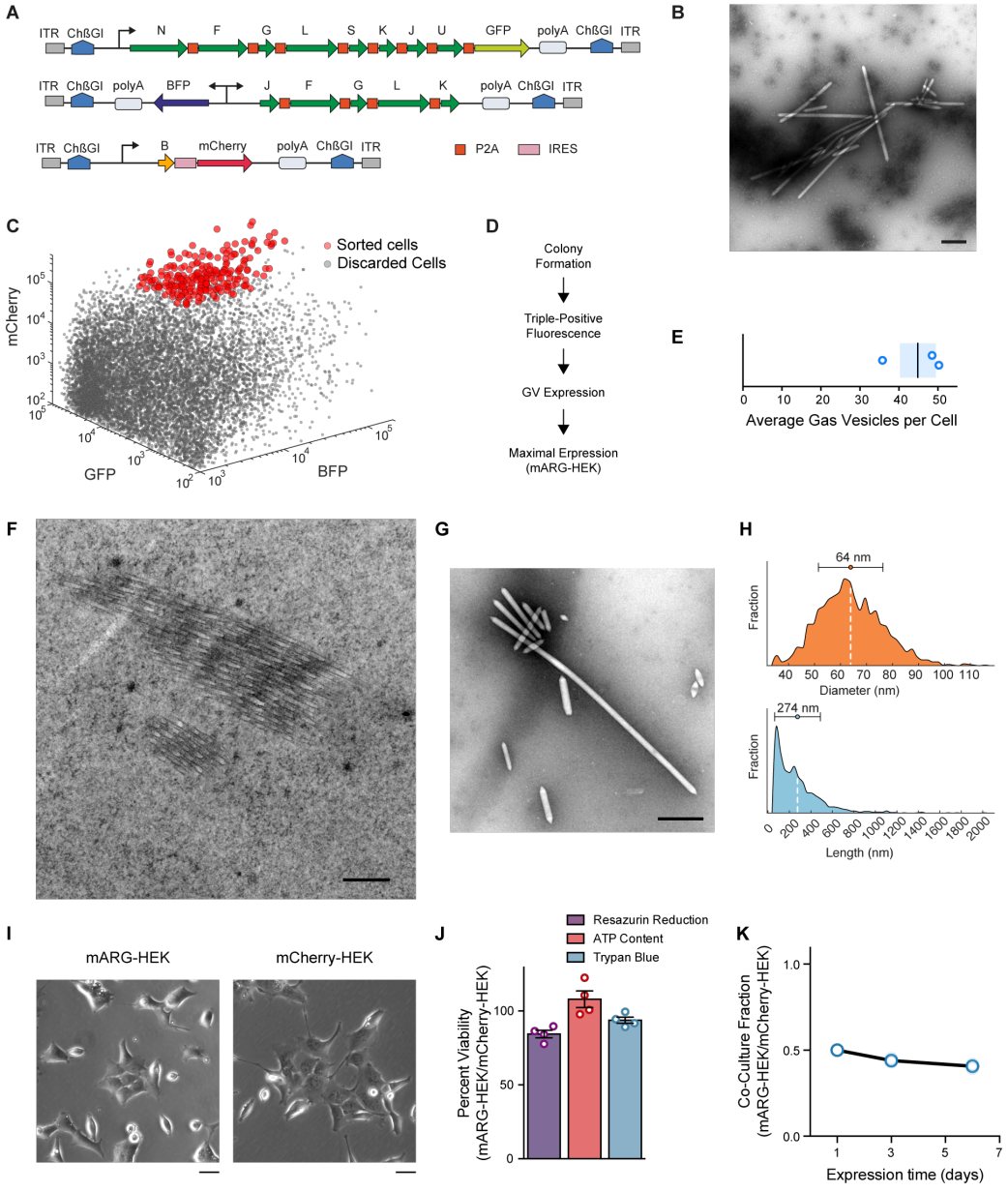


**Figure 4-2:** (Caption on next page.)

**Figure 4-2: Formation, properties and non-toxicity of gas vesicles in cells with genome-integrated mammalian acoustic reporter genes.** (a) Schematic of mARG constructs used for genomic integration into cells with the piggyBac transposase system. ITR, inverted terminal repeat; Ch$\beta$GI, Chicken beta-globin insulator; GFP, Emerald green fluorescent protein; BFP, enhanced blue fluorescent protein 2. (b) Representative TEM image of buoyancy-enriched lysate from HEK293-tetON cells transfected with the constructs in (a) and sorted for high expression of all three operons. (c) Fluorescence-activated cell sorting of HEK293-tetON cells transfected with the constructs in (a). Red circles denote individual cells selected by sorting to form monoclonal cell lines. (d) Selection process for monoclonal cell lines, including assays for viability, fluorescence intensity and gas vesicle yield. (e) Number of gas vesicles expressed by monoclonal HEK293-tetON cells after 72 hours of induced expression, as counted in lysates using TEM. Bar represents the mean and the shaded area represents SEM (n=3, each from two technical replicates). (f) Representative TEM image of a 60-nm section through an mARG-HEK cell showing an angled slice through two bundles of gas vesicles in the cytosol. (g) Representative TEM image of gas vesicles purified from mARG-HEK cells. (h) Size distribution of gas vesicles expressed in mARG-HEK cells. The mean and standard deviation of both distributions is illustrated as a circle and with error bars. (n=1828) (i) Phase contrast images of mARG-HEK and mCherry-HEK cells 72 hours after induction with 1 µg/mL doxycycline and 5 mM sodium butyrate. (j) Cell viability of mARG-HEK cells relative to mCherry-HEK cells after 72 hours of gene expression. Error bars indicate SEM. (k) Fraction of mARG-HEK cells in co-culture with mARG-mCherry cells seeded in equal numbers over 6 days of gene expression (n=3 biological replicates, each from 4 technical replicates, with darker symbols showing the mean). Scale bars in (b), (f), (g) represent 500 nm. Scale bar in (i) represents 20 µm.

dusal mARG-HEK cells (Fig. 4-2f). From TEM images of cell lysates, we measured the average dimensions of gas vesicles produced in this cell line to be 64 ± 12 nm wide (standard deviation, n=1828) and 274 ± 212 nm long (standard deviation, n=1828), with some reaching lengths greater than 1 micron (aspect ratios greater than 30) (Fig. 4-2g-h). This corresponds to an average gas vesicle volume of 0.605 attoliters. Together, the 45 gas vesicles expressed in an average mARG-HEK cell are expected to occupy just 0.0027% of the cell's cytosolic volume.

The expression of gas vesicles did not change the gross morphology of mARG-HEK cells (Fig. 4-2i), and was non-toxic as determined by three different assays (Fig. 4-2j), as compared to a similarly prepared control cell line (mCherry-HEK) (Fig. 4-S5a-b). During a 6-day co-culture, mARG-HEK cells showed only a minor growth disadvantage compared to mCherry-HEK cells (Fig. 4-2k). As expected, both engineered cell lines grew more slowly than wild-type HEK293T cells (Fig. 4-S6).

Having engineered mARG-HEK cells, we sought to image their expression of acoustic reporters with ultrasound. Gas vesicles encoded by the *B. megaterium*

gene cluster are expected to produce linear ultrasound scattering[22]. However, since mammalian cells themselves also produce significant linear contrast, detecting gas vesicles expressed in such cells using linear methods is challenging. To enable more selective imaging of mARG-expression, we took advantage of the ability of gas vesicles to collapse irreversibly above specific ultrasound pressure thresholds[9,10,14,22]. A switch in the incident ultrasound pressure from below to above such a threshold results in a strong transient signal from the gas vesicles, which decays to a lower level in the next ultrasound frame due to immediate dissolution of their gas contents and the elimination of ultrasound scattering (Fig. 4-3a-b). Meanwhile, background tissue scattering rises with the increase in incident pressure and remains constant at the new level. Thus, images formed by taking the difference in signal between the collapsing and post-collapse frames reveal specifically the presence of gas vesicles.

We implemented this collapse-based imaging approach using an amplitude modulation pulse sequence[11], which we found to provide the best cancellation of non-gas vesicle signals. When hydrogels containing mARG-HEK cells were imaged using this technique at 18 MHz, they were easily distinguishable from mCherry-HEK controls based on their contrast dynamics (Fig. 4-3c). Critically, while this imaging paradigm requires the collapse of gas vesicles inside cells, this does not affect cell viability (Fig. 4-3d).

To determine whether mARGs can faithfully monitor circuit-driven gene expression[26,27], we measured the dynamic ultrasound response of mARG-HEK cells under the control of a doxycycline-inducible promoter (Fig. 4-3e). After induction with 1 μg/mL doxycycline, the cells showed a gradual buildup of ultrasound signal, with clear contrast appearing on day two and increasing over the next 4 days (Fig. 4-3e). These kinetics are similar to those observed with fluorescent indicators (Fig. 4-S7a). When the gene circuit was driven using a range of inducer concentrations, the ultrasound contrast followed the expected transfer function of the promoter (Fig. 4-3g, Fig. 4-S7b).

To determine how sensitively mARG-expressing cells could be detected in a mixed cell population, we combined mARG-HEK cells with mCherry-HEK cells at varying ratios. We were able to detect the presence of mARG-expressing cells in these mixtures down to 2.5% of total cells (Fig. 4-3h), corresponding to less than 0.5% volumetric density, or approximately 3 cells or 135 gas vesicles per voxel with dimensions of 100 μm. A similar voxel-averaged concentration of gas vesicles was detectable in a monoculture of mARG-HEK cells induced to express 1.4 ± 0.6 gas vesicles per cell (Fig. 4-S8).

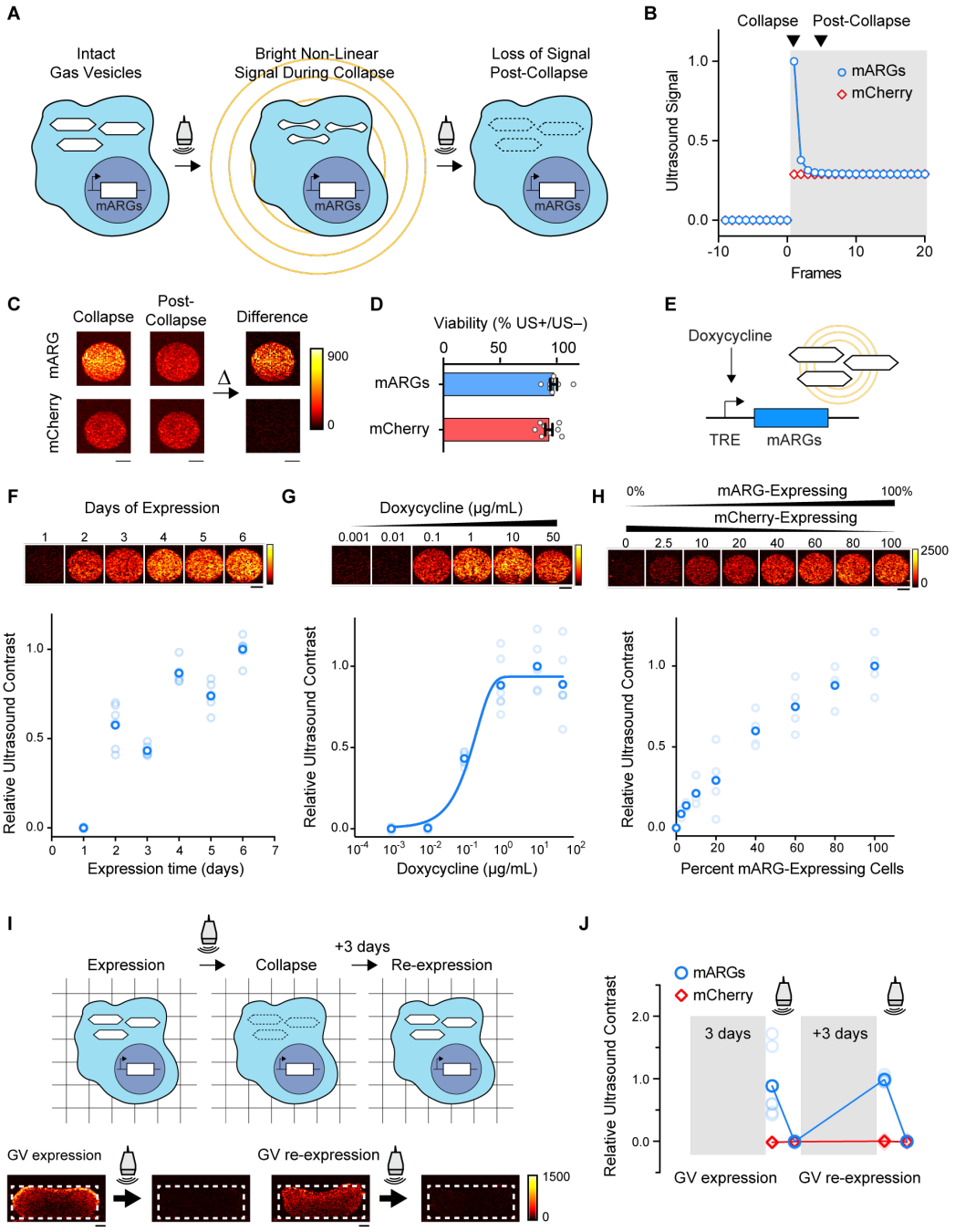


**Figure 4-3: Ultrasound imaging of mammalian gene expression *in vitro*.** (a) Illustration of the collapse-based ultrasound imaging paradigm used to generate gas vesicle-specific ultrasound contrast from mARG-expressing cells. (b) Representative non-linear signal recorded during a step change in the incident acoustic pressure, from 0.27 MPa in the white-shaded region to 1.57 MPa in the grey-shaded region. (c) Representative collapse and post-collapse ultrasound images of mARG-HEK and mCherry-HEK cells acquired during this ultrasound imaging paradigm and their difference, indicating gas vesicle-specific contrast. (d) Cellular viability after being insonated under 3.2 MPa acoustic pressures, as measured

**Figure 4-3:** (continued from above) using the MTT assay. (e) Schematic of a chemically inducible gene circuit with mARG expression as its output. All three mARG cassettes in mARG-HEK cells are under the control of the doxycycline-inducible TRE3G promoter (TRE), with expression triggered by incubation with doxycycline. (f) Representative ultrasound images and contrast measurements in mARG-HEK cells as a function of time following induction with 1 μg/mL of doxycycline and 5 mM sodium butyrate (n=6, with the darker dots showing the mean). (g) Representative ultrasound images and contrast measurements in mARG-HEK cells as a function of doxycycline induction concentrations. Cells were allowed to express gas vesicles for 72 hours in the presence of 5 mM sodium butyrate. (n=6, with the darker dots showing the mean). A sigmoidal function is fitted as a visual guide. (h) Representative ultrasound images and contrast measurements in mARG-HEK cells mixed with mCherry-HEK cells in varying proportions. Cells were induced with 1 μg/mL of doxycycline and 5 mM sodium butyrate for 72 hours prior to imaging. (n=4, with the darker dots showing the mean) (i) Schematic and representative ultrasound images from mARG-HEK cells in Matrigel re-expressing gas vesicles after acoustic collapse. Cells were induced with 1 μg/mL of doxycycline and 5 mM sodium butyrate for 72 hours before and after 3.2 MPa acoustic insonation. Ultrasound images were acquired after an additional 72 hours in culture following collapse. (j) Ultrasound contrast in mARG-HEK and mCherry-HEK cells after initial expression, after collapse, after re-expression and after second collapse. (n=7, with the darker dots showing the mean). GV, gas vesicles. All scale bars represent 1 mm.

In many imaging experiments, the output of a gene circuit is read out only once. However, in some cases it may be desirable to track gene expression over time. We therefore tested whether mARG-expressing cells in which the gas vesicles have been collapsed during imaging could re-express these reporters to allow additional imaging. mARG-HEK cells cultured a nutrient-supported hydrogel produced clear ultrasound contrast 3 days after induction, and were able to re-express their acoustic reporters over 3 additional days (Fig. 4-3i-j).

Having engineered mammalian cells to stably express gas vesicles and characterized their ability to produce ultrasound contrast *in vitro*, we next tested the ability of mARG expression to be visualized *in vivo* with high spatial resolution. We formed model tumor xenografts in immunocompromised mice by inoculating mARG-HEK cells in Matrigel subcutaneously in their left flanks (Fig. 4-4a). In the same mice, the right flanks were inoculated with mCherry-HEK control cells. We induced reporter gene expression in both tumors for 4 days through systemic injections of doxycycline and sodium butyrate (Fig. 4-4b). We expected these nascent tumors to be mostly vascularized at their perimeter, resulting in the strongest inducible gene expression at the tumor periphery (Fig. 4-4a). Ultrasound, with its sub-100-μm spatial resolution (at 18 MHz), should be able to discern this gene expression pattern,

whereas attaining such resolution would be challenging with optical techniques.

After 4 days of induction, we observed clear ultrasound contrast in the flank inoculated with mARG-HEK cells, which was absent from the contralateral side (Fig. 4-4c-d). As expected, the pattern observed with ultrasound revealed mARG expression at the perimeter of the tumor, while the core remained dark, and the imaging of adjacent ultrasound planes revealed this pattern of gene expression to persist across the tumor mass (Fig. 4-4e, Fig. 4-S9).

The ultrasound-observed spatial distribution of gene expression was consistent with the low vascularity in the tumor core, as observed with Doppler ultrasound (Fig. 4-S10). The peripheral gene expression pattern was confirmed with subsequent histological examination of the tissue (Fig. 4-4f, Fig. 4-S11). In comparison, our *in vivo* fluorescence images just showed the presence of signal somewhere in the tissue and not its precise distribution (Fig. 4-4g). These results, which were consistent across 5 animals (Fig. 4-S12a), demonstrate that mARGs enable gene expression imaging *in vivo* and highlight the ability of ultrasound to visualize intricate patterns of gene expression noninvasively. We imaged 3 of the animals again after an additional 4 days to look for re-expression of the collapsed gas vesicles, and observed ultrasound contrast in each case (Fig. 4-S12b).

## 4.4 Conclusions

Our results establish the ability of an engineered genetic construct encoding prokaryote-derived gas vesicles to serve as a mammalian reporter gene for ultrasound, providing the ability to monitor cellular location and function inside living organisms. mARGs provide many of the capabilities associated with established genetically encoded optical reporters, including imaging cellular dynamics via promoter-driven expression and mapping cellular populations in complex samples. While optical reporter genes mainly provide these capabilities in culture and surgically accessed tissues, mARGs enable gene expression to be resolved noninvasively *in vivo*.

While the genetic constructs described in this work should be immediately useful in a variety of contexts, significant scope exists for further optimization to make acoustic reporter genes as widely useful as GFP[6,13]. For example, accelerating mARG expression beyond the day-scale kinetics shown in this study and developing sensitive imaging paradigms that do not require gas vesicle collapse would enable the imaging of more dynamic cellular processes. In addition, while this study demonstrated essential mARG functionality with clonally selected cell lines, the expression of mARGs in primary cells, their delivery to endogenous cells via viral

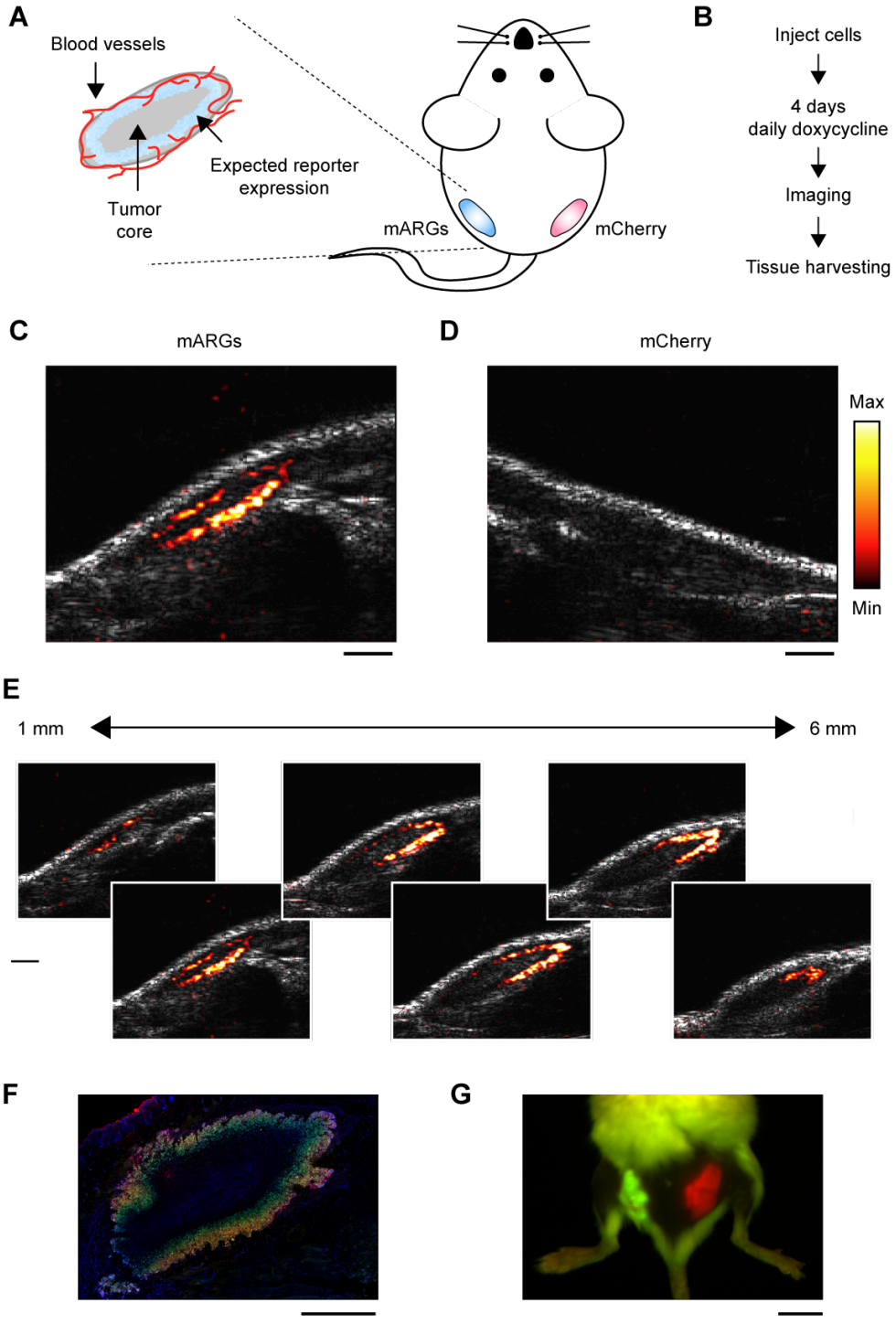


**Figure 4-4:** (Caption on the next page.)

**Figure 4-4: Ultrasound imaging of mammalian gene expression *in vivo*.** (a) Diagram of a mouse implanted with a subcutaneous tumor model, and the expected spatial pattern of vascularization and doxycycline-induced reporter gene expression. (b) Experimental timeline. (c) Representative ultrasound image of tumors containing mARG-HEK cells after 4 days of doxycycline administration. mARG-specific contrast shown in the hot colormap is overlaid on an anatomical B-mode image showing the background anatomy. (d) Representative ultrasound image of tumors containing mCherry-HEK cells after 4 days of doxycycline administration. (e) Ultrasound images of adjacent planes in the mARG-HEK tumor acquired at 1 mm intervals. The minimum and maximum values of color bars in C-E are 4000 and 40000 au, respectively. (f) Representative fluorescence image of a histological tissue section of an mARG-HEK tumor. Blue color shows the TO-PRO3 nucleus stain, green color shows GFP fluorescence and red color shows mCherry fluorescence. (g) Fluorescence image of a mouse implanted with mARG-HEK and mCherry-HEK tumors on the left and right flanks, respectively, after 4 days of expression. Scale bars for are 1 mm for (c-f) and 1 cm for (g).

vectors, and their expression in transgenic animals would greatly expand the utility of this technology. To facilitate such uses, it would be helpful to further condense the mARG constructs. For example, genes could be consolidated into fewer clusters, and preliminary experiments show that *gvpB* can be combined with the 8-gene polycistron encoding *gvpN-gvpU* via an internal ribosome entry sequence (IRES) (Fig. 4-S13). In addition, the total length of the coding sequence contained in mARG could be reduced from 7.6 kb to 4.8 kb by eliminating the need for redundant booster genes, relying instead on non-coding elements such as different-strength promoters to tune expression stoichiometry. Further optimization of mARG genetic constructs is also needed to reduce epigenetic silencing and metabolic burden[28–30]. Just as the engineering of GFP over many years yielded brighter and more colorful reporters enabling new uses of fluorescence microscopy, further engineering of the genetic constructs comprising mARGs would help cellular ultrasound penetrate and enable new areas of mammalian biology and biomedicine.

## 4.5 Methods

**Chemicals, cell lines and synthesized DNA.** All chemicals were purchased from Sigma Aldrich unless otherwise noted. HEK293T and CHO-K1 cell lines were ordered from American Type Culture Collection (ATCC) and HEK293-tetON cells and CHO-tetON cells were purchased from Clontech (Takara Bio). Synthetic DNA was ordered from Twist Bioscience.

**Cloning.** Monocistronic plasmids used for transient transfection of HEK293T cells of gas vesicle genes used the pCMVSport backbone. Codon optimized gas vesi-

cle genes were assembled in each plasmid using Gibson assembly. To test the effect of N- and C-terminal P2A modification each *B. megaterium* gas vesicle gene on the pNL29 plasmid (addgene 91696) was individually cloned using standard mutagenesis techniques. To test the N-terminal modification, the CCT codon was inserted following the start codon. To test the C-terminal modification, a linker-P2A sequence (GGAGCGCCAGGTTCCGGG-GCTACTAACTTCAGCCTCCTTAAACAGGCC GGCGACGTGGAAGAGAATCCTGGC) was inserted upstream of the stop codon for each gene.

The polycistronic plasmid containing *GvpN, GvpF, GvpG, GvpL, GvpS, GvpK, GvpJ, GvpU* and Emerald GFP (EmGFP) were codon optimized, and synthesized in three fragments. The three fragments were Gibson assembled in the pCMVSport plasmid. The booster plasmid was assembled by multi-fragment Gibson assembly from PCR amplified fragments of the above plasmid.

The piggyBac transposon system (System Biosciences) was used to genomically integrate the mARG cassettes. To clone the mARG cassettes to the piggyBac transposon backbone, the plasmid was first digested using the SpeI and HpaI restriction enzymes and the mARG cassettes were Gibson assembled in the backbone. For doxycycline-inducible expression, the CMV promoter upstream of the gas vesicle genes was replaced with the TRE3G promoter. Internal ribosome entry site (IRES) and mCherry were cloned downstream GvpB as a marker for genomic integration. For the booster plasmid, CMVmin followed by enhanced BFP2 (eBFP2) and a polyadenylation element were cloned in the reverse direction upstream of the TRE3G promoter (creating a bi-directional doxycycline-inducible promoter) and used as a marker for genomic integration. A piggyBac transposon plasmid containing TRE3G and mCherry was Gibson assembled similarly to above.

**Cell culture, transient transfection and TEM analysis.** HEK293T and CHO-K1 cells were cultured in DMEM with 10% FBS and penicillin/streptomycin and seeded in a 6-well plate for transfection experiments. When the cells reached 70-80% confluency, 2 µg of total DNA (comprising the indicated mixtures of plasmids) was complexed with 2.58 µg polyethyleneimine (PEI-MAX; Polysciences Inc.) per µg of DNA, added to the cell culture, and incubated for 12-18 hours. The transfection of monocistronic plasmids encoding *Halobacterium salinarum, Anabaena flos-aquae* and *Bacillus megaterium* were all at equal molar ratios. Thereafter, the media containing the PEI-DNA complex was changed with fresh media. Cells were allowed to express the recombinant proteins for 72 hours.

To look for gas vesicles, fully confluent cells cultured in 6-well plates were

lysed with 400 µL of Solulyse-M (Genlantis Inc) per well for one hour at 4°C. The lysate was then transferred to 2 mL tubes, diluted with 800 µL of 10 mM HEPES buffer at pH 8.0 and centrifugated overnight at 300 g and 8°C. Then, 60 µL of the supernatant was transferred to a fresh tube to be analyzed using transmission electron microscopy (TEM).

From this top fraction, 2 µL of sample was added to Formvar/carbon 200 mesh grids (Ted Pella) that were rendered hydrophilic by glow discharging (Emitek K100X). The samples were then stained with 2% uranyl acetate. The samples were imaged on a FEI Tecnai T12 transmission electron microscope equipped with a Gatan Ultrascan CCD.

To estimate gas vesicle yield and analyze size distribution, the cells were seeded in 6-well plates and gas vesicle expression was induced with 1 µg/mL of doxycycline and 5 mM sodium butyrate for 72 hours. The cells were lysed using Solulyse-M and buoyancy enriched at 300 g at 8°C overnight. The top fraction of the supernatant was mixed with 2M urea and spotted on Formvar/carbon grids. The TEM grids were washed with water before staining with 2% uranyl acetate. To calculate gas vesicle yield per cell, the total number of gas vesicles per sub-grid on the TEM grid was manually counted and related via lysate volume to the number of source cells. Gas vesicle size distribution was quantified using FIJI[31].

To visualize gas vesicles inside cells, mARG-HEK cells were seeded in 6-well plates and allowed to express gas vesicles for 72 hours. The cells were fixed in 1.25% glutaraldehyde in PBS, post-fixed in 1% aqueous osmium tetroxide, reduced with ferrocyanide and block-stained in 1% uranyl acetate (all reagents from Electron Microscopy Sciences). The material was then dehydrated through a graded ethanol series and embedded in Eponate12 (Ted Pella). Sections were cut 60 nm thin onto formvar-filmed copper grids, stained with 2% uranyl acetate and Reynolds lead citrate, and imaged at 80 kV in a Zeiss EM10C (Oberkochen) equipped with an ES1000W Erlangshen CCD camera (Gatan).

**Genomic integration and FACS.** HEK293-tetON and CHO-tetON cells were used for genomic integration of the mARGs. The cells were cultured in a 6-well plate containing 2 mL DMEM with 10% tetracycline-free FBS (Clontech) and penicillin/streptomycin. Cells were transfected with the piggyBac transposon backbone containing the mARGs and the piggyBac transposase plasmid at a transposon:transposase molar ration of 2.5:1. Transfection was conducted using parameters mentioned above and the cells were allowed to incubate for 72 hours. Cells were induced with 1 µg/mL of doxycycline 24 hours prior to FACS (BD FACSAria III).

Polyclonal subpopulations of mARG-expressing HEK293-tetON cells were sorted into the following four bins: (subtype 1) cells with eBFP2 fluorescence greater than $10^4$ and EmGFP fluorescence greater than $10^4$ and mCherry fluorescence greater than $2x10^4$ au, (subtype 2) cells with eBFP2 fluorescence between $3x10^3$ and $2x10^4$ and EmGFP fluorescence between $2x10^3$ and $2x10^4$ and mCherry fluorescence between $2x10^3$ and $2x10^4$ au, (subtype 3) cells with eBFP2 fluorescence between $10^3$ and $6x10^3$ and EmGFP fluorescence between $2x10^2$ and $10^3$ and mCherry fluorescence greater than $2x10^4$ au, (subtype 4) cells with eBFP2 fluorescence greater than $10^4$ and EmGFP fluorescence greater than $2x10^4$ and mCherry fluorescence between $2x10^3$ and $2x10^4$ au. CHO-tetON cells were transfected with mARGs and the piggyBac transposase plasmid similar to above. mARG-expressing CHO-tetON cells with eBFP2 fluorescence greater than $10^4$, EmGFP fluorescence greater than $10^4$ and mCherry fluorescence greater than $2x10^4$ au were sorted.

For monoclonal cell lines, naïve HEK293-tetON cells were transfected with mARGs and the piggyBac transposase similar to above. mARG-expressing cells with eBFP2 fluorescence greater than $10^4$, EmGFP fluorescence greater than $10^4$ and mCherry fluorescence greater than $2x10^4$ au were sorted. 576 cells were sorted in individual wells of 96-well plate and the surviving 30 cells were analyzed for gas vesicle expression as described above.

To generate mCherry-HEK cells, HEK293-tetON cells were transfected with piggyBac transposon plasmid containing TRE3G promoter driving mCherry and the transposase plasmid similar to above. mCherry-HEK cells were sorted from cells with mCherry fluorescence between $1.5x10^4$ and $10^5$ au.

Monoclonal cell lines (mARG-HEK and mCherry-HEK cells) were maintained in tetracycline-free media without butyrate and all imaging and toxicity experiments were conducted with cells that were less than 16 generations.

***In vitro* toxicity assays.** The viability of the mARG-expressing cells was determined using three different assays involving cellular metabolic activity (resazurin reduction, MTT assay), quantification of cellular ATP content (CellTiter-Glo, Promega Corp.), and dye exclusion (Trypan Blue, Caisson Labs). The measurements were all quantified as percent viability compared to control cells that expressed mCherry only (mCherry-HEK). For the MTT and CellTiter-Glo assays, cells were grown in 96-well plates and induced with 1 μg/mL doxycycline and 5 mM sodium butyrate for 72 hours. They were then treated with reagents according to the manufacturers' protocols. Luminescence (CellTiter-Glo) and absorbance at 540 nm (MTT) was measured using a SpectraMax M5 spectrophotometer (Molecular Devices). For

the Trypan Blue assay, the cells were first grown in 6-well plates and treated with 1 µg/mL doxycycline and 5 mM sodium butyrate for 72 hours. They were then trypsinized and resuspended in media before being stained 1:1 with Trypan Blue dye. Ten µL of the solution was loaded in a disposable hemocytometer (C-chip DHC S02, Incyto) and total cell count and blue-stained dead cells were quantified by bright field microscopy. Cellular morphology was imaged from mARG-HEK and mCherry-HEK cells after 3 days of expression with 1 µg/mL doxycycline and 5 mM sodium butyrate. Phase images were acquired using a Zeiss Axio Observer with a 20x objective. For the co-culture cell competition assay, cells were counted and $2x10^5$ cells from each type were mixed together and seeded in 6-well plates. One day after seeding, cells were induced with 1 µg/mL doxycycline and 5 mM sodium butyrate and the media was exchanged daily. At each time point, cells were trypsinized and sorted using the MACSQuant VYB Flow Cytometer (Miltenyi Biotech) to quantify relative cell ratios. At one day and three days post induction, cells were passaged to ensure continuous exponential growth.

***In vitro* ultrasound imaging.** To create phantoms for *in vitro* ultrasound imaging, wells were casted with molten 1% w/v agarose in PBS using a custom 3D-printed template. mARG-HEK and mCherry-HEK cells were allowed to express their transgenes using the specified inducer concentrations and expression duration. They were then trypsinized and counted via disposable hemocytometers in bright field microscopy. Next, cells were mixed at a 1:1 ratio with 50°C agarose and loaded into the wells before solidification. The volume of each well was 60 µl and contained $6x10^6$ cells. The phantoms were submerged in PBS, and ultrasound images were acquired using a Verasonics Vantage programmable ultrasound scanning system and L22-14v 128-element linear array transducer with a 0.10-mm pitch, an 8-mm elevation focus, a 1.5-mm elevation aperture, and a center frequency of 18.5 MHz with 67% -6 dB bandwidth (Verasonics, Kirkland, WA). Each frame was formed from 89 focused beam ray lines, each with a 40-element aperture and 8 mm focus. A 3-half-cycle transmit waveform at 17.9 MHz was applied to each active array element. For each ray line, the amplitude modulation (AM) code was implemented using one transmit with all elements in the active aperture followed by 2 transmits in which first the odd- and then the even-numbered elements are silenced[11]. Each image captured a circular cross-section of a well with a 4-mm diameter and center positioned at a depth of 8 mm. In AM mode, the signal was acquired at 0.27 MPa (2V) for 10 frames and the acoustic pressure was increased to 1.57 MPa (10V) to collect 46 additional frames. Ultrasound images were constructed by subtracting

the collapsing frame by frame 4 post-collapse.

For Fig. 4-3f-h, the high gas vesicle content of some samples resulted in acoustic shielding and a residual amount of gas vesicles remained intact after 46 frames of insonation at 1.57 MPa. To fully collapse all the gas vesicles and collect the background signal, the acoustic pressure was increased to 3.2 MPa (25V), then a second set of images was acquired with 10 frames at 0.27 MPa and 46 frames at 1.57 MPa. Gas vesicle-specific signal was determined by subtracting the total ultrasound signal from the 46 frames acquired before 3.2 MPa ultrasound by the total ultrasound signal from the 46 frames post collapse.

**Cytotoxicity assay on cells exposed to ultrasound.** mARG-HEK and mCherry-HEK cells were cultured on custom made Mylar-bottom 24-well plates. Cells were cultured on fibronectin-coated Mylar films until they reached 80% confluency and induced for gas vesicle expression (1 µg/mL doxycycline and 5 mM sodium butyrate) for 3 days. The cells were then insonated from the bottom using an L22-14v 128-element linear array transducer (Verasonics). The transducer was mounted on a computer-controlled 3D translatable stage (Velmex). The bottom of the plates was acoustically coupled to the transducer with water and positioned 8 mm away from the transducer face. The cells were exposed to 3.2 MPa of pressure and the transducer was translated at a rate of 3.8 mm/s. The plates were returned to the incubator for 24 hours. Cytotoxicity was then assayed using resazurin reduction (MTT) on cells exposed to ultrasound and compared to non-insonated control cells.

**3D cell culture and *in vitro* acoustic recovery after collapse.** mARG-HEK and mCherry-HEK cells were mixed in Matrigel (Corning) containing 1 µg/mL of doxycycline and 5 mM sodium butyrate. The cell-laden hydrogels were placed in a 1% w/v agarose base to prevent cell migration out of the hydrogel and to separate the cells away from the bottom of the plates during imaging. Cells were cultured for total of 6 days and imaged every 3 days from the top using an L22-14v 128-element linear array transducer (Verasonics). The transducer was wiped with 70% ethanol, and imaging was conducted in a laminar flow biosafety cabinet to preserve sterility. After imaging, to ensure complete collapse of all gas vesicles in the cells, the entire hydrogel was exposed to 3.2 MPa ultrasound and the transducer was translated three times across the gel at a rate of 1-2 mm/s. The culture media was changed daily and contained 1 µg/mL of doxycycline and 5 mM sodium butyrate.

***In vivo* expression of gas vesicles and ultrasound imaging.** All *in vivo* experiments were performed on NOD SCID mice (NOD.CD17 *Prkdc*$^{scid}$*/NCrCrl*; Charles River), aged 10-15 weeks, under a protocol approved by the Institutional

Animal Care and Use of Committee of the California Institute of Technology. mARG-HEK and mCherry-HEK cells were cultured in tetracycline-free media in T225 flasks. 1-1.2x$10^7$ cells were trypsinized and the 200 µl cell-pellet was mixed with 200 µl Matrigel (Corning) containing 5 mM sodium butyrate. The mixture of mARG-HEK cells and Matrigel was injected subcutaneously in the left flank of mice and the mixture of mCherry-HEK cells and Matrigel was injected subcutaneously in the right flank of mice. Starting from the day of tumor inoculation, mice we interperitoneally injected with 200 µl of saline containing 75 µg doxycycline and 25 mg of sodium butyrate daily. The lower half of mice were depilated to allow for fluorescence imaging and ultrasound coupling.

For ultrasound imaging, the mice were anesthetized with 2% isoflurane and maintained at 37°C using a heating pad. Ultrasound imaging was carried out using the pulse sequence described above with an L22-14v transducer attached to a custom-made manual translation stage. Using B-mode ultrasound imaging, the center of the tumor was positioned approximately 8 mm from the surface of the transducer, and gas vesicle-specific ultrasound images were acquired. The transducer was translated laterally with 1 mm steps to collect ultrasound images of most of the tumor. High framerate ultrasound datasets for Doppler imaging were acquired with the same ultrasound transducer and scanner. The Doppler pulse sequence consisted of 11 tilted plane wave transmissions (varying from -10 to 10 degrees) at a 5.5 kHz framerate, leading to a 500 Hz framerate after coherent compounding. Plane wave transmissions lasted 0.5 s (or 250 frames). A power Doppler image representing blood flow was computed from each ensemble of 250 frames using a singular value decomposition filter that separates clutter from red blood cell echoes[32].

To obtain tissue samples after the mice were euthanized, tumors were resected and placed in 3.7% formaldehyde solution (4°C) for 24 hours and transferred to sterile 30% sucrose for an additional 24 hours. Tumors were embedded in OCT compound (Tissue-Tek), flash frozen and sectioned to 60 µm slices using a Cryostat (Leica CM3050). Sections were stained with TO-PRO3 nucleus stain, mounted (Fluoromount Aqueous Mounting Medium) and imaged using a Zeiss LSM 800 confocal microscope.

## References


1. Farhadi, A., Ho, G. H., Sawyer, D. P., Bourdeau, R. W. & Shapiro, M. G. Ultrasound imaging of gene expression in mammalian cells. *Science* **365,** 1469–1475 (2019).
2. Tsien, R. Y. Imagining imaging's future. *Nature Reviews Molecular Cell Biology* **4,** SS16–SS21 (2003).
3. Piraner, D. I. *et al.* Going Deeper: Biomolecular Tools for Acoustic and Magnetic Imaging and Control of Cellular Function. *Biochemistry* **56,** 5202–5209 (2017).
4. Chu, J. *et al.* A bright cyan-excitable orange fluorescent protein facilitates dual-emission microscopy and enhances bioluminescence imaging in vivo. *Nat Biotech* **34,** 760–767 (2016).
5. Santos, E. B. *et al.* Sensitive in vivo imaging of T cells using a membrane-bound Gaussia princeps luciferase. *Nature Medicine* **15,** 338–344 (2009).
6. Maresca, D. *et al.* Biomolecular Ultrasound and Sonogenetics. *Annu Rev Chem Biomol Eng* **9,** 229–252 (2018).
7. Pfeifer, F. Distribution, formation and regulation of gas vesicles. *Nat Rev Microbiol* **10,** 705–15 (2012).
8. Walsby, A. E. Gas vesicles. *Microbiol Rev* **58,** 94–144 (1994).
9. Shapiro, M. G. *et al.* Biogenic gas nanostructures as ultrasonic molecular reporters. *Nature Nanotechnology* **9,** 311–316 (2014).
10. Lakshmanan, A. *et al.* Molecular Engineering of Acoustic Protein Nanostructures. *ACS Nano* **10,** 7314–7322 (2016).
11. Maresca, D. *et al.* Nonlinear ultrasound imaging of nanoscale acoustic biomolecules. *Applied Physics Letters* **110** (2017).
12. Maresca, D., Sawyer, D. P., Renaud, G., Lee-Gosselin, A. & Shapiro, M. G. Nonlinear X-Wave Ultrasound Imaging of Acoustic Biomolecules. *Physical Review X* **8** (2018).
13. Lu, G. J., Farhadi, A., Mukherjee, A. & Shapiro, M. G. Proteins, air and water: reporter genes for ultrasound and magnetic resonance imaging. *Curr Opin Chem Biol* **45,** 57–63 (2018).
14. Bourdeau, R. W. *et al.* Acoustic reporter genes for noninvasive imaging of microorganisms in mammalian hosts. *Nature* **553,** 86–90 (2018).
15. Davis, M. M., Tato, C. M. & Furman, D. Systems immunology: just getting started. *Nature Immunology* **18,** 725–732 (2017).
16. Marblestone, A. H. *et al.* Physical principles for scalable neural recording. *Front Comput Neurosci* **7,** 137 (2013).

17. Schroeder, T. Imaging stem-cell-driven regeneration in mammals. *Nature* **453,** 345–51 (2008).

18. Gradinaru, V. *et al.* Molecular and cellular approaches for diversifying and extending optogenetics. *Cell* **141,** 154–165 (2010).

19. Shieh, Y. W. *et al.* Operon structure and cotranslational subunit association direct protein assembly in bacteria. *Science* **350,** 678–80 (2015).

20. Natan, E., Wells, J. N., Teichmann, S. A. & Marsh, J. A. Regulation, evolution and consequences of cotranslational protein complex assembly. *Curr Opin Struct Biol* **42,** 90–97 (2017).

21. Close, D. M. *et al.* Autonomous bioluminescent expression of the bacterial luciferase gene cassette (lux) in a mammalian cell line. *PLoS One* **5,** e12441 (2010).

22. Farhadi, A. *et al.* Recombinantly Expressed Gas Vesicles as Nanoscale Contrast Agents for Ultrasound and Hyperpolarized MRI. *AIChE J* **64,** 2927–2933 (2018).

23. Szymczak, A. L. & Vignali, D. A. A. Development of 2A peptide-based strategies in the design of multicistronic vectors. *Expert Opinion on Biological Therapy* **5,** 627–638 (2005).

24. Ding, S. *et al.* Efficient transposition of the piggyBac (PB) transposon in mammalian cells and mice. *Cell* **122,** 473–83 (2005).

25. Wilson, M. H., Coates, C. J. & George A. L., J. PiggyBac transposon-mediated gene transfer in human cells. *Mol Ther* **15,** 139–45 (2007).

26. Elowitz, M. B. & Leibler, S. A synthetic oscillatory network of transcriptional regulators. *Nature* **403,** 335–8 (2000).

27. Gardner, T. S., Cantor, C. R. & Collins, J. J. Construction of a genetic toggle switch in Escherichia coli. *Nature* **403,** 339–42 (2000).

28. Gaidukov, L. *et al.* A multi-landing pad DNA integration platform for mammalian cell engineering. *Nucleic Acids Res* **46,** 4072–4086 (2018).

29. Jusiak, B. *et al.* Comparison of Integrases Identifies Bxb1-GA Mutant as the Most Efficient Site-Specific Integrase System in Mammalian Cells. *ACS Synth Biol* **8,** 16–24 (2019).

30. Neville, J. J., Orlando, J., Mann, K., McCloskey, B. & Antoniou, M. N. Ubiquitous Chromatin-opening Elements (UCOEs): Applications in biomanufacturing and gene therapy. *Biotechnol Adv* **35,** 557–564 (2017).

31. Schindelin, J. *et al.* Fiji: an open-source platform for biological-image analysis. *Nature methods* **9,** 676–682 (2012).

32. Demené, C. *et al.* Spatiotemporal clutter filtering of ultrafast ultrasound data highly increases Doppler and fUltrasound sensitivity. *IEEE transactions on medical imaging* **34,** 2271–2285 (2015).

## 4.6 Supplementary Information

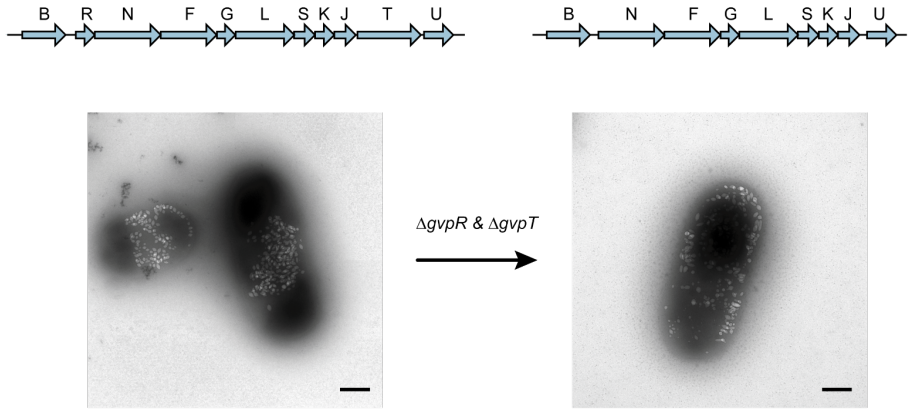


**Figure 4-S1: *GvpR* and *GvpT* genes in the *B. megaterium* gene cluster are not necessary for gas vesicle formation.** Schematic of bacterial gas vesicle gene clusters used for heterologous expression of gas vesicles in *E. coli* (top). Representative whole cell TEM images of *E. coli* Rosetta 2(DE3)pLysS cells after expression of gas vesicles genes for 22 hours (bottom). Scale bars represent 500 nm. Expression performed as in Farhadi *et al.*[22] and TEM imaging as in Bourdeau *et al.*[14].

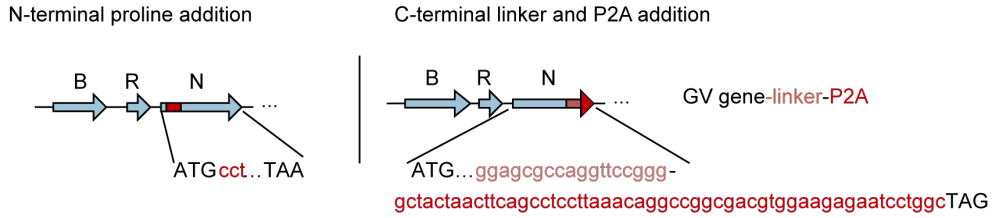


**Figure 4-S2: Assay for tolerability of P2A peptide additions.** Illustration of gas vesicle gene cluster with N- or C-terminal modifications of each gene to test tolerability of P2A peptides, tested one-by-one in *E. coli*.

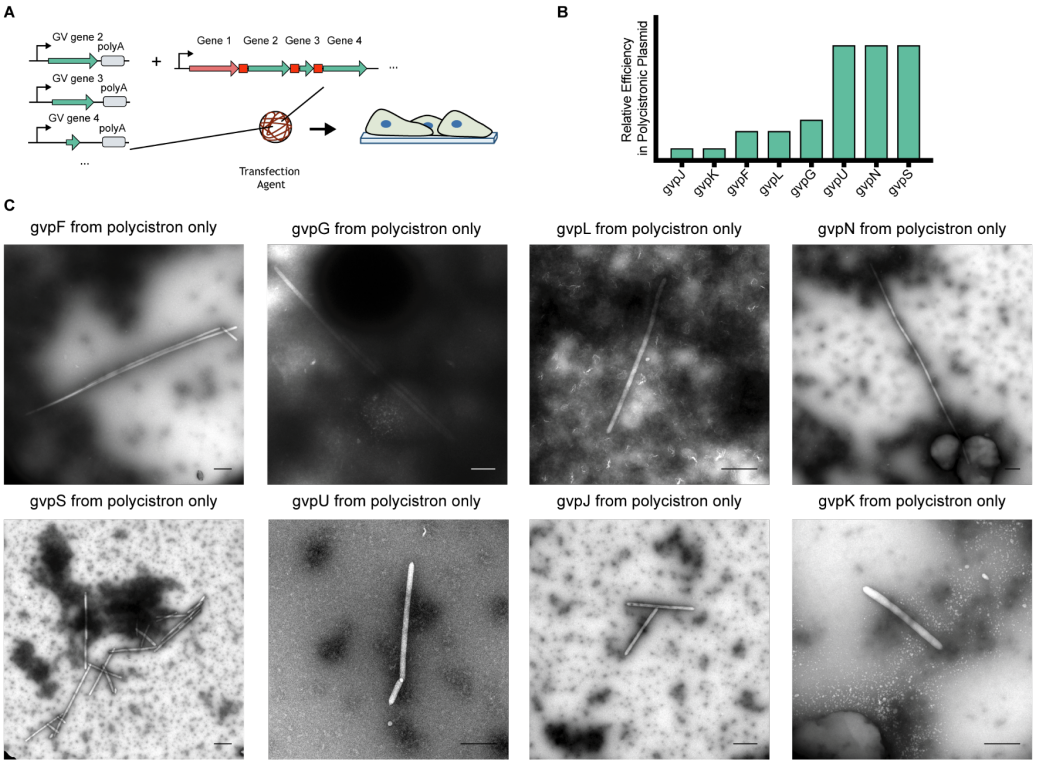


**Figure 4-S3: Identification of bottleneck genes on the polycistronic gas vesicle gene plasmid.** (a) Schematic of the experiment. To test the efficiency with which gas vesicles could be formed when a given gene was supplied only on the polycistronic plasmid, and thereby identify "bottleneck" genes, cells were co-transfected with a monocistronic plasmid containing *GvpB*, 7 other monocistronic plasmids including all but the gene being assayed, and the polycistronic plasmid. (b) Qualitative estimate of the relative number of gas vesicles produced when each indicated gene was supplied solely by the polycistronic plasmid. (c) Representative TEM images of gas vesicles in the lysate of HEK293T cells for all 8 assays. Scale bars represent 500 nm. These results suggest that *GvpN, GvpS* and *GvpU* supplied in either monocistronic or polycistronic form supported abundant gas vesicle assembly. However, the production of gas vesicles was significantly reduced when *GvpJ, GvpF, GvpG, GvpL* or *GvpK* was supplied from the polycistronic vector. We therefore suspected that these genes represented a bottleneck in gas vesicle formation.

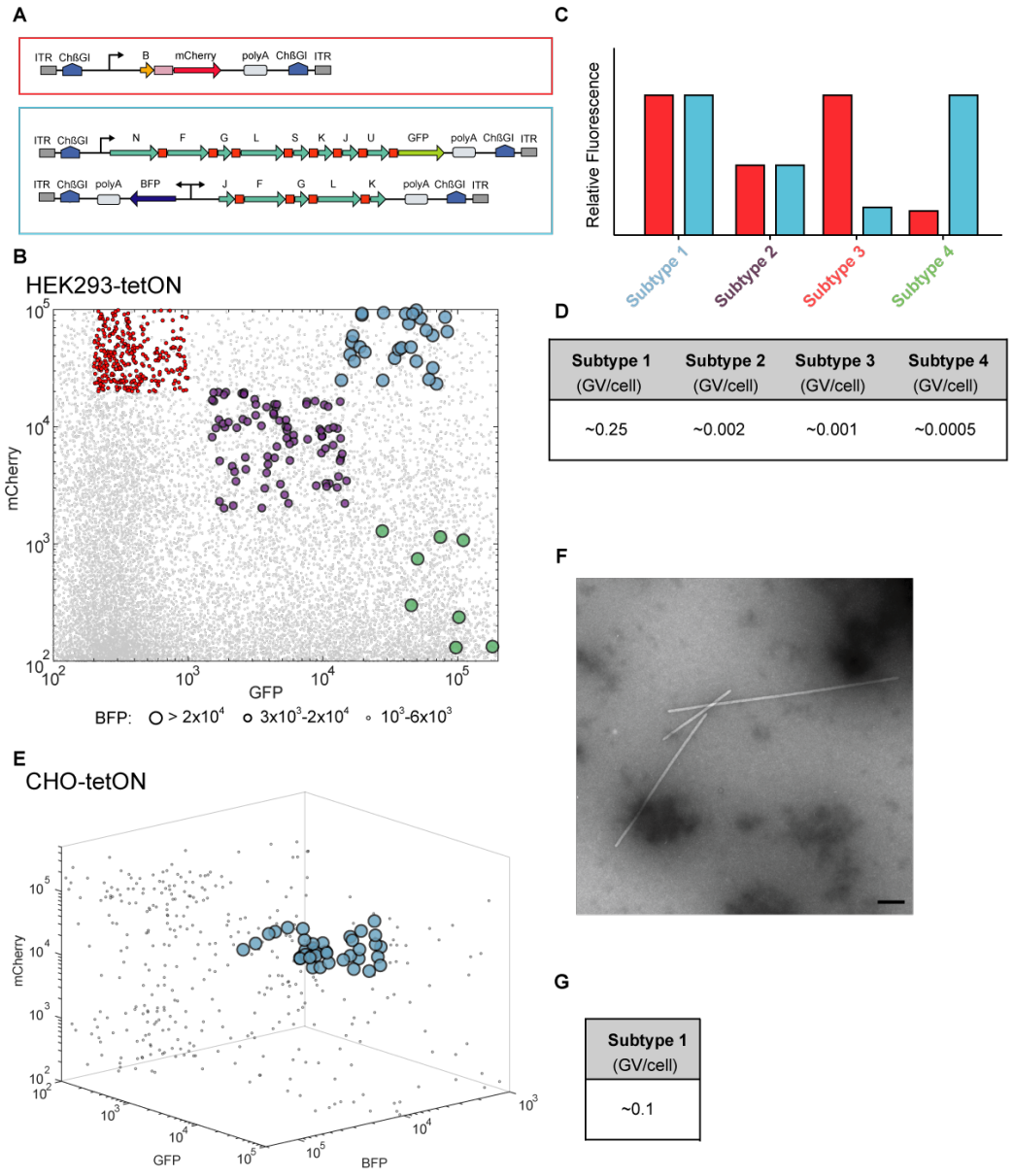


**Figure 4-S4: Fluorescence activated cell sorting of HEK293-tetON and CHO-tetON cells transfected with integrating mARG constructs.** (a) Diagram of the integrating constructs used to generate polyclonal cell lines. (b) FACS of mARG-expressing HEK293-tetON cells. Colored data indicate cells sorted for each group and gray dots are unsorted population. (c) Illustration of the four polyclonal subtypes sorted to study the impact of polycistron stoichiometry on gas vesicle expression. Red bars indicate mCherry expression; cyan bars indicate EmGFP and eBFP2 expression. (d) Approximate gas vesicle yield from polyclonal cells in each subtype. (e) FACS of mARG-expressing CHO-tetON cells. Colored data indicate cells sorted in subtype 1 and gray dots are unsorted cells. (f) Representative TEM image of buoyancy-enriched lysate from CHO-tetON cells sorted as indicated in (e). Scale bar represents 500 nm. (g) Approximate gas vesicle yield for the sorted mARG-expressing CHO-tetON cells.

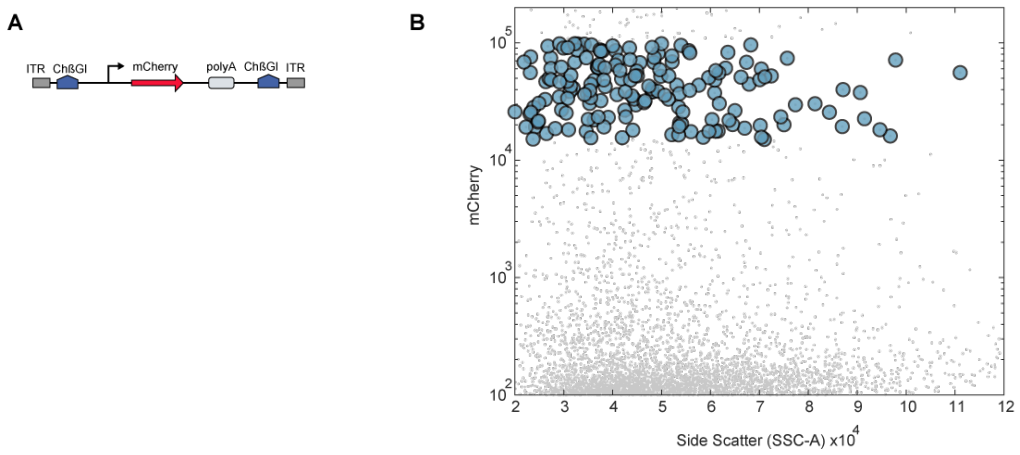


**Figure 4-S5: Genetic construct and sorting of mCherry-HEK cell line.** (a) Genetic construct for stable genomic integration of mCherry containing a TRE3G promoter upstream and SV40 polyadenylation element downstream of mCherry. (b) FACS of mCherry cells, with selected cells indicated with blue dots.

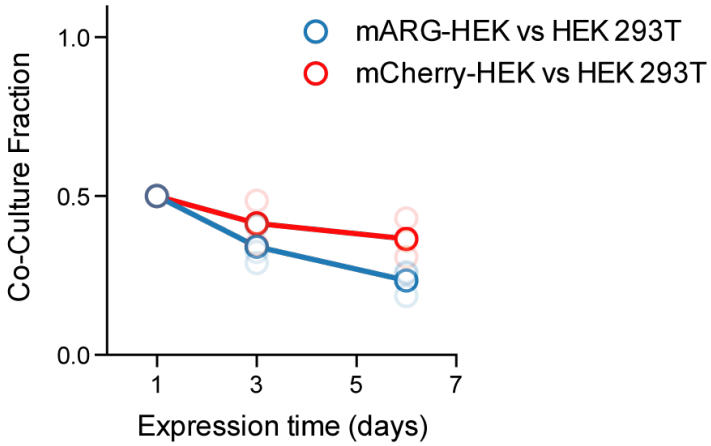


**Figure 4-S6: Co-culture of reporter gene expressing cells with HEK293T cells.** Fraction of mARG-HEK cells in co-culture with HEK293T cells (blue) or mARG-mCherry cells in co-culture with HEK293T cells (red) seeded in equal numbers over 6 days of gene expression (n=3 biological replicates, each from 4 technical replicates, with darker dots showing the mean).

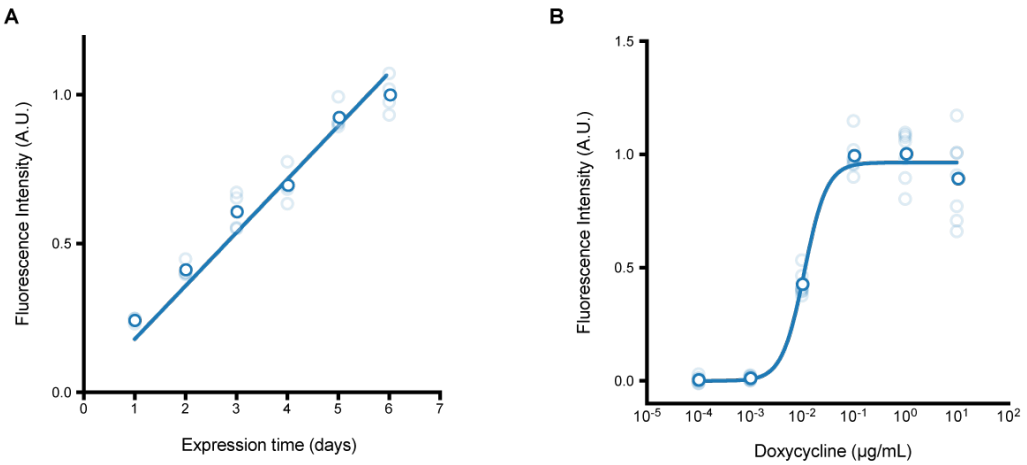


**Figure 4-S7: Fluorescence measurements of gene expression as a function of time and inducer concentration in mARG-HEK cells.** (a) mCherry fluorescence of mARG-HEK cells induced with 1 µg/mL doxycycline and 5 mM sodium butyrate at the indicated times after induction (n=4, with the darker dots showing the mean). (b) mCherry fluorescence of mARG-HEK cells with the indicated inducer concentration and 5 mM sodium butyrate after 72 hours of induction (n=7, with the darker dots showing the mean).

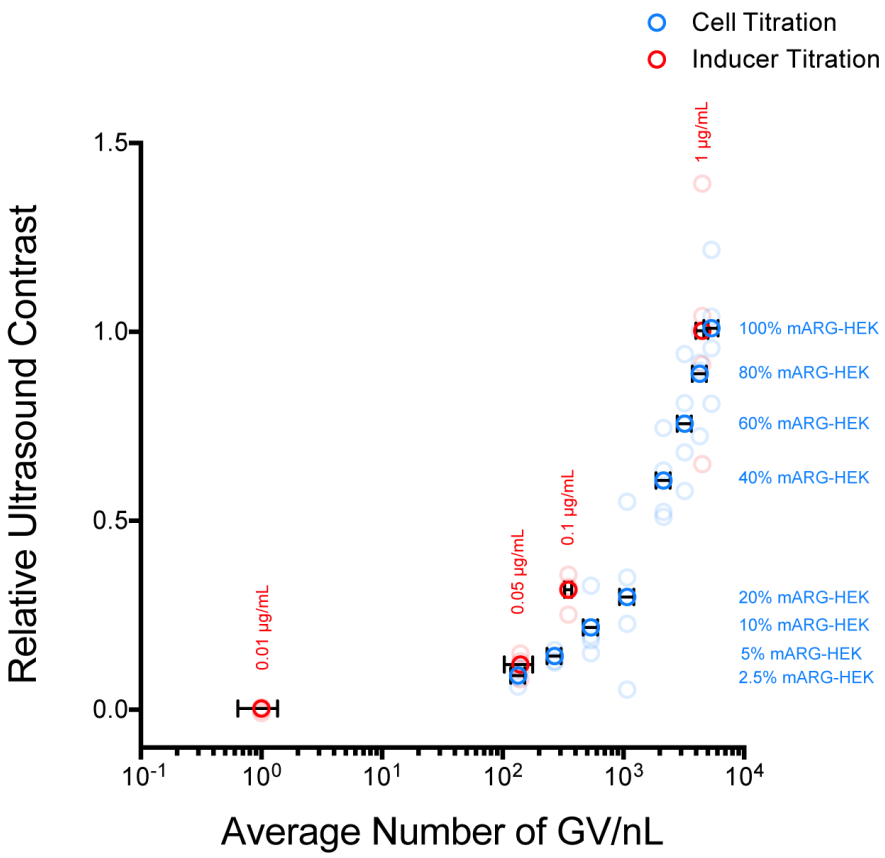


**Figure 4-S8: Dependence of ultrasound contrast on gas vesicle density.** Relative ultrasound contrast produced by mARG-HEK cells in hydrogel as a function of the estimated average number of gas vesicles (GV) per nanoliter present after a monoculture of mARG-HEK cells was induced with different concentrations of doxycycline, or after fully-induced mARG-HEK cells were mixed with mCherry-HEK cells at different ratios. Blue symbols represent results from mARG-HEK cells induced with 1 µg/mL doxycycline for 3 days (producing on average 45 gas vesicles per cell) mixed with mCherry-HEK cells (expressing no gas vesicles) in varying proportions, as presented in Fig. 4-3H. Red symbols represent results from mARG-HEK cells induced with 0.01, 0.05, 0.1 and 1 µg/mL doxycycline for 3 days; expressing on average 0.01 ± 0.004, 1.4 ± 0.4, 3.5 ± 0.3, 45 ± 5.1 (mean ± SEM) gas vesicles per cell, respectively, as quantified by TEM. All cells were cultured with 5 mM sodium butyrate during expression. The number of gas vesicles was quantified after 72 hours of induced expression, as counted in lysates using TEM. Ultrasound contrast was normalized to the maximum in each type of titration. Dark symbols show the mean of ultrasound contrast for 4 replicates. Error bars represent SEM of 4 biological replicates for 0.01, 0.05, 0.1 µg/mL induction and n=3 biological replicates (each from two technical replicates) for 1 µg/mL samples.

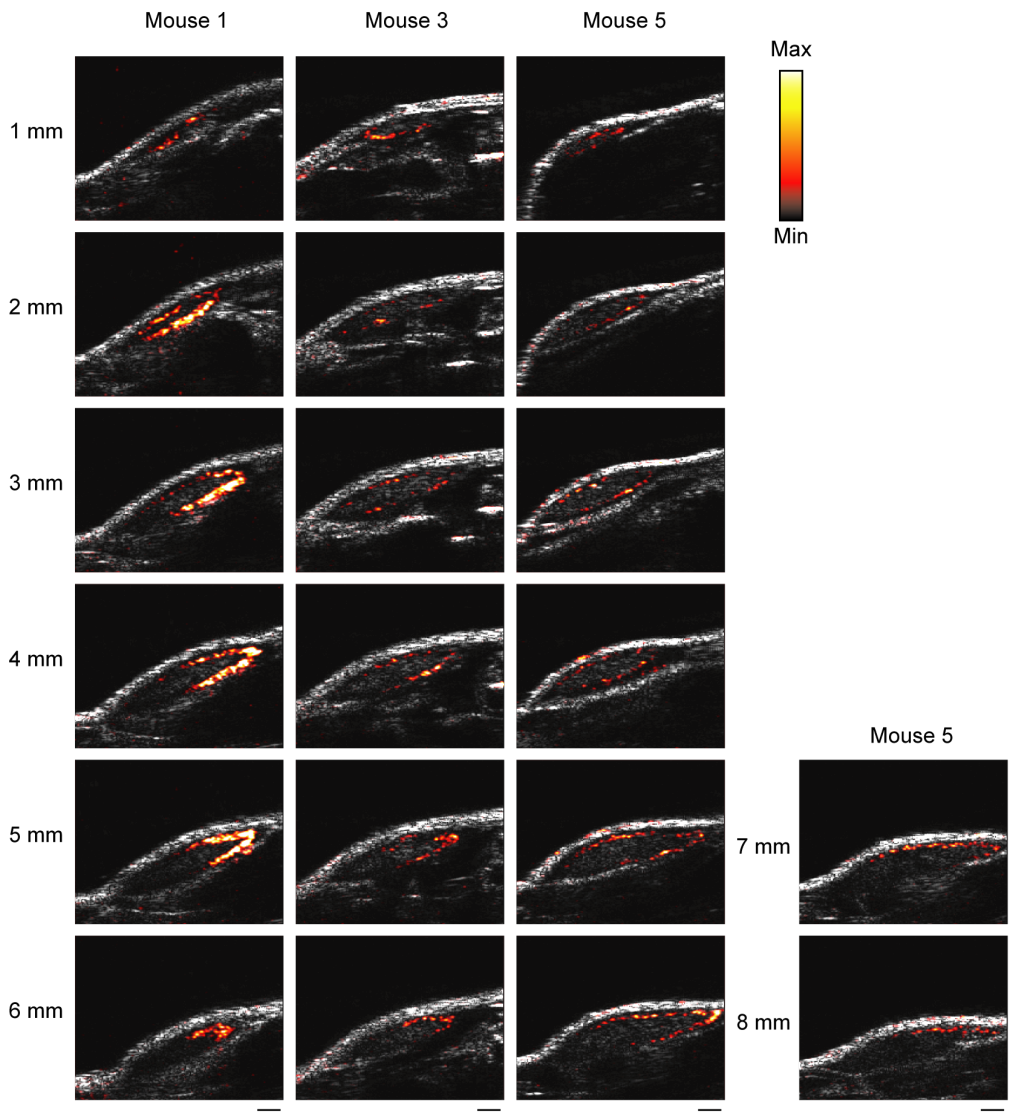


**Figure 4-S9: Additional examples of *in vivo* ultrasound images of adjacent planes in mARG-HEK tumors acquired at 1 mm intervals.** For each imaging slice the difference heatmap of nonlinear signal between frame 1 and frame 4 is overlaid on grayscale anatomical scale. Minimum and maximum values of color bar are 4000 and 40000, respectively. Scale bars are 1 mm.

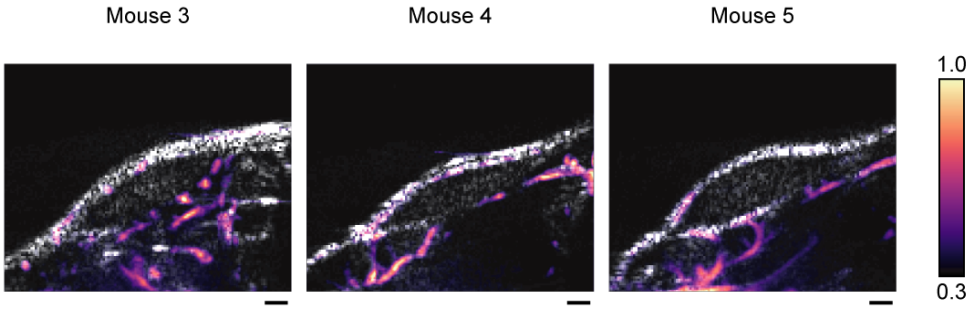


**Figure 4-S10: Representative Doppler ultrasound images of tumors containing mARG-HEK cells.** Doppler ultrasound images were acquired using 250 frames of ultrafast planewaves at 25V and used to reconstruct vascular maps plotted as normalized power doppler signal overlaid on anatomical images in grayscale. Scale bars represent 1 mm.

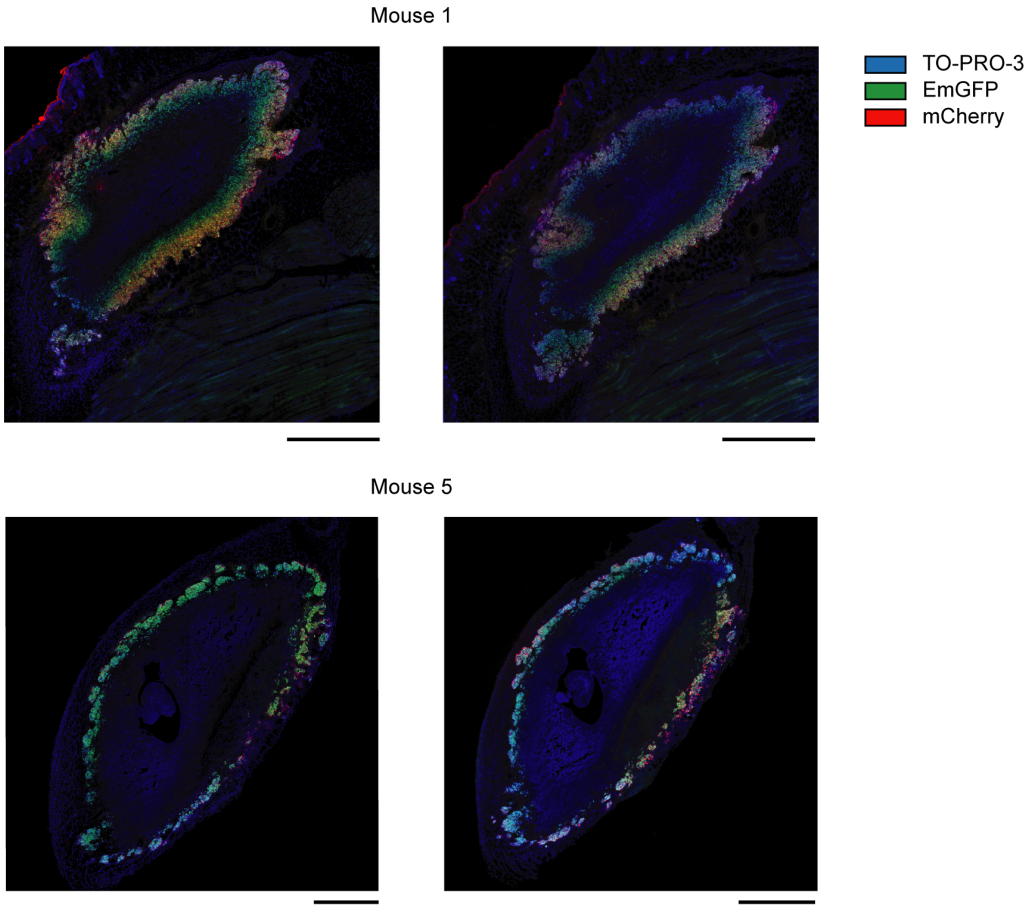


**Figure 4-S11: Representative histology sections of tumors containing mARG-HEK cells.** For each mouse, two neighboring sections are presented. Blue color indicates cell nuclear staining using TO-PRO-3, green color represents GFP fluorescence and red color represents mCherry fluorescence. All scale bars are 1 mm.

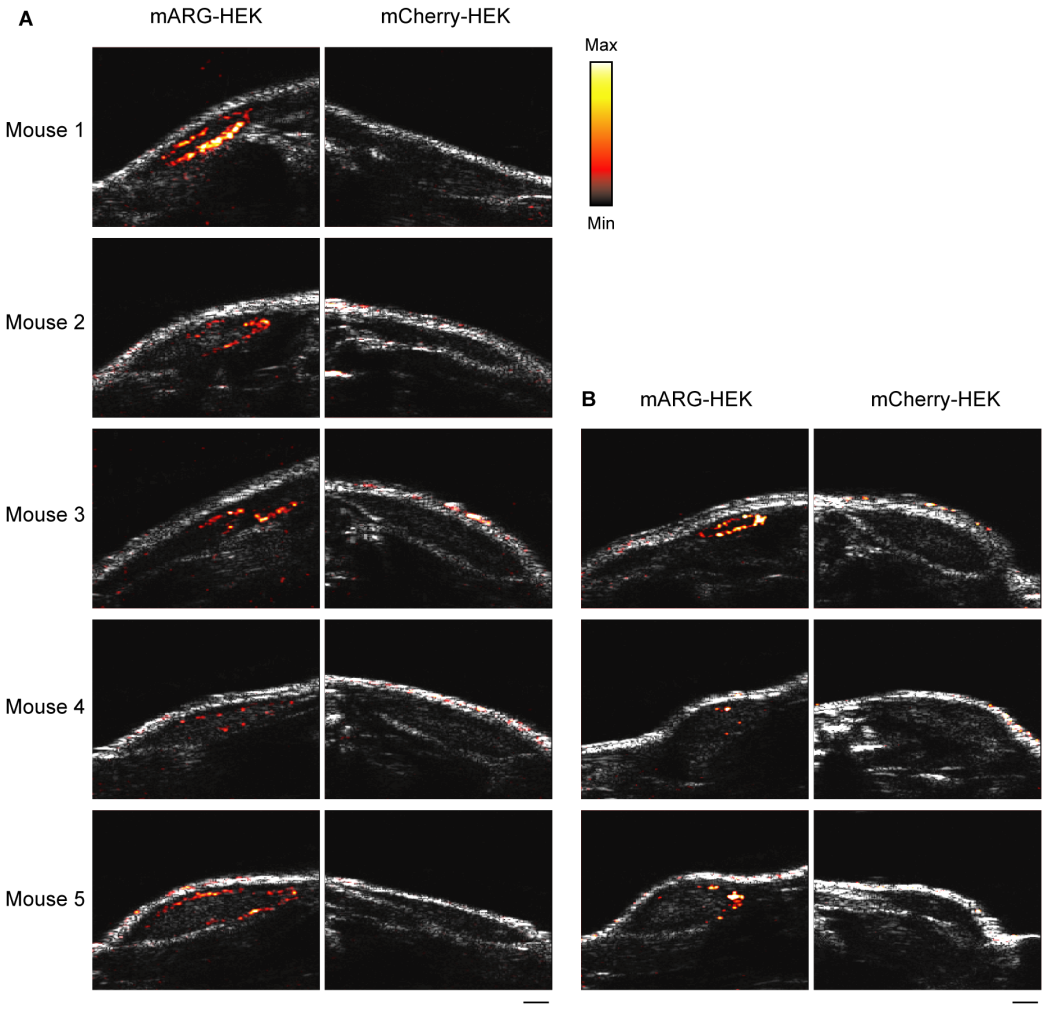


**Figure 4-S12: Biological replicates of *in vivo* ultrasound imaging of gene expression.** (a) The left column shows ultrasound images of tumors containing mARG-HEK cells after 4 days of doxycycline administration. The right column shows ultrasound images of tumors containing mCherry-HEK cells after 4 days of doxycycline administration. After imaging the tumors were insonated with 3.2 MPa of ultrasound to collapse the expressed gas vesicles. (b) The left column shows ultrasound images of tumors containing mARG-HEK cells re-expressing gas vesicles after an additional 4 days of doxycycline administration. The right column shows ultrasound images of tumors containing mCherry-HEK cells after an additional 4 days of doxycycline administration. Difference heatmap of nonlinear signal between frame 1 and frame 4 is overlaid on a grayscale anatomical ultrasound image. Min and max on color bar represent 4000 and 40000, respectively. Scale bars represent 1 mm.

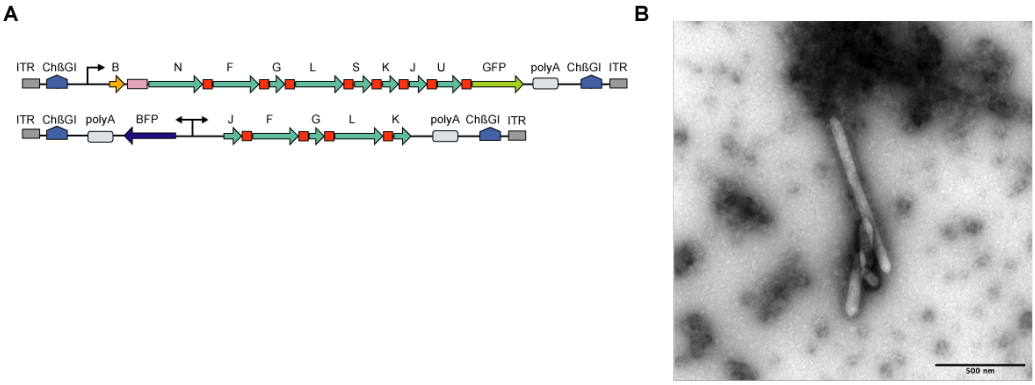


**Figure 4-S13: Consolidated mARG construct comprising 2 gene cassettes enables mammalian gas vesicle expression.** (a) Schematic of two gene cassettes integrated to the genome of HEK293-tetON cells. In the top construct *GvpB* is separated from *GvpN* by an internal ribosome entry sequence (shown in purple). (b) Representative TEM image of GVs in the lysate of HEK293-tetON cells transfected with the constructs in (a) and induced with 1 µg/mL doxycycline.

| Gene | GVs after N-term addition? | GVs after C-term addition? |
|---|---|---|
| *GvpB* | -- | No |
| *GvpR* | Yes | Yes |
| *GvpN* | Yes | Yes |
| *GvpF* | Yes | Yes |
| *GvpG* | Yes | Yes |
| *GvpL* | Yes | Yes |
| *GvpS* | Yes | Yes |
| *GvpK* | Yes | Yes |
| *GvpJ* | Yes | Yes |
| *GvpT* | Yes | Yes |
| *GvpU* | Yes | Yes |

**Table 4-S1: Tolerability of P2A peptide additions to *B. megaterium* gas vesicle genes.** Each gene of the *B. megaterium* gene cluster was modified with an N-terminal proline after the start codon or with a linker and P2A peptide at the C-terminus, resulting in a total of 21 unique GV gene clusters as illustrated in Fig. 4-S2. *E. coli* were transformed with each plasmid and gas vesicles were induced for expression for a total of 22 hours and assayed for the presence of gas vesicles using TEM. The table indicates whether gas vesicles were observed by TEM. Expression and TEM imaging performed as in Farhadi *et al.*[22].

| Collected from FACS | Formed colonies | Triple positive fluorescence | Formed GVs (TEM) | >1 GVs/cell |
|---|---|---|---|---|
| 576 | 30 | 21 | 12 | 6 |

**Table 4-S2: Selection funnel for monoclonal mARG-HEK cells.** The numbers indicate the number of cells or cell lines selected at each stage.

*Chapter 5*

# ACOUSTICALLY MODULATED MAGNETIC RESONANCE IMAGING OF GAS-FILLED PROTEIN NANOSTRUCTURES

This chapter is in large part a reformatted version of the manuscript entitled "Acoustically modulated magnetic resonance imaging of gas-filled protein nanostructures" published by Lu, G., Farhadi, A., Szablowski, J.Z., Lee-Gosselin, A., Barnes, S.R., Lakshmanan, A., Bourdeau, R.W., and Shapiro, M.G., in *Nature Materials*[1]. Under the supervision of Mikhail Shapiro, my contributions to the work was to help design and conduct the experiments in addition to analyzing and interpreting the data, in particular experiments related to cluster-based MRI sensors.

## 5.1 Abstract

Noninvasive biological imaging requires materials capable of interacting with deeply penetrant forms of energy such as magnetic fields and sound waves. Here, we show that gas vesicles, a unique class of gas-filled protein nanostructures with differential magnetic susceptibility relative to water, can produce robust contrast in magnetic resonance imaging (MRI) at sub-nanomolar concentrations, and that this contrast can be inactivated with ultrasound *in situ* to enable background-free imaging. We demonstrate this capability *in vitro*, in cells expressing these nanostructures as genetically encoded reporters, and in three model *in vivo* scenarios. Genetic variants of gas vesicles, differing in their magnetic or mechanical phenotypes, allow multiplexed imaging using parametric MRI and differential acoustic sensitivity. Additionally, clustering-induced changes in MRI contrast enable the design of dynamic molecular sensors. By coupling the complementary physics of MRI and ultrasound, this nanomaterial gives rise to a distinct modality for molecular imaging with unique advantages and capabilities.

## 5.2 Introduction

The imaging of cellular and molecular processes inside living animals and patients requires contrast agents compatible with noninvasive imaging modalities such as magnetic resonance imaging (MRI) and ultrasound. Ideally, such contrast agents should be non-toxic, possess the smallest possible dimensions, enable detection at sub-nanomolar concentrations, be expressible by cells through genetic encoding, and

produce dynamic contrast in response to local molecular signals. Existing contrast agents for MRI, primarily based on heavy metal chelates[2], superparamagnetic iron oxides[3], metalloproteins[4,5], and molecules with chemically exchangeable nuclei[6–8], do not fully satisfy these reporter requirements. Here, we show that a unique class of gas-filled, genetically encoded, nanoscale reporters produce robust MRI contrast via differential magnetic susceptibility and can be erased with ultrasound to enable background-free molecular imaging at sub-nanomolar concentrations.

These reporters are based on gas vesicles (GVs), gas-filled protein nanostructures expressed in certain photosynthetic microbes as flotation devices to maintain optimal access to light and nutrients[9,10]. GVs possess a hollow gas interior, a few hundred nanometers in size, enclosed by a 2 nm protein shell that is permeable to gas but excludes liquid water (Fig. 5-1a, b). GVs are physically stable under ambient conditions, and can be collapsed with pressure above genetically determined thresholds of 2-6 atmospheres, leading to the rapid dissolution of their gaseous contents[9]. As a genetically encoded nanomaterial, GVs can be expressed heterologously[11,12] and have their properties modified through genetic engineering[13].

Air is a well-known source of contrast in MRI due to its positive magnetic susceptibility compared to diamagnetic water, as seen in image artefacts near gas-filled organs such as the lungs[14]. We reasoned that the air inside GVs would also produce susceptibility-based MRI contrast, which could be observed by $T_2$/$T_2^*$-weighted imaging and quantitative susceptibility mapping (QSM). Additionally, because GVs can be collapsed with acoustic pressure[13,15], we hypothesized that the MRI contrast produced by GVs could be erased remotely *in situ* using ultrasound, an orthogonal noninvasive modality. Such acoustically modulated reporters would overcome a major challenge in MRI posed by background contrast from endogenous sources[16] by allowing reporters to be identified specifically based on their acoustic responses. Moreover, this imaging mechanism would be complementary to other recent uses of GVs[15,17], creating possibilities for multimodal imaging. In this study, we set out to test these fundamental hypotheses through *in vitro* and *in vivo* experiments and computational modelling. In addition, we sought to demonstrate that the unique material properties of GVs could enable multiplexed, functional and genetically encoded molecular imaging.

## 5.3 Results and Discussions

**GVs produce susceptibility-based MRI contrast.** To assess the ability of GVs to produce susceptibility-based MRI contrast, we performed computational modelling

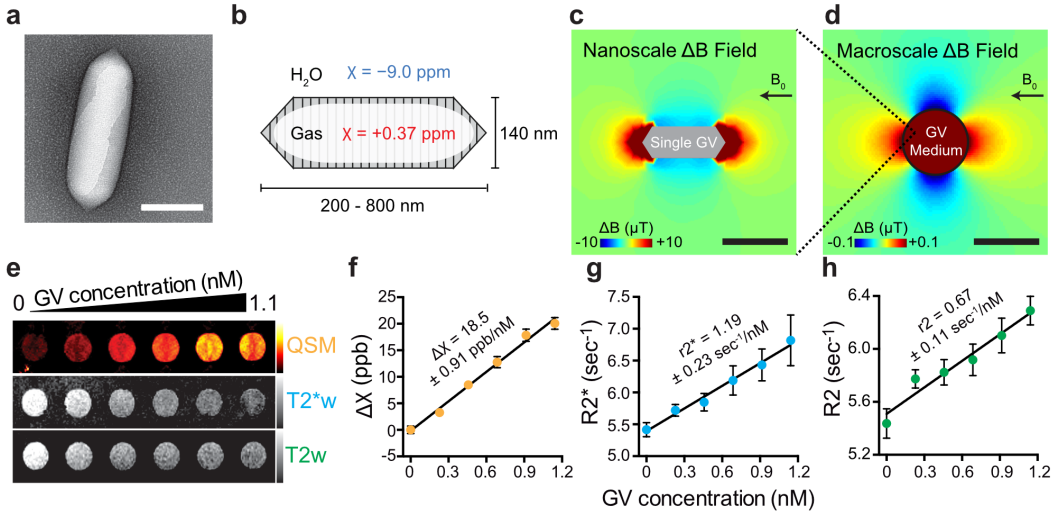


**Figure 5-1: Gas vesicles (GVs) produce susceptibility-based MRI contrast.** a, Transmission electron microscopy (TEM) image of a GV from *Anabaena flos-aquae* (Ana) b, Schematic drawing of a GV, whose air-filled interior has magnetic susceptibility (red) different from that of surrounding $H_2O$ (blue). c, Finite element model of the magnetic field gradient produced by a single air-filled Ana GV in water exposed to a 7 Tesla horizontal magnetic field ($B_0$). d, Finite element model of the magnetic field gradient produced by a cylindrical sample of 1 nM Ana GVs embedded in an agarose phantom. e, Quantitative susceptibility map (QSM), $T_2^*$-weighted ($T2^*w$) and $T_2$-weighted (T2w) images of wells containing Ana GVs at concentrations ranging from 0 to 1.1 nM. The color schemes for QSM (red hot), $T_2^*w$ (grey) and $T_2w$ (grey) images are used across all figures. The QSM color scale ranges linearly from -2 to +50 parts per billion (ppb), and $T_2^*w$ and $T_2w$ images at echo time (TE) = 144 msec have linear scales adjusted for optimal contrast. f, g, h, Magnetic susceptibility, $T_2^*$ relaxation rate and $T_2$ relaxation rate, respectively for different concentrations of Ana GVs. The value and the standard error of the slope from the linear regression fitting are shown for each plot and corresponds to molar susceptibility (f), $r_2^*$ relaxivity (g) and $r_2$ relaxivity (h). N = 9 independent samples in (f, g) and N = 6 independent samples in (h). Error bars represent SEM. Scale bars represent 150 nm (a), 300 nm (c) and 3 mm (d).

and *in vitro* imaging experiments. The air contents of the GV interior have an expected magnetic susceptibility of +0.37 ppm, differing significantly from water, which is diamagnetic at -9.0 ppm (Fig. 5-1b). As a result of this mismatch, individual GVs in aqueous media under a uniform magnetic field are predicted by finite element modelling to produce nanoscale magnetic field gradients (Fig. 5-1c). The proton nuclear spins on water molecules experiencing such gradients are expected to dephase, leading to enhanced $T_2/T_2^*$ relaxation and a concomitant reduction of local signal intensity in $T_2$- and $T_2^*$-weighted images, which can be acquired with widely used spin-echo and gradient-echo MRI pulse sequences[18]. In addition, macroscale volumes containing GVs have a different average susceptibility than surrounding

voxels, producing macroscale field gradients (Fig. 5-1d), which should cause a patterned change of spin phase beyond the site of the GVs (Supplementary Fig. 5-S1). These phase changes can be decoded by QSM algorithms to produce contrast maps with additional sensitivity beyond magnitude-only $T_2/T_2^*$ images[19,20].

To test the ability of GV nanostructures to produce these forms of contrast, we purified GVs from the cyanobacterium *Anabaena flos-aquae* (Ana GVs) and imaged them in agarose phantoms with a 7 Tesla MRI scanner. As predicted, GVs produced robust contrast in $T_2^*$- and $T_2$-weighed images and QSM maps (Fig. 5-1e). Quantification of this MRI contrast revealed $T_2^*$ and $T_2$ relaxivities of 1.19 ± 0.23 $nM^{-1}$ $s^{-1}$ and 0.67 ± 0.11 $nM^{-1}s^{-1}$, respectively, and molar susceptibility of 18.53 ± 0.91 parts-per-billion (ppb) $nM^{-1}$ (Fig. 5-1f-h and Supplementary Table 5-S1), wherein the nanomolar concentration refers to GV particles. The lowest tested concentration of Ana GVs, at 230 pM, or 73 μg/mL protein, was readily detectable by QSM ($p = 0.0014$, unpaired *t*-test, the first two data points of Fig. 5-1f, degrees of freedom (d.f.) = 11.86). This protein concentration is within the range of other protein-based MRI reporters such as haem-containing cytochromes, ferritin, aquaporin and chemical exchange saturation transfer polypeptides[21]. At these concentrations, GVs produce negligible $T_1$ contrast (Supplementary Fig. 5-S2), and have an insignificant effect on proton density due to water exclusion (< 0.1% v/v), preserving these contrast modes for use by orthogonal reporters or anatomical imaging. GVs purified from *Halobacterium salinarum* NRC-1 (Halo GVs) and GVs formed by expressing a GV gene cluster from *Bacillus megaterium* in *Escherichia coli* (Mega GVs) produced similar contrast to Ana GVs (Supplementary Fig. 5-S2).

**Background-free acoustically modulated imaging.** Conventional $T_2$ and $T_2^*$contrast agents such as superparamagnetic iron oxide nanoparticles (SPIONs) are widely used in MRI applications such as *in vivo* cell tracking[22]. However, the specificity with which they can be detected in biological tissues is sometimes confounded by the presence of background contrast from endogenous sources such as blood vessels and tissue interfaces[16]. MR pulse sequences and post-processing methods designed to selectively acquire signals only from SPIONs[23–25] often sacrifice molecular sensitivity, while alternative imaging approaches such as magnetic particle imaging (MPI) and $^{19}$F-MRI lack tissue context[26–29]. Unlike SPIONs, GVs have a built-in mechanism by which their identity as the source of any given MRI contrast can be ascertained. Namely, the collapse of their gaseous interior under pressure should eliminate GV's susceptibility mismatch with water (Fig. 5-2a), allowing GV-specific contrast to be revealed by differential imaging. Importantly,

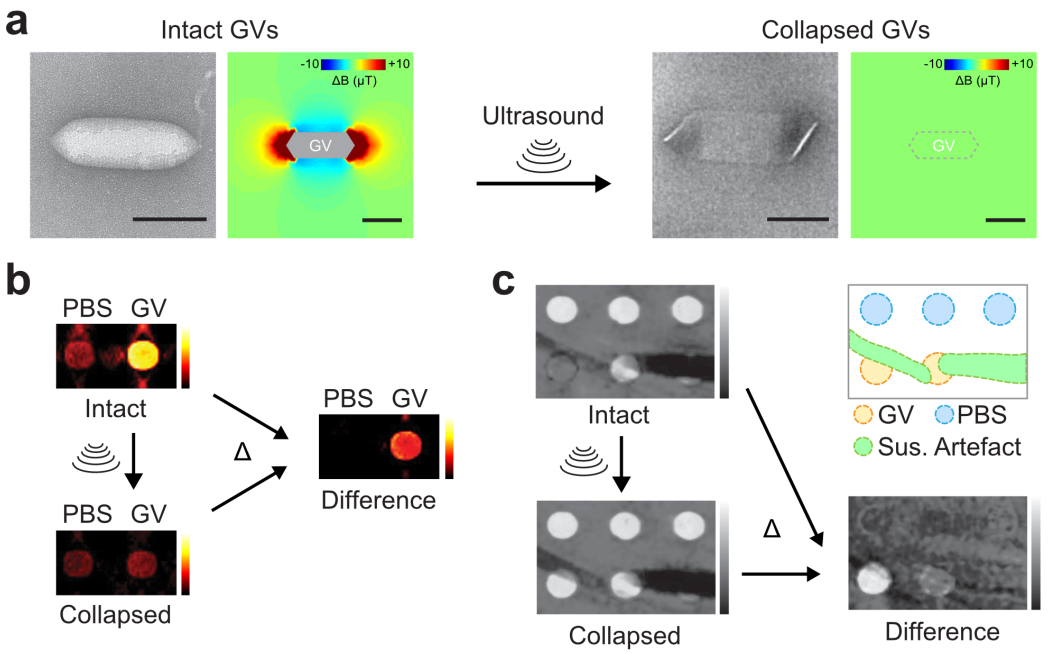


**Figure 5-2: Background-free acoustically modulated imaging.** a, TEM images and simulated magnetic field profiles generated by intact and collapsed Mega GVs. Scale bars represent 100 nm. b, Magnetic susceptibility maps of wells containing phosphate-buffered saline (PBS) or 4.9 nM Mega GVs before and after the application of ultrasound, and the resulting difference image. c, $T_2^*$-weighted images of a phantom containing wells with 8.1 and 4.9 nM Mega GVs alongside background hyperintense contrast from wells with PBS in low-percentage agarose and hypointense susceptibility artefact from the nearby 40 μm (inner diameter) capillary tubes containing 500 mM $NiSO_4$, before and after the application of ultrasound, and the resulting difference image. The diagram outlines the different regions of the phantom.

such pressure can be applied remotely using ultrasound, rendering the entire imaging paradigm noninvasive and depth-unlimited.

We tested this concept by acquiring QSM images of samples containing Mega GVs or buffer before and after acoustic collapse with ultrasound. Subtraction of the pre-collapse image from the image acquired after collapse resulted in background-free contrast specific to the GVs (Fig. 5-2b). To demonstrate that this method can distinguish GVs from susceptibility artefacts in $T_2^*$-weighted imaging, we prepared a phantom containing GVs, regions with lower concentration of agarose and capillary tubes filled with paramagnetic nickel. While GVs are difficult to distinguish from other hyper- and hypo-intense regions in the raw initial image, acoustic collapse and background subtraction enable the specific observation of GVs even at concentrations that were initially difficult to spot by naked eye (Fig. 5-2c). This differential contrast is positive because GV collapse leads to a longer

$T_2^*$.

To test the acoustically modulated molecular imaging paradigm *in vivo*, we began by stereotaxically injecting Ana GVs in the striatum of adult C57 mice and imaging them using $T_2^*$-weighted MRI (Fig. 5-3a). We then collapsed the GVs *in situ* using brief pulses of MRI-guided focused ultrasound[30] and acquired a post-collapse MRI image. The resulting differential image, overlaid on a separately acquired anatomical reference, shows specific background-free contrast from the brain region injected with GVs (Fig. 5-3b, c). A contralateral injection of phosphate-buffered saline (PBS) without GVs, subjected to the same MRI and ultrasound pulses, produced no significant contrast. The mean collapse-dependent contrast in the GV-injected region was 23.5 ± 3.8% (Mean ± SEM, N = 9) compared to 0.4 ± 2.6% for PBS (Mean ± SEM, N = 6, p = 0.0002, unpaired *t*-test, d.f. = 12.73). Although we mainly used $T_2^*$-weighted images for *in vivo* background-free imaging due to their convenience, QSM-processed susceptibility maps also visualized GVs with a high contrast-to-noise ratio (Supplementary Fig. 5-S3).

Next, we tested the ability of GVs to be imaged *in vivo* after intravenous (IV) administration. GVs injected into the bloodstream are efficiently taken up by the liver[15], a tissue whose ability to clear particles from circulation serves as an important indicator of hepatic health and tumor diagnosis[31]. Because the liver and surrounding tissues also have high endogenous contrast, hepatic imaging serves as a good test bed for background-subtracted imaging techniques. After administering GVs to mice (Fig. 5-3d), we performed $T_2^*$-weighted imaging before, during and after applying focused ultrasound to the liver. A dynamic jump in average signal intensity in the insonated region was readily observed in mice injected with GVs, but not in mice injected with PBS (Fig. 5-3e), producing a clear spot of background-subtracted contrast (Fig. 5-3f). The mean collapse-dependent signal change in the GV-injected mice was 5.4 ± 1.4% compared to 0.1 ± 0.1% for PBS (Mean ± SEM, N = 8, p = 0.0068, unpaired *t*-test, d.f. = 7.14) (Fig. 5-3g).

**Acoustically modulated imaging of gene expression.** After establishing the basic acoustically modulated imaging capabilities of GVs *in vitro* and *in vivo*, we tested the ability of these genetically encoded nanostructures to act as reporters of gene expression in living cells. In particular, given the great interest in imaging the mammalian microbiome and bacterial infections[32], we assessed whether GVs could image inducible gene expression in the model bacterium *E. coli*. Heterologous expression of a recently developed GV variant comprising a combination of genes from *A. flos-aquae* and *B. megaterium*[12] (A2C) was placed under the control of a

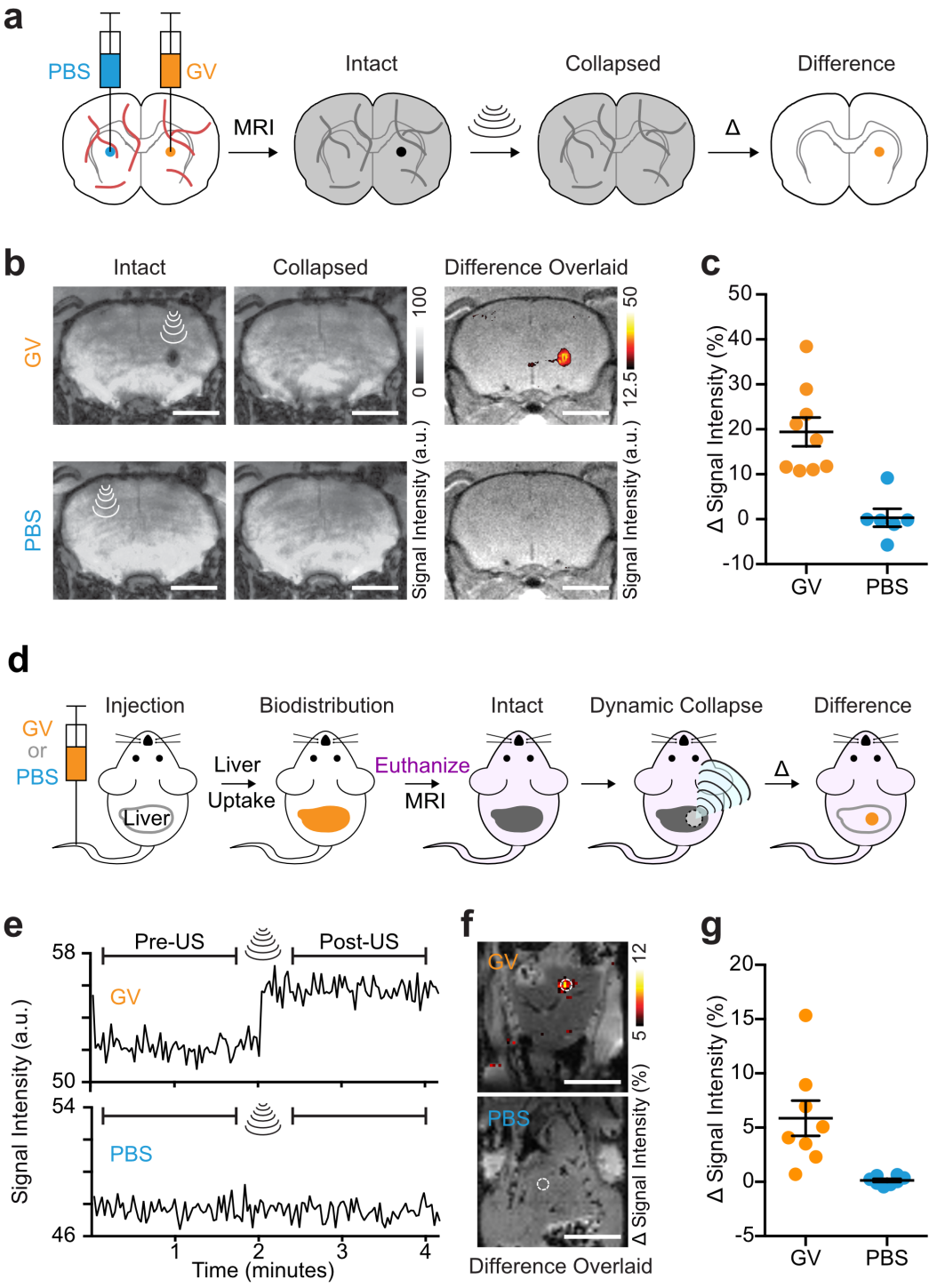


**Figure 5-3: Background-free imaging of GVs in mammalian tissues.** a, Diagram of the *in vivo* experiment in the living mouse brain. GVs or PBS buffer (sham control) were injected into contralateral striatum. $T_2^*$-weighted images taken before the insonation were subtracted from those taken after, and difference images were calculated to reveal contrast specific to the GVs, giving rise to a background-free image. b, Representative $T_2^*$-weighted images (TE = 15 msec) of a mouse injected with 2 µL GVs ($Ana_{WT}$, 3.4 nM) or PBS,

**Figure 5-3:** (continued from above.) acquired before and after ultrasound was applied to the site of injection. The resulting difference images are overlaid on anatomical images. c, Changes in signal intensity upon insonation at the sites of injection (N = 9 and 6 injections for GV and PBS, respectively, in a total of 8 mice) normalized by the intensity of the surrounding brain region. d, Diagram of dynamic imaging of the mouse liver after intravenous administration of GVs. 200 µL PBS with or without 13.7 nM GVs ($Ana_{\Delta C}$, clustered form) were injected. After allowing 1 min for the biodistribution of GVs to the liver, mice were euthanized, and $T_2^*$-weighted images (1.9 sec/frame) were acquired continuously before, during and after a 5-second application of ultrasound pulses to a spot in the liver. e, Representative time course of signal intensity at an insonated spot (1 mm radius) of mouse liver after intravenous injection with GVs or PBS. f, Difference in intensity between images acquired before and after ultrasound application, overlaid on anatomical images. g, Average signal intensity change in the insonated region upon the application of focused ultrasound to the liver tissue (N = 8 spots for each condition in a total of 8 mice). a.u. denotes arbitrary units. Error bars represent SEM, and scale bars represent 3 mm (b) and 10 mm (e).

promoter inducible by isopropyl b-D-1-thiogalactopyranoside (IPTG, Fig. 5-4a). Overnight induction resulted in GV expression and robust, acoustically erasable QSM contrast that was absent from cells that were not induced or cells induced to express a control fluorescent protein (Fig. 5-4b, c). Notably, the *E. coli* concentration in the phantom, estimated from $OD_{600}$ to be about 14 g/L wet cellular weight[33], indicates that the GV-containing cells can be detected while comprising less than 1.4% of the imaged volume.

**Acoustically modulated multiplexing.** Many imaging applications in biomedicine would benefit from the ability to image multiple molecular or cellular signals in the same tissue[34]. Because GVs with different protein composition collapse at substan-

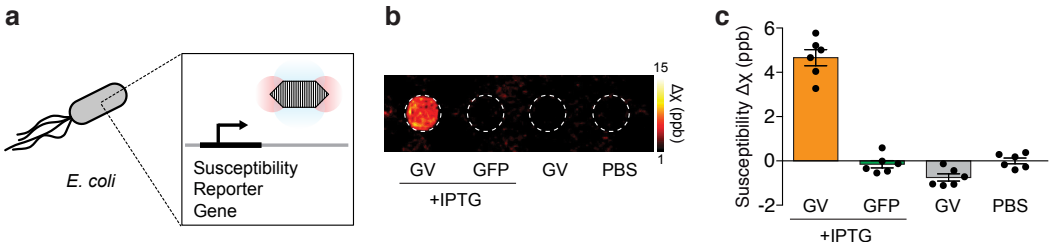


**Figure 5-4: Acoustically modulated reporter gene imaging in living cells.** a, Diagram of the inducible expression of GV genes in *E. coli* leading to the intracellular formation of GVs and the generation of susceptibility-based MRI contrast. b, Representative background-subtracted QSM image of agarose phantom containing *E. coli* expressing GVs or a green fluorescent protein (GFP) under the control of an IPTG-inducible promoter, in the presence or absence of the inducer, compared to a well containing buffer. c, Mean differential susceptibility values relative to buffer. N = 6 biological replicates. Error bars represent SEM. All bacterial cells were loaded in the phantom at a final $OD_{600}$ of 8.0.

tially different acoustic pressures[13,15], this suggests the possibility of performing acoustically modulated imaging in multiplex by collapsing one population of GVs at a time with ultrasound while acquiring a sequence of MR images (Fig. 5-5a). Voxel-wise intensity changes between successive images should then encode the signal corresponding to each multiplexed GV population.

GVs with different collapse pressures can be obtained by isolating genetically distinct variants or by modifying their shell[13]. Here, we used a variant of Ana GVs (referred to as $Ana_{\Delta C}$) whose acoustic collapse pressure has been lowered by removing its outer scaffolding protein, GvpC[13] (Fig. 5-5b). Since GvpC removal does not alter the morphology of the GV, $Ana_{\Delta C}$ produces MRI contrast equivalent to wildtype Ana GVs ($Ana_{WT}$). To demonstrate multiplexing, we prepared a phantom with three wells containing $Ana_{\Delta C}$, $Ana_{WT}$ and a 1:1 mixture (Fig. 5-5c). We then acquired three sequential MR images interspersed by ultrasound pulses at $Ana_{\Delta C}$- and $Ana_{WT}$-collapsing pressures. Changes in the measured magnetic susceptibility of each voxel between the relevant pairs of images revealed the contents of each sample (Fig. 5-5, c-d).

Next, to test the multiplexing paradigm and demonstrate the imaging of bacterial gene expression *in vivo*, we injected $Ana_{\Delta C}$ GVs and *E. coli* cells expressing A2C GVs subcutaneously and acquired sequential MR images interspersed by ultrasound pulses selectively collapsing, first $Ana_{\Delta C}$ GVs, then A2C GVs, at each location (Fig. 5-5e). Difference images revealed significant signal for $Ana_{\Delta C}$ GVs only upon low-pressure collapse, since few GVs were left intact to be collapsed at high pressure (Fig. 5-5f and Supplementary Fig. 5-S4). In contrast, *E. coli* expressing the more mechanically robust A2C GVs produced a signal change specifically in response to higher pressure. Subtracting the signal change generated by low-pressure ultrasound from the change generated by high-pressure ultrasound enables quantitative assignment of the contrast source (Fig. 5-5, g-h). $Ana_{\Delta C}$ GVs and A2C-expressing *E. coli* cells yield positive and negative values, respectively, with +9.0 ± 2.7% for $Ana_{\Delta C}$ and -8.5 ± 3.3% for A2C GVs (Mean ± SEM, N = 4, p = 0.0072, unpaired *t*-test, d.f. = 5.73).

**Multiparametric MRI multiplexing.** In addition to acoustic multiplexing, we hypothesized that GVs with different shapes and sizes could be distinguished on the basis of their differential effects on $T_2$ and QSM contrast. GV morphology should alter the nanoscale magnetic field patterns generated by a given quantity of gas, affecting $T_2$ relaxation[35]. In contrast, the magnetic susceptibility calculated from QSM is expected to depend on the total amount of gas in the sample, independent

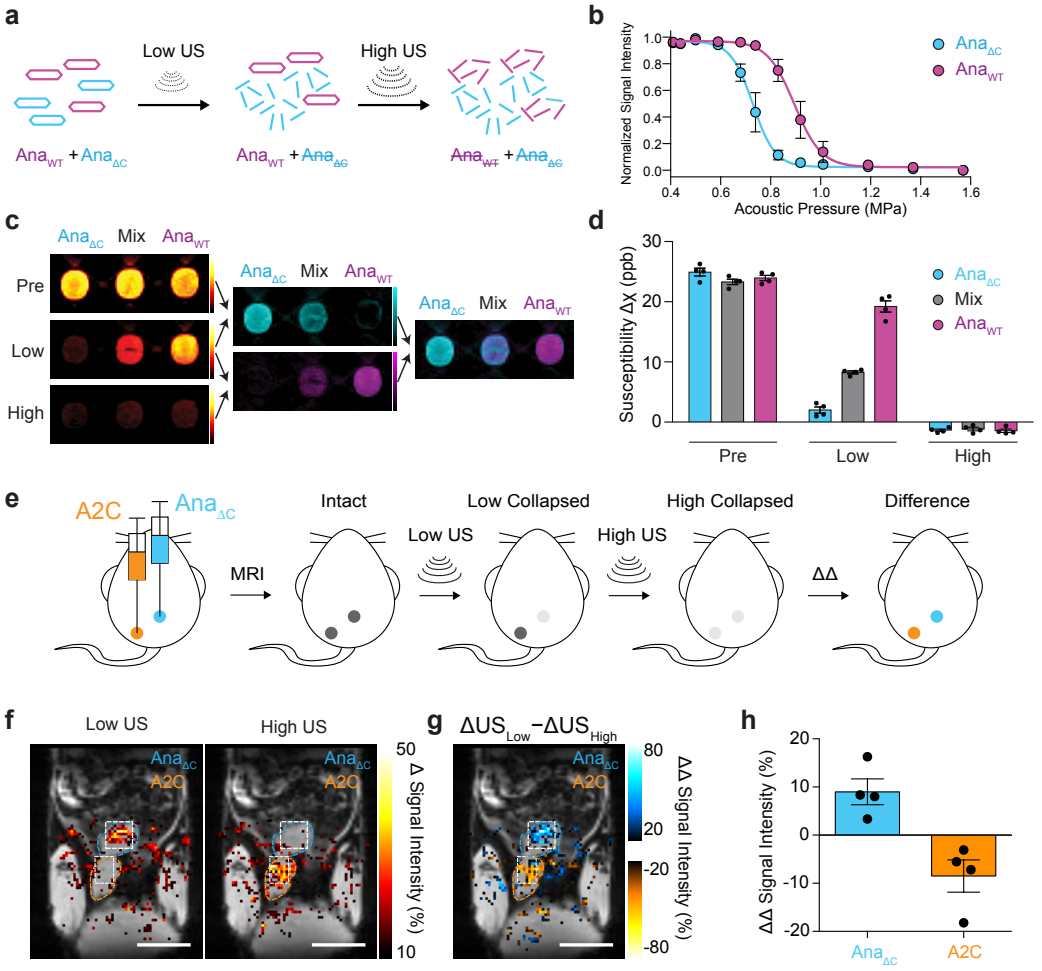


**Figure 5-5: Acoustically multiplexed magnetic resonance imaging.** a, Schematic of the pressure-scanning paradigm, wherein sequential ultrasound pulses are applied between MR images. The low-pressure ultrasound (Low US) selectively collapses $Ana_{\Delta C}$ GVs and eliminates their MRI contrast; subsequently, high-pressure ultrasound (High US) collapses $Ana_{WT}$ GVs. b, Acoustic collapse measurement of AnaΔC and AnaWT. N = 3 independent samples for each point. Fitted curves represent a sigmoid function obtained by nonlinear least-square fitting. c, Representative QSM images taken before ultrasound application (Pre), after the low-pressure ultrasound (Low) and after high-pressure ultrasound (High) of wells containing $Ana_{WT}$, $Ana_{\Delta C}$ or a 1:1 mixture of the two, as indicated, followed by difference images obtained by pairwise subtraction, color mapped to distinguish variants collapsing at different pressures, followed by an overlay of the two difference images. The total GV concentrations were 1.37 nM in all three samples and the images were displayed from -10 to +50 ppb. d, Average susceptibility of each sample type relative to PBS buffer at each stage of the pressure-scanning paradigm. N = 4 independent samples. Complete collapse of GV specimens resulted in slightly negative susceptibility relative to the PBS solution, as expected since proteins are more diamagnetic than water. e, Diagram of the *in vivo* multiplexing experiment in the living mouse lower abdomen. f, Maps of changes in MRI signal intensity in insonated regions overlaid on anatomical MR image. The insonated

**Figure 5-5:** (continued from above) regions are outlined in white, while the subcutaneously injected areas are outlined in blue or orange, corresponding to their contents. g, Map of the differential change in the change in signal intensity after the application of Low US relative to High US. h, Average signal change at 8 injection sites (4 of each type from a total of 4 mice). a.u. denotes arbitrary units. Error bars represent SEM (b, d, h), and scale bars represent 10 mm (f, g).

of its nanoscale arrangement. Each type of GV should therefore have its own parametric fingerprint. We tested this hypothesis using Ana GVs, GVs purified from *E. coli* expressing a GV gene cluster from *B. megaterium*[11] and GVs purified from *Halobactrium salinarum* (Halo) (Fig. 5-6a). After measuring the $T_2$ relaxivity and molar susceptibility values for each molecule (Fig. 5-6a, Supplementary Fig. 5-S2), we used Mega and Halo GVs to demonstrate multiplexed imaging. Each GV type had a distinct appearance under susceptibility contrast relative to its $T_2$ relaxivity (Fig. 5-6b), and voxel-wise unmixing of susceptibility ($\Delta\chi$) and relaxation rate ($R_2$) according the equation

$$\begin{bmatrix} R_2^{exp} \\ \Delta\chi^{exp} \end{bmatrix} = \begin{bmatrix} r_{2,\alpha} & r_{2,\beta} \\ \Delta\chi_{m,\alpha} & \Delta\chi_{m,\beta} \end{bmatrix} \cdot \begin{bmatrix} c_\alpha \\ c_\beta \end{bmatrix}$$

revealed the quantities of the two GV types in each sample, $C_\alpha$ and $C_\beta$ (Fig. 5-6c). This multiparametric MRI paradigm[36] has the advantage of being non-destructive compared to acoustic multiplexing, but is statistically less accurate (Supplementary Fig. 5-S5).

**Clustering-based molecular sensors.** In addition to contrast agents reporting their location, there is considerable interest in the development of dynamic molecular sensors[37–40]. For example, superparamagnetic nanostructures that cluster in response molecular signals of interest can increase or decrease $T_2$ or $T_2^*$ contrast[37,40,41]. We hypothesized that GVs would also produce differential MRI contrast based on clustering. In particular the size and magnetic character of GVs places them in the so-called motional averaging regime[35,42–44] of $T_2$/ $T_2^*$ relaxation, such that their clustering in response to a target analyte should result in an increase in both $T_2^*$ and $T_2$ relaxivity. We tested this hypothesis using biotin-functionalized Ana GVs mixed with tetrameric streptavidin (Fig. 5-6d and Supplementary Fig. 5-S6). At appropriate streptavidin concentrations, GVs form micron-size clusters (Fig. 5-6e), predicted to produce a magnetic field profile with correspondingly large spatial dimensions (Fig. 5-6f-g). Upon clustering, $T_2^*$- and $T_2$-weighted images showed dramatic relaxation enhancement compared to controls lacking biotinylation

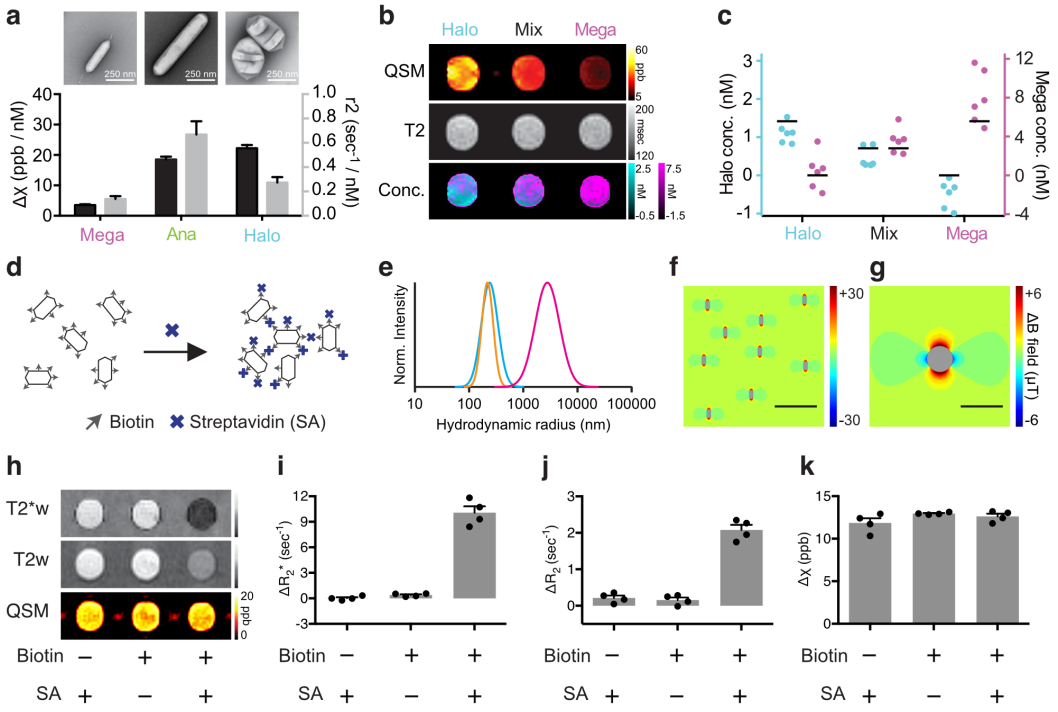


**Figure 5-6: Multiparametric MRI fingerprinting and clustering-based molecular sensors.** a, TEM images and magnetic susceptibility and $r_2$ relaxivitiy values for Mega, Ana and Halo GVs. The molar susceptibility ($\Delta\chi$) values are referenced to blank PBS buffer. Error bars represent the standard error of the slope from linear regression fitting (Supplementary Fig. 5-S2). b, Representative susceptibility map (QSM), $T_2$ relaxivity map (T2) and calculated GV concentrations (Conc.) of three samples that contain Halo GVs, Mega GVs or a 1:1 mixture of both GV types. The concentration of Mega (magenta) and Halo (cyan) GVs were pixel-wise calculated and displayed in overlay. c, GV concentrations calculated from MRI images in N = 6 independent samples. Black bars represent the expected GV concentration. d, Diagram of the clustering experiment using biotinylated Ana GVs and streptavidin (SA). e, Dynamic light scattering (DLS) measurement of the size distributions of biotinylated GVs with SA (magenta), biotinylated GVs without SA (cyan) and non-biotinylated GVs with SA (orange). f, g, Finite element model of the magnetic field pattern expected from individual (f) and clustered (g) GVs. Scale bars represent 2 μm (f) and 4 μm (g). h, Representative $T_2^*$-weighted (T2*w) and $T_2$-weighted (T2w) images and QSM maps of agarose phantom wells containing GVs with the indicated biotinylation state and presence or absence of SA. i, j, k, Average change in $R_2^*$ (i), $R_2$ (j) and $\chi$ (k) relative to PBS buffer. N = 4 independent samples. Error bars represent SEM. All the GV samples contained Ana GVs at 0.57 nM.

or streptavidin (Fig. 5-6h), with $R_2^*$ and $R_2$ increasing approximately 15- and 5-fold, respectively (Fig. 5-6i-j). Remarkably, the QSM image was largely unaltered (Fig. 5-6k), as expected given the conservation of total air between the three samples; this allows a change in clustering to be distinguished from an increase in the number of particles, thereby enhancing sensing robustness.

## 5.4 Conclusions

Our results establish GV as protein-based acoustically modulated MRI contrast agents, using the combination of ultrasound and MRI to enable background-free and multiplexed molecular imaging. This imaging modality takes advantage of the material properties of GVs, including both, the magnetic susceptibility of their interior as a perturbation of the magnetic field in liquid media, and the mechanics of their protein shell allowing collapse at specific acoustic pressures. Acoustically modulated reporters should be particularly useful in imaging scenarios with confounding background contrast[16,45–47].

The distinct size, shape and mechanical properties of genetic variants of GVs provide opportunities for future molecular engineering. For example, GV morphology could be optimized to maximize spin dephasing and $T_2/T_2^*$ contrast, or to facilitate multiplexing of several GV types on the basis of differential relaxivity. At the same time, engineering GV shells with a greater variety of critical collapse pressures could expand multiplexing ability using acoustic collapse. Between these two modes of multiplexing, non-acoustic multiplexing has the advantage of not requiring an ultrasound system. However, the acoustic approach is more accurate in distinguishing GV concentrations, and is independent of the microscale spatial arrangement of GVs. Genetic or chemical engineering of the GV shell[13,48] also provides a route to designing targeted MRI reporters and sensors, the delivery of which may be facilitated by engineering GVs with smaller sizes[10,49]. In parallel, engineered genetic circuits incorporating GV reporter genes could be used to image bacteria *in vivo*.

Several limitations must be addressed in future studies to establish the wider applicability of GVs as acoustically modulated susceptibility contrast agents. First, while the three mouse experiments presented in this study provide proofs of concept for the *in vivo* implementation of acoustically modulated GV imaging, additional work is needed to demonstrate applications of this technique in biomedically useful scenarios. Such applications could include evaluating hepatic health by imaging the uptake of intravenously injected GVs, labelling specific endothelial or extra-vascular biomarkers or monitoring bacterial biodistribution. To facilitate such applications, additional experiments are needed to establish the tolerability and immunogenicity of injected GVs. Mice injected with repeated doses of GVs over several days in our study did not exhibit any behavioural abnormality, consistent with previous veterinary assessments[15]. However, more detailed histological and biochemical studies are needed.

In addition, the acoustically modulated imaging protocol can be simplified to replace focused ultrasound with an unfocused source, allowing larger areas of the specimen to experience GV collapse. Unlike ultrasound imaging, which requires sound wave coherence for image reconstruction, acoustically modulated MRI only requires enough ultrasound pressure to reach tissues to collapse GVs, facilitating transmission through bone and providing flexibility in instrument design. Finally, the expression of GVs is currently limited to bacterial hosts. Making mammalian cells capable of producing GVs is an active area of ongoing research.

Together with other recent literature, this study establishes GVs as a tri-modal imaging agent. GVs have recently been explored for ultrasound imaging based on their ability to scatter sound waves[15], and for hyperpolarized $^{129}$Xe CEST imaging based on the ability of xenon gas to exchange across the GV shell[17]. Compared with pulse-echo ultrasound, acoustically modulated MRI has an advantage in accessing bone-enclosed structures such as the brain. It is also much simpler to implement than hyperpolarized $^{129}$Xe imaging, which requires specialized procedures for gas hyperpolarization and delivery. Nevertheless, the ability of GVs to be visualized with multiple modalities increases their appeal as a molecular imaging nanomaterial.

## 5.5 Methods

**Expression and purification of gas vesicles.** Ana and Halo GVs were purified after expression in their respective host bacteria. *Anabaena flos-aquae* (CCAP strain 1403/13F) was cultured in Gorham's media supplemented with BG-11 solution (Sigma, St. Louis, MO) and 10 mM $NaHCO_3$ at 25°C, 100 rpm shaking and 1% $CO_2$ under a 14 h light−10 h dark cycle and confluency was reached in ~ 2 weeks. *Halobacteria NRC-1* (Carolina Biological Supply, Burlington, NC) were cultured at 42°C in ATCC medium 2185 under ambient light and with shaking at 100 rpm. Confluency was reached in ~ 1 week. Both types of cultures were transferred to sterile separating funnels. The buoyant cells were allowed to float to the top over a 48 h period. The subnatant was discarded and the floating cells were collected. *Anabaena* cells were lysed with 500 mM sorbitol and 10% Solulyse solution (Genlantis, San Diego, CA), and *Halobacteria* cells were hypotonically lysed with the addition of excess low-salt TMC buffer (10 mM Tris, pH = 7.5, 2.5 mM $MgCl_2$, 2mM $CaCl_2$). GVs were separated from cell debris by repeated centrifugally assisted floatation followed by resuspension in 1x PBS (Teknova, Hollister, CA). The centrifugation speed was carefully controlled to avoid the hydrostatic collapse of GVs. To prepare solution for *in vivo* experiments, purified GVs were dialyzed

overnight in 1 x PBS solution. The concentration of gas vesicles (GVs) was estimated based on the pressure-sensitive optical density at 500 nm ($OD_{500,PS}$) due to the ability of intact GVs to scatter light[9].

$Ana_{\Delta C}$ was prepared by treating Ana GVs with a solution of 6 M urea and 20 mM Tris-HCl (pH = 8.0). Two rounds of centrifugally assisted buoyancy purification were performed to remove GvpC. The solution was then dialyzed overnight in 1x PBS buffer to remove urea.

GVs from *Bacillus megaterium* (Mega) were heterologously expressed in *E. coli* Rosetta$^{TM}$2(DE3)pLysS (EMD Millipore, Billerica, MA). The pNL29 region of the Mega GV gene cluster[11] was cloned into the pST39 plasmid for expression under the control of the T7 promoter[17]. The transformed cells were grown at 30°C in LB media supplemented with 0.2% glucose. 20 μM isopropyl $\beta$-D-1-thiogalactopyranoside (IPTG) was added at $OD_{600}$ between 0.4 and 0.6 to induce the expression of GVs, and the cells were grown overnight before harvesting by centrifugation. The clear subnatant was removed by a syringe, while both the floating and the pelleted cells were collected. The cells were lysed in 10% Solulyse (Genlantis, San Diego, CA), 250 μg/ml lysozyme and 10 μg/ml DNaseI. Centrifugally assisted floatation and $OD_{500}$ measurement followed the procedure used for Halo and Ana GV. Mega GVs, which are natively clustered after purification from bacteria, were unclustered using the same urea treatment, buoyancy purification and dialysis procedure described for the preparation of $Ana_{\Delta C}$ GVs. Gas vesicle concentrations were determined using the relationships summarized in Supplementary Table 5-S1 ref.[48].

**Reporter gene expression.** For reporter gene experiments, the gene cluster encoding a hybrid GV variant named A2C[12] was cloned into pET28a plasmid (Novagen, Temecula, CA), and the resulting plasmid was transformed into BL21(A1) cells (Thermo Fisher Scientific, Waltham, MA). The transformed cells were first grown overnight at 30°C in LB media supplemented with 1% glucose, and this starter culture was subsequently diluted 1:100 into LB media supplemented with 0.2% glucose. When $OD_{600}$ reached between 0.4 and 0.6, 400 μM IPTG and 0.5% arabinose were added to induce expression of GVs. The control green fluorescent protein mNeonGreen[50] was inserted into the same plasmid and followed the identical culturing protocol.

Cell density was measured after collapsing any intracellular GVs to eliminate their contribution to optical scattering (Supplementary Fig. 5-S7). A sample of each *E. coli* specimen at $OD_{600} \sim 1.0$ was loaded onto a flow-through, 1 cm path-length quartz cuvette (Hellma Analytics, Plainview, NY), which was pressurized by an

$N_2$ cylinder and a digital pressure controller (Alicat Scientific, Tucson, AZ). The pressure was incremented in 20 kPa steps from 0 to 1.2 MPa and $OD_{600}$ was recorded using a spectrophotometer (EcoVis, OceanOptics, Winter Park, FL). $OD_{600}$ at 1.2 MPa was used to measure cell density. Prior to the preparation of MRI phantoms, the cells were concentrated by centrifugation to the indicated density. For *in vivo* imaging, the buoyant fraction of cells was concentrated and collected after several rounds of centrifugation at 350 g (4 hrs).

Transmission electron microscopy (TEM). GVs at $OD_{500,PS} \sim 0.2$ were prepared in a buffer of 10 mM HEPES, 150 mM NaCl (pH 8) and spotted on Formvar/Carbon 200 mesh grids (Ted Pella) that were rendered hydrophilic by glow discharging (Emitek K100X). GV samples were negatively stained using 2% uranyl acetate. Images were acquired using a Tecnai T12 LaB6 120kV TEM.

***In vitro* MRI and relaxometry.** Purified GVs or *E. coli* cells were embedded in agarose phantoms. 1% agarose stock solution was prepared in PBS and maintained at 60°C until use. The size of the phantom was ~18 × 6 × 4 cm (length × width × height). Using a custom 3D-printed caster, the bottom half was first cast with cylindrical wells of the size 3 × 5 mm (diameter × depth) separated by 3 mm. The cylindrical geometry perpendicular to $B_0$ was chosen to ensure a homogeneous field in the sample wells to facilitate susceptibility-based imaging. The gel was allowed to solidify and exposed to air for 1 h for gas equilibration. Two-times concentrated GVs or *E. coli* cells in PBS were mixed 1:1 with the melted agarose stock solution and immediately loaded into the wells. Subsequently, the top half of the phantom was cast so that all the wells were surrounded by agarose. Care was taken to avoid bubbles.

MRI was performed on a 7T horizontal bore Bruker-Biospin scanner, using a 7.2 cm diameter volume coil for transmit and receive. $T_2^*$ relaxivity was measured with 3D Multi Gradient Echo (MGE) experiments with the following parameters: repetition time (TR) = 500 ms, 32 echos, echo spacing (TE) = 9.0 ms, field of view (FOV) = 12 × 6 × 0.8 $cm^3$, spatial resolution = 0.25 × 0.25 × 0.25 $mm^3$ and 1 average. $T_2$ relaxometry was performed by 2D Multi Slice Multi Echo (MSME) spin echo experiments with the following parameters: TR = 2500 ms, 16 echos, TE = 16.0 ms, FOV = 8 × 6 $cm^2$, and spatial resolution = 0.25 × 0.25 $mm^2$. Slice thickness = 1 mm and 16 averages were used for multiparametric multiplexing experiments and 0.5 mm and 4 averages for all other experiments. $T_1$ relaxometry was performed by 2D Rapid Acquisition with Relaxation Enhancement with Variable TR (RAREVTR) with the following parameters: Effective TE = 9.68 ms, RARE factor = 12, FOV = 8

× 6 $cm^2$, spatial resolution = 0.25 × 0.25 $mm^2$, slice thickness = 0.5 mm, 2 average and 8 variable TR times including: 126.4, 738.4, 1461.2, 2344.1, 3478.7, 5068.5, 7746.6, 20000.0 ms.

For data analysis, a circular region of interest (ROI) was drawn for each well using Fiji[51]. The average intensity of the ROI was imported into Matlab for exponential fitting to derive the $T_2^*$, $T_2$ and $T_1$ values. Voxel-wise $T_2^*$ and $T_2$ maps were generated by ImageJ plugin, MRI Processor, using Simplex fitting. For $T_2^*$ relaxometry, the ROI excluded the rim of the wells. Multiparametric multiplexing of GVs was achieved by solving the matrix equation:

$$\begin{bmatrix} c_\alpha \\ c_\beta \end{bmatrix} = \begin{bmatrix} r_{2,\alpha} & r_{2,\beta} \\ \Delta\chi_{m,\alpha} & \Delta\chi_{m,\beta} \end{bmatrix}^{-1} \begin{bmatrix} R_2^{exp} \\ \Delta\chi^{exp} \end{bmatrix}$$

where the concentrations of the two GV species, $c_\alpha$ and $c_\beta$, were the two unknowns. $r_{2,\alpha}$ and $r_{2,\beta}$ were the $r_2$ relativity and $\Delta\chi_{m,\alpha}$ and $\Delta\chi_{m,\beta}$ were the molecular susceptibility of the GVs, and $R_2^{exp}$ and $\Delta\chi^{exp}$ were the experimentally measured relaxation rate and susceptibility (Supplementary Table 5-S1).

**Quantitative susceptibility mapping.** Magnitude and phase images of 3D MGE or 3D fast low angle shot (FLASH) experiments were obtained in ParaVision 5.1 (Bruker), and the images from a single echo served as the input to the Susceptibility Mapping and Phase artifacts Removal Toolbox (SMART) (MRI Institute for Biomedical Research, Detroit, MI). This software performed phase unwrapping using the 3D-SRNCP algorithm[52], background field removal by the SHARP algorithm[53] and susceptibility map generation using the SWIM algorithm[54]. The resulting QSM images were analyzed in Fiji[51]. Unless specified otherwise, all QSM images were processed from the 5$^{th}$ echo (TE = 45.0 ms) of a 3D MGE experiment.

**Gas vesicle clustering.** Purified Ana GVs were biotinylated using a $10^5$ molar excess of EZ-Link Sulfo-NHS-LC-biotin (Thermo Scientific, Rockford, IL) for 4 h in PBS buffer. The excess biotin was removed by two rounds of overnight dialysis in PBS buffer. Biotinylated or control GVs at $OD_{500,PS}$ = 10 were incubated with streptavidin (Geno Technology, St. Louis, MO) at the ratio specific to each experiment for 30 minutes at room temperature before loading into MRI phantom. Dynamic light scattering measurements were performed using a Zeta-PALS instrument (Brookhaven Instruments, Hotsville, NY) at a concentration equivalent to $OD_{500,PS}$ = 0.2 in PBS.

***In vitro* acoustic collapse.** Acoustic GV collapse was performed outside the MRI scanner for *in vitro* experiments. Multiplexing experiments were performed

with a single element immersion transducer (Olympus) with transmit frequency = 2.25 MHz, element size = 0.75 inch, focal length = 1.5 inch, pulse duration = 10 μs, duty cycle = 0.1%. A waveform generator (Model WS8352, Tabor Electronics, Tel Hanan, Israel) and a power amplifier (Model 3100LA, Electronics & Innovation, Rochester, NY) were used to drive the transducer. The input voltages to the transducer were 57 V and 131 V for collapsing $Ana_{\Delta C}$ and $Ana_{WT}$ GVs in the agarose phantom, respectively. The output peak positive pressures were estimated by a fiber optic hydrophone (Precision Acoustics, Dorchester, UK) to be 0.74 MPa and 1.41 MPa, respectively. For collapsing the intracellular GVs in *E. coli*, a Verasonics Vantage programmable ultrasound scanning system using the L11-4v 128-element linear array transducer (Verasonics, Kirkland, MA) was used with the following parameters: transmit frequency = 6.25 MHz, transmit voltage = 15 V.

Acoustic collapse curves were measured with ultrasound as described previously[13]. Briefly, $Ana_{\Delta C}$ at $OD_{500}$ = 1, $Ana_{WT}$ at $OD_{500}$ = 1, buoyancy-enriched A2C-expressing *E. coli* at $OD_{600}$ = 1, and clustered $Ana_{\Delta C}$ at $OD_{500}$ = 0.5 (measured prior to clustering) were prepared in agarose phantoms. An 128-element linear array transducer (L22-14v, Verasonics, Kirkland, MA) was used at f-number 2.0 to collapse GVs, and to determine the intact fraction via backscattered ultrasound signal intensity. A ray line script with 15.625 MHz transmit frequency was used for both collapsing GVs and acquiring ultrasound images. To achieve uniform collapse at each acoustic pressure, a mechanical motor system was used to move the transducer over a 6-mm vertical distance at the speed of 0.2 mm/sec for 6 repetitions to cover the depth of the agarose well. In addition to the imaging plane, two additional planes spaced ± 300 μm along the azimuth were subjected to acoustic collapse to ensure completeness. Transducer output pressure was calibrated by a fiber optic hydrophone (Precision Acoustics, Dorchester, UK).

***In vivo* injections, MRI and acoustic collapse.** All animal experiments were approved by the Institutional Animal Care and Use Committee (IACUC) of the California Institute of Technology. Animals were randomized between experimental groups; blinding was not necessary. Mice were anesthetized using 1-2.5% isoflurane in all the injection procedures. For intracranial injection, 2 μL PBS buffer with or without 3.4 nM $Ana_{WT}$ GVs was injected into the striatum or the thalamus of male C57BL6J mice between 12 and 18 weeks of age (Jackson Laboratory, Bar Harbor, ME) using a Nanofil blunt-end 35g needle coupled with a motorized pump (World Precision instruments, Sarasota, FL) at 100 nL/min using a stereotaxic frame (Kopf, Tujunga, CA). The coordinates of the two pairs of sites with respect to the

bregma were: +1 mm anterior-posterior, ±2 mm medio-lateral, -3.25 to -3.5 mm dorso-ventral and -2.5 mm anterior-posterior, ±1.5 mm medio-lateral, -3.25 mm dorso-ventral. The needles remained in place after injection for 5 minutes to avoid backflow along the needle tract. $OD_{500,PS}$ of the GV solution inside the syringe was measured post-injection to confirm GV integrity. For intravenous injection, female Nu/J mice 8-20 weeks of age (Jackson Laboratory, Bar Harbor, ME) were infused with 200 µL PBS buffer with or without clustered $Ana_{\Delta C}$ (13.7 nM, measured before clustering) using 29G syringe (BD, Franklin Lakes, NJ) at a flow rate of 75 µL/min. The mice were euthanized by cervical dislocation 1 minute after the end of infusion to enable imaging of the liver without respiratory motion artefacts. For multiplexing experiments, PBS solution containing clustered $Ana_{\Delta C}$ (13.7 nM, measured before clustering) or *E. coli* cells expressing A2C GVs ($OD_{600}$ = 150 measured without collapse) were chilled on ice and mixed 1:1 v/v with Matrigel HC (Corning Inc., Corning, NY), then injected subcutaneously into the lower abdomen of female Nu/J mice 8-20 weeks of age using 21G syringes in volumes of approximately 200 µl before live-animal imaging.

For imaging, live mice were anaesthetized using 1-2% isoflurane and were placed in an acrylic cradle where respiration and body temperature were continuously monitored using a pressure transducer (Biopac Systems) and fiber optic rectal thermometer (Neoptix). Warm air was circulated to maintain body temperature at 30°C. For brain imaging, a 72 mm diameter volume coil was used for RF transmission and a 30 mm diameter surface coil for detection. $T_2^*$-weighted images were acquired by 2D or 3D FLASH experiments with the following parameters: TE = 15.0 ms, TR = 50.6 ms, flip angle = 20°, FOV = 40 × 28 $mm^2$, spatial resolution = 0.1 × 0.1 $mm^2$, slice thickness = 1.0 mm and 64 averages (2D) or 64 averages and 1 average (3D). Anatomical images were acquired by 2D RARE experiments with the following parameters: effective TE = 19.98 ms, RARE factor = 8, TR = 300 ms, FOV = 140 × 512 $mm^2$, spatial resolution = 0.1 × 0.1 $mm^2$, slice thickness = 1.0 mm and 1 average. For liver imaging, 2D FLASH experiments were repeated at the rate of 1.9 sec per image with the following parameters: TE = 8.0 ms, TR = 23.4 ms, flip angle = 21°, FOV = 64 × 40 $mm^2$, spatial resolution = 0.5 × 0.5 $mm^2$, slice thickness = 2.5 mm and 1 averages. For multiplexing experiment, 3D MGE experiments were performed with the following parameters: TR = 46.8 ms, 8 echos, first echo time 3.66 ms, TE = 4.78 ms, FOV = 128 × 40 × 48 $mm^3$, spatial resolution = 0.5 × 0.5 × 0.5 $mm^3$ and 1 average. The $T_2^*$-weighted images from the $7^{th}$ echo (TE = 32.3 ms) were used to calculate the change of intensity upon acoustic collapse.

*In situ* collapse of GVs was achieved using an MRI-guided focused ultrasound system comprising an 8-channel signal generator, a motorized MRI-compatible transducer positioning system and an annular array transducer operating at 1.5 MHz (Image Guided Therapy, Pessac, France). For brain imaging, two ultrasound pulse schemes were used to transcranially collapse Ana GVs, with the following parameters: (1) pulse length (PL) = 10 µs, duty cycle = 0.01%, peak positive pressure (PPP) = 5.7 MPa, 10 to 200 shots; (2) PL = 50 ms, duty cycle = 5%, PPP = 3.0 MPa, 100 to 600 shots. Both schemes were capable of collapsing GVs and were tested for both the GV and the control PBS injection sites. For liver imaging, focused ultrasound pulses were applied at a single lateral position, with 5 axial spots 1 mm apart from each other (using electronic focusing without movement of the transducer) using the following parameters: PL = 10 µs, duty cycle = 0.1%, PPP = 2.3 MPa and 100 shots for each spot. For multiplexing experiments, regions of interest sized 3.5 x 5 mm or 5 mm x 5 mm laterally were insonated at an average lateral density of 7 focal spots per $mm^2$. Each lateral spot received 1 or 2 pulses at each of 6 different electronically focused axial depths, set apart by 1 mm. The pulse parameters were PL = 1 ms, duty cycle = 5%, PPP = 1.3 MPa for $Ana_{\Delta C}$ and PPP = 3.2 MPa for A2C. All PPPs were measured by a fibre optic hydrophone (Precision Acoustics, Dorset, UK) in degased water. 18% attenuation was assumed for the mouse skull[55] in brain imaging, and no attenuation was assumed for the other experiments.

Data analysis was performed in Fiji[51]. For brain imaging quantification, an elliptical ROI was manually drawn for the hypointense region containing GVs. Another concentric ROI with twice the radius was drawn, and the intensity of the region between the two ROI was used to measure the intensity of the background tissue. The intensity of the GV region normalized by the background was used to calculate the percentage contrast change upon ultrasound exposure. For liver imaging, a circular ROI of 1 mm in radius was drawn at the focal point of the ultrasound for quantification. To obtain the difference images, 50 frames of the 2D-imaging sequence acquired before and after ultrasound application were averaged, and the post-collapse average was subtracted from the pre-collapse average. For quantification, the average intensity change of the pixels within each ROI was divided by that of the post-collapse image, resulting in the percentage signal intensity change. For the multiplexing experiment, images acquired after ultrasound application (averages of 3 neighbouring planes reconstructed from 3D imaging) were subtracted from the immediately preceding images, and ROIs were drawn corresponding to the

insonated areas. To normalize the signal intensity of pre- and post-collapse images, the average intensity of the pixels in an oval area of 20 × 28 mm (width × length) that encompassed the majority of the mouse body was first subtracted from that in each ROI before the change of signal intensity within ROIs upon insonation was calculated. To obtain the percentage of the ΔΔ signal intensity, the average intensity change of the pixels within each ROI was divided by that of the post-collapse image, and the resulting percentage of Δ signal intensity of low-pressure insonation was subtracted by that of high-pressure insonation.

**Finite element simulations.** The magnetic field simulation was performed in Finite Element Method Magnetics (FEMM) version 4.2 (ref.[56]). GVs were simulated as an axisymmetric object with its longitudinal axis aligned parallel to the magnetic field. The ratio of the susceptibility between inside and outside ($\chi_{in}/\chi_{out}$) of the GVs was taken to be $1 + 9.395 \times 10^{-6}$, which corresponds to the susceptibility difference between air and water. For the inside of the cylindrical well, GVs were assumed to be homogenously distributed, and the ratio of the susceptibility between inside and outside of the well ($\chi_{in}/\chi_{out}$) was set to be $1 + 3.426 \times 10^{-8}$, which was the volume-weighted average for 0.36% air in water, the amount expected for 1 nM concentration of Ana GVs. Then the cylindrical well in an agarose phantom was simulated as a circle in a 2D planar domain. Similarly, the GV cluster was simulated as a single sphere in the axisymmetric domain occupying a volume equivalent of 200 GVs packed at 20% density and ($\chi_{in}/\chi_{out}$) of $1 + 1.879 \times 10^{-6}$ for 20% air. In all cases, the external field was set at 7.0 T to correspond to the experimental condition.

**Monte Carlo simulation for multiplexing accuracy.** The simulation was performed in MATLAB, with N = 100 points simulated for each condition. For simple acoustic multiplexing (Supplementary Fig. 5-S6a), the apparent concentration of each GV type was calculated from simulated data using the simple multiplexing assumptions that all GVs of type $\alpha$ were collapsed by low-pressure ultrasound, while all GVs of type $\beta$ were collapsed only by high-pressure ultrasound. Under this assumption of complete segregation, the molar concentration of the two types of GVs, $c_\alpha$ and $c_\beta$, was calculated as:

$$c_\alpha = \frac{\Delta\chi_{low}^{exp}}{\Delta\chi_{m,\alpha}}$$

$$c_\beta = \frac{\Delta\chi_{high}^{exp}}{\Delta\chi_{m,\beta}}$$

where $\Delta\chi_{m,\alpha}$ and $\Delta\chi_{m,\beta}$ were the molecular susceptibilities of GVs of types $\alpha$ and $\beta$ (Supplementary Table S1), and $\Delta\chi_{low}^{exp}$ and $\Delta\chi_{high}^{exp}$ were the simulated experimental

measurements of susceptibility change upon the application of low-pressure and high-pressure ultrasound. These values were simulated according to:

$$\Delta\chi_{low}^{exp} = \Delta\chi_{m,\alpha} * c_\alpha * (f_{\alpha,low} + \delta f_{\alpha,low}) + \Delta\chi_{m,\beta} * c_\beta * (f_{\beta,low} + \delta f_{\beta,low}) + \delta\chi_{low}$$

$$\Delta\chi_{high}^{exp} = \Delta\chi_{m,\alpha} * c_\alpha * (f_{\alpha,high} + \delta f_{\alpha,low}) + \Delta\chi_{m,\beta} * c_\beta * (f_{\beta,high} + \delta f_{\beta,low}) + \delta\chi_{high}$$

$f_{\alpha,low}$, $f_{\alpha,high}$, $f_{\beta,low}$ and $f_{\beta,high}$ were values corresponding to the fractions of GV types $\alpha$ and $\beta$ that were collapsed specifically upon the application of low- and high-pressure ultrasound with the assumption that $f_{\alpha,low} + f_{\alpha,high} = 1$ and $f_{\beta,low} + f_{\beta,high} = 1$, and $\delta f_{\alpha,low}$ and $\delta f_{\beta,low}$ were random numbers generated based on the standard deviations of the collapsed fractions of $Ana_{\Delta C}$ and $Ana_{WT}$ at low-pressure ultrasound (Fig. 5-5b), assuming high-pressure ultrasound was sufficiently strong to collapse all GVs. $\delta\chi_{low}$ and $\delta\chi_{high}$ were independent random numbers generated according to the standard deviation observed in regression fitting of $\Delta\chi$ measurements (Supplementary Fig. 5-S1a).

Note that, in reality, a fraction of GV type $\beta$ collapses at the low pressure, while a fraction of GV type $\alpha$ is left over to be collapsed at the high pressure, leading to a systematic error in the apparent concentration (Supplementary Fig. 5-S6a). This error can be reduced with linear spectral unmixing, which takes into account knowledge of the unique acoustic collapse profile of each GV type[13] (Supplementary Fig. 5-S6b). In this case, the apparent molar concentrations of the two types of GVs, $c_\alpha$ and $c_\beta$, are calculated as:

$$\begin{bmatrix} c_\alpha \\ c_\beta \end{bmatrix} = \begin{bmatrix} f_{\alpha,low} x \Delta\chi_{m,\alpha} & f_{\beta,low} x \Delta\chi_{m,\beta} \\ f_{\alpha,high} x \Delta\chi_{m,\alpha} & f_{\beta,high} x \Delta\chi_{m,\beta} \end{bmatrix}^{-1} \begin{bmatrix} \Delta\chi_{low}^{exp} \\ \Delta\chi_{high}^{exp} \end{bmatrix}.$$

Finally, for multiparametric multiplexing (Supplementary Fig. 5-S6c), the molar GV concentrations were calculated according to

$$\begin{bmatrix} c_\alpha \\ c_\beta \end{bmatrix} = \begin{bmatrix} r_{2,\alpha} & r_{2,\beta} \\ \Delta\chi_{m,\alpha} & \Delta\chi_{m,\beta} \end{bmatrix}^{-1} \begin{bmatrix} R_2^{exp} \\ \Delta\chi^{exp} \end{bmatrix}$$

where $r_{2,\alpha}$ and $r_{2,\beta}$ were $r_2$ relaxivities of GVs of types $\alpha$ and $\beta$, and $R_2^{exp}$ and $\Delta\chi^{exp}$ were the simulated experimental measurements of $R_2$ and susceptibility of the sample, simulated according to:

$$R_2^{exp} = c_\alpha x r_{2,\alpha} + c_\beta x r_{2,\beta} + \delta R_2$$

$$\chi^{exp} = c_\alpha * \chi_{m,\alpha} + c_\beta * \Delta\chi_{2,\beta} + \delta\chi_2$$

where $\delta\chi$ and $\delta R_2$ were normally distributed random numbers using standard deviations observed in $\Delta\chi$ and $R_2$ measurements. In simulating the multiplexing between Halo and Mega GVs, $\delta\chi$ and $\delta R_2$ represented weighted averages of the standard deviations for Halo and Mega GVs (Supplementary Fig. 5-S1) according to $c_\alpha$ (representing Halo GVs) and $c_\beta$ (representing Mega GVs).

**Statistical Analysis.** Sample sizes were chosen on the basis of preliminary experiments so as to have sufficient power for the reported statistical comparisons. Unless stated otherwise, statistical comparisons used two-tailed heteroscedastic *t*-tests with Welch's correction.

## References


1. Lu, G. J. *et al.* Acoustically modulated magnetic resonance imaging of gas-filled protein nanostructures. *Nature Materials* **17,** 456–463 (2018).

2. Caravan, P., Ellison, J. J., McMurry, T. J. & Lauffer, R. B. Gadolinium(III) Chelates as MRI Contrast Agents: Structure, Dynamics, and Applications. *Chemical Reviews* **99,** 2293–2352 (1999).

3. Weissleder, R. *et al.* Ultrasmall superparamagnetic iron oxide: characterization of a new class of contrast agents for MR imaging. *Radiology* **175,** 489–493 (1990).

4. Genove, G., DeMarco, U., Xu, H., Goins, W. F. & Ahrens, E. T. A new transgene reporter for in vivo magnetic resonance imaging. *Nat Med* **11,** 450–454 (2005).

5. Cohen, B., Dafni, H., Meir, G., Harmelin, A. & Neeman, M. Ferritin as an Endogenous MRI Reporter for Noninvasive Imaging of Gene Expression in C6 Glioma Tumors. *Neoplasia* **7,** 109–117 (2005).

6. Gilad, A. A. *et al.* Artificial reporter gene providing MRI contrast based on proton exchange. *Nat Biotech* **25,** 217–219 (2007).

7. Zhang, S., Merritt, M., Woessner, D. E., Lenkinski, R. E. & Sherry, A. D. PARACEST Agents: Modulating MRI Contrast via Water Proton Exchange. *Accounts of Chemical Research* **36,** 783–790 (2003).

8. Taratula, O. & Dmochowski, I. J. Functionalized $^{129}$Xe contrast agents for magnetic resonance imaging. *Current Opinion in Chemical Biology* **14,** 97–104 (2010).

9. Walsby, A. E. Gas vesicles. *Microbiological Reviews* **58,** 94–144 (1994).

10. Pfeifer, F. Distribution, formation and regulation of gas vesicles. *Nat Rev Micro* **10,** 705–715 (2012).

11. Li, N. & Cannon, M. C. Gas Vesicle Genes Identified in Bacillus megaterium and Functional Expression in Escherichia coli. *Journal of Bacteriology* **180,** 2450–2458 (1998).

12. Bourdeau, R. W. *et al.* Acoustic reporter genes for non-invasive imaging of microorganisms in mammalian hosts. *Nature* (2018).

13. Lakshmanan, A. *et al.* Molecular Engineering of Acoustic Protein Nanostructures. *ACS Nano* **10,** 7314–7322 (2016).

14. Puderbach, M. *et al.* MR imaging of the chest: A practical approach at 1.5 T. *European Journal of Radiology* **64,** 345–355 (2007).

15. Shapiro, M. G. *et al.* Biogenic gas nanostructures as ultrasonic molecular reporters. *Nat Nano* **9,** 311–316 (2014).

16. Terreno, E., Castelli, D. D., Viale, A. & Aime, S. Challenges for Molecular Magnetic Resonance Imaging. *Chemical Reviews* **110,** 3019–3042 (2010).

17. Shapiro, M. G. *et al.* Genetically encoded reporters for hyperpolarized xenon magnetic resonance imaging. *Nat Chem* **6,** 629–34 (2014).

18. Brown, R. W., Cheng, Y.-C. N., Haacke, E. M., Thompson, M. R. & Venkatesan, R. *Magnetic resonance imaging: physical principles and sequence design* ISBN: 1118633970 (John Wiley & Sons, 2014).

19. Haacke, E., Mittal, S., Wu, Z., Neelavalli, J. & Cheng, Y.-C. Susceptibility-Weighted Imaging: Technical Aspects and Clinical Applications, Part 1. *American Journal of Neuroradiology* **30,** 19–30 (2009).

20. Wang, Y. & Liu, T. Quantitative susceptibility mapping (QSM): Decoding MRI data for a tissue magnetic biomarker. *Magnetic Resonance in Medicine* **73,** 82–101 (2015).

21. Mukherjee, A., Davis, H. C., Ramesh, P., Lu, G. J. & Shapiro, M. G. Biomolecular MRI reporters: Evolution of new mechanisms. *Progress in Nuclear Magnetic Resonance Spectroscopy* **102-103,** 32–42 (2017).

22. Ahrens, E. T. & Bulte, J. W. M. Tracking immune cells in vivo using magnetic resonance imaging. *Nature Reviews: Immunology* **13,** 755–763 (2013).

23. Cunningham, C. H. *et al.* Positive contrast magnetic resonance imaging of cells labeled with magnetic nanoparticles. *Magnetic Resonance in Medicine* **53,** 999–1005 (2005).

24. Stuber, M. *et al.* Positive contrast visualization of iron oxide-labeled stem cells using inversion-recovery with ON-resonant water suppression (IRON). *Magnetic Resonance in Medicine* **58,** 1072–1077 (2007).

25. Mani, V., Briley-Saebo, K. C., Itskovich, V. V., Samber, D. D. & Fayad, Z. A. Gradient echo acquisition for superparamagnetic particles with positive contrast (GRASP): Sequence characterization in membrane and glass superparamagnetic iron oxide phantoms at 1.5T and 3T. *Magnetic Resonance in Medicine* **55,** 126–135 (2006).

26. Bulte, J. W. *et al.* Quantitative "Hot Spot" Imaging of Transplanted Stem Cells using Superparamagnetic Tracers and Magnetic Particle Imaging (MPI). *Tomography* **1,** 91–97 (2015).

27. Gleich, B. & Weizenecker, J. Tomographic imaging using the nonlinear response of magnetic particles. *Nature* **435,** 1214–1217 (2005).

28. Goodwill, P. W. *et al.* X-Space MPI: Magnetic Nanoparticles for Safe Medical Imaging. *Advanced Materials* **24,** 3870–3877 (2012).

29. Ahrens, E. T., Flores, R., Xu, H. & Morel, P. A. In vivo imaging platform for tracking immunotherapeutic cells. *Nat Biotech* **23,** 983–987 (2005).

30. Jolesz, F. A. MRI-Guided Focused Ultrasound Surgery. *Annual Review of Medicine* **60,** 417–430 (2009).

31. Gandhi, S. N., Brown, M. A., Wong, J. G., Aguirre, D. A. & Sirlin, C. B. MR Contrast Agents for Liver Imaging: What, When, How. *RadioGraphics* **26,** 1621–1636 (2006).

32. Donaldson, G. P., Lee, S. M. & Mazmanian, S. K. Gut biogeography of the bacterial microbiota. *Nat Rev Microbiol* **14,** 20–32 (2016).

33. Milo, R., Jorgensen, P., Moran, U., Weber, G. & Springer, M. BioNumbers—the database of key numbers in molecular and cell biology. *Nucleic Acids Research* **38,** D750–D753 (2010).

34. McMahon, M. T. *et al.* New "multicolor" polypeptide diamagnetic chemical exchange saturation transfer (DIACEST) contrast agents for MRI. *Magnetic Resonance in Medicine* **60,** 803–812 (2008).

35. Yablonskiy, D. A. & Haacke, E. M. Theory of NMR signal behavior in magnetically inhomogeneous tissues: The static dephasing regime. *Magnetic Resonance in Medicine* **32,** 749–763 (1994).

36. Hung, A. H., Lilley, L. M., Hu, F., Harrison, V. S. & Meade, T. J. Magnetic barcode imaging for contrast agents. *Magnetic resonance in medicine* (2016).

37. Perez, J. M., Josephson, L., O'Loughlin, T., Hogemann, D. & Weissleder, R. Magnetic relaxation switches capable of sensing molecular interactions. *Nat Biotech* **20,** 816–820 (2002).

38. Zabow, G., Dodd, S. J. & Koretsky, A. P. Shape-changing magnetic assemblies as high-sensitivity NMR-readable nanoprobes. *Nature* **520,** 73–U157 (2015).

39. Shapiro, M. G. *et al.* Directed evolution of a magnetic resonance imaging contrast agent for noninvasive imaging of dopamine. *Nat Biotech* **28,** 264–270 (2010).

40. Atanasijevic, T., Shusteff, M., Fam, P. & Jasanoff, A. Calcium-sensitive MRI contrast agents based on superparamagnetic iron oxide nanoparticles and calmodulin. *Proceedings of the National Academy of Sciences* **103,** 14707–14712 (2006).

41. Shapiro, M. G., Szablowski, J. O., Langer, R. & Jasanoff, A. Protein Nanoparticles Engineered to Sense Kinase Activity in MRI. *Journal of the American Chemical Society* **131,** 2484–2486 (2009).

42. Brooks, R. A., Moiny, F. & Gillis, P. On T2-shortening by weakly magnetized particles: The chemical exchange model. *Magnetic Resonance in Medicine* **45,** 1014–1020 (2001).

43. Gillis, P. & Koenig, S. H. Transverse relaxation of solvent protons induced by magnetized spheres: Application to ferritin, erythrocytes, and magnetite. *Magnetic Resonance in Medicine* **5,** 323–345 (1987).

44. Matsumoto, Y. & Jasanoff, A. T2 relaxation induced by clusters of superparamagnetic nanoparticles: Monte Carlo simulations. *Magnetic Resonance Imaging* **26,** 994–998 (2008).

45. Jaffer, F. A., Libby, P. & Weissleder, R. Molecular and Cellular Imaging of AtherosclerosisEmerging Applications. *Journal of the American College of Cardiology* **47,** 1328–1338 (2006).

46. Barrett, T., Brechbiel, M., Bernardo, M. & Choyke, P. L. MRI of tumor angiogenesis. *Journal of Magnetic Resonance Imaging* **26,** 235–249 (2007).

47. Li, Z. *et al.* Comparison of Reporter Gene and Iron Particle Labeling for Tracking Fate of Human Embryonic Stem Cells and Differentiated Endothelial Cells in Living Subjects. *Stem Cells* **26,** 864–873 (2008).

48. Lakshmanan, A. *et al.* Preparation of biogenic gas vesicle nanostructures for use as contrast agents for ultrasound and MRI. *Nature protocols* **12,** 2050 (2017).

49. Strunk, T. *et al.* Structural model of the gas vesicle protein GvpA and analysis of GvpA mutants in vivo. *Molecular Microbiology* **81,** 56–68 (2011).

50. Shaner, N. C. *et al.* A bright monomeric green fluorescent protein derived from Branchiostoma lanceolatum. *Nature methods* **10,** 407 (2013).

51. Schindelin, J. *et al.* Fiji: an open-source platform for biological-image analysis. *Nat Meth* **9,** 676–682 (2012).

52. Abdul-Rahman, H. S. *et al.* Fast and robust three-dimensional best path phase unwrapping algorithm. *Applied optics* **46,** 6623–6635 (2007).

53. Schweser, F., Deistung, A., Lehr, B. W. & Reichenbach, J. R. Quantitative imaging of intrinsic magnetic tissue properties using MRI signal phase: An approach to in vivo brain iron metabolism? *NeuroImage* **54,** 2789–2807 (2011).

54. Tang, J., Neelavalli, J., Liu, S., Cheng, Y.-C. N. & Haacke, E. M. in *Susceptibility Weighted Imaging in MRI* 461–485 (John Wiley & Sons, Inc., 2011).

55. Choi, J. J., Pernot, M., Small, S. A. & Konofagou, E. E. Noninvasive, transcranial and localized opening of the blood-brain barrier using focused ultrasound in mice. *Ultrasound in Medicine & Biology* **33,** 95–104 (2007).

56. Meeker, D. Finite element method magnetics. *FEMM* **4,** 32 (2010).

57. Gillis, P., Moiny, F. & Brooks, R. A. On T2-shortening by strongly magnetized spheres: a partial refocusing model. *Magnetic Resonance in Medicine* **47,** 257–263 (2002).

58. Jensen, J. & Chandra, R. NMR relaxation in tissues with weak magnetic inhomogeneities. *Magnetic Resonance in Medicine* **44,** 144–156 (2000).

59. Bowen, C. V., Zhang, X., Saab, G., Gareau, P. J. & Rutt, B. K. Application of the static dephasing regime theory to superparamagnetic iron-oxide loaded cells. *Magnetic Resonance in Medicine* **48,** 52–61 (2002).

## 5.6 Supplementary Information

**Theoretical consideration of the $T_2$/$T_2^*$ relaxation produced by gas vesicles.** Relaxation theory[35,42–44,57–59] describes the $T_2$/$T_2^*$ relaxation of water near a contrast agent in three primary regimes: (1) the motional averaging regime, where $\Delta\omega_r \cdot \tau_D \ll 1$; (2) the static dephasing regime, where $\Delta\omega_r \cdot \tau_D \gg 1$; and (3) the intermediate regime, where $\Delta\omega_r \cdot \tau_D \sim 1$. Here $\Delta\omega_r$ is the root-mean-square frequency shift at the surface of the contrast agent and $\tau_D$ is the time for a water molecule to diffuse across the distance of the contrast agent's radius. Considering a single gas vesicle (GV) at high field (Fig. 5-1b), we obtain $\Delta\omega_r \approx \Delta\chi \cdot \gamma B_0 \approx 10^3 Hz$ and $\tau_D \approx 10^{-6} sec$; therefore $T_2$/$T_2^*$ relaxation on the nanoscale (*e.g.*, everywhere inside an agarose well containing GVs) occurs in the motional averaging regime. At the same time, the macroscale $\Delta$B field around a millimetre-sized agarose well containing GVs (at a volume fraction of 0.01%) (Fig. 5-1d) has a predicted $\Delta\omega_r \approx 10^{-1} Hz$ and $\tau_D \approx 10^3 sec$, resulting in $T_2$/$T_2^*$ relaxation in the static dephasing regime.

These relaxation regimes are manifest in the $T_2$-weighted and $T_2^*$-weighted images shown in Supplementary Fig. 5-S1. The spin relaxation at the centre of the well is predominantly a result of the nanoscale $\Delta$B field, while the spin relaxation near the rim of the wells results from the macroscale $\Delta$B field. The rim usually appears darker than the centre of the well in $T_2^*$-weighted images because of the more efficient relaxation of water $^1$H in the static dephasing regime than in the motional averaging regime. On the other hand, the rim of the wells lacks hypointense contrast in $T_2$-weighted images, since $\pi$ pulses can effectively refocus the dephasing of $^1$H spins in the static dephasing regime.

Relaxation theory also sheds light on the behaviour of clustered GVs. The micron-size GV clusters are predicted to have $\tau_D \approx 10^{-3} sec$ and are therefore shifting the water $^1$H relaxation from the motional averaging regime to the intermediate regime, resulting in strong enhancement of both $T_2^*$ and $T_2$ relaxation (Fig. 5-6).

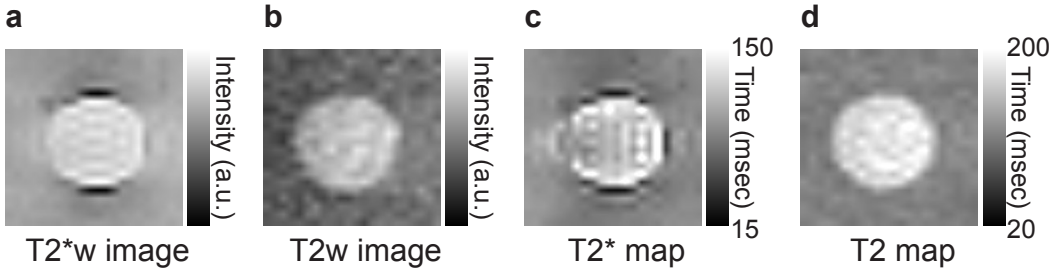


**Figure 5-S1: Representative images of GV-containing well in the agarose phantom**. a, $T2^*$-weighted ($T2^*w$) and b, T2-weighted (T2w) images at echo time TE = 45 msec. c, $T2^*$ and T2 map, where pixel-wise $T2/T2^*$ relaxation times are plotted. The rim of the wells is marked by the hypointense contrast in the T2*w image and $T2^*$ map (a, c) and the absence of the contrast in the T2w image and T2 map (b, d). In all the images, $B_0$ fields are along the vertical direction, and the well contained 1.42 nM Halo GVs.

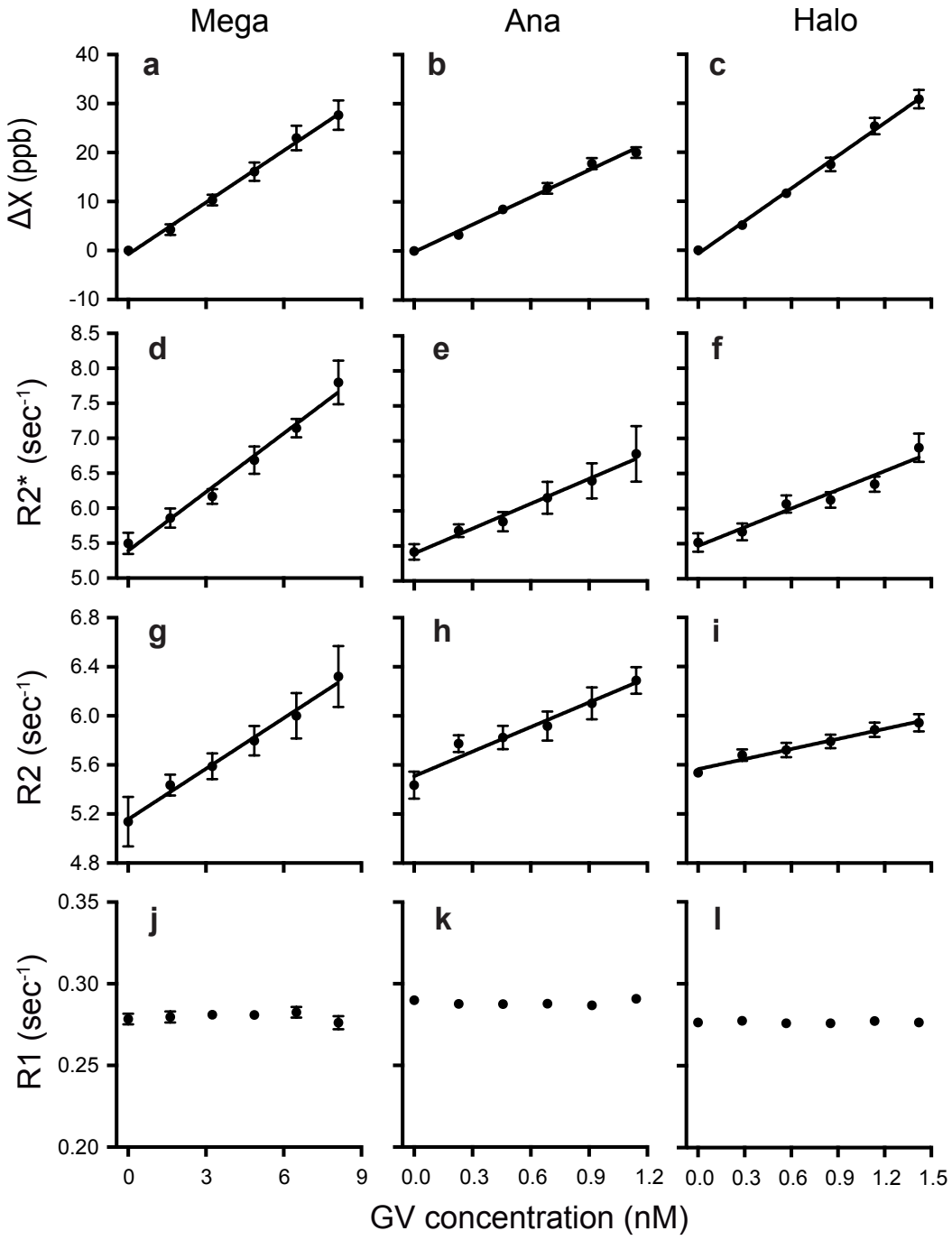


**Figure 5-S2: Molar magnetic susceptibility and T2*, T2 and T1 relaxivities of the three types of GVs used in this study.** a-c, susceptibility in the unit of parts per billion (ppb), d-f, T2* relaxometry, g-i, T2 relaxometry and j-l T1 relaxometry measurements on GVs from *Bacillus megaterium* (Mega, a, d, g, j), *Anabaena flos-aquae* (Ana, b, e, h, k) and *Halobacterium salinarum* (Halo, c, f, i, l). Error bars represent SEM. N = 9 independent samples for all susceptibility and R2* measurements. For T2 and T1 measurements, N = 6 independent samples for Mega and Ana GVs and N = 9 for Halo GVs. Relaxivity values calculated from linear regression fitting of the slope are listed in Supplementary Table 5-S1.

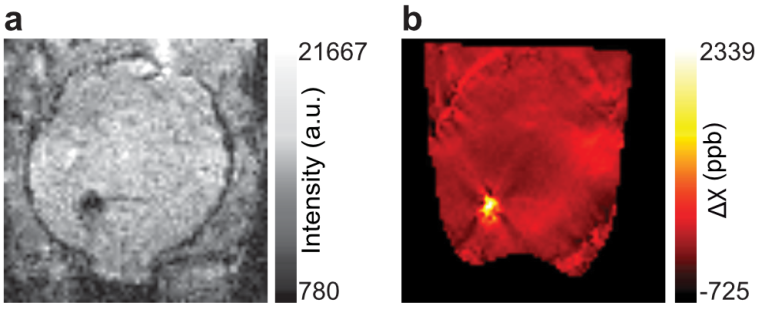


**Figure 5-S3: Quantitative susceptibility mapping (QSM) of GV contrast *in vivo*.** a, $T2^*$-weighted image of a coronal slice from a 3D multi gradient echo (MGE) image of the mouse brain. The hypointense contrast inside the brain tissue corresponds to the site of GV injection. b, The same slice rendered from QSM processing of the 3D image.

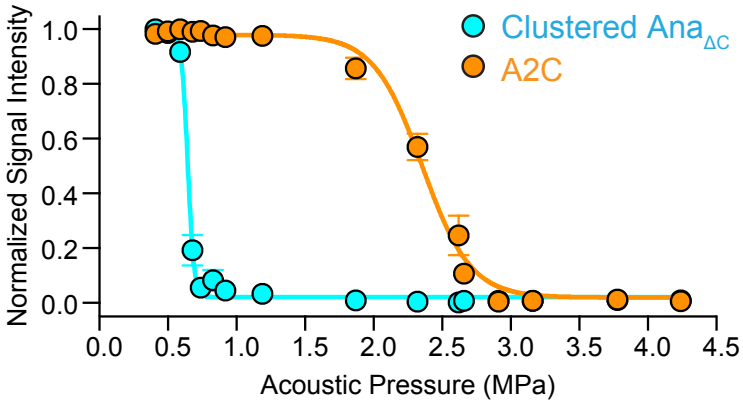


**Figure 5-S4: Acoustic collapse measurement of clustered $Ana_{\Delta C}$ and *E. coli* expressing A2C GVs.** Ultrasound images were acquired after sequentially exposing the samples to insonation at increasing acoustic pressures, and the collapse of GVs were monitored as a decrease of the image intensity. N = 3 independent samples, and the error bars represent SEM. Sigmoidal collapse curve was obtained by nonlinear least-square fitting.

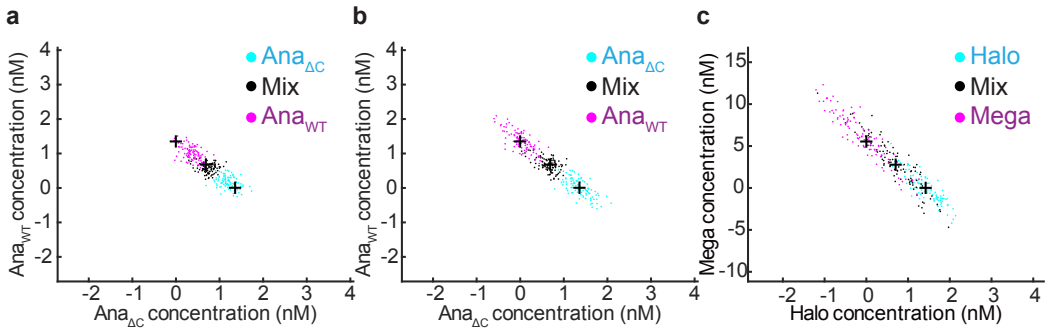


**Figure 5-S5: Monte Carlo simulation of error distributions in the two multiplexing methods.** a-b, Simulated distribution of apparent GV concentrations calculated by (a) simple acoustic multiplexing or (b) acoustic multiplexing with the help of spectral unmixing, based on experimental values in Fig. 5-5c-d. c, Simulated distribution of apparent GV concentrations by multiparametric multiplexing using the inputs derived from the experimentally measured values in Fig. 5-6b-c. Black plus signs represent true values of GV concentrations, and individual dots (magenta, cyan or black) represent individual simulations with randomized input of errors. Details of the simulation are provided in Methods.

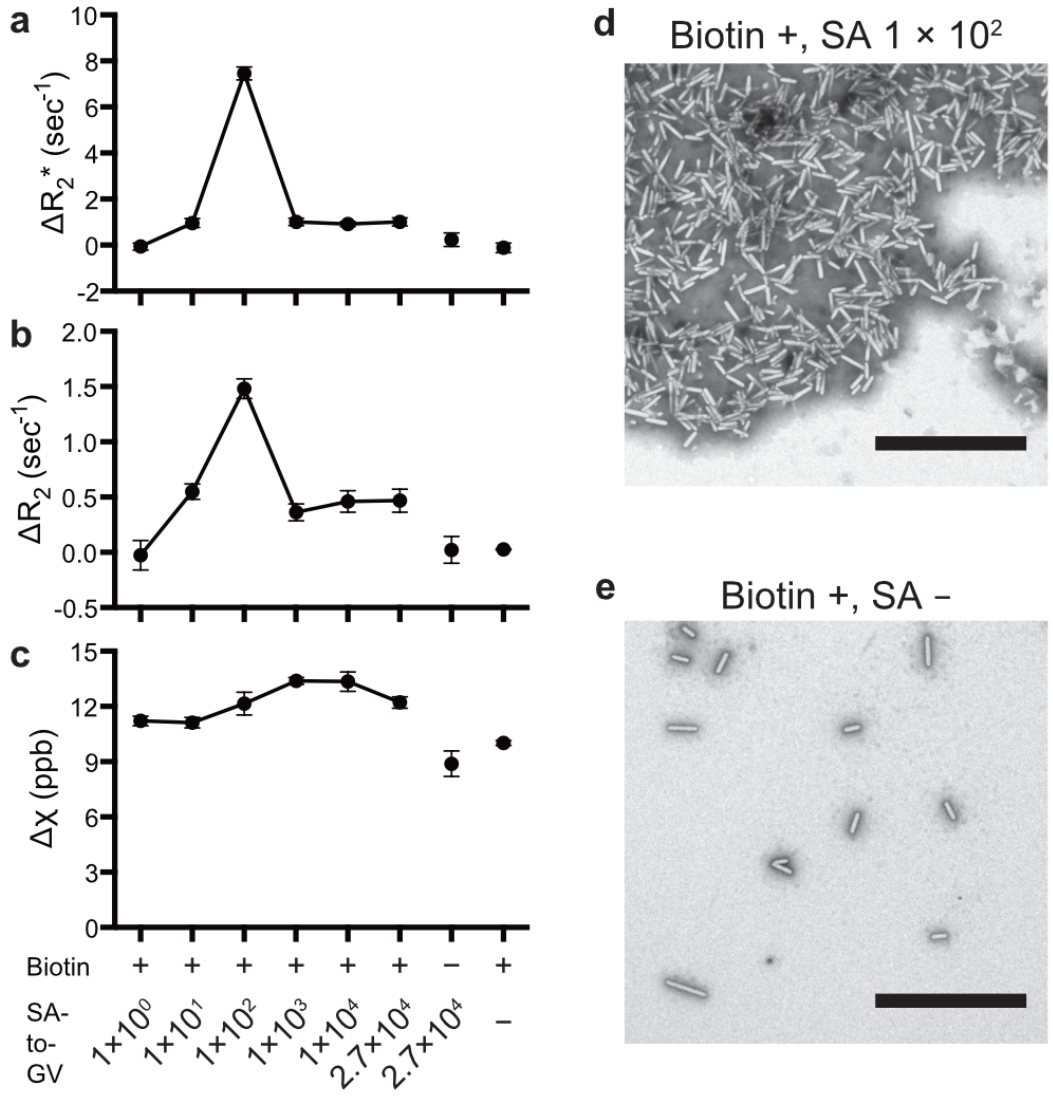


**Figure 5-S6: Impact of streptavidin to gas vesicle (SA-to-GV) stoichiometry on T2/T2* relaxation.** a-c, $\Delta R2^*$, $\Delta R2$ and $\Delta\chi$, respectively, of samples with various SA-to-GV ratios and the two control samples that lack either SA or biotin. The SA-to-GV ratios are listed below the graph, and the values of susceptibility are relative to sample containing PBS buffer. N = 3 independent samples. Error bars represent SEM. d, e, Representative TEM images of clustered and unclustered GV, respectively. A large number of GVs were observed inside each cluster, while the clusters were distributed much more sparsely than single GVs on the TEM grid. Scale bars represent 4 μm.

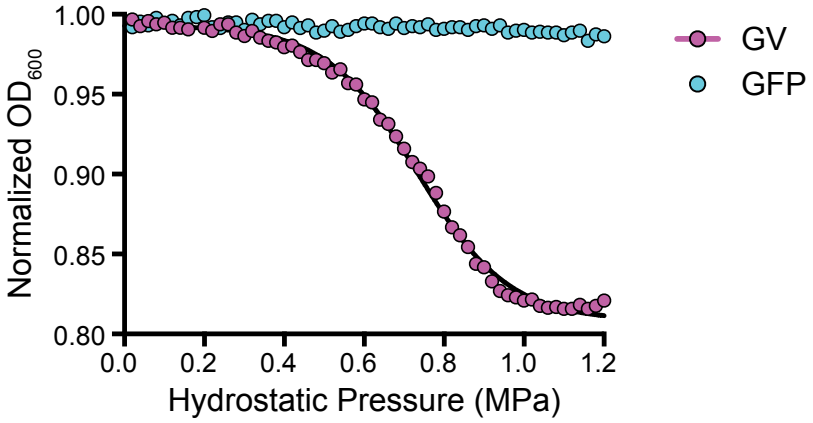


**Figure 5-S7: Representative hydrostatic collapse measurement of *E. coli* cells.** *E. coli* cells at optical density at 600 nm ($OD_{600}$) ~ 1.0 were loaded into a sealed cuvette with path length 1.00 cm. Hydrostatic pressure was ramped stepwise from 0 to 1.2 MPa and $OD_{600}$ was recorded in each step. Cells expressing A2C GVs (magenta) showed a sigmoidal drop in $OD_{600}$, characteristic of the collapse of intracellular GV. Cells that do not contain GV, such as those expressing the green fluorescent protein (GFP), did not show a drop in $OD_{600}$. The ratios of post- to pre-collapse optical density were between 0.806 and 0.853 (N = 6 independent samples), and the post-collapse $OD_{600}$ of each sample was used for quantifying cell density for preparing MRI phantoms.

| | Mega | Ana | Halo |
|---|---|---|---|
| **GV geometry** | | | |
| Length (nm) | 249 ± 13 | 519 ± 15 | 400 ± 10 |
| Width (nm) | 72.5 ± 1.7 | 136.3 ± 2.0 | 250.8 ± 4.6 |
| Number of particles measured | N=61 | N=107 | N=125 |
| **GV concentration relationships** | | | |
| Protein concentration to $OD_{500}$ ratio ([μg/mL] / OD) | 145.5 ± 6.4 | 36.6 ± 2.6 | 13.4 ± 2.2 |
| Estimated molecular weight (MDa) | 71.7 | 320 | 282 |
| Molar protein concentration to $OD_{500}$ ratio (pM / OD) | 2,030 | 114 | 47.3 |
| **GV MRI properties** | | | |
| Molar susceptibility (ppb / nM) | 3.52 ± 0.27 | 18.53 ± 0.91 | 22.2 ± 1.0 |
| Mass susceptibility (ppb / [mg/mL]) | 39.2 ± 3.0 | 57.2 ± 2.8 | 80.9 ± 3.8 |
| Relaxivity r2* ($sec^{-1}$ / nM) | 0.280 ± 0.027 | 1.19 ± 0.23 | 0.89 ± 0.11 |
| Relaxivity r2* ($sec^{-1}$ / [mg/mL]) | 3.11 ± 0.30 | 3.66 ± 0.71 | 3.24 ± 0.42 |
| Relaxivity r2 ($sec^{-1}$ / nM) | 0.138 ± 0.023 | 0.67 ± 0.11 | 0.273 ± 0.045 |
| Relaxivity r2 ($sec^{-1}$ / [mg/mL]) | 1.53 ± 0.26 | 2.06 ± 0.34 | 1.00 ± 0.16 |

**Table 5-S1: Summary of the geometrical, optical and magnetic properties of three types of gas vesicles (GVs).** Although the size and shape of GVs are determined primarily by the genotype, each type possesses certain degree of heterogeneity. For example, Ana GVs has length distribution with a standard deviation of 35% of the mean[10]. Errors of GV geometry represent SEM. The protein concentrations of GVs were measured by Pierce 660 nm protein assay (N = 4, 5, 3 measurements of independent samples of Mega, Ana and Halo GVs, respectively). Molar susceptibility and relaxivity correspond to the slopes from linear regression fitting of the MRI measurements in Supplementary Fig. 5-S2, and the errors are the standard error of the slope. $r2^*$ relaxivity was quantified from the center of the agarose wells and excluded the high contrast at the rim of the wells (Supplementary Figure 5-1).

| | ΔX (ppb) | | ΔR2* ($sec^{-1}$) | | ΔR2 ($sec^{-1}$) | |
|---|---|---|---|---|---|---|
| | Before US | After US | Before US | After US | Before US | After US |
| GV + IPTG | 1.93 ± 0.31 | −2.73 ± 0.26 | 0.97 ± 0.13 | 0.45 ± 0.08 | 0.65 ± 0.03 | 0.34 ± 0.04 |
| GFP + IPTG | −1.97 ± 0.36 | −1.82 ± 0.39 | 0.32 ± 0.10 | 0.50 ± 0.09 | 0.28 ± 0.04 | 0.26 ± 0.04 |
| GV | −2.75 ± 0.17 | −2.00 ± 0.19 | 0.34 ± 0.10 | 0.29 ± 0.03 | 0.35 ± 0.05 | 0.33 ± 0.05 |
| PBS | 0 ± 0.14 | 0 ± 0.16 | 0 ± 0.09 | 0 ± 0.04 | 0 ± 0.02 | 0 ± 0.03 |

**Table 5-S2: MRI measurements of *E. coli* in agarose phantom.** All the values were normalized by those of PBS samples. Errors represent SEM, and N = 6 independent samples.

*Chapter 6*

# GENETICALLY ENCODED PHASE CONTRAST AGENTS FOR DIGITAL HOLOGRAPHIC MICROSCOPY

This chapter is in large part a reformatted version of the manuscript entitled "Genetically Encoded Phase Contrast Agents for Digital Holographic Microscopy" by Farhadi, A., Bedrossian, M., Lee, J., Ho, G.H., Shapiro, M.G., Nadeau, J.L. currently under peer-review[1]. Under the supervision of Mikhail Shapiro and Jay L. Nadeau, Manuel Bedrossian and I contributed equally to this work. Manuel, Mikhail, Jay and I conceived and planned the experiments. With the help of Justin Lee and Gabrielle Ho, I prepared the biological samples. I assisted Manuel and Jay collect the digital holographic data. All the authors analyzed the data. Manuel, Mikhail, Jay and I wrote the manuscript with input from all authors.

## 6.1 Abstract

Quantitative phase imaging and digital holographic microscopy have shown great promise for visualizing the motion, structure and physiology of microorganisms and mammalian cells in three dimensions. However, these imaging techniques currently lack molecular contrast agents analogous to the fluorescent dyes and proteins that have revolutionized fluorescence microscopy. Here we introduce the first genetically encodable phase contrast agents based on gas vesicles, a unique class of air-filled protein nanostructures derived from buoyant microbes. The relatively low index of refraction of the air-filled core of gas vesicles results in optical phase advancement relative to aqueous media, making them a "positive" phase contrast agent easily distinguished from organelles, dyes, or microminerals. We demonstrate this capability by identifying and tracking the motion of gas vesicles and gas vesicle-expressing bacteria using digital holographic microscopy, and by imaging the uptake of engineered gas vesicles by mammalian cells. These results give phase imaging a biomolecular contrast agent, greatly expanding the capabilities of this powerful technology for three-dimensional biological imaging.

## 6.2 Introduction

Precise acquisition of 4-dimensional data, comprising spatial coordinates and time, is important for studying many microscopic processes in biology. However, conventional optical microscopy suffers from a narrow depth of field due to its reliance on focusing lenses to encode spatial depth. Volumetric information is only obtained through step-wise acquisition of points or planes, and the resulting sequential acquisition typically necessitates low resolution in at least one of the 4 dimensions. Digital holographic microscopy (DHM), an inherently volumetric recording technique, provides an alternative for instantaneous sampling of thick volumes. Successful applications have been made to studies of microbial motility, chemotaxis, flow of ions through ion channels, and migration of cancer cells[2–8].

With DHM, optical interferometry is used to record a series of holograms at frame rates limited only by the camera. Off-line reconstruction yields plane-by-plane images of image intensity (brightfield) and phase. In DHM, as in other forms of quantitative phase imaging (QPI), phase contrast at any point $x$, $y$ is related to the difference in indices of refraction between the medium ($n_m$) and objects in the light path ($n_c$) multiplied by the object height $h$[9]:

$$\Delta\phi = \frac{2\pi}{\lambda} h(x, y)(n_m - n_c(x, y)).$$

Because the typical values of $n_c$ for the cytoplasm and organelles are approximately 1.38, which is very close to the $n_m$ of 1.33 for water, it is challenging for DHM to visualize cells, particularly when they are small[10]. This challenge could be overcome with suitable contrast agents or reporter genes, which would make cells more visible or highlight subcellular features and processes. In fluoresce microscopy, this function is provided by targeted small-molecule dyes and fluorescent proteins, which have revolutionized the utility of this technique in biological research[11–14]. Unfortunately, these same molecules are not effective as phase contrast agents due to their small refractive index difference relative to $H_2O$ and its similarity to other intracellular materials[15–19]. An ideal phase contrast agent would have a more dramatically different index of refraction, and preferably one that is lower than that of $H_2O$ to be categorically distinguishable from other cellular components.

Here we introduce genetically encodable contrast agents for phase imaging. These contrast agents are based on a unique class of hollow protein nanostructures called gas vesicles (GVs). GVs are all-protein nanostructures natively expressed in a number of waterborne microorganisms as a means to regulate their buoyancy[20,21]. GVs are air-filled compartments with dimensions on the order of 200 nm, enclosed

by a 2 nm-thick protein shell (Fig. 6-1a), which is permeable to dissolved gas but prevents water from condensing into a liquid in the GV core. GVs have previously been described as contrast agents for ultrasound[22] and magnetic resonance imaging[23–25], but have not been applied to optical microscopy. Recently, the genes encoding GVs have been heterologously expressed in commensal bacteria (e.g. *Escherichia coli* Nissle 1917 and *Salmonella typhimurium*)[24,26] and mammalian cells[27].

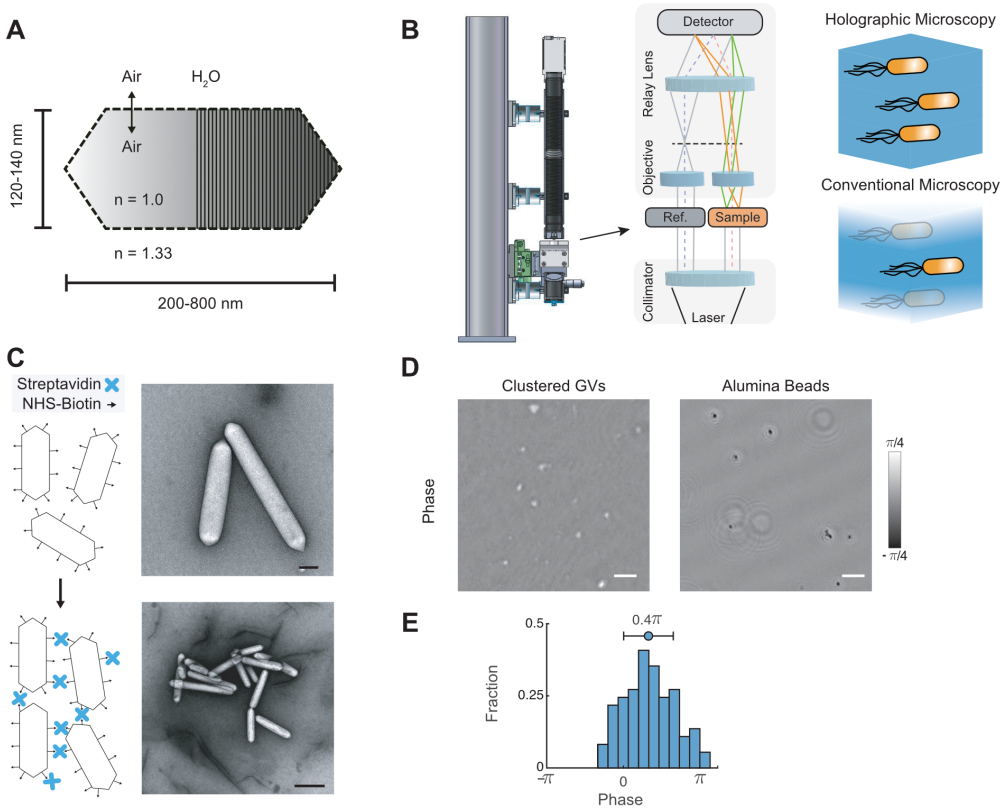


**Figure 6-1: Gas vesicles as phase contrast agents.** (a) Schematic of a single GV, indicating the index of refraction, $n$, inside the GV and in typical aqueous media. (b) Schematic of common path DHM system used in this work, and an illustration of the inherent volumetric imaging of DHM compared to conventional microscopy. (c) Biotinylated GVs purified from *Anabaena flos-aquae* can be clustered using streptavidin. Shown are a schematic and representative transmission electron micrograph of biotinylated GVs (top) and clustered GVs (bottom). Scale bars 100 nm and 500 nm, respectively. (d) Representative DHM images of clustered GVs and alumina beads. Scale bars represent 10 μm. (e) Histogram of phase change observed from clustered GVs with apparent diameters from 0.6-2.2 μm.

In this work, we test the hypothesis that the large difference in the index of refraction of GVs' gaseous interior ($n = 1.0$) relative to water and cytoplasm would produce strong positive phase contrast. We use a DHM system capable of providing sub-micron resolution to visualize the phase contrast produced by purified

GVs, allowing 4-dimensional tracking of their motion. In addition, we show that *S. typhimurium* cells expressing GVs as a genetically encoded reporter produce a unique pattern of phase contrast reflecting the sub-cellular distribution of these nanostructures. Furthermore, we demonstrate the use of GVs as targeted molecular contrast sources in mammalian cells by visualizing the uptake of engineered GVs into a mammalian cell line. This work establishes GVs as a tool for molecular and genetically encodable phase contrast, greatly expanding the utility of DHM and related methods.

### 6.3 Results and Discussions

**Gas vesicles produce positive phase contrast.** To establish the ability of GVs to produce phase contrast, we imaged GVs purified from *Anabaena flos-aquae*. These nanostructures are approximately 120-140 nm wide and 200-800 nm long as measured by transmission electron microscopy (TEM) (Fig. 6-1a). Individually, purified GVs were too small to resolve on our DHM system, which uses numerical aperture (NA) of 0.3 aspheric lenses to achieve a spatial resolution of 0.8 μm (Fig. 6-1b). We therefore assembled GV clusters by biotinylation of the GVs followed by the addition of streptavidin. This yielded clusters with hydrodynamic diameters of 690±56 nm (Fig. 6-1c and Supplemental Fig. 6-S1). Holograms were collected of GV clusters and of comparably sized alumina beads (1524±470 nm diameter as measured by dynamic light scattering) suspended in phosphate-buffered saline (PBS). We reconstructed these holograms into phase images as described in the supplementary text and Supplemental Fig. 6-S2. The phase shifts from the GV clusters and alumina beads were opposite in sign, with the GV clusters exhibiting positive phase contrast, while the alumina beads exhibited negative phase contrast (Fig. 6-1d). The average phase shift produced by the GV clusters was $0.4\pm0.32\pi$ (Fig. 6-1e). GV phase contrast could be erased by irreversibly collapsing the GVs with hydrostatic pressure[28], providing a convenient internal control. After collapse, the positive phase contrast of GVs was eliminated (Supplemental Fig. 6-S3).

Having established GVs as phase contrast agents, we sought to determine if DHM could be used to distinguish them and track their motion in a mixed particle population. First, we tracked the motion of both GV clusters and alumina beads in a 1 mm-deep well. The average speed of GV clusters rising along the depth axis due to their buoyancy was $0.43\pm0.58$ $\mu$m s$^{-1}$ (95% C.I.) (Fig. 6-2a-c), while alumina beads sank with an average speed of $-0.47\pm1.02$ $\mu$m s$^{-1}$ (95% C.I.) (Fig. 6-2d-f). When GV clusters and alumina beads were mixed together and tracked, the

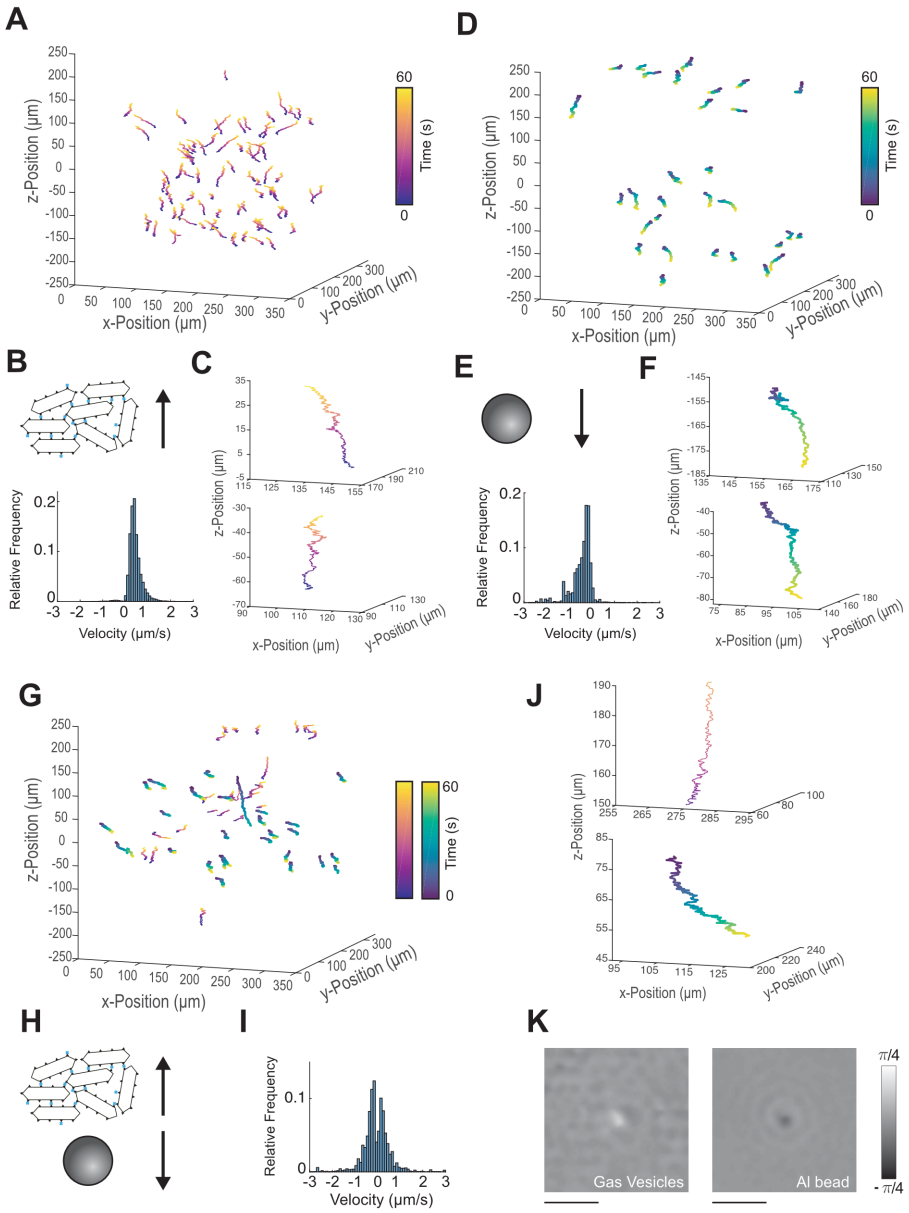


**Figure 6-2: Volumetric tracking of particles in a mixed population suspension.** (a) 3D trajectory plots of tracked GVs over 60 seconds. (b) Clustered GVs rise in solution (Top). Histogram of the z-component velocities of clustered GVs (Bottom). (c) Two example 3D tracks of clustered GVs. Each trajectory is color-coded with respect to time. (d) 3D trajectory plots of tracked alumina beads over 60 seconds. (e) Alumina beads sink over time (Top). Histogram of z-component velocities of alumina particles (Bottom). (f) Two example 3D tracks of alumina beads. Each trajectory is color-coded with respect to time. (g) 3D trajectory plots of the mixed population over 60 seconds. (h) Mixed population of clustered GVs and alumina beads. (i) Velocity histograms show two velocity populations, one for GVs and another for alumina beads. (j) Example trajectory of a rising and another of sinking particle chosen at random from (g). (k) Phase images of the two particles from (j). The buoyant particle has a positive phase contrast while the particle sinking has a negative phase contrast. Scale bars represent 5 µm.

two particle types were readily distinguished (Fig. 6-2g-j), with the particles that were rising having positive phase contrast and the particles that were sinking having negative phase contrast (Fig. 6-2k). This demonstrated the ability of GVs to serve as a categorical contrast agent for 4-dimensional DHM.

**Engineered gas vesicles serve as targeted contrast agents.** Among the advantages of GVs as phase contrast agents is their ability to be genetically engineered to modify their surface biochemical properties and enable molecular targeting[28,29]. To demonstrate that engineered, targeted GVs could be used for phase imaging in living cells, we used a fusion of the *A. flos-aquae* sequence to a polyarginine (R8) peptide. This peptide is a mimic of the human immunodeficiency virus 1 trans-activating (HIV-1 TAT) peptide and allows tagged proteins and particles to penetrate into mammalian cells (Fig. 6-3a)[30]. Polyarginine-modified GVs were purified and added to Chinese hamster ovary (CHO) cells at 114 pM for 45 minutes, washed and imaged by a DHM system. This allowed for rapid 3-dimensional reconstruction of GV location on the surface of and within the cells (Fig. 6-3b & 6-3c). GVs were fluorescently labeled with Alexa Fluor 488-NHS ester dyes to independently confirm the location of GV labeling on the cells (Fig. 6-3d & 6-3e). These experiments demonstrate the ability of GVs to label living cells for 3-dimensional phase imaging.

**Gas vesicles as genetically expressed contrast agents in *Salmonella typhimurium*.** Following the characterization of GVs as targeted DHM contrast agents, we tested the ability of genetically encoded GVs to act as phase contrast reporter genes in living bacteria. A recently developed gene cluster encoding GVs, comprising a combination of genes from *Anabaena flos-aquae* and *Bacillus megaterium*[26], was used to heterologously express GVs in *Salmonella typhimurium* (Fig. 6-4a). Upon induction with N-($\beta$-ketocaproyl)-L-homoserine lactone (AHL), Salmonella formed numerous intracellular GVs, which were visualized under TEM and seen to typically cluster into distinct subcellular regions (Fig. 6-4b). This pattern was expected to perturb the electromagnetic wavefront passing through a GV-expressing Salmonella cell so as to produce a distinct pattern in phase images, as shown in simulated holograms (Fig. 6-4c, Supplemental Text).

As expected, under DHM, GV-expressing Salmonella exhibited clear phase contrast that was different from control cells in which the GVs had been collapsed with hydrostatic pressure[28]. Phase values of interior cellular regions of 50 GV-expressing salmonella cells were analyzed and found to exhibit an average phase value of $0.06\pm0.05\pi$ (95% C.I., $n$ = 50 cells) (Fig. 6-4d & 6-4f). The subcellular

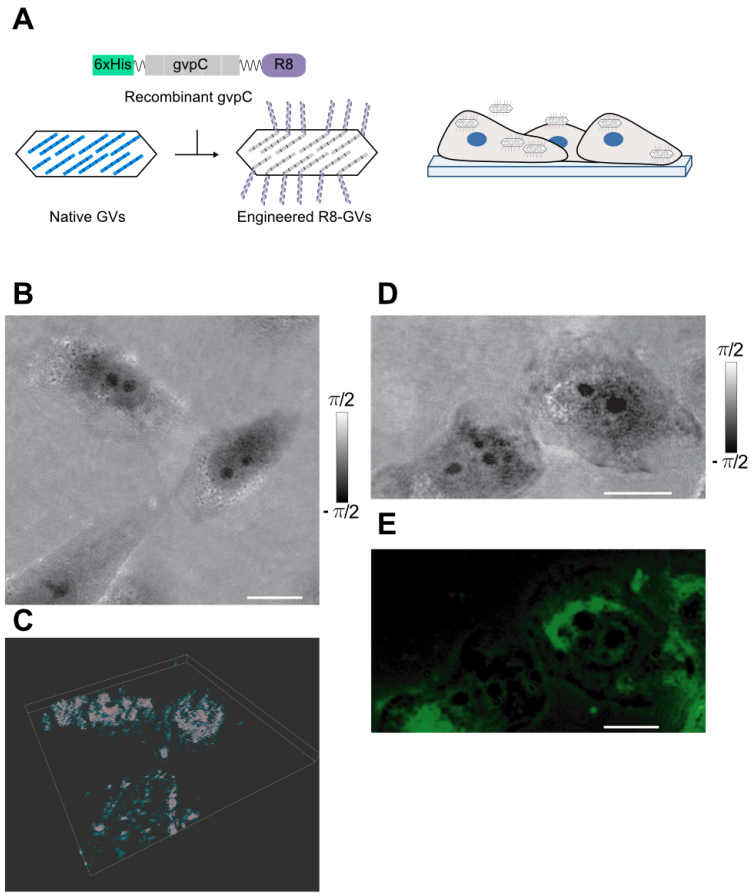


**Figure 6-3: DHM imaging of mammalian cells labeled with engineered gas vesicles.** (a) Diagram of engineered GVs genetically functionalized with R8 peptides for attachment to and internalization by mammalian cells. Illustration of mammalian cells labeled with R8-GVs. (b) DHM phase image of CHO cells labeled with R8-GVs. Scale bar represents 25 μm. (c) Pseudocolored 3D rendering of GVs decorating CHO cells. For details see supplemental text. (d) Phase image of CHO cells labeled with Alexa Fluor 488 conjugated R8-GVs under the high power DHM showing positive phase contrast in correspondence with (e) a fluorescence image of the same CHO cells. All scale bars represent 25 μm.

regions of these cells which contained high GV concentrations exhibited even higher phase values of 0.42±0.10$\pi$ (95% C.I., $n$ = 110 sub-cellular regions). The phase values of interior cellular regions of 50 GV-expressing Salmonella cells after their GVs were hydrostatically collapsed were measured to be -0.06±0.10$\pi$ (95% C.I., $n$ = 50 cells) (Fig. 6-4e & 6-4f). The histogram of all pixels in Salmonella cells with and without GVs illustrates increased phase contrast due to GV-expression (Fig. 6-4g). GV-expression increased the average signal to noise ratio of Salmonella cells in phase images by more than three-fold, making the cells easier to detect in solution.

Our results demonstrate that GVs serve as molecular and genetically encodable contrast agents for phase imaging due to the large difference in their index of refraction compared with aqueous media and organelles, resulting in positive phase contrast. The opposite sign of their refractive index difference from water compared to most other biological structures is especially beneficial for studying small samples such as microorganisms or subcellular features. The rapid volumetric image acquisition of DHM makes it possible to identify and dynamically track GVs in a mixed solution containing other particles. In addition, the modular protein make-up of GVs enables protein engineering to confer novel targeting properties for cellular imaging. This may facilitate future studies of cell-nanoparticle interactions and other dynamic cellular processes. Furthermore, introducing GV gene encoded phase contrast allows cells to activate the expression of these reporter genes and to be distinguished from cells without reporter expression. These studies result in a QPI toolkit that will permit specific labeling in a large number of biological scenarios.

## 6.4 Conclusions

While the results presented in this study provide the key scientific evidence supporting the ability of GVs to serve as genetically encoded reporters for phase imaging, future work is needed to apply these agents to specific biological problems. To enable such applications, there exists significant scope for improvement and optimization. In using GVs as a contrast agent for arbitrary samples, phase wrapping must be considered. In a typical QPI system, phase measurements are constrained to a modulo-2$\pi$ (e.g. -$\pi$ to $\pi$). As a result, samples that introduce a phase shift of $\phi = 2\pi + m$, will only be seen to show a phase shift of $m$. Targeted efforts in the development of robust phase unwrapping algorithms will aid in the use of GVs in arbitrarily thick samples, eliminating the loss of contrast due to aliasing[31–36]. Given the ability of GVs to be collapsed with acoustic pressure, additional contrast

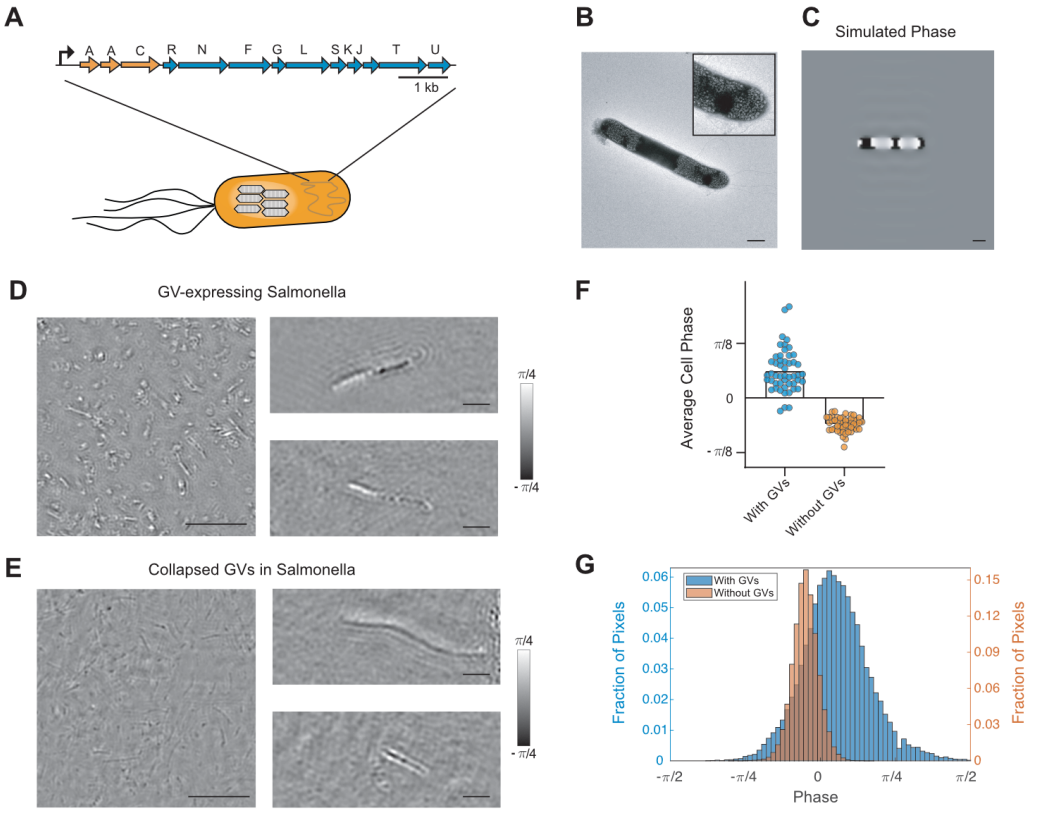


**Figure 6-4: Gas vesicles as genetically encoded phase contrast agents in Salmonella.** (A) Schematic of engineered GV gene cluster comprising genes from *Anabaena flos-aquae* (orange genes) and *Bacillus megaterium* (blue genes) that enable heterologous expression of GVs in *Salmonella typhimurium*. (B) Representative transmission electron micrograph of *S. typhimurium* expressing GVs. Inset is a 2x zoom in of a GV containing region of the salmonella cell. Scale bar represents 1 μm. (C) Numerical simulation of phase images of a GV-expressing Salmonella cell. Scale bar represents 1 μm. (D) Representative phase images of GV-expressing *S. typhimurium* cells under DHM. Two examples of zoomed in images are shown on the right. Scale bars for full field of view are 25 μm, and 5 μm for the zoomed in images. (E) Representative phase images of GV-expressing *S. typhimurium* cells after collapsing GVs using 1.2 MPa of hydrostatic pressure. Two examples of zoomed in images are shown on the right. Scale bars for full field of view are 25 μm, and 5 μm for the zoomed in images. (F) Quantified average phase contrast from *S. typhimurium* cells with intact GVs compared with collapsed GVs ($n$ = 50 cells). (G) Histogram of quantified phase contrast from all pixels in *S. typhimurium* cells with intact GVs ($n$ = 50 cells) compared with collapsed GVs ($n$ = 50 cells).

specificity could be obtained by integrating the ability to apply ultrasound waves to DHM samples *in situ* and monitoring the resulting change in phase[24,26,28]. In addition, the engineering of GV variants that collapse under different applied pressures may enable multiplexed phase contrast imaging. Furthermore, while genetic encoding facilitates the use of GVs to study genetically tractable organisms, there is also substantial interest in using DHM for field studies, taking advantage of the microscopes' robust solid-state design[37]. In such studies, the relevant microorganisms may be genetically intractable, requiring the development of targeting moieties to bind GVs to such species. Such labeling would additionally facilitate the application of machine learning algorithms to the detection of microorganisms in 4-dimensional data, where low image contrast is currently a challenge[38]. We anticipate that the development of dedicated molecular and genetically encodable contrast agents will usher in a new phase in holographic microscopy.

## 6.5 Methods

**Digital holographic microscopy.** Two instruments were used: a "high power" instrument and a "low power" instrument. The design of the "high power" microscope was a modified Mach-Zehnder as described previously[39], containing identical objective lenses in the object and reference beams. The objective lenses used were Mitotoyo 100x, NA=0.7 dry long working distance objectives, infinity-corrected to an achromatic field lens (200 mm focal length), which was used to form the image on a digital CCD camera (Baumer TXG50-P). The effective magnification of this instrument was 78x. The diffraction-limited lateral resolution was roughly 0.3 μm with a 405 nm illumination source. Illumination was through a single-mode fiber coupled diode laser that was collimated before the first beamsplitter.

The design of the "low power" microscope was a common path Mach-Zehnder as described previously[37,40]. The objectives were simple aspheric lenses (Asphericon) with NA=0.3. The effective magnification was 19.6x with a diffraction limited lateral resolution of 0.8 μm. The wavelength used in this work for both DHM instruments was 405 nm, supplied by a diode laser (Thorlabs S1FC405).

DHM images of GV-labeled mammalian cells were acquired using the "high power" microscope and all other DHM data were collected using the "low power" microscope.

**Gas vesicle expression, purification and clustering.** *Anabaena flos-aquae* (CCAP strain 1403/13F) was cultured for 2 weeks in Gorham's media supplemented with BG-11 solution (Sigma) and 10 mM $NaHCO_3$ at 25°C, 100 rpm under 1% $CO_2$

and a 14 hours light/10 hours dark cycle[29]. At confluency, the buoyant cell fraction was isolated by floating to the top of a separating funnel over a 48h period, after which the subnatant was discarded. The collected cells were then lysed using 500 mM sorbitol and 10% Solulyse solution (Genlantis). GVs were purified through repeated rounds of isolating the buoyant fraction through centrifugation and resuspension in PBS.

GV clusters were prepared by first biotinylating purified GVs with $10^5$ molar excess of EZ-Link Sulfo-NHS-LC-biotin (Thermo Scientific) in PBS for 4 hours. Afterwards, the sample underwent two rounds of overnight dialysis in PBS. The biotinylated GVs were then clustered by incubation with streptavidin (Geno Technology) for 30 minutes at room temperature at a streptavidin to GV molecular ratio of 100:1.

**Dynamic light scattering.** The hydrodynamic size of the GVs, GV clusters and alumina beads was measured in 50 $\mu$L samples at $OD_{500}$=0.2 using a Zeta-PALS analyzer (Brookhaven Instruments). Samples were mixed thoroughly and measured five times for each reported hydrodynamic diameter.

**Engineered gas vesicles for cell labelling.** Genetically engineered GVs were prepared using a previously described protocol[28]. In brief, the GvpC DNA sequence from *Anabaena flos-aquae* was codon-optimized for *E. coli* expression and cloned into a pET28a(+) plasmid (Novagen) with an N-terminal hexahistidine-tag and C-terminal GSGRRRRRRRR sequence. Plasmids were transformed into BL21(DE3) cells (Invitrogen), which were induced to express the recombinant GvpC for 6 hours at 30°C. GvpC contained in inclusion bodies was purified by lysing the cells using 10% Solulyse (Genlantis) supplemented with DNaseI (10 $\mu$g/mL) and lysozyme (400 $\mu$g/mL) at room temperature. Inclusion bodies were recovered by centrifugation at 27,000g for 15 min. The inclusion body pellets were resuspended in 20 mM Tris-HCl buffer with 500 mM sodium chloride and 6 M urea (pH=8.0) and incubated with Ni-NTA resin (Qiagen, Valencia, CA) for 2 hours at 4°C. After washing, proteins were eluted using 250 mM imidazole.

Purified GVs were treated with 6 M urea and 20 mM Tris-HCl (pH=8.0) to remove their wild-type GvpC. The stripped GVs were isolated with two rounds of centrifugally assisted buoyancy purification in urea. Purified polyarginine modified-GvpC was then added according to the formula: 2 x optical density x 198 nM x liters GVs = nmol of recombinant GvpC and dialyzed in PBS for 8 hours. $10^5$ molar excess of Alexa Fluor 488 NHS (Thermo Fisher) was then added to the GVs and incubated at room temperature for 4 hours under gentle rotation, before being

quenched with 20 mM Tris-HCl (pH=8.0) and dialyzed in PBS to remove excess dye.

**Cell culture and gas vesicle labeling.** Chinese hamster ovary cells (CHO-K1; ATCC) were cultured in DMEM (Corning) with 10% FBS (Thermo Fisher) and penicillin/streptomycin (Corning). Coverslips (18x18 mm) were sterilized with 70% ethanol, washed twice in PBS and placed in 6-well plates. Fibronectin (Sigma) was diluted 1:20 in PBS and 200 $\mu$L were added to each well over the entire surface of the coverslip and incubated for 1 hour at room temperature. Excess solution was aspirated, and CHO-K1 cells were seeded on the coverslips and grown to 75% confluency.

For GV labeling, the surface of a 6-well plate was covered with paraffin and UV sterilized. Then, 300 $\mu$L of 37°C DMEM media and 300 $\mu$L of 114 pM (36.6 $\mu$g/mL or $OD_5$00=1) of R8-GVs was added to the bottom of the well and mixed. The cells cultured on coverslips were inverted onto the DMEM and GV mixture, so the cells were facing the bottom of the plate. The coverslips and GVs were incubated at 37°C. Following incubation, the cells were washed three times with 200 $\mu$L of PBS and fixed with 1 mL of formaldehyde for 30 minutes. The coverslips were mounted using Diamond Antifade mountant (Thermo Fisher) and sealed using clear nail polish.

**Fluorescence imaging.** Fluorescence images were taken on an Olympus IX-71 inverted microscope using Hg lamp illumination through a 1.4 NA oil immersion objective and using the enhanced green fluorescent protein filter set (Chroma). To register fluorescence images with phase images, a 1-$\mu$m tip glass pipette was secured to the specimen and cells were imaged in the vicinity of the tip across the two instruments.

**Gas vesicle expression in Salmonella.** GV expression in *Salmonella typhimurium* (strain ELH1301) cells was performed as described previously[26]. Briefly, the hybrid GV gene cluster, under the control of the luxI promoter (addgene 106475), was transformed into *S. typhimurium* cells. Monoclonal cells from an individual plated colony were cryostocked. Cells containing the GV genes were grown in 5 mL of 2xYT media with 50 $\mu$g/mL kanamycin for 16 hours at 37°C, 250 rpm. Cultures in 50 mL 2xYT media with 50 $\mu$g/mL kanamycin were then inoculated with 500 $\mu$L of the starter culture and grown on the shaker at 37°C until $OD_{600}$=0.4 to 0.6. These cultures were induced with 3 nM N-($\beta$-ketocaproyl)-L-homoserine lactone (AHL) and then grown for 22 hours at 30°C, 250 rpm. Cells were then harvested by centrifugation at 300g at 30°C for 2 hours. The buoyant cell fraction was transferred

into clean tubes. To collapse the GVs inside cells, GV-expressing salmonella were placed in a quartz cuvette (Hellma Analytics) connected to a $N_2$ cylinder through a pressure controller (Alicat Scientific) set to 1.2 MPa.

**TEM sample preparation and imaging.** Electron microscopy was performed at the Beckman Institute Resource Center for Transmission Electron Microscopy at Caltech. Purified GVs were diluted to $OD_{500}$=0.2 in 10 mM HEPES buffer and Salmonella cells were diluted to $OD_{600}$ 0.2 in 10 mM HEPES buffer or PBS. Samples were then spotted on Formvar/Carbon 200 mesh grids (Ted Pella), which were rendered hydrophilic by glow discharging (Emitek K100X). Purified GV samples were stained with 2% uranyl acetate, while cells were imaged unstained. Image acquisition was performed using a Tecnai T12 Lab6 120 kV transmission electron microscope equipped with a Gatan Ultrascan 2k x 2k CCD camera.

**Simulations.** Holograms were simulated with MATLAB (R2017b) using a custom hologram simulation routine. First, a two-dimensional projection image was created using a series of Radon Transforms, modeling a typical GV-expressing Salmonella cell as a cylinder, with a diameter of 1 $\mu$m and a length of 5 $\mu$m, with bands of lower refractive index corresponding to areas dense in GVs as seen in TEM images. This projection is then downsampled, via bicubic interpolation, in order to accommodate and emulate the diffraction limited resolution of the low-power DHM instrument. Within this projection, GVs were simulated using index of refraction values of 1.00. Other intracellular areas were simulated using an index of refraction of 1.37. The index of refraction used to simulate the cell's surrounding medium is 1.33.

The wavefront perturbations as a result of a collimated plane wave passing through the simulated cell is then propagated using the angular spectrum method[41]. The resulting diffracted wavefront is numerically propagated and recombined with a reference (undisturbed) plane wave in order to simulate an off-axis hologram. Code for the simulator is provided in the Supplemental Material. The simulated holograms were reconstructed into phase images using the commercially available software KOALA (LynceeTec). No image noise was added to the simulation besides quantization noise when the holograms were saved as unsigned 8-bit image files whereas in reality there are numerous sources of noise including, but not limited to, photon 'shot' noise, temporal and spatial noise due to changes in the coherence of the illumination laser, as well as various sources of noise introduced by the digital CCD used to record the holograms[10].

**Tracking.** Tracking of GVs and alumina beads was performed using the

Manual Tracking plug-in in the open source image analysis tool FIJI[42].

**Phase quantification of Salmonella cells.** Data recorded using the DHM system was reconstructed into phase images using the commercially available software Koala (LynceeTec). Raw 8-bit phase images were reconstructed with quantitative phase bounds of $-\pi$ to $\pi$ corresponding to pixel values of 0 and 255, respectively (described in supplementary text). After reconstruction, cell boundaries were identified with the freehand selection tool of the open source image analysis software FIJI by team members blinded to the identity of the sample. The cell boundaries were used to isolate the interior pixel values within the cell by creating a binary mask about the cell boundary. These interior pixel values were converted from their 8-bit values to quantitative phase values and analyzed using MATLAB (2017b).

## References


1. Farhadi, A. *et al. Genetically encoded phase contrast agents for digital holographic microscopy* 2019.
2. Dubois, F. *et al.* Digital holographic microscopy for the three-dimensional dynamic analysis of in vitro cancer cell migration. *Journal of biomedical optics* **11,** 054032 (2006).
3. Miniotis, M. F., Mukwaya, A. & Wingren, A. G. Digital holographic microscopy for non-invasive monitoring of cell cycle arrest in L929 cells. *PloS one* **9,** e106546 (2014).
4. Jourdain, P. *et al.* Determination of transmembrane water fluxes in neurons elicited by glutamate ionotropic receptors and by the cotransporters KCC2 and NKCC1: a digital holographic microscopy study. *Journal of Neuroscience* **31,** 11846–11854 (2011).
5. Kemper, B. *et al.* Investigation of living pancreas tumor cells by digital holographic microscopy. *Journal of biomedical optics* **11,** 034005 (2006).
6. Pavillon, N. *et al.* Early cell death detection with digital holographic microscopy. *PloS one* **7,** e30912 (2012).
7. Rappaz, B., Breton, B., Shaffer, E. & Turcatti, G. Digital holographic microscopy: a quantitative label-free microscopy technique for phenotypic screening. *Combinatorial chemistry & high throughput screening* **17,** 80–88 (2014).
8. Sheng, J. *et al.* Digital holographic microscopy reveals prey-induced changes in swimming behavior of predatory dinoflagellates. *Proceedings of the National Academy of Sciences* **104,** 17512–17517 (2007).
9. Rappaz, B. *et al.* Measurement of the integral refractive index and dynamic cell morphometry of living cells with digital holographic microscopy. *Optics express* **13,** 9361–9373 (2005).
10. Bedrossian, M., Nadeau, J., Serabyn, E. & Lindensmith, C. *Sources and propagation of errors in quantitative phase imaging techniques using optical interferometry* in *Quantitative Phase Imaging III* **10074** (2017), 100740E.
11. Atanasova, M. *et al.* Brewing yeast viability measured using a novel fluorescent dye and image cytometer. *Biotechnology & Biotechnological Equipment,* 1–11 (2019).
12. LV, W. *et al.* Long-Term Tracking of Cancer Cell Nucleus and Identification of Colorectal Cancer with an Aggregation-Induced Emission-Based Fluorescent Probe. *Journal of biomedical nanotechnology* **15,** 1033–1042 (2019).
13. Papadopoulos, J. & Müller, T. J. Rapid synthesis of 4-alkynyl coumarins and tunable electronic properties of emission solvatochromic fluorophores. *Dyes and Pigments* (2019).

14. Xue, J., Li, Z., Xu, H. & Pu, Y. *A novel fluorescent gold nanoparticle inhibiting migration and invasion of tumor cells* in *Reporters, Markers, Dyes, Nanoparticles, and Molecular Probes for Biomedical Applications XI* **10893** (2019), 108930S.

15. Gaigalas, A. K., Choquette, S. & Zhang, Y.-Z. Measurement of scattering and absorption cross sections of dyed microspheres. *Journal of research of the National Institute of Standards and Technology* **118,** 15 (2013).

16. Cherkezyan, L. *et al.* Targeted alteration of real and imaginary refractive index of biological cells by histological staining. *Optics letters* **37,** 1601–1603 (2012).

17. Rappaz, B., Charrière, F., Depeursinge, C., Magistretti, P. J. & Marquet, P. Simultaneous cell morphometry and refractive index measurement with dual-wavelength digital holographic microscopy and dye-enhanced dispersion of perfusion medium. *Optics letters* **33,** 744–746 (2008).

18. Nadeau, J. L., Cho, Y. B., Kühn, J. & Liewer, K. Improved tracking and resolution of bacteria in holographic microscopy using dye and fluorescent protein labeling. *Frontiers in chemistry* **4,** 17 (2016).

19. Nadeau, J. L., Cho, Y. B. & Lindensmith, C. A. Use of dyes to increase phase contrast for biological holographic microscopy. *Optics letters* **40,** 4114–4117 (2015).

20. Pfeifer, F. Distribution, formation and regulation of gas vesicles. *Nature Reviews Microbiology* **10,** 705 (2012).

21. Walsby, A. E. Gas vesicles. *Microbiology and Molecular Biology Reviews* **58,** 94–144 (1994).

22. Shapiro, M. G. *et al.* Biogenic gas nanostructures as ultrasonic molecular reporters. *Nature nanotechnology* **9,** 311 (2014).

23. Shapiro, M. G. *et al.* Genetically encoded reporters for hyperpolarized xenon magnetic resonance imaging. *Nature chemistry* **6,** 629 (2014).

24. Lu, G. J. *et al.* Acoustically modulated magnetic resonance imaging of gas-filled protein nanostructures. *Nature materials* **17,** 456 (2018).

25. Farhadi, A. *et al.* Recombinantly expressed gas vesicles as nanoscale contrast agents for ultrasound and hyperpolarized MRI. *AIChE Journal* **64,** 2927–2933 (2018).

26. Bourdeau, R. W. *et al.* Acoustic reporter genes for noninvasive imaging of microorganisms in mammalian hosts. *Nature* **553,** 86 (2018).

27. Farhadi, A., Ho, G. H., Sawyer, D. P., Bourdeau, R. W. & Shapiro, M. G. Ultrasound Imaging of Gene Expression in Mammalian Cells. *Science* **365,** 1469–1475 (2019).

28. Lakshmanan, A. *et al.* Molecular engineering of acoustic protein nanostructures. *ACS nano* **10,** 7314–7322 (2016).

29. Lakshmanan, A. *et al.* Preparation of biogenic gas vesicle nanostructures for use as contrast agents for ultrasound and MRI. *Nature protocols* **12,** 2050 (2017).

30. Brock, R. The uptake of arginine-rich cell-penetrating peptides: putting the puzzle together. *Bioconjugate chemistry* **25,** 863–868 (2014).

31. Ghiglia, D. C. & Romero, L. A. Robust two-dimensional weighted and unweighted phase unwrapping that uses fast transforms and iterative methods. *JOSA A* **11,** 107–117 (1994).

32. Kaufmann, G. H., Galizzi, G. E. & Ruiz, P. D. Evaluation of a preconditioned conjugate-gradient algorithm for weighted least-squares unwrapping of digital speckle-pattern interferometry phase maps. *Applied optics* **37,** 3076–3084 (1998).

33. Herráez, M. A., Burton, D. R., Lalor, M. J. & Gdeisat, M. A. Fast two-dimensional phase-unwrapping algorithm based on sorting by reliability following a noncontinuous path. *Applied optics* **41,** 7437–7444 (2002).

34. Bian, Y. & Mercer, B. Weighted regularized preconditioned conjugate gradient (PCG) phase unwrapping method. *Journal of Optics A: Pure and Applied Optics* **11,** 015504 (2008).

35. Zuo, C., Huang, L., Zhang, M., Chen, Q. & Asundi, A. Temporal phase unwrapping algorithms for fringe projection profilometry: A comparative review. *Optics and Lasers in Engineering* **85,** 84–103 (2016).

36. Yu, H., Lan, Y., Yuan, Z., Xu, J. & Lee, H. Phase Unwrapping in InSAR: A Review. *IEEE Geoscience and Remote Sensing Magazine* **7,** 40–58 (2019).

37. Lindensmith, C. A. *et al.* A submersible, off-axis holographic microscope for detection of microbial motility and morphology in aqueous and icy environments. *PloS one* **11,** e0147700 (2016).

38. Bedrossian, M., El-Kholy, M., Neamati, D. & Nadeau, J. A machine learning algorithm for identifying and tracking bacteria in three dimensions using Digital Holographic Microscopy. *AIMS Biophysics* (2018).

39. Kühn, J. *et al.* A Mach-Zender digital holographic microscope with submicrometer resolution for imaging and tracking of marine micro-organisms. *Review of Scientific Instruments* **85,** 123113 (2014).

40. Wallace, J. K. *et al.* Robust, compact implementation of an off-axis digital holographic microscope. *Optics express* **23,** 17367–17378 (2015).

41. Schnars, U. & Jüptner, W. P. Digital recording and numerical reconstruction of holograms. *Measurement science and technology* **13,** R85 (2002).

42. Schindelin, J. *et al.* Fiji: an open-source platform for biological-image analysis. *Nature methods* **9,** 676 (2012).

43. Schnars, U. & Jüptner, W. P. Digital recording and numerical reconstruction of holograms. *Measurement science and technology* **13,** R85 (2002).

## 6.6 Supplementary Information

### Image Processing and Handling.

In the analysis of off-axis holograms, image reconstruction and post-processing steps are necessary in order to interpret the electric field intensity recorded in a hologram into a useful three-dimensional data set. Furthermore, post-processing methods are used to de-noise the resulting reconstructed images.

This supplemental text outlines the methods and work flows associated with the processing and handling of off-axis holographic images. This includes the reconstruction process from hologram to phase images, and all de-noising steps used to reach the final images that are presented in the main text above.

**Image Reconstruction.** An off-axis hologram is recorded as a single image that contains interference patterns (or fringes) that contain the 3D information of the sample being imaged. The spatial frequency of the fringes act as the carrier frequency of this information. In order to reconstruct this information into a usable form, the high spatial frequency information in the hologram must be isolated. Supplementary Figure 6-S1a shows an example hologram, its Fourier Transform plotted on a logarithmic scale (note the high frequency 'lobes' which contain the 3D information of the sample (Supplementary Figure 6-S1b), the same Fourier transform that has been multiplied by a binary mask to isolate one of the high frequency lobes (Supplementary Figure 6S-1c), and that isolated lobe that has been shifted to the center of the Fourier Transform (Supplementary Figure 6-S1d).

In the formation of an off-axis hologram, two collimated beams of light are recombined at the digital detector at an angle (off-axis of each other). This off-axis recombination causes interference between the two beams. The spatial frequency of these fringes is proportional to the wavelength of light used as well as the recombination angle. If the two beams of light are named the 'specimen' and 'reference' beam where the 'specimen' beam interacts with the sample being imaged, and the 'reference' beam remains undisturbed, then the resulting hologram can be represented mathematically as the superposition of the two beams at the detector (Equation 6.1).

$$S(x, y) = A_S * e^{i(\Phi_S(x,y)-\omega t)} \tag{6.1a}$$

$$R(x, y) = R_S * e^{i(\Phi_R(x,y)-\omega t)} \tag{6.1b}$$

$$\Psi(x, y) = S(x, y) + R(x, y) \tag{6.1c}$$

$$h = \int \Psi\Psi^* dt = (I_S + I_R) + SR^* + S^*R \tag{6.1d}$$

where $A_S$ and $A_R$ are the amplitudes of the Specimen and Reference beam, $\Phi_S$ and $\Phi_R$ are the phase differences between the specimen and reference beams, $\Psi$ is the resulting wave from the superposition of the specimen and reference beams, and h is the hologram.

In Supplementary Figure 6-S1b there are three discrete lobes present. The center most lobe corresponds to the summation of intensities of the specimen and reference beams ($I_S + I_R$) from equation 6.1d, while the two higher spatial frequency lobes correspond to $SR^*$ and $S^*R$ from Equation 6.1d. These two lobes are complex conjugates of each other, but for the purposes of this work, the lobe corresponding to $SR^*$ is the chosen lobe to be isolated in Supplementary Figure 6-S1c & S1d.

With the 3D information encoded in the hologram isolated, it is then convolved with the discrete solution to the Fresnel Diffraction Integral (G) as described by Schnars, *et al*.[43] The reconstructed complex wavefront Γ is

$$\Gamma(x, y, z) = \mathfrak{F}^{-1}[\mathfrak{F}(h(x, y)) * G(z)] \tag{6.2a}$$

$$G(z) = exp\left[\frac{-2\pi i z}{\lambda}\sqrt{1 - \frac{\lambda^2(n + \frac{N^2\Delta x^2}{2z\lambda})^2}{N^2\Delta x^2} - \frac{\lambda^2(m + \frac{N^2\Delta y^2}{2z\lambda})^2}{N^2\Delta y^2}}\right] \tag{6.2b}$$

$$A(x, y, z) = |\Gamma(z)| \tag{6.2c}$$

$$\Psi(x, y, z) = arctan(\frac{\mathfrak{F}(\Gamma(z))}{\Re(\Gamma(z))}) \tag{6.2d}$$

where $\mathfrak{F}$ is the Fourier Transform operator, the amplitude image is calculated as the magnitude of the complex wavefront Γ, and the quantitative phase image Ψ is defined as the inverse tangent of the imaginary parts of Γ divided by the real parts of Γ. The function G is a pure phase object that describes the propagation of an electric field through the focal plane (z) and can be modulated to calculate the reconstructed wavefront throughout an entire volume. For a more in-depth derivation of this function, see Schnars, *et al*[43].

**Post-Processing.** With the reconstructed amplitude $A(x, y, z, t)$, and phase images $\Psi(x, y, z, t)$, post-processing is necessary to eliminate noise from various sources including, but not limited to, photon/shot noise, speckle noise, digitization noise, as well as detector noise. In addition, low spatial frequency artifacts are also common in phase reconstructions due to tilt in the sample chamber relative to the optical axis as well as objective lens curvature.

To remove as much noise from the reconstructed images as possible, temporally averaged images are calculated and subtracted from each phase image, as well as

conducting spatial frequency band-pass filtering. In the subtraction of temporally averaged phase (referred to as 'mean subtraction'), the mean of each pixel location is calculated through time. This mean image is then subtracted from the image used to calculate that mean. This effectively removes any stationary artifacts from the image highlighting any transient particle in the image.

After this mean subtraction, band-pass filtering is done to remove any low and high spatial frequency noise from the images. Low spatial frequency noise can be caused by tilt in the sample chamber relative to the optical axis, as well as by the curvature of the lenses used in the DHM instrument. Because the DHM is an instrument that is capable of achieving diffraction limited resolution, there is a physical limit of the spatial frequencies that can be recorded. This presents a clear upper limit to the spatial frequencies that carry useful information in the image. Any higher frequency artifacts in the image are by definition pure noise and can be filtered out.

Because the phase images obtained using off-axis DHM are of a quantitative nature, this is the extent of the post-processing performed in order to preserve the quantitative information contained in the image. Other methods are more useful in enhancing contrast and suppressing noise but were not performed in this work.

**Physical Properties**

| Property | GV Cluster (air) | Alumina | Water |
|---|---|---|---|
| **Density** ($kg/m^3$) | 1.2 | 2700 | 1000 |
| **Viscosity** ($Ns/m^2$) | - | - | $8.9\times10^{-4}$ |

**Hologram Simulator**

The optical theory used in the MATLAB code discussed in this document are well reviewed by Schnars, *et al.*[43]. The main function ('OAhologramSimulator.m') expects as an input, two variables. The first is called 'waveFront'. This is a complex matrix of the size of the final image. This matrix describes the normalized amplitude and phase of the electric field of the sample we wish to simulate. For the purposes of this manuscript, the variable 'waveFront' is provided in the file 'waveFront.mat'. The second input variable is 'desiredFileName', which is the desired file path and name of the output. The output is the final 8-bit TIFF hologram.

The variable 'waveFront' is generated by creating two 3-dimensional matrices of the electric field attenuation and the index of refraction of light that passes through a cylindrical simulated 'salmonella cell' with the morphology as shown in the main manuscript.

With the two 3D matrices, a series of radon transforms are used to project a collimated beam of light through the object. These projections are then used to calculate the resultant wave front as a result of the projected electric field attenuation and phase delay (introduced by the index of refraction matrix).

The hologram simulation code can be separated and described in eight sections.

**1 DHM Parameters**

This section establishes the optical performance parameters of the DHM instrument that is to be simulated. In this implementation, the off-axis holograms that are being simulated are of the 'low-power' instrument and have the appropriate performance parameters for that instrument.

Note that the numerical aperture of the objective lenses is not necessary because the geometric properties of the objective lens is inputted as 'fl' and 'DiaLens' (lens focal length and lens diameter, respectively).

**2 Create the undisturbed reference beam**

This section creates the reference wave. The reference wave by definition is undisturbed and unattenuated and thus the reference wave is a simple matrix of ones.

**3 Propagate target and ref to lens object focal plane**

This section takes the input variable 'waveFront' and the newly created reference wave front 'U2ref' and propagates the two waves to the focal plane of the objective lens. The propagation of the two waves is conducted using the Angular Spectrum Method (ASM) as described in Schnars, *et al*[43]. The propagation is done by calling an external function 'ang_spec_prop.m'. The output of this section are the variables 'U3' and 'U3ref', corresponding to the propagated wave front of the sample (U3) and reference (U3ref).

**4 Propagate to the lens**

This section takes the output from the previous section and propagates the two wave fronts to the objective lens. This section uses the same external function as the previous section. The outputs are 'U4' and 'U4ref'

**5 Simulate the phase delay introduced by the lens**

This section models an ideal objective lens that introduces a phase delay into light as it travels through the lens. This simulates an ideal lens because it introduces no wave front aberrations or electric field attenuation.

In addition to simulating the phase delay caused by the objective lens, it applies this phase delay to 'U4' and U4ref'. The output of this section is 'Alens' and 'Alensref'.

**6 Propagate to focal plane**

This section takes the output of the previous section and propagates the two wave fronts to the back focal plane of the objective lens. The outputs of this section are the variables 'U5' and 'U5ref'.

**7 Combine wavefront with reference wave**

This section acts as the relay lens of the 'low-power' instrument by recombining the object wave front (U5) with the reference wave front (U5ref) as well as introducing a tilt angle between them so that they create interference patterns at the 'detector'. The output of this section becomes a single complex wave front 'Uccd'.

**8 Generate and save the hologram**

Because optical detectors such as CCD's only image electric field intensities, the intensity of 'Uccd' is calculated and saved as an 8-bit TIFF image with the file path and location inputted at the very beginning of this routine.

**3D Pseudo-Colored Rendering**

The 3D rendering was generated using the commercially available software ARIVIS Vision4D. This software allows the import of a multidimensional image that is to be visualized in a variety of ways. The 2D images that comprise the 3D image stack used in ARIVIS were first processed using the methods described in the Image Processing & Handling section of this document. These processed images were then thresholded using a user defined threshold. Next the magnitude of the image gradient was calculated and stored as a separate stack of 2D images. The two 3D image stacks were then imported to ARIVIS Vision4D. The pixel values were plotted using a pseudo-colored lookup table. The opacity of each pixel was plotted as a weighted function of the magnitude of the image gradient at that pixel. This was done to highlight areas of large changes in phase signal within the cell.

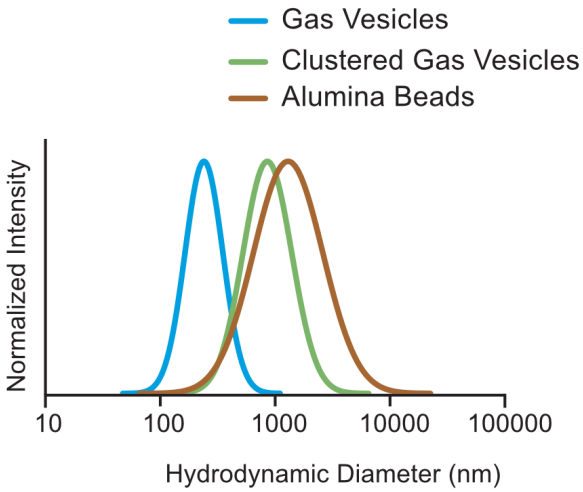


**Figure 6-S1:** Representative dynamic light scattering of the hydrodynamic diameter of pristine gas vesicles, clustered gas vesicles and alumina beads.

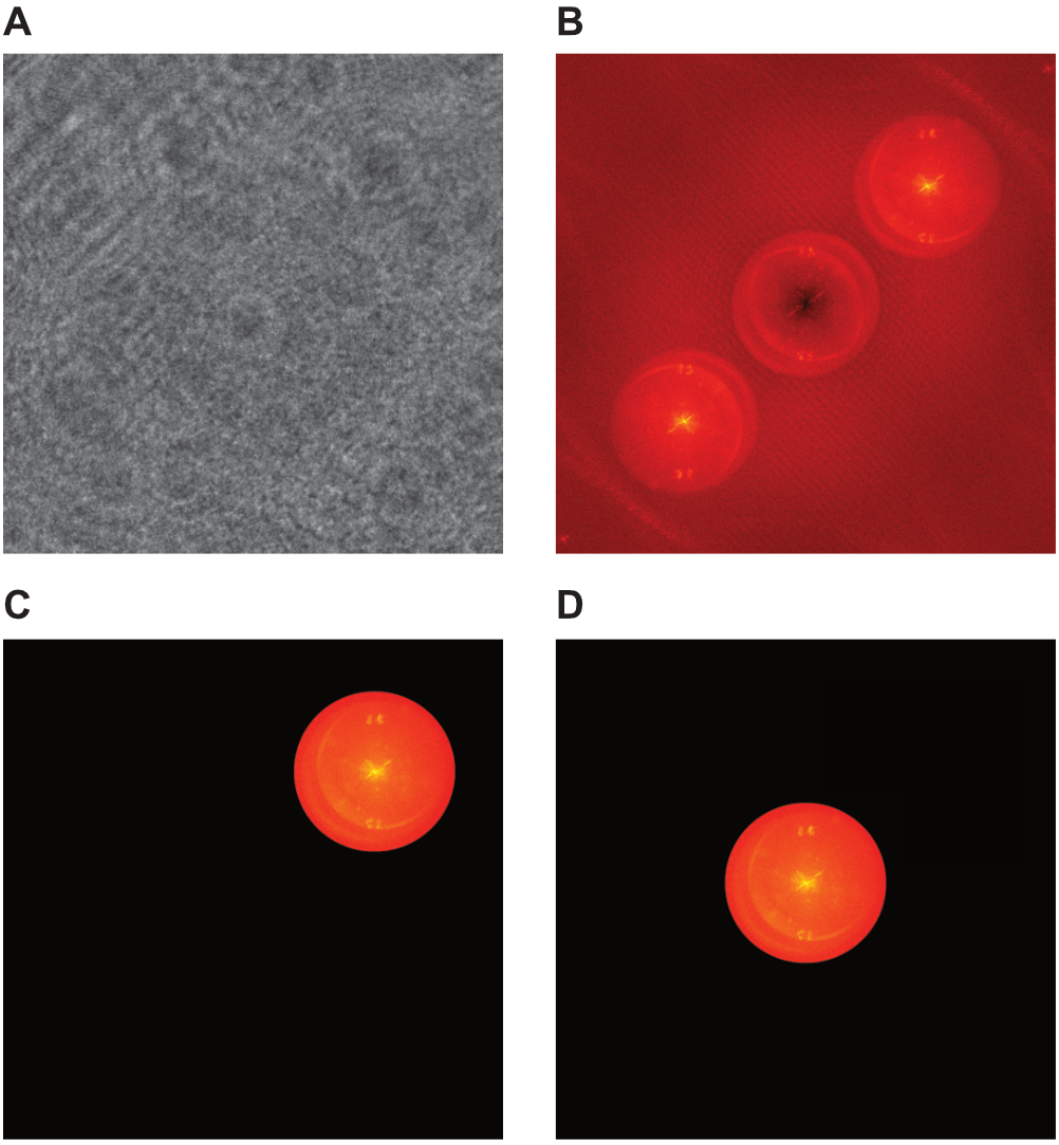


**Figure 6-S2:** The workflow for the initial processing of holographic data. (a) A raw hologram. (b) The Fourier Transform of the raw hologram, plotted on a logarithmic scale. (c) The Fourier Transform of the hologram multiplied by a mask to isolate one of the high spatial frequency lobes. (d) The isolated lobe from (c) that has been linearly shifted to the center.

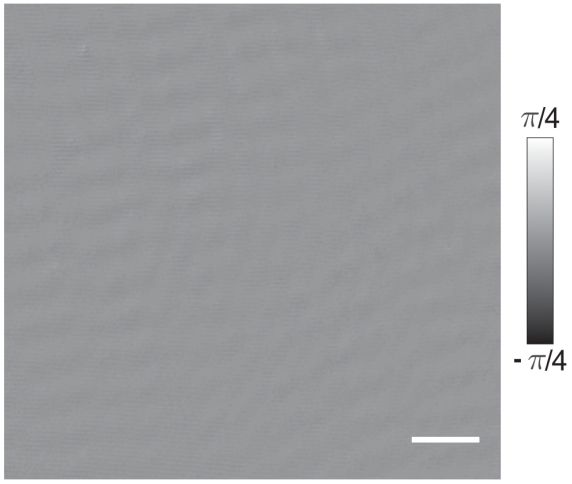


**Figure 6-S3:** Representative phase DHM images of clustered GVs collapsed using 1.2 MPa of hydrostatic pressure. Scale bars represent 25 μm.

*Chapter 7*

# TOWARDS ROUTINE ULTRASOUND IMAGING OF CELLULAR FUNCTION IN VIVO

This thesis describes some of the initial progress on genetic engineering of gas vesicles and acoustic reporter genes along with applications in magnetic resonance imaging (MRI) and quantitative phase microscopy. Chapter 2 introduced a platform for biomolecular engineering of the acoustic and surface properties of gas vesicles as nanoscale ultrasound contrast agents for delivery to the body. Chapter 3 extended this platform by characterizing the recombinant expression of gas vesicles in common-lab strain bacteria to make the genetic engineering of gas vesicles more versatile, and to increase access for non-specialist labs. In Chapter 4, following our success of developing a hybrid gene cluster that allowed probiotic microbes to express gas vesicles and be visualized with ultrasound imaging *in vivo*[1], we designed the first mammalian acoustic reporter genes – a genetic code that when introduced to mammalian cells enables ultrasound imaging of the cell's gene expression and location deep inside the body. In Chapter 5, the air inside the gas vesicles was used to acquire MRI contrast (based on the magnetic susceptibility mismatch of air and water), and with simultaneous use of ultrasound to collapse the gas vesicles *in situ*, background-free MRI was acquired. Chapter 6 described the ability of the air-filled structure of gas vesicles to interact with light and produce phase contrast for quantitative phase imaging and digital holographic microscopy.

The potential opportunities in biomedical research and medicine for the tools and technologies described above are numerous. However, much work remains for gas vesicles and acoustic reporter genes to be commonly used tools in many laboratories and clinics. Several possible future directions will be discussed below.

**Future directions for mammalian acoustic reporter genes.**

The first generation mammalian acoustic reporter genes (mARGs) should be immediately useful for a number of biological investigations. However, there are challenges that should be addressed in future studies.

mARGs currently encode a gas vesicle variant that produces linear ultrasound signals difficult to detect over the strong linear backscattering of mammalian cells when using conventional ultrasound imaging schemes. To image mARGs, an ultra-

sound scheme was developed that acquires non-linear signal from gas vesicles as they were being collapse with a high-pressure ultrasound pulse. This resulted in a snapshot image. For a follow-up imaging experiment, the same cells will need to re-express gas vesicles, which can take several days, thereby limiting the time resolution of the study. Future designs of mARGs should be detectable using non-destructive imaging schemes. One option would be to further optimize the mARGs to increase the number of gas vesicles expressed per mammalian cells in order to overcome the background signal from the cells; this strategy has been used to image probiotic bacteria in the gastrointestinal tract of mice with bacterial ARGs[1]. To achieve this an approximate increase of two orders of magnitude in gas vesicle expression per cell will be required. Alternatively, a broader search for gas vesicle variants which produce non-linear ultrasound signal that can be expressed in mammalian cells would be desirable. Our initial study was not successful at transferring gas vesicle gene clusters from *Anabaena flos-aquae* and *Halobacterium salinarum* to mammalian cells. The need for non-linear signal merits further investigation into these two gene clusters and the numerous other micro-organisms that encode gas vesicles gene clusters in their genome[2–4].

In many scenarios it would be advantageous to simultaneously image multiple biomolecules or biological processes. Multiplexed ultrasound imaging of mARGs will require additional variants with different physical properties that can be distinguished from each other. Using the collapse-based ultrasound imaging paradigm, one approach could be to design or search for mARG variants that collapse at ultrasound pressures far apart from one another, allowing different populations to be independently collapsed and imaged[5]. Standard signal unmixing algorithms can be used to produce multiplexed images. The accuracy and multiplexability of this approach will rely on gas vesicle variants that collapse over a narrow range of ultrasound pressures in order to reduce spectral overlaps. Alternatively, if mARG variants can be engineered to produce non-linear ultrasound without the need to be collapsed, using some of the strategies discussed above, the added ultrasound signature can be used to unmix their signals. An example experiment would acquire amplitude modulation images, to detect the new mARG variant, and a collapsed-based ultrasound image to reveal both mARG variants; spectral unmixing can produce post-processed duplexed images.

To advance the utility of mARGs beyond cell lines, future studies should engineer mARGs for viral delivery to primary cells for *in vitro* and *in vivo* investigations. Currently, mARGs are encoded by three gene cassettes that can be packaged in a

single adenovirus for gene delivery. However, more commonly used viral vectors (namely adeno-associated and lenti virus) contain smaller genome size[6] and require mARGs to be divided among different virons. Lentivirus should be a suitable starting point as it can deliver a genetic payload up to 8-10 kilo-basepairs, allowing the three mARG cassettes to fit into two virons that transduce the same cell. The challenge may be that the heterogeneity in viral transduction will result in a mosaic genetic delivery that would cause variable transgene-expression in cells. To make the system more robust, future studies should consolidate the mARG architecture to fit inside a single lentivirus genome. This can be achieved by optimizing the stoichiometry of gas vesicle genes to eliminate the need for duplicate booster genes.

**Future directions for injectable acoustic biomolecules.**

Ultrasound is one of the most widely used medical imaging modalities in clinics. The few contrast agents available for ultrasound limits its impact on functional and molecular imaging, which are important for many biomedical applications. The work in this thesis describes gas vesicles as injectable nanoscale ultrasound contrast agents. However, for gas vesicles to be widely adopted as the standard injectable ultrasound contrast agent, several challenges will need to be addressed.

It is expected that the size of gas vesicles will affect their behavior in complex biological environment of the body[7,8] and will affect the intensity of the backscattered ultrasound. Accordingly, the size distribution of recombinantly expressed gas vesicles should ideally be narrow and preferably tunable. In Chapter 3, the size distribution of recombinantly expressed gas vesicles was measured. The diameter of these gas vesicles was tightly centered at 59 ± 9 nm but their length had a broad distribution centered around 129 ± 70 nm. To control the length of gas vesicles in cells the process of nucleation and elongation into fully formed gas vesicles needs to be tuned[3]. One approach to expressing uniform gas vesicles is to develop genetic circuits that initially favor the nucleation process and then switch to the elongation phase. Alternatively, the rate of nucleation could be reduced relative to the elongation rate. This would bias the system towards the elongation of the particles if the nucleation rate is much slower than the elongation rate. The length of gas vesicles would be dictated by the steady-state of the two rates. Both of these approaches will need to account for the effects of cellular growth and division on the assembly of the gas vesicles inside the cell. Engineering of the gas vesicle gene circuits will require biochemical understanding of the role that different gas vesicles proteins play in the nucleation and elongation processes.

Gas vesicles as injectable contrast agents for *in vivo* ultrasound imaging will benefit from optimization of their surface properties to increase their circulation time inside the body[7,8]. Over two decades of investigations on various nanoscale particles have resulted in general strategies for reducing the clearance of nanoparticles from the body via the renal and reticuloendothelial systems (RES). Using single-photon emission computerized tomography (SPECT imaging) we have determined that gas vesicles are minimally cleared through the renal system[9]. This is expected due to their hydrodynamic diameter being larger than the fenestrations in the renal system. Future work should focus on reducing gas vesicles' RES clearance rate. To do so the surface charge (zeta potential) of gas vesicles should be slightly negative but close to neutral (-20 to 0 mV)[8]. In Chapter 3, recombinantly expressed gas vesicles were measured to have a zeta potential of -32.8 ± 10 mV. Genetic methods similar to Chapter 2 or bioconjugate chemistries can be used to engineer gas vesicles with more desirable zeta potential for *in vivo* applications. Another important parameter to reduce RES clearance of gas vesicles is the protein corona that forms around the nanoparticles as they circulate through the vasculature. The protein corona are serum proteins and antibodies (opsonins) that coat the surface of gas vesicles and assist macrophages and endothelial cells to recognize and clear them. Typical strategies to reduce the protein corona entail decorating the nanoparticle's surface with biopolymers (for example polyethylene glycol)[8]. Future designs that enable gas vesicles to circulate in the bloodstream for several hours will be beneficial to many studies such as brain imaging. With further optimization to extend circulation time to order of days will be exciting for the context of imaging diseases such as cancer.

In conclusion, gas vesicles as acoustic reporter genes and acoustic biomolecules are exciting emerging tools for a great many biological research and medical applications. Gas vesicles' unique physical properties and engineerability makes them an ideal platform for creative and challenging problem solving. It is my hope that future biomolecular engineering will address many of the outstanding challenges discussed in this thesis – allowing gas vesicles to float to new heights.

## References


1. Bourdeau, R. W. *et al.* Acoustic reporter genes for non-invasive imaging of microorganisms in mammalian hosts. *Nature* (2018).
2. Pfeifer, F. in *Complex Intracellular Structures in Prokaryotes* 115–140 (Springer, 2006).
3. Pfeifer, F. Distribution, formation and regulation of gas vesicles. *Nature Reviews Microbiology* **10,** 705–715 (2012).
4. Tashiro, Y., Monson, R. E., Ramsay, J. P. & Salmond, G. P. Molecular genetic and physical analysis of gas vesicles in buoyant enterobacteria. *Environmental microbiology* **18,** 1264–1276 (2016).
5. Walsby, A. E. Gas vesicles. *Microbiology and Molecular Biology Reviews* **58,** 94–144 (1994).
6. Dunbar, C. E. *et al.* Gene therapy comes of age. *Science* **359,** eaan4672 (2018).
7. Albanese, A., Tang, P. S. & Chan, W. C. The effect of nanoparticle size, shape, and surface chemistry on biological systems. *Annual review of biomedical engineering* **14,** 1–16 (2012).
8. Blanco, E., Shen, H. & Ferrari, M. Principles of nanoparticle design for overcoming biological barriers to drug delivery. *Nature biotechnology* **33,** 941 (2015).
9. Le Floc'h, J. *et al.* In vivo biodistribution of radiolabeled acoustic protein nanostructures. *Molecular Imaging and Biology* **20,** 230–239 (2018).